Titre: Title:	Electromagnetic Modeling and Simulation of Anisotropic Structures Using the Equivalent Source Method
Auteur: Author:	Kai Wang
Date:	2019
Type:	Mémoire ou thèse / Dissertation or Thesis
Référence: Citation:	Wang, K. (2019). Electromagnetic Modeling and Simulation of Anisotropic Structures Using the Equivalent Source Method [Thèse de doctorat, Polytechnique Montréal]. PolyPublie. https://publications.polymtl.ca/3976/

URL de PolyPublie: PolyPublie URL:	https://publications.polymtl.ca/3976/
Directeurs de recherche: Advisors:	Ke Wu, & Jean-Jacques Laurin
Programme: Program:	Génie électrique

POLYTECHNIQUE MONTRÉAL
affiliée à l'Université de Montréal

Electromagnetic modeling and simulation of anisotropic structures using the equivalent source method

KAI WANG
Département de génie électrique

Thèse présentée en vue de l'obtention du diplôme de *Philosophiæ Doctor*
Génie électrique

Août 2019

POLYTECHNIQUE MONTRÉAL
affiliée à l'Université de Montréal

Cette thèse intitulée :

Electromagnetic modeling and simulation of anisotropic structures using the equivalent source method

présentée par **Kai WANG**
en vue de l'obtention du diplôme de *Philosophiæ Doctor*
a été dûment acceptée par le jury d'examen constitué de :

Mohammad S. SHARAWI, président
Ke WU, membre et directeur de recherche
Jean-Jacques LAURIN, membre et codirecteur de recherche
Cevdet AKYEL, membre
Abdel Razik SEBAK, membre externe

DEDICATION

To my family and my beloved girlfriend

ACKNOWLEDGEMENTS

I want to express my most sincere gratitude and appreciation to my supervisor, Dr. Ke Wu, and my co-supervisor, Dr. Jean-Jacques Laurin, for their guidance, for their support, for their time, and above all, for their patience throughout the entire course of my PhD study. They have provided me a free and active environment where I can explore the enjoyment of research.

I would like to acknowledge the financial support of China Scholarship Council (CSC) for my 4 year PhD study.

I would like to thank Dr. Mohammad Sharawi, Dr. Abdel Razik Sebak and Dr. Cevdet Akyel for serving as jury members of my PhD examination committee.

I would like to thank the technical team of Poly-Grames, Mr. Jules Gauthier, Mr. Traian Antonescu, Mr. Steve Dube and Mr. Maxime Thibault, for their perfect work and help.

I would like to thank Mr. Jean-Sébastien Décarie for the assistance of software problems, also Mrs. Rachel Lortie and Mrs. Nathalie Lévesque for the administrative procedures of the department.

Many thanks to my friends, Desong Wang, Xiaoqiang Gu, Tongfeng Guo, Wentao Lin, Yunlong Lu, Gaoming Xu, Chunmei Liu, Tao Zhang, Pierre-Luc Theriault etc., in Montreal, I can't forget the time we spent together in the gym, in the badminton court, on the football pitch. I also thank Dr. Chao Li and Dr. Mohamed A. Moharram for their constructive and helpful discussions about my research.

I would like to thank my parents and my sister for their support, endless love, understanding and encouragement throughout my entire PhD time. Finally, I want to express my deepest love and thanks to my girlfriend Shuzhen Yan for her love, company and patience during many days and nights.

RÉSUMÉ

Le développement de nouvelles technologies de fabrication ouvre de nouvelles possibilités au niveau du développement de matériaux possédant des anisotropies complexes. Les caractéristiques anisotropes, comparativement aux caractéristiques isotropes, permettent de contrôler aisément aux ondes électromagnétiques. Ces propriétés pourraient s'avérer intéressantes pour la conception de futurs dispositifs faisant partie de systèmes de communication sans-fil. Jusqu'à maintenant, les méthodes de simulations intégrées dans les logiciels commerciaux se basent sur la discrétisation volumétrique comme la méthode des éléments finis (FEM) et la méthode des différences finies dans le domaine temporel (FDTD). Ces méthodes permettent de traiter la plupart des cas généraux de matériaux anisotropes, mais elles nécessitent une discrétisation de l'entièreté du volume de l'objet. Cela représente un fardeau de calcul important lorsqu'un matériau plus volumineux est traité. La méthode des moments basée sur les équations intégrales de surface (SIE-MoM) peut simplifier le problème en restreignant le problème à la surface du volume. Cette méthode se heurte toutefois aux problèmes de singularités. Pour surmonter ceux-ci et dans le but de fournir un outil de simulation efficace, nous présenterons une méthode d'équivalence de source (ESM) qui est une solution par moments permettant l'évaluation électromagnétique de matériaux anisotropes. Les fonctions de Green tensorielles en deux et trois dimensions des matériaux analysés seront abordées en détails et appliquées dans la formulation de la ESM qui permet d'analyser les diffuseurs anisotropes. Le placement de sources filamentaires et des points de test qui jouent un grand rôle dans la méthode ESM seront détaillés car il favorise l'obtention de solutions stables. Le problème des singularités, un problème majeur de la SIE-MoM, peut facilement être résolu par la ESM. De plus, les conditions frontières anisotropes, plus spécifiquement les conditions aux frontières d'impédance tensorielle (TIBC) utilisées dans la représentation de matériaux composites en fibre de carbone multicouche et la condition des feuilles de transition généralisée (GSTC) utilisée dans la caractérisation de métasurfaces cylindriques sont aussi intégrées dans la ESM pour analyser les évaluations électromagnétiques. Comparativement aux logiciels commerciaux et aux recherches déjà publiées, la ESM possède clairement l'avantage au niveau de la performance de la simulation. En outre, dans cette thèse, on s'intéressera aux limitations de la ESM dans les cas en trois dimensions. Même si la simulation par ESM d'objets en trois dimensions possédant des géométries complexes engendrent un coût de calcul important, la ESM demeure un outil de simulation puissant dans les cas de géométries en deux et trois dimensions possédant des frontières lisses.

ABSTRACT

The development of manufacturing technology provides possibility to build artificial materials possessing complex anisotropy. The anisotropic characteristic, compared with the isotropic one, provides additional freedom to control electromagnetic waves. This property makes the anisotropic material a competitive alternative in the design of devices for future wireless communication systems. So far, the simulation methods integrated in commercial software packages for anisotropic materials are volumetric discretization-based, such as Finite-Element Method (FEM) and Finite-Difference Time-Domain (FDTD). These methods can handle the most general case of anisotropic materials whereas they require to discretize the entire volume of an object, therefore it generates computational burden when a larger scatterer is encountered. The surface integral equations-based method of moment (SIE-MoM) can simplify the problem by formulating the problem only on the physical surface. Yet the complexities, especially on the singularity issue, are still there. To overcome mentioned problems and to provide an efficient simulation tool, this thesis presents the equivalent source method (ESM), a moment solution, to analyze anisotropic materials. The dyadic Green's functions in two-dimensional and three-dimensional cases of investigated anisotropic materials are discussed in detail, and subsequently deployed in the formulation of the ESM to analyze electromagnetic phenomena involving anisotropic scatterers. The placements of filamentary sources and the testing points, playing the key role in the ESM, are discussed and specified in detail to provide a stable solution. The singularity issue, usually a tough problem in SIE-MoM, can be solved easily by using the ESM. In addition, the anisotropic boundary conditions, specifically the tensorial impedance boundary condition (TIBC) used for representing multilayered carbon-fiber composite materials and the generalized sheet transition condition (GSTC) used for characterizing cylindrical metasurfaces, are also incorporated in the ESM. In comparison to commercial software packages and published researches, the ESM has a clear advantage on the simulation performance. For example, the CPU time and required memory are 611 s/7.50 GB for the FEM (CST) whereas only 1.58 s/0.00037 GB for the ESM when computing the field on the surface of an elliptical cylinder in two-dimensional (2D) case under the illumination of a TM plane wave, and in three-dimensional (3D) case, the CPU time and required memory are 82980 s/170.2 GB for the FEM (HFSS) whereas only 4421.52 s/2.40 GB for the ESM when computing scattering from an uniaxial sphere with a 2λ radius. In addition, the limitations of the ESM in three-dimensional scenario are investigated in this thesis. Although the ESM on simulations of objects with complex geometries in three-dimensional case suffers from a highly computational cost, the ESM can be a powerful simulation tool in 2D situation

and 3D situation when objects with a smooth boundary are considered.

TABLE OF CONTENTS

DEDICATION iii

ACKNOWLEDGEMENTS iv

RÉSUMÉ v

ABSTRACT vi

TABLE OF CONTENTS viii

LIST OF TABLES xi

LIST OF FIGURES xii

LIST OF SYMBOLS AND ACRONYMS xix

LIST OF APPENDICES xx

CHAPTER 1 INTRODUCTION 1
- 1.1 Literature review and motivations 2
- 1.2 Objectives 5
- 1.3 Outline of the thesis 5

CHAPTER 2 TWO-DIMENSIONAL SCATTERING FROM ANISOTROPIC HOMOGENEOUS CYLINDERS 7
- 2.1 2D dyadic Green's functions of anisotropic materials 7
- 2.2 Problem formulation 12
  - 2.2.1 Fields Expressions 12
  - 2.2.2 Boundary Conditions 14
  - 2.2.3 Source Location 15
- 2.3 Scattering analyses of cylinders with different shapes 17
- 2.4 The behaviors of filament currents in terms of scattered fields singularities and matrix ill-conditioning 23
- 2.5 Possible applications and conclusion 29

CHAPTER 3 ELECTROMAGNETIC SIMULATIONS USING ANISOTROPIC BOUND-

ARY CONDITIONS 32
3.1 Formulation of the TIBC of the multilayered CFC material 32
3.1.1 Generalized impedance boundary condition (GIBC) 32
3.1.2 Propagation modes in unbounded CFC-filled region 33
3.1.3 TIBC of a multilayered CFC-based shell 35
3.2 EM evaluations of multilayered CFC-based shells 40
3.2.1 Problem formulation 40
3.2.2 Scattering analysis 44
3.2.3 Shielding effectiveness (SE) analysis 49
3.3 Slot shells 52
3.3.1 Formulation 53
3.3.2 Numerical examples 58
3.4 Simulation of cylindrical metasurfaces using GSTC-MFCM 61
3.4.1 Impedance-type GSTC and Metasurface Synthesis Procedure 62
3.4.2 GSTC-MFCM Formulation 64
3.4.3 Illustrating examples 68
3.5 Analyses of induced current on a CFC-based shell excited by line sources . . 73
3.5.1 Convergence study 75
3.5.2 Calculation of induced currents 78
3.6 Conclusion 79

CHAPTER 4 THREE-DIMENSIONAL SCATTERING FROM OBJECTS MADE OF UNIAXIAL MATERIALS 80
4.1 Closed-form dyadic Green's functions of uniaxial material 80
4.2 Problem formulation for an object with a smooth boundary 84
4.2.1 Fields Expressions in Regions 1 And 2 84
4.2.2 Placements of matching points and sources 87
4.3 Problem formulation for an object with sharp edges 89
4.3.1 Placement of matching points 90
4.3.2 Placement of sources 92
4.4 Boundary conditions, singularities in using dyadic Green's functions and convergence study 95
4.4.1 Boundary conditions 95
4.4.2 Singularities in using dyadic Green's functions 96
4.4.3 Convergence study 97
4.5 Computations of scattering analyses 97

4.5.1 Scattering from uniaxial spheres 98
4.5.2 Scattering from uniaxial cylinders and limitations 105
4.6 Conclusion 110

CHAPTER 5 APPLICATIONS TO LARGE SCATTERERS 111
5.1 Problem formulation 111
5.2 Construction of the impedance matrix 113
5.3 Numerical examples and discussions 114
5.4 Conclusion 118

CHAPTER 6 CONCLUSIONS AND FUTURE WORK 119
6.1 Summary of the contributions 119
6.2 Future Research 121

REFERENCES 124

APPENDICES 138

LIST OF TABLES

Table 4.1 The numbers of matching points and infinitesimal dipole doublets in single-layer and double-layer sources placement strategies. 98

Table 4.2 The comparisons of CPU time (s) and memory (GB) between the proposed method and commercial software (HFSS and FEKO)(All simulations were run on the same server with an Intel(R) Xeon(R) E5-2680@2.70 GHz) 102

Table 4.3 The comparisons of CPU time (s) and memory (GB) between the proposed method and commercial software HFSS (All simulations were run on the same server with an Intel(R) Core(TM) i7-7700@3.6 GHz) 105

Table 5.1 The matrix sizes and unknowns as well as the CPU time (s) of the matrix construction and matrix solution (All simulations were run on the same server with an Intel(R) Xeon(R) E5-2680@2.70 GHz) 115

Table 5.2 The comparisons of CPU time (s) and memory (GB) between the proposed method and commercial software FEKO (All simulations were run on the same server with an Intel(R) Xeon(R) E5-2680@2.70 GHz) 117

LIST OF FIGURES

Figure 1.1 Material used in Boeing 787 body. [1] 3

Figure 1.2 Basic description of CFC material 6

Figure 2.1 Geometry of the problem. 8

Figure 2.2 Problem description for the MFCM. 13

Figure 2.3 Source location strategies for (a) circular and (b) rectangular cross sections. 16

Figure 2.4 Configuration of a rectangular cylinder. 16

Figure 2.5 Normalized scattering width response of a circular cylinder under the TE polarization. (case 1: bistatic scattering width response with $k_0 r = \pi/2$, $\epsilon_{xx} = 4\epsilon_{yy} = 4$, $\epsilon_{xy} = \epsilon_{yx} = 0$, $\mu_{zz} = 2$, $\phi_{inc} = 0^\circ$; case 2: bistatic scattering width response with $k_0 r = \pi/2$, $\epsilon_{xx} = \epsilon_{yy} = 4$, $\epsilon_{xy} = -\epsilon_{yx} = 2$, $\mu_{zz} = 2$, $\phi_{inc} = 0^\circ$; case 3: monostatic scattering width response versus ϕ_{inc} with $k_0 r = \pi/2$, $\epsilon_{xx} = 4-j$, $\epsilon_{xy} = 3-j$, $\epsilon_{yx} = 1+j$, $\epsilon_{yy} = 2-j$, $\mu_{zz} = (23-37j)/26$). 18

Figure 2.6 (a) E-field and (b) H-field boundary condition error of an anisotropic square cylinder under the TM polarization. ($k_0 a = 2.5$, $\mu_{xx} = 2$, $\mu_{yy} = 4$, $\mu_{xy} = \mu_{yx} = 0$, $\epsilon_{zz} = 2$, $\phi_{inc} = 270^\circ$). Variable s is a parameter controlling the position around the cylinder, as illustrated in the inset. 19

Figure 2.7 Bistatic normalized scattering width response of an anisotropic square cylinder under the TM polarization. ($k_0 a = 2.5$, $\mu_{xx} = 2$, $\mu_{yy} = 4$, $\mu_{xy} = \mu_{yx} = 0$, $\epsilon_{zz} = 2$, $\phi_{inc} = 270^\circ$). 20

Figure 2.8 Bistatic scattering width response of a gyrotropic-type square cylinder under the TM polarization. ($\mu_{11} = \mu_{22} = 4$, $\mu_{12} = -\mu_{21} = 2$, $\epsilon_{33} = 2$, $\phi_{inc} = 180^\circ$). 21

Figure 2.9 Monostatic scattering width response of an anisotropic rectangular cylinder under the TM polarization. ($k_0 b = 5$, $\mu_{xx} = 4$, $\mu_{xy} = -\mu_{yx} = 2-j$, $\mu_{yy} = 2$, $\epsilon_{zz} = 2$). 21

Figure 2.10 The PEC cylinder coated with an anisotropic material scenario. (a)Geometry and (b) locations of matching points and sources 22

Figure 2.11 Bistatic scattering width response of an anisotropic shell coated PEC cylinder with various incident angles under the TM polarization. ($k_0 r_a = 1$, $k_0 r_b = 2$, $\mu_{xx} = 1.5$, $\mu_{yy} = 2.5$, $\mu_{xy} = -\mu_{yx} = 3$, $\epsilon_{zz} = 1.5$). 24

Figure 2.12 (a) Configuration of an anisotropic elliptical cylinder, and (b) locations of matching points and sources. (The two crosses represent the position of singular points). 24

Figure 2.13 The computed real and imaginary parts of normalized inside currents on virtual internal surface C_1 using $\xi_{in} = 0.75$, (a) $\xi_{out} = 1.25$ and (b) $\xi_{out} = 1.55$ versus filament index l. (E is the complete elliptic integral of the second kind, and the normalization method of currents is referred to [2]). (c) The comparison between the calculated electric field on the boundary using FEM (CST) and proposed MFCM. In all cases, the first filament current is located at $\phi = 0^\circ$. 26

Figure 2.14 The computed real and imaginary parts of normalized filament currents on virtual surfaces C_1 (internal region) with $\xi_{in} = 0.45$, (a) $\xi_{out} = 1.55$ and (b) $\xi_{out} = 1.25$ versus filament current index l. (c) The comparison between the calculated electric field on the boundary using FEM (CST) and proposed MFCM. 27

Figure 2.15 The responses of condition number of matrix $[Q]$ and average E-field boundary condition error $\Delta\tilde{E}_{bc}$ versus the parameter ξ_{in} with different N values. ($\xi_{out} = 1.5$.) 30

Figure 2.16 The description of a slab embedded with periodic anisotropic cylinders which could be made by stacking two distinct dielectric slabs periodically. 30

Figure 2.17 The geometry of the wire medium: a rectangular lattice of parallel ideally conducting thin wires. 30

Figure 3.1 The description of a dielectric slab with notation of fields. 33

Figure 3.2 Layout of the single CFC-based planar layer. 34

Figure 3.3 (a)Carbon fiber path of the single CFC-based cylindrical layer. (b) Homogenized cylinder discretization approach. 36

Figure 3.4 An arbitrary cross section with local orthogonal coordinates. 39

Figure 3.5 The multilayered CFC-based cylindrical shell. 39

Figure 3.6 Problem description for the MFCM. 41

Figure 3.7 Formulation of the MFCM. 42

Figure 3.8 Two different fiber patterns, (a) [0/45/90/-45] and (b) [0/90]. 45

Figure 3.9 Monostatic co- and cross-polarization echo widths of a cylindrical shell in various situations, $\phi_{inc} = 180^\circ$. The multilayered CFC-based shell situations under (a) TM and (b) TE cases, and (c) the single layered CFC-based shell with fiber orientation as 30°. ($\epsilon_a = 5.0\epsilon_0 - j40000/\omega$, $\epsilon_b = 5.0\epsilon_0 - j50/\omega$ and d=0.127 mm for each single CFC-based layer, r_a=2 m). 46

Figure 3.10 Bistatic echo widths of a cylindrical multilayered CFC-based shell under (a) TM and (b) TE polarizations. (c) Co- and (d) cross-polarization bistatic echo widths of a single CFC-based shell with fiber orientation as 30°, $\phi_{inc} = 180°$. ($\epsilon_a = 5.0\epsilon_0 - j40000/\omega$, $\epsilon_b = 5.0\epsilon_0 - j50/\omega$ and d=0.127 mm for each single CFC-based layer, r_a=2 m). 47

Figure 3.11 SE performances under various situations in the low frequency range. (a) TM and (b) TE cases. ($\epsilon_a = 3.4\epsilon_0 - j40000/\omega$, $\epsilon_b = 5.0\epsilon_0 - j50/\omega$ and d=0.127 mm for each single CFC material layer, r_a=1 m). 49

Figure 3.12 SE performance under various situations in the high frequency range with fiber orientation patterns (a) [0/90] and (b) [0/45/90/-45]. ($\epsilon_a = 3.4\epsilon_0 - j40000/\omega$, $\epsilon_b = 5.0\epsilon_0 - j50/\omega$ and d=0.127 mm for each single CFC-based layer, r_a=1 m). 50

Figure 3.13 The normalized magnitude of E_z component at the center of shell versus frequency under the TM incidence. The shell is made by four layered CFC material and the fiber orientation is [90/90/90/90]. ($\epsilon_a = 3.4\epsilon_0 - j40000/\omega$, $\epsilon_b = 5.0\epsilon_0 - j50/\omega$ and d=0.127 mm for each single CFC-based layer, r_a=1 m). 51

Figure 3.14 Layout of the single CFC-based planar layer. 54

Figure 3.15 Formulation of MFCM for a multilayered CFC-based slotted shell . . 54

Figure 3.16 The distributions of sources inside and outside as well as matching points for a slot CFC-based shell with radius r_a=2 m and $\phi_0 = 5°$. The locations of inside sources are marked with star, and outside sources are marked with triangle. The matching points are marked with dots.($N_1 = 5$ and $N_2 = 85$). 57

Figure 3.17 A convergence study regarding to the boundary condition error of a 4-layered CFC-based slotted shell with $\phi_0 = 5°$ and $k_0 r_a = 5$ 59

Figure 3.18 Comparisons of the E-field along x-axis within the slotted lossy shell between the proposed method and FEKO, for different slot angles.(σ=10000 S/m, d=0.5 mm, $r_a = \lambda = 1$ m. $N_1 = 5, 12, 22$ and $N_2 = 35, 28, 22$ are used for the MFCM to do the simulations of $\phi_0 = 5°, 15°, 60°$, respectively.) 59

Figure 3.19 The monostatic scattering responses of the 4 layered CFC-based slotted shell for different slot angles.($\epsilon_a = 5.0\epsilon_0 - j40000/\omega$, $\epsilon_b = 5.0\epsilon_0 - j200/\omega$ and d=0.127 mm for each single CFC-based layer, r_a=2 m, $N_1 = 12, 16, 22$ and $N_2 = 78, 68, 63$ are used for the MFCM to do the simulations of $\phi_0 = 15°, 30°, 60°$, respectively.) 60

Figure 3.20 The SE responses of the 4 layered CFC-based slotted shell under (a) different slot angles, and $\epsilon_a = 5.0\epsilon_0 - j40000/\omega$, $\epsilon_b = 5.0\epsilon_0 - j200/\omega$ for each single CFC-based layer, $N_1 = 5, 9, 12$ and $N_2 = 85, 83, 78$ are used for the MFCM to do the simulations of $\phi_0 = 5^\circ, 10^\circ, 15^\circ$, respectively, and (b) different σ_a, and $\epsilon_a = 5.0\epsilon_0 - j\sigma/\omega$, $\epsilon_b = 5.0\epsilon_0 - j200/\omega$, $N_1 = 5$ and $N_2 = 85$ are used for the CFC-based shell and $N_1 = 5$ and $N_2 = 35$ are used for the PEC shell in the MFCM.) (d=0.127 mm for each single CFC-based layer, r_a=2 m.) 60
Figure 3.21 Problem description. 62
Figure 3.22 Formulation of MFDCM 65
Figure 3.23 Source location strategies for (a) circular and (b) rectangular contours. . . 67
Figure 3.24 Problem description of a camouflaged rectangular metasurface. 69
Figure 3.25 (a) The magnitude difference between the calculated and preset E_z in the two regions. (b) The E_z component of the total electric fields in the two regions. 70
Figure 3.26 The magnitude differences between the calculated and preset (a) electric and (b) magnetic fields in two regions. (c) Phase distribution of H_z component of total magnetic field in two regions for the case that the metasurface is solely illuminated by a TE_z polarized plane wave propagating in -x direction. 72
Figure 3.27 The problem description of a CFC-based shell excited by a set of line sources 74
Figure 3.28 Convergence responses on the boundary with respect to the locations of the two differential line sources for the case $k_z = 0.5k_0$. (a) $\Delta C(E_\phi)$, (b)$\Delta C(E_z)$, (c) $\Delta C(H_\phi)$ and (d) $\Delta C(H_z)$. ($r_s = r_{sa} = r_{sb}$, $\phi_{sa} = 5^\circ$, and $\phi_{sb} = -5^\circ$). 76
Figure 3.29 The magnitudes of induced currents (a) J_ϕ and (b)J_z for the first scenario. 77
Figure 3.30 The magnitudes of induced currents (a) J_ϕ and (b)J_z for the second scenario. 77
Figure 4.1 The configurations of local and global coordinates. 81
Figure 4.2 Geometry of the problem. 85
Figure 4.3 The concept of the MIDM. 85
Figure 4.4 The strategy of matching points placement for a spherical object. 87
Figure 4.5 The strategies of sources placement for a spherical object. (a) Single-layered and (b) double-layered. 88
Figure 4.6 Problem description for an anisotropic cylinder. 90

Figure 4.7 (a) RWG adaptive mesh for a cylinder in the commercial software FEKO. (b) The triangle patches generated by the RWG mesh. (c) Placement of matching points for a cylinder with $r_a = 0.5\lambda$ and $h = 0.25\lambda$. (λ=1 m, TELe=0.035 and TELg=0.07 are set in FEKO to generate adaptive RWG mesh). 91

Figure 4.8 Inside sources placements of (a) single-layered and (b) double-layered schemes for a cylinder with $r_a = 0.5\lambda$ and $h = 0.25\lambda$. (λ=1 m, $SPWs$=16 and $SPWd$=13 are set to generate the placement. $S_1 = 0.85$ for single-layered strategy and $S_{11} = 0.5$ and $S_{12} = 0.85$ for double-layered one). 93

Figure 4.9 The proposed filtering strategy used to eliminate the singularity of the type $|\boldsymbol{R_c}| = 0$. 96

Figure 4.10 Normalized bistatic RCS responses of a uniaxial sphere illuminated by a plane wave with $\hat{\boldsymbol{x}}$ polarized electric field propagating along the z axis in (a) xoz plane and (b) yoz plane. ($r_a = 0.5\lambda$, $\epsilon_1 = 2\epsilon_0, \epsilon_2 = 4\epsilon_0, \mu_1 = 3\mu_0, \mu_2 = 5\mu_0, \theta_c = 0^\circ, \varphi_c = 0^\circ$). 99

Figure 4.11 Normalized bistatic RCS responses of a uniaxial sphere illuminated by a plane wave with $\hat{\boldsymbol{x}}$ polarized electric field propagating along the $-z$ axis in (a) xoz plane, (b) yoz plane and (c) both xoz and yoz planes whereas less numbers of matching points and IDDs of the single-layered scheme are used. ($r_a = 1\lambda$, $\epsilon_1 = 5\epsilon_0, \epsilon_2 = 9\epsilon_0, \mu_1 = \mu_2 = \mu_0, \theta_c = 45^\circ, \varphi_c = 90^\circ$). 99

Figure 4.12 Normalized bistatic RCS responses of a uniaxial T_iO_2 sphere illuminated by a plane wave with $\hat{\boldsymbol{x}}$ polarized electric field propagating along the z axis in (a) xoz plane, (b) yoz plane and (c) both xoz and yoz planes whereas more numbers of matching points and IDDs of the single-layered scheme are used. ($r_a = 2\lambda$, $\epsilon_1 = 5.913\epsilon_0, \epsilon_2 = 7.197\epsilon_0, \mu_1 = \mu_2 = \mu_0, \theta_c = 0^\circ, \varphi_c = 180^\circ$). . . . 100

Figure 4.13 The boundary condition error of electric field under different numbers of matching points and IDDs (a) the single-layered scheme and (b) the double-layered scheme. ($r_a = 2\lambda$, $\epsilon_1 = 5.913\epsilon_0, \epsilon_2 = 7.197\epsilon_0, \mu_1 = \mu_2 = \mu_0, \theta_c = 0^\circ, \varphi_c = 180^\circ$). 103

Figure 4.14 Geometry of the PEC sphere coated with an T_iO_2 layer. 103

Figure 4.15 Normalized bistatic RCS responses of a T_iO_2 layer coated PEC sphere with different values of r_b illuminated by a plane wave with $\hat{\boldsymbol{x}}$ polarized electric field propagating along the z axis in (a) xoz plane and (b) yoz plane. ($r_a = 2\lambda$, $\epsilon_1 = 5.913\epsilon_0, \epsilon_2 = 7.197\epsilon_0, \mu_1 = \mu_2 = \mu_0, \theta_c = 0^\circ, \varphi_c = 180^\circ$). 104

Figure 4.16 Normalized bistatic RCS responses of a uniaxial cylinder illuminated by a plane wave with $\hat{\boldsymbol{x}}$ polarized electric field propagating along the $-z$ axis in (a) xoz plane and (b) yoz plane. ($r_a = 0.5\lambda$, $h = 0.25\lambda$, $\epsilon_1 = 5\epsilon_0, \epsilon_2 = 9\epsilon_0, \mu_1 = \mu_2 = \mu_0, \theta_c = 0^\circ$). 106
Figure 4.17 Normalized bistatic RCS responses of a T_iO_2 cylinder illuminated by a plane wave with $\hat{\boldsymbol{x}}$ polarized electric field propagating along the $-z$ axis in (a) xoz plane and (b) yoz plane. ($r_a = 0.25\lambda$, $h = 0.5\lambda$, $\epsilon_1 = 5.913\epsilon_0, \epsilon_2 = 7.197\epsilon_0, \mu_1 = \mu_2 = \mu_0, \theta_c = 0^\circ, \varphi_c = 0^\circ$). 106
Figure 4.18 Normalized bistatic RCS simulations of a dielectric cylinder with different mesh parameters illuminated by a plane wave with $\hat{\boldsymbol{z}}$ polarized electric field propagating along the -x axis in (a) xoz plane and (b) yoz plane. 108
Figure 4.19 The triangle patches generated by the RWG mesh. 108
Figure 4.20 Normalized bistatic RCS simulations of a dielectric cylinder using the RWG testing method of different mesh parameters illuminated by a plane wave with $\hat{\boldsymbol{z}}$ polarized electric field propagating along the -x axis in (a) xoz plane and (b) yoz plane. 109
Figure 5.1 The symmetric sphere with respect to three coordinate planes 112
Figure 5.2 Constructed impedance matrix. 114
Figure 5.3 Normalized bistatic RCS responses of a PEC sphere illuminated by a plane wave with $\hat{\boldsymbol{x}}$ polarized electric field propagating along the -z axis in (a) xoz plane and (b) yoz plane for $r_a = 5\lambda$, and (c) xoz plane and (b) yoz plane for $r_a = 10\lambda$. 115
Figure 5.4 The magnitudes of scattered electric field of a PEC sphere illuminated by a plane wave with $\hat{\boldsymbol{x}}$ polarized electric field propagating in the z direction in (a) xoz plane and (b) yoz plane at $r = 1.2r_a$, $r_a = 10\lambda$. 116
Figure 5.5 Normalized bistatic RCS responses of a dielectric sphere with $\epsilon_r = 4$ illuminated by a plane wave with $\hat{\boldsymbol{x}}$ polarized electric field propagating in the -z direction in (a) xoz plane and (b) yoz plane for $r_a = 5\lambda$. 116
Figure 6.1 Iterative RAS procedure flowchat. [3] 122
Figure 6.2 Adaptive mesh of a cone-sphere structure and the placement of random sources near the edges. [4] 122
Figure B.1 Constructed impedance matrix in different levels. 140
Figure C.1 $|E_z|$ (dB) component of the first four TM modes for a 4-layer CFC-based shell with with a fiber orientation pattern [0/45/90/-45] under the TM plane wave illumination.($\epsilon_a = 3.4\epsilon_0 - j40000/\omega$, $\epsilon_b = 5.0\epsilon_0 - j50/\omega$ and d=0.127 mm for each single CFC-based layer, r_a=1 m). 142

Figure C.2 $|H_z|$ (dB) component of the first six TE modes for a 4-layer CFC-based shell with with a fiber orientation pattern [0/45/90/-45] under the TM plane wave illumination.($\epsilon_a = 3.4\epsilon_0 - j40000/\omega$, $\epsilon_b = 5.0\epsilon_0 - j50/\omega$ and d=0.127 mm for each single CFC-based layer, r_a=1 m). 143
Figure D.1 Problem description. 145
Figure E.1 Constructed impedance matrix in different levels. 147
Figure E.2 (a)Real and (b) imaginary parts of I^{error} with respect to a matrix generated in the RCS calculation of a sphere illuminated by a plane wave. 151
Figure E.3 (a)Real and (b) imaginary parts of I^{error} with respect to a matrix generated randomly. 151

LIST OF SYMBOLS AND ACRONYMS

ESM	Equivalent Source Method
EM	Electromagnetic
MoM	Method of Moment
FD	Finite Difference
FEM	Finite Element Method
2D	Two-dimensional
3D	Three-dimensional
GMT	Generalized Multipole Technique
TIBC	Tensorial Impedance Boundary Condition
CFC	Carbon-fiber Composite
GSTC	Generalized Sheet Transition Condition
VIE	Volume Integral Equation
CFIE	Combined Field Integral Equation
SIE	Surface Integral Equation
MFCM	Multifilament Current Method
RCS	Radar Cross Section
EMT	Effective Medium Theory
FDTD	Finite-Difference Time Domain
FE-BI	Finite Element-Boundary Integral
MMP	Multiple Multipole Method
DSM	Discrete Sources Method
MFS	Method of Fictitious Sources
MAS	Method of Auxiliary Sources
RAS	Random Auxiliary Sources
MIDM	Multiple Infinitesimal Dipole method
SPW	Samples Per Wavelength
IDD	Infinitesimal Dipole Doublet
IDT	Infinitesimal Dipole Triplet
TEL	Triangle Edge Length
BDA	Block Decomposition Algorithm

LIST OF APPENDICES

Appendix A PROPAGATION MODES OF UNBOUND REGION CONSTITUTE OF CARBON-FIBER COMPOSITE MATERIAL 138

Appendix B INCIDENT ANGLE INDEPENDENT TIBC 139

Appendix C MODES DISTRIBUTIONS OF A CFC-BASED CYLINDRICAL SHELL UNDER TM PLANE WAVE ILLUMINATION 141

Appendix D DERIVATION OF IMPEDANCE-TYPE GSTC 144

Appendix E LIMITATION ON USE OF BLOCK DECOMPOSITION ALGORITHM 146

CHAPTER 1 INTRODUCTION

Electromagnetic (EM) scattering theory is fundamental to modelling the interaction of EM waves with matter. It is a wide topic that has been researched for over a century. The study of EM scattering is not solely of academic interest, but of practical importance in many application areas, such as modern radar and remote sensing. These efforts have led to a development of a large number of analysis tools and modeling techniques for quantitative evaluation of EM scattering by various objects. Many computational techniques, such as analytical solutions reported in [5–7], MoM [8–11], Finite Difference (FD) methods [12], FEM [13] and so on, have been developed to evaluate the scattering from a scatterer with arbitrary shapes in 2D and 3D scenarios. Most reported research work focuses on the scattering from objects made of isotropic materials. Artificial materials, such as uniaxial wire medium, carbon-fiber composite material, ferromagnetic nanowire metamaterial, behaves as anisotropic materials and have found growing applications in practice. By considering the potential applications of anisotropic materials, an accurate and efficient solution to study the EM interactions with anisotropic materials should be addressed.

The ESM is a variant of MoM featuring a simple implementation, simple meshes, avoidance of a singularity extraction, and a fast computation by avoiding the integration of surface currents when calculating the fields. It has found many applications not only on electromagnetic problems but also in acoustic [14–16] and light scattering problems [17–20]. From the EM point of view, the ESM is also known as generalized multipole techniques (GMT) [17]. A common basic concept of ESM is that the scattered fields inside and outside of a scatterer are respectively simulated by a set of equivalent sources located outside and inside of the scatterer with a certain distance away from the physical boundary, rather than being formulated in terms of equivalent surface currents flowing on the physical surface. In this case, no integrals have to be computed numerically, which reduces the computation time and simplifies the problem formulation. Also, the solution features no singularity since testing points and sources never coincide. Although the ESM has found many applications on the scattering evolutions of isotropic objects, there is a a need for its implementation in anisotropic materials, considering the wide applications of such materials in the future. In this thesis, we will explore applications of the ESM on EM estimations with respect to the anisotropic materials in both 2D and 3D scenarios.

In addition, an object could be accurately represented by a specific boundary condition without considering the inside details in some scenarios. The boundary conditions, such as the sur-

face impedance boundary condition [21] and generalized impedance boundary condition [22], are commonly used to characterize isotropic materials, and they have been deployed in many numerical techniques [23–27]. Yet there is little work about EM evaluations of anisotropic materials by exploiting its correspond impedance boundary conditions. In this thesis, we will consider two types of anisotropic boundary conditions. One is the tensorial impedance boundary condition (TIBC), which is used to represent multilayered carbon-fiber composite (CFC) material, and the other is the generalized sheet transition condition (GSTC), which is used to represent a metasurface possessing anisotropic characteristics. They are subsequently employed in the ESM to do the calculation of interested EM evaluations.

1.1 Literature review and motivations

A literature review regarding to the applications of various numerical methods on EM estimations of anisotropic materials is conducted in both 2D and 3D situations and introduced below.

In the 2D situation, several remarkable research contributions about scattering evaluations of anisotropic materials have been generated and presented in [28–41]. A volumetric integral equation (VIE) method was developed in [28, 29] to deal with scattering performances from a linear, lossy, and anisotropic material. This approach can handle the most general case of material whereas it requires to mesh the entire volume of an object. Combined field integral equation (CFIE) formulated in [30–32] was exploited to overcome the size restriction of the VIE. Appropriate electromagnetic potentials were derived and utilized to represent the fields inside an anisotropic medium. Subsequently, a set of coupled surface integral equations were constructed and solved with the help of the equivalence principle. A SIE was formulated in [33] by mapping the anisotropic object into a complex isotropic space. Integral equations for the scattering analysis of an homogeneous circular anisotropic rod under normal [34] and oblique [35] incidences were introduced based on the plane wave representation of the field. The integral equations based on the Mathieu functions and Fourier series were proposed in [36] and a formal series solution was introduced in [37] to analyze the scattering performance from an elliptical anisotropic cylinder. The method presented in [36] was also deployed to analyze the scattering from an anisotropic shell coated elliptic conducting cylinder [38]. A variational reaction theory was formulated in [39] and further employed in a FEM to solve the scattering problems from an anisotropic $LiNbO_3$ cylinder illuminated with an oblique plane wave incidence. Those proposed techniques provide an accurate and more simplified approach compared to VIE, yet the complexity of the formulation is still there. The integral equations-based methods have the necessity of integrating surface currents when computing fields.

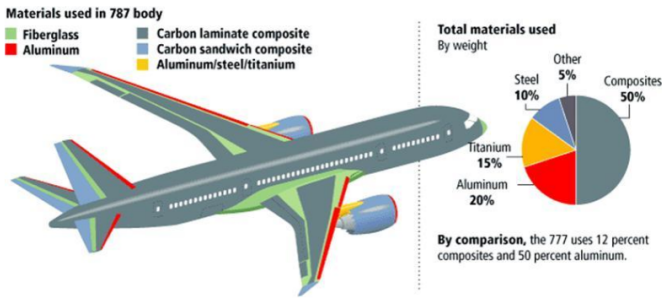

Figure 1.1 Material used in Boeing 787 body. [1]

In addition, the solutions presented in [34–37] are highly restricted to the cylinder geometry. Hybrid numerical techniques, like finite-element method-multifilament current method (FEM-MFCM) in [40] and finite difference-measured equation of invariance (FD-MEI) in [41], are alternative approaches to analyze the scattering from anisotropic objects in 2D.

In the 3D situation, several remarkable research contributions have been made and presented in [42–52]. The VIE-based methods were introduced in [42–47] to solve scattering performances from an arbitrarily shaped object made of a linear, lossy, and anisotropic material. The VIE-based approaches can handle the most general cases of materials whereas they require to discretize the entire volume of an object, therefore becoming computationally challenging with large scatterers. The same issue rises in the FDTD [50] and finite element-boundary integral (FE-BI) [51] methods. The SIE is a good candidate to overcome the computational burden of the methods based on volumetric discretization. A SIE-based MoM scheme combined with uniaxial dyadic Green's functions [53,54] was proposed in [48,49] for scattering evaluation from arbitrarily shaped objects filled with uniaxial materials. The SIE-based solutions provide an accurate and more simplified approach compared to the VIE-based ones, yet the complexity of formulations is still there. In addition, the integral equations-based methods have the necessity of integrating surface or volumetric currents when computing fields.

From the EM point of view, the ESM is also called GMT. The GMT is a generic name of several similar numerical methods [55–58] developed independently by several research groups. In the GMT, the scattered fields are usually expanded in terms of a set of multipole sources. However, not only the multipoles can be used for fields expansion, but other equivalent sources are also possible. Therefore, other names for similar methodologies have been given like multiple multipole method (MMP) [55], discrete sources method (DSM) [56], multifilament current method (MFCM) [58], method of fictitious sources (MFS) [59], method of auxiliary sources (MAS) [57], fundamental solutions [60], random auxiliary sources (RAS) [3],

or multiple infinitesimal dipole method (MIDM) [61]. In this thesis, we will use the name, MFCM, to represent the ESM in the 2D scenario whereas the name, MIDM, is used for the 3D case. In the 2D case, various applications of the MFCM-like techniques were introduced in [18, 27, 62–69] regarding isotropic materials, and in [18, 70–72] regarding anisotropic materials. The tensor permittivity and permeability of the anisotropic material considered in published works are restricted to specific forms, yet the anisotropic material considered in this thesis has no restrictions. In addition, the behavior of filament currents in the MFCM regarding scattered fields' singularities is investigated for the first time. In the 3D case, the MIDM was extended to anisotropic scatterers by introducing the plane wave representation of an anisotropic material into Bessel multipoles [73], but it resulted in integrals which cannot be evaluated analytically to represent the scattered fields. The DSM was extended to 3D anisotropic scatterers in [74], but the entire body of the scatterer needed to be discretized. As a result, DSM also suffers from a high computational burden as in the case of the VIE-based method when larger objects are involved.

Anisotropic materials have found a variety of applications in the design of antennas [75–81], integrated-circuit structures [82], reduction of RCS of scatterers [83], optical signal processing [84] and so on. The uniaxial characteristic seems to be the most widely used type of anisotropic materials. This is because the uniaxial material can be either easily found in many natural crystals [82, 85], or artificially made by a stacked dielectric sheet structure consisting of alternative layers of two isotropic materials [78,79,86], or obtained by homogenizing a mixture of several different materials via effective medium theory [87, 88]. The CFC material is a kind of uniaxial material, and it has been widely used in modern spacecraft and aircraft industries as a replacement for metal due to its properties such as low-weight, high strength, high stiffness, etc. [1, 89]. Fig. 1.1 shows different materials used in Boeing 787 fuselage. Fifty percent of all the materials used in the 787 fuselage are CFC material. CFC materials usually appear in a laminated multilayered form, and each layer is typically composed of a resin matrix reinforced by carbon fiber inclusions having different shapes as indicated in Fig. 1.2. The EM characterization of CFC materials have been well studied in [90–94]. The effective medium theory (EMT) is known as an accurate and effective approach to characterize CFC materials by a tensor permittivity. Based on this tensor model, an effective boundary condition and a matrix surface impedance for flat CFC material are introduced in [95–99], and further applied to time domain analyses of EM performances.

Considering the aspects introduced above and potential applications of anisotropic materials in the future, the motivation of this thesis is to bring applications of ESM from isotropic materials to anisotropic materials and therefore to implement an effective computational tool with respect to anisotropic materials in both 2D and 3D scenarios. Although scattering

phenomena are investigated in details in this thesis, the proposed technique can be extended to consider more practical aspects, especially in the dielectric antenna designs and 2D light scattering problems.

1.2 Objectives

The main objective of this thesis is to extend the application of ESM from isotropic materials to anisotropic materials in 2D and 3D scenarios. Several issues should be addressed according to the main object, and they are:

1. In the 2D scenario, the radiation fields generated by a filamentary source placed in unbounded anisotropic region should be derived in order to apply the equivalent principle in the ESM;

2. The constructions of an effective and accurate anisotropic impedance boundary condition for multilayered CFC material and artificial surface should be introduced and discussed in detail; The formulation with respect to different boundary conditions should be investigated in the ESM;

3. In the 3D scenario, the dyadic Green's functions, the placements of sources and the testing strategy in the formulation of the ESM are required to be discussed in detail;

4. When a relatively large scatterer is considered, the construction of the impedance matrix and the solution for a dense linear system require more considerations in the ESM in order to have a fast simulation time;

5. The advantages and limitations of the ESM in comparison to other numerical techniques should be addressed.

The above five objectives will be presented throughout this thesis. In general, an efficient, concise and accurate simulation tool will be proposed, formulated and utilized in 2D and 3D scenarios for the EM evaluations of anisotropic objects.

1.3 Outline of the thesis

The thesis is arranged in six chapters. In Chapter 2, the 2D scattering problems of an anisotropic cylinder are considered. The 2D anisotropic Green's functions are derived and deployed in the proposed numerical technique. Instead of considering a whole anisotropic region, an anisotropic shell is considered in Chapter 3. The tensorial impedance boundary condition (TIBC) for a multilayered carbon fiber composites-based shell is constructed and subsequently employed in the proposed numerical technique to evaluate the EM performances

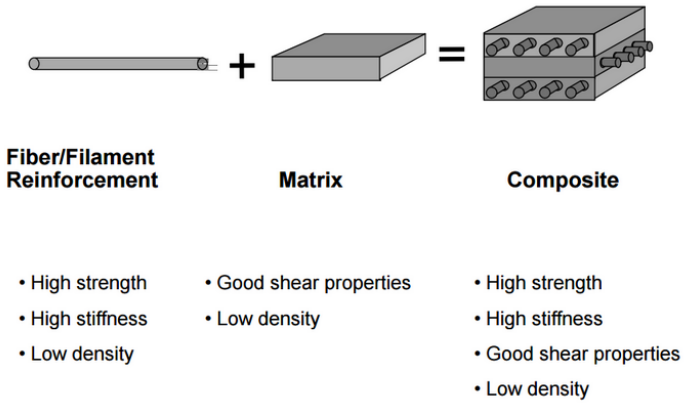

Figure 1.2 Basic description of CFC material

under various situations. The generalized sheet transition condition (GSTC), which is used to characterize a metasurface, is also exploited in the proposed method to study the EM phenomena of a cylindrical metasurface. In Chapter 4, we address the 3D case. We only focus on the uniaxial material, yet the proposed technique can also be applied to other kinds of anisotropic materials as long as the corresponding dyadic Green's functions are available. The derivation of uniaxial dyadic Green's functions is briefly introduced and further deployed in the formulation. The placements of testing points and sources with respect to the shape of a structure are discussed in detail. In addition, we also propose a double-layered distribution scheme of sources which can handle the scattering from a relatively larger object efficiently and with a good stability in comparison to the traditional single-layered distribution scheme. Finally, we bring the ESM to the application on large scatterers in Chapter 5. The construction of the impedance matrix in the ESM is accelerated by considering the symmetry of an investigated object. Chapter 6 presents the thesis conclusions, contributions, limitations, and expected future work.

CHAPTER 2 TWO-DIMENSIONAL SCATTERING FROM ANISOTROPIC HOMOGENEOUS CYLINDERS

The 2D scattering from homogeneous anisotropic cylinders will be discussed in detail in this chapter. The multifilament current method (MFCM) is a commonly used name to designate the ESM in the 2D scenario. Therefore the MFCM is used throughout this chapter. We start with a derivation of 2D Green's functions of anisotropic materials. This derivation is presented in Section 2.1. Subsequently, the formulation procedure of the MFCM is introduced in Section 2.2. Several numerical examples, under different scenarios such as incident wave polarizations and cylinder geometries as well as permittivity and permeability tensors, are investigated in Section 2.3. To complete the analysis of the proposed MFCM on anisotropic materials, the oscillation phenomenon of the filament currents with respect to the singularities of the analytic continuation of scattered field within an elliptical scatterer and the ill-conditioning issue of the constructed matrix in terms of the number of matching points and sources are also studied and discussed, and presented in Section 2.4. Computed results are compared with published ones and results obtained with commercial software packages. Good agreements are achieved. Possible applications are introduced in Section 2.5.

2.1 2D dyadic Green's functions of anisotropic materials

Let us consider a z-directed filamentary electric line source placed in an unbounded space filled with an anisotropic material characterized by

$$\overline{\epsilon} = \epsilon_0 \overline{\epsilon_r} = \epsilon_0 \begin{pmatrix} \epsilon_{xx} & \epsilon_{xy} & 0 \\ \epsilon_{yx} & \epsilon_{yy} & 0 \\ 0 & 0 & \epsilon_{zz} \end{pmatrix} \tag{2.1a}$$

$$\overline{\mu} = \mu_0 \overline{\mu_r} = \mu_0 \begin{pmatrix} \mu_{xx} & \mu_{xy} & 0 \\ \mu_{yx} & \mu_{yy} & 0 \\ 0 & 0 & \mu_{zz} \end{pmatrix} \tag{2.1b}$$

where $\overline{\epsilon_r}$ and $\overline{\mu_r}$ are the relative permittivity and permeability tensors, respectively. The expression of a z-directed electric line source is $\boldsymbol{J} = I_0 \delta(x - x_s)\delta(y - y_s)\hat{\boldsymbol{z}}$, where (x_s, y_s) is the location of the line source and I_0 is a complex coefficient. We will focus on the solution of radiation fields from an electric line source firstly, while the solution of a magnetic line source is straightforwardly obtained through duality.

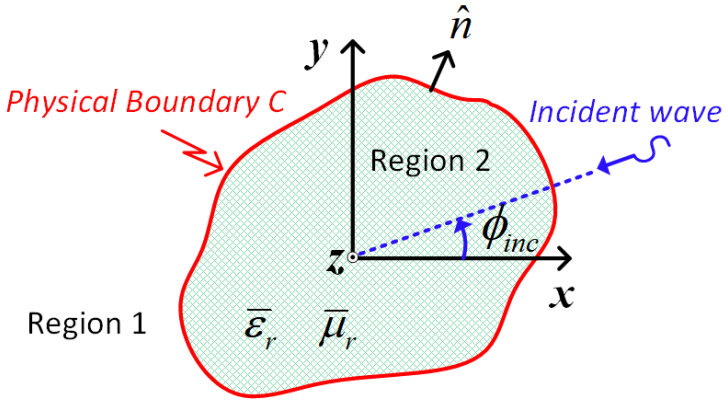

Figure 2.1 Geometry of the problem.

The first two Maxwell's equations with an electric line source placed in the anisotropic region read

$$\nabla \times \boldsymbol{E} = -j\omega\mu_0\overline{\mu_r}\boldsymbol{H} \tag{2.2a}$$

$$\nabla \times \boldsymbol{H} = j\omega\epsilon_0\overline{\epsilon_r}\boldsymbol{E} + \boldsymbol{J} \tag{2.2b}$$

where ϵ_0 and μ_0 are the permittivity and permeability of vacuum, respectively. The time dependence $e^{j\omega t}$ has been assumed and suppressed.

The wave equation obtained from (2.2a) and (2.2b) reads

$$\nabla \times (\overline{\mu_r}^{-1}\nabla \times \boldsymbol{E}) - k_0^2\overline{\epsilon_r}\boldsymbol{E} = -j\omega\mu_0\boldsymbol{J} \tag{2.3}$$

where $k_0 = \omega\sqrt{\epsilon_0\mu_0}$ is the wavenumber of free space. On substituting $\partial/\partial z = 0$ in (2.2), it is known that the electromagnetic field is separable into TM and TE modes [34] which are excited, respectively, by electric and magnetic line sources. Equation (2.3) is then expanded into the following matrix form

$$\begin{pmatrix} A_{11} & A_{12} & 0 \\ A_{21} & A_{22} & 0 \\ 0 & 0 & A_{33} \end{pmatrix} \begin{pmatrix} E_x \\ E_y \\ E_z \end{pmatrix} = -j\omega\mu_0 I_0 \begin{pmatrix} 0 \\ 0 \\ \delta(\boldsymbol{\rho} - \boldsymbol{\rho_s}) \end{pmatrix} \tag{2.4}$$

with

$$A_{11} = -p_{33}\frac{\partial^2}{\partial y^2} - k_0^2\epsilon_{xx}, \quad A_{12} = p_{33}\frac{\partial^2}{\partial x \partial y} - k_0^2\epsilon_{xy},$$
$$A_{21} = p_{33}\frac{\partial^2}{\partial x \partial y} - k_0^2\epsilon_{yx}, \quad A_{22} = -p_{33}\frac{\partial^2}{\partial x^2} - k_0^2\epsilon_{yy},$$
$$A_{33} = -p_{22}\frac{\partial^2}{\partial x^2} - p_{11}\frac{\partial^2}{\partial y^2} + (p_{12}+p_{21})\frac{\partial^2}{\partial x \partial y} - k_0^2\epsilon_{zz},$$
$$\overline{\mu_r}^{-1} = \begin{pmatrix} p_{11} & p_{12} & 0 \\ p_{21} & p_{22} & 0 \\ 0 & 0 & p_{33} \end{pmatrix}$$

where $\boldsymbol{\rho} = x\hat{\boldsymbol{x}} + y\hat{\boldsymbol{y}}$ and $\boldsymbol{\rho_s} = x_s\hat{\boldsymbol{x}} + y_s\hat{\boldsymbol{y}}$. Since only the electric line source is present, only the TM mode is excited, and therefore, $E_x = E_y = H_z = 0$. E_z, reads from the last equation in (2.4) as

$$\begin{aligned}(\mu_{xx}\frac{\partial^2}{\partial x^2} + \mu_{yy}\frac{\partial^2}{\partial y^2} + (\mu_{xy}+\mu_{yx})\frac{\partial^2}{\partial x \partial y} + k_0^2\epsilon_{zz}\gamma)E_z \\ = j\omega\mu_0 I_0 \gamma \delta(\boldsymbol{\rho} - \boldsymbol{\rho_s})\end{aligned} \tag{2.5}$$

with

$$\gamma \triangleq \mu_{xx}\mu_{yy} - \mu_{xy}\mu_{yx}$$

In order to convert (2.5) into the standard Helmholtz equation form, a linear coordinate transformation is proposed by letting:

$$\begin{aligned}\xi &= t_3 y \\ \zeta &= t_1 x + t_2 y\end{aligned} \tag{2.6}$$

with

$$t_1 = -\mu_{yy}; \quad t_2 = (\mu_{xy}+\mu_{yx})/2; \quad t_3 = -\sqrt{\mu_{xx}\mu_{yy} - t_2^2}$$

We then substitute (2.6) into (2.5) to obtain the standard Helmholtz equation form as

$$(\nabla_{\xi\zeta}^2 + \frac{k_0^2\epsilon_{zz}\gamma}{M})E_z(\xi,\zeta) = j\frac{\omega\mu_0 I_0 \gamma}{M}\delta(\xi - \xi_s)\delta(\zeta - \zeta_s) \tag{2.7}$$

with

$$M = t_1(t_1\mu_{xx} + t_2^2)$$

A similar coordinate transformation was derived in [30] but restricted to the condition $\mu_{xy} + \mu_{yx} = 0$. The proposed coordinate transformation in (2.6) is general and has no restrictions on the parameters in (2.1). It is noteworthy that the linear relationship between (ξ, ζ) and (x, y) expressed in (2.6) is not unique. As long as the two coefficients in the term $\nabla^2_{\xi\zeta}$ are equal and the coefficient of the term $\partial^2/\partial\xi\partial\zeta$ is zero after a transformation, the constructed linear coordinate relationship is applicable to solve (2.7). The proposed transformation will not be applicable when $M = 0$, i.e., the situation $(\mu_{xy} + \mu_{yx})^2 = 4\mu_{xx}\mu_{yy}$. In this case, (2.7) becomes singular. The solution for (2.7) is known [100] to be

$$E_z(\xi, \zeta) = -\frac{k_0\eta_0}{4M}\gamma I_0 H_0^{(2)}(kR_m) \tag{2.8}$$

with

$$\begin{aligned} k^2 &= \frac{k_0^2\epsilon_{zz}\gamma}{M} \\ R_m &= \sqrt{(\xi - \xi_s)^2 + (\zeta - \zeta_s)^2} \\ &= \sqrt{t_1^2(x - x_s)^2 + (t_2^2 + t_3^2)(y - y_s)^2 + 2t_1t_2(x - x_s)(y - y_s)}. \end{aligned}$$

The transformation of (2.8) back to the original coordinates can be accomplished via the following relation

$$E_z(x, y) = \frac{E_z(\xi, \zeta)}{J(\xi, \zeta; x, y)} = \frac{k_0\eta_0}{4t_1t_3M}\gamma I_0 H_0^{(2)}(kR_m) \tag{2.9}$$

where $J(\xi, \zeta; x, y)$ is the Jacobian determinant of the coordinate transformation. Equation (2.9) is the radiation electric field of an electric line source placed in an unbounded anisotropic region.

Through equation (2.2a), the other two remaining field components H_x and H_y are obtained as:

$$\begin{aligned} H_x &= \frac{j}{\omega\mu_0\gamma}(\mu_{yy}\frac{\partial E_z}{\partial y} + \mu_{xy}\frac{\partial E_z}{\partial x}) \\ H_y &= -\frac{j}{\omega\mu_0\gamma}(\mu_{yx}\frac{\partial E_z}{\partial y} + \mu_{xx}\frac{\partial E_z}{\partial x}) \end{aligned} \tag{2.10}$$

where

$$\begin{aligned}
\frac{\partial E_z}{\partial x} &= -\frac{k_0\eta_0}{4Mt_1t_3}\gamma I_0 k H_1^{(2)}(kR_m)R_{e1} \\
\frac{\partial E_z}{\partial y} &= -\frac{k_0\eta_0}{4Mt_1t_3}\gamma I_0 k H_1^{(2)}(kR_m)R_{e2} \\
R_{e1} &= \frac{t_1^2(x-x_s)+t_1t_2(y-y_s)}{R_m} \\
R_{e2} &= \frac{(t_2^2+t_3^2)(y-y_s)+t_1t_2(x-x_s)}{R_m}.
\end{aligned}$$

The three field components, E_z, H_x and H_y, generated by the electric line source belong to the TM mode. In the case of the TE mode, when a magnetic line source expressed as $\boldsymbol{K} = K_0\delta(x-x_s)\delta(y-y_s)\hat{\boldsymbol{z}}$ is placed in an unbounded space constituted of the homogeneous anisotropic material defined in (2.1), the radiation field expressions are straightforwardly obtained via duality, that is [34]

$$\begin{aligned}
&\overline{\epsilon} \to \overline{\mu} \quad k_0 \to k_0 \quad \boldsymbol{H} \to -\boldsymbol{E} \\
&\overline{\mu} \to \overline{\epsilon} \quad \eta_0 \to 1/\eta_0 \quad \boldsymbol{E} \to \boldsymbol{H}
\end{aligned} \tag{2.11}$$

According to (2.11), three field components, H_z, E_x and E_y, constitute the TE mode. It is important to mention is that our proposed method is not valid in the case of $\gamma = 0$. Since $\overline{\mu_r}$ (or $\overline{\epsilon_r}$ for the TE case) would be not invertible under $\gamma = 0$, therefore equation (2.3) would not be applicable. The frequency-domain solver using a finite-element method (FEM) in the commercial software package CST [101] also fails when $\gamma = 0$ for the scattering evaluation of an infinite anisotropic cylinder. The physical restriction behind this phenomenon needs more investigations and is not addressed in this thesis.

Although the handling of anisotropic material by MFCM-like techniques is reported in [18, 70–72], there are still many differences between our work and these references. The anisotropic materials investigated in [18, 70, 71] are limited to the cases of diagonal $\overline{\epsilon}$ or $\overline{\mu}$, and in [72], they have to satisfy the conditions $\epsilon_{xy} + \epsilon_{yx} = 0$ and $\mu_{xy} + \mu_{yx} = 0$. The proposed method can handle the anisotropic material with arbitrary ten parameters defined in (2.1). Indeed, many anisotropic materials have a diagonal $\overline{\epsilon}$ or $\overline{\mu}$ such as the natural crystals, and most of the anisotropic material with non-zero ϵ_{xy}, ϵ_{yx}, μ_{xy} and μ_{yx} satisfy the conditions $\epsilon_{xy} + \epsilon_{yx} = 0$ and $\mu_{xy} + \mu_{yx} = 0$, such as the gyrotropic materials. However, as discussed in [102], the nonreciprocal characteristic of an anisotropic material can be tuned by varying the values of ϵ_{xy} and ϵ_{yx}. This phenomenon provides an attracting motivation to design an artificial material with tunable non-diagonal elements in $\overline{\epsilon}$ or $\overline{\mu}$. In addition, the

isotropic but noncentrosymmetric materials, such as cadmium telluride (CdTe), cadmium sulfide (CDS), gallium arsenide (GaAs), and zinc telluride (ZnTe) as introduced in [103], act like an anisotropic material with $\epsilon_{xy} = \epsilon_{yx}$ when a dc electric field is applied. In this case, our proposed method can conduct the electromagnetic evaluations of the anisotropic materials introduced in [102] [103] whereas the MFCM-like techniques introduced in [18, 70–72] are not applicable.

The fields derived in this section play a key role in the MFCM when dealing with anisotropic scatterers since they are the basis of field representations in the anisotropic medium filled region.

2.2 Problem formulation

Based on the findings of the previous section, it is possible to introduce the formulation of the MFCM in an anisotropic case. The problem is depicted in Fig. 2.1. The outer region 1 is considered as vacuum and the inner region 2 is occupied by the anisotropic material characterized by (2.1). Regions 1 and 2 are separated by the boundary of the cylinder.

The concept of the MFCM is the same as described in [58] for the isotropic case and is illustrated in Fig. 2.2 for reference. We place a set of z-directed filamentary currents with unknown complex coefficients in regions 1 and 2. The electric line source is used for the TM polarization scenario whereas the magnetic line source answers for the TE situation. The formulation of the MFCM is conducted through two equivalences. Firstly, the scattered fields in region 1 are generated by equivalent line sources placed in region 2, and those line sources are treated as source currents radiating in an unbounded vacuum. Secondly, the internal fields in region 2 are generated by equivalent line sources placed in region 1, and those line sources are radiating in an unbounded space filled with a homogeneous anisotropic material identical to that constituting the cylinder.

2.2.1 Fields Expressions

Only TM polarization is considered herein, the formulation of TE case can be obtained straightforwardly via duality theorem and will not be presented in this Section. Region 1 contains the incident and scattered fields. The incident wave propagates in a direction perpendicular to the z-axis, therefore a 2D problem is considered. The incident fields can be written as:

$$\boldsymbol{E}_{inc} = e^{jk_0(x\cos\phi_{inc}+y\sin\phi_{inc})}\hat{\boldsymbol{z}} \tag{2.12a}$$

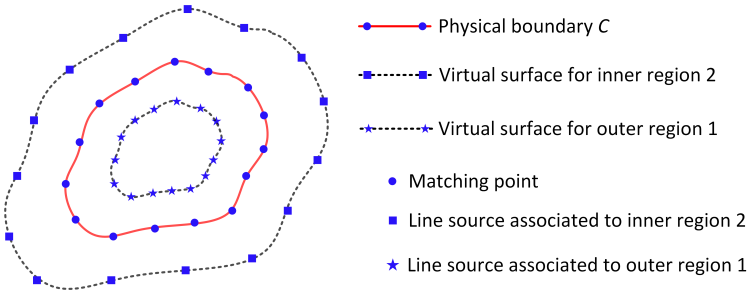

Figure 2.2 Problem description for the MFCM.

$$\boldsymbol{H}_{inc} = \frac{-\sin\phi_{inc}\hat{\boldsymbol{x}} + \cos\phi_{inc}\hat{\boldsymbol{y}}}{\eta_0} e^{jk_0(x\cos\phi_{inc}+y\sin\phi_{inc})} \tag{2.12b}$$

for the TM case, where k_0 and η_0 are the free space wavenumber and intrinsic impedance, respectively. Although only plane wave incidence is considered in our numerical examples, the proposed method has no restriction of the external field excitation as long as it is invariable along the z-axis.

The scattered fields in region 1 are due to all z-directed current filaments in region 2, radiating in the unbounded free space. The field expressions are given by

$$\boldsymbol{E}_1^s = -\frac{k_0\eta_0}{4}\sum_{i=1}^{N_1} I_{1i} H_0^{(2)}(k_0 R_{1i})\hat{\boldsymbol{z}} \tag{2.13a}$$

$$\boldsymbol{H}_1^s = \frac{k_0}{4j}\sum_{i=1}^{N_1} I_{1i}\frac{(y_{1is}-y)\hat{\boldsymbol{x}} + (x-x_{1is})\hat{\boldsymbol{y}}}{R_{1i}} H_1^{(2)}(k_0 R_{1i}) \tag{2.13b}$$

for the TM case. The term I_{1i} is the unknown complex coefficient of ith electric current source placed in region 2. N_1 is the number of line sources in region 2, couple $(x_{1is},\ y_{1is})$ is the coordinate of the ith filament source position in region 2 and $(x,\ y)$ is the observation point. The term R_{1i} is the distance between the ith filament source in region 2 and the observation point, and it is calculated with:

$$R_{1i} = \sqrt{(x-x_{1is})^2 + (y-y_{1is})^2} \tag{2.14}$$

The fields in region 2 are due to z-directed current filaments in region 1, radiating in the unbounded space occupied by homogeneous anisotropic material. In light of the derived radiation fields studied in Section 2.1, the total fields in region 2 could be expressed as

$$\boldsymbol{E}_2 = \sum_{i=1}^{N_2} E_{iz}\hat{\boldsymbol{z}} \tag{2.15a}$$

$$\boldsymbol{H}_2 = \sum_{i=1}^{N_2} (H_{ix}\hat{\boldsymbol{x}} + H_{iy}\hat{\boldsymbol{y}}) \tag{2.15b}$$

for the TM case, where E_{iz}, H_{ix} and H_{iy} are found in (2.9)-(2.10). N_2 is the number of line sources in region 1. The coefficient I_0 in (2.9) should be replaced by I_{2i}, representing unknown complex coefficient of ith electric filament placed in region 1, in (2.15), and couple (x_{2is}, y_{2is}) expresses the ith filament source position in region 1.

2.2.2 Boundary Conditions

The connection between the fields in regions 1 and 2 is dictated by the boundary conditions at the cross section surface C of the cylinder indicated in Fig. 2.1. Specifically, the tangential components of electric and magnetic fields must be continuous along the physical boundary C, which leads to

$$\begin{aligned} \hat{\boldsymbol{n}} \times (\boldsymbol{E}_{inc} + \boldsymbol{E}_1^s) &= \hat{\boldsymbol{n}} \times \boldsymbol{E}_2 \\ \hat{\boldsymbol{n}} \times (\boldsymbol{H}_{inc} + \boldsymbol{H}_1^s) &= \hat{\boldsymbol{n}} \times \boldsymbol{H}_2 \end{aligned} \tag{2.16}$$

where $\hat{\boldsymbol{n}}$ is a unit vector normal to the cylinder surface C as shown in Fig. 2.1. A linear system is then created by imposing the boundary condition over a number of matching points on C, as suggested in Fig. 2.2. The number of matching points (N_m) must satisfy the inequality

$$N_m \geqslant N_1; \quad N_m \geqslant N_2 \tag{2.17}$$

in order to determine the total unknown current coefficients (N_1 in region 2 and N_2 in region 1).

Upon the application of a point-matching procedure, we will finally obtain a matrix expression of the type

$$[Q]\,\boldsymbol{X} = \boldsymbol{B} \tag{2.18}$$

where $\boldsymbol{X}$ is a column vector containing the unknown current coefficients (K_1 and K_2, or I_1 and I_2), and $\boldsymbol{B}$ is another column vector containing samples of the incident tangential fields at the matching points. $[Q]$ is a matrix whose entries are obtained from the tangential fields of filaments at matching points, and it could be rectangular or square depending whether oversampling is used or not. If it is in a square form, a unique solution can be found, otherwise

the smallest least-square error solution is pursued [58] and will be (4.25) in Sec. 4.4.1. In the numerical examples of Section 2.3, we will always adopt the square matrix $[Q]$ by letting $N_1 = N_2 = N_m = N$.

2.2.3 Source Location

The source location is dependent on the shape of the cylinder. The *ad hoc* $R/2-2R$ rule used in [58, 104] is effective for a circular boundary. In Fig. 2.3(a), a smooth circular boundary is presented, the *ad hoc* $R/2 - 2R$ rule is performed by uniformly placing filament currents with a radius $2r$ in region 1 whereas with a radius $r/2$ in region 2, where r is the radius of the circular cylinder. The location of the matching point is also uniformly placed on the physical boundary C. For an unsmooth boundary as suggested in Fig. 2.3(b) which contains sharp edges, the *ad hoc* $R/2 - 2R$ rule is not applicable. Previous work have shown that better results are obtained by locating sources closer to the edges and then gradually place the others a distance away in order to better approximate the singular field behavior near the edges [27, 105]. The inner and outer source locations are symmetrical with respect to the boundary, as shown in Fig. 2.3(b). The location of matching points on the physical boundary also obey the same rule, that is, the matching points density increases near the edges. It is noteworthy that the singularity problem appears in [30–33] when the distance between source and field points vanishes, therefore a special treatment on Hankel function with argument approaching zero should be considered. However, this singularity is avoided in the MFCM by placing sources at a prescribed distance away from the matching points. A useful empirical formula [105] for the source and matching point locations is given below. Taking the upper side boundary in Fig. 2.3(b) as an example, the ith source position (ρ_{s2}, ϕ_{s2}) (the cylindrical coordinate system is exploited herein for the convenience) in region 1 is given by

$$\rho_{s2}(i) = \rho_{max} - (\rho_{max} - \rho_{min}) \sin(\frac{\pi(i-1)}{N_v - 1}), \qquad 1 \leqslant i \leqslant N_v \tag{2.19a}$$

$$\phi_{s2}(i) = \pi/2 - (\pi/2 - \beta - \Delta\phi_s) \cos(\frac{\pi(i-1)}{N_v - 1}), \qquad 1 \leqslant i \leqslant N_v \tag{2.19b}$$

where $\rho_{max} = c_1 r$, $\rho_{min} = c_2 r$, $r = \sqrt{a^2 + b^2}$ and $\beta = \arctan(b/a)$ as Fig. 2.4 shows. c_1 and c_2 are two coefficients yet to be determined with a convergence study. N_v is the number of sources associated with the upper side boundary of the rectangular cylinder. For the ith matching point (ρ_b, ϕ_b) on the upper side boundary is given by

$$\phi_b(i) = \pi/2 - (\pi/2 - \beta - \Delta\phi_s) \cos(\frac{\pi(i-1)}{N_v - 1}), \qquad 1 \leqslant i \leqslant N_v \tag{2.20a}$$

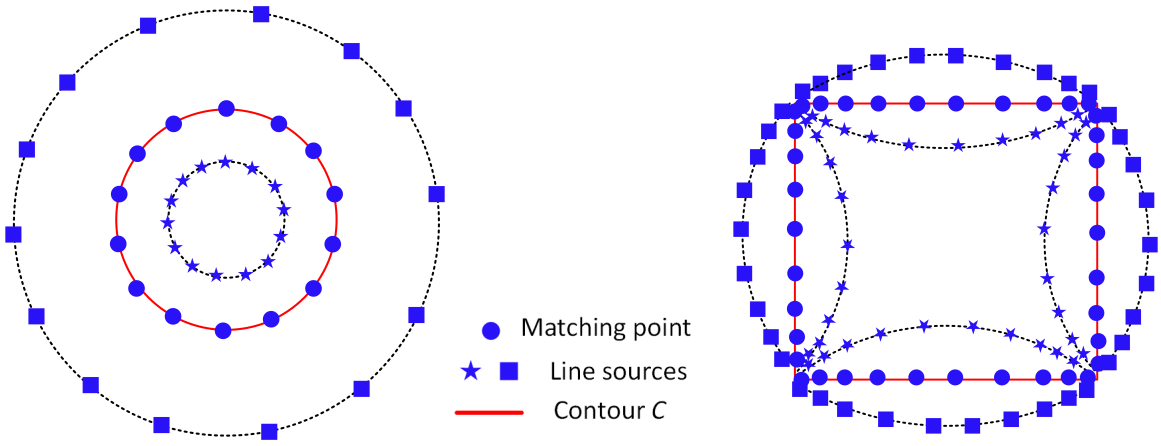

Figure 2.3 Source location strategies for (a) circular and (b) rectangular cross sections.

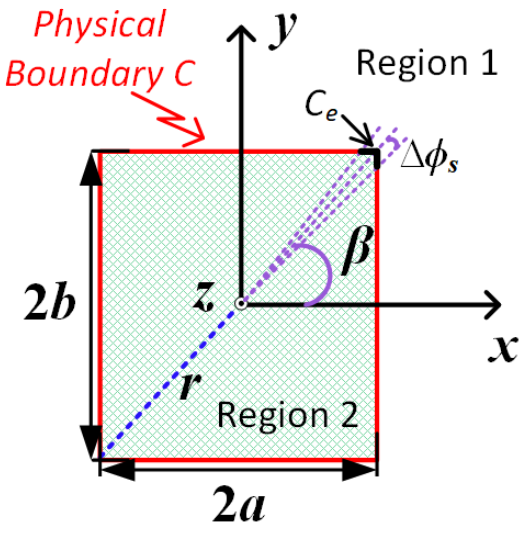

Figure 2.4 Configuration of a rectangular cylinder.

$$\rho_b(i) = \frac{b}{|\sin(\phi_b(i))|}, \qquad 1 \leqslant i \leqslant N_v \tag{2.20b}$$

where $\Delta\phi_s$ denotes a suitably chosen angular shift in the azimuthal direction relative to each edge position as shown in Fig. 2.4. A small section of the boundary C_e in terms of the $2\Delta\phi_s$ is defined at each edge of the rectangular cylinder as depicted in Fig. 2.4. The C_e at each edge is untouched in the MFCM, which means no matching points are placed on it. In our numerical examples which involve rectangular cylinders, the $\Delta\phi_s$ is chosen as $\pi r/(360\lambda)$, which makes the length of the C_e is very small compared with the incident wavelength and therefore the scattered far-field is not expected to be greatly affected.

So far, all information has been presented for setting up the linear system. Once the current magnitudes are determined, the fields and related parameters of interest can be evaluated in a straightforward manner.

2.3 Scattering analyses of cylinders with different shapes

Based on the numerical scheme described in previous sections, a computer program has been implemented. The program computes the 2D scattering width (σ) normalized to the incident wavelength (λ), defined as

$$\frac{\sigma_e}{\lambda} = \lim_{r\to\infty}(2\pi r\frac{|E_z^s|^2}{\lambda\,|E_z^i|^2}) \tag{2.21a}$$

for the TM case, and

$$\frac{\sigma_h}{\lambda} = \lim_{r\to\infty}(2\pi r\frac{|H_z^s|^2}{\lambda\,|H_z^i|^2}) \tag{2.21b}$$

for the TE case. It is noteworthy that ϵ_{xx}, ϵ_{xy}, ϵ_{yx}, ϵ_{yy}, and μ_{zz} are presented in the field expressions for the TE case whereas μ_{xx}, μ_{xy}, μ_{yx}, μ_{yy}, and ϵ_{zz} are used for the field expressions of the TM case. The parameters of $\overline{\epsilon}$ and $\overline{\mu}$ in our numerical examples are referred to existing publications to allow comparisons with previously computed results.

The first example is a circular anisotropic cylinder under a TE polarized incident wave. Fig. 2.5 shows the normalized scattering width response of a circular cylinder under three different cases. The first case is a cylinder with $k_0 r = \pi/2$, where r is the radius of the cylinder, characterized by $\epsilon_{xx} = 4\epsilon_{yy} = 4$, $\epsilon_{xy} = \epsilon_{yx} = 0$, and $\mu_{zz} = 2$. The incident wave is assumed to propagate normally along the negative x-direction ($\phi_{inc} = 0^\circ$). The bistatic normalized scattering width response versus ϕ is presented in Fig. 2.5. Case 2 corresponds to a gyrotropic-type cylinder characterized by the following medium parameters: $\epsilon_{xx} = \epsilon_{yy} = 4$, $\epsilon_{xy} = -\epsilon_{yx} = 2$, and $\mu_{zz} = 2$. The size of the cylinder and the incident wave are the same as in the previous example. The bistatic normalized scattering width computation is also depicted

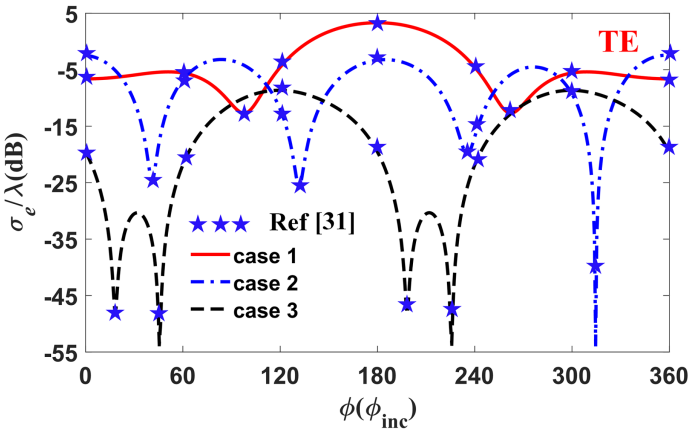

Figure 2.5 Normalized scattering width response of a circular cylinder under the TE polarization. (case 1: bistatic scattering width response with $k_0 r = \pi/2$, $\epsilon_{xx} = 4\epsilon_{yy} = 4$, $\epsilon_{xy} = \epsilon_{yx} = 0$, $\mu_{zz} = 2$, $\phi_{inc} = 0^\circ$; case 2: bistatic scattering width response with $k_0 r = \pi/2$, $\epsilon_{xx} = \epsilon_{yy} = 4$, $\epsilon_{xy} = -\epsilon_{yx} = 2$, $\mu_{zz} = 2$, $\phi_{inc} = 0^\circ$; case 3: monostatic scattering width response versus ϕ_{inc} with $k_0 r = \pi/2$, $\epsilon_{xx} = 4 - j$, $\epsilon_{xy} = 3 - j$, $\epsilon_{yx} = 1 + j$, $\epsilon_{yy} = 2 - j$, $\mu_{zz} = (23 - 37j)/26$).

in Fig. 2.5. Case 3 is the monostatic normalized scattering width response of an arbitrary anisotropic cylinder with the same size as the previous two cases, while characterized by the medium parameters: $\epsilon_{xx} = 4-j$, $\epsilon_{xy} = 3-j$, $\epsilon_{yx} = 1+j$, $\epsilon_{yy} = 2-j$, and $\mu_{zz} = (23-37j)/26$. The monostatic normalized scattering width response is plotted in Fig. 2.5. The results for the three cases are compared with those presented in [34]. An excellent agreement can be observed in all cases.

In order to study the convergence of the results, we make use of the error on the imposed tangential E-field and H-field boundary condition as metrics, whose definition read

$$\Delta E_{bc} = \frac{|\hat{n} \times (\boldsymbol{E}_1^s + \boldsymbol{E}_{inc} - \boldsymbol{E}_2)|}{|\boldsymbol{E}_{inc}|} \tag{2.22a}$$

$$\Delta H_{bc} = \frac{|\hat{n} \times (\boldsymbol{H}_1^s + \boldsymbol{H}_{inc} - \boldsymbol{H}_2)|}{|\boldsymbol{H}_{inc}|} \tag{2.22b}$$

ΔE_{bc} and ΔH_{bc} are evaluated on contour C, between the matching points used to solve (2.18). The necessary numbers of sources and matching points in MFCM-based numerical calculation are increased until ΔE_{bc} and ΔH_{bc} reach the desired level of accuracy. Convergence for the case of a circular anisotropic cylinder is easy to achieve, and therefore the convergence study is omitted herein. The numbers of matching points and the sources in each region are selected to be equal ($N_1 = N_2 = N_m$) in the above three examples. Placing 16 filamentary currents per region ($N_1 = N_2 = 16$) and 16 matching points on the boundary has led to a stable

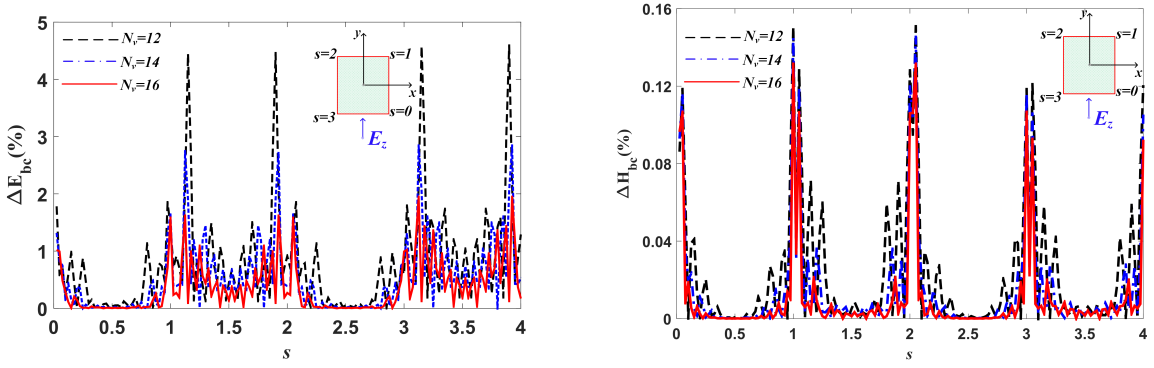

(a) (b)

Figure 2.6 (a) E-field and (b) H-field boundary condition error of an anisotropic square cylinder under the TM polarization. ($k_0a = 2.5$, $\mu_{xx} = 2$, $\mu_{yy} = 4$, $\mu_{xy} = \mu_{yx} = 0$, $\epsilon_{zz} = 2$, $\phi_{inc} = 270^\circ$). Variable s is a parameter controlling the position around the cylinder, as illustrated in the inset.

result.

We will now consider an anisotropic square cylinder ($a = b$) with $k_0a = 2.5$ under the TM scenario, characterized by $\mu_{xx} = 2$, $\mu_{yy} = 4$, $\mu_{xy} = \mu_{yx} = 0$, and $\epsilon_{zz} = 2$. The incident plane wave is assumed to propagate along the positive y-direction ($\phi_{inc} = 270^\circ$). The result of the convergence study is depicted in Fig. 2.6. The reason why ΔE_{bc} has a larger value than the ΔH_{bc} is not clear and requires more investigations in the future work. N_v is the number of sources associated with each side boundary per region and defined in (2.19). Constants c_1 and c_2 in (2.19) are found to be 0.99 and 0.8, respectively. Using (2.22), the field discontinuity is calculated at 160 sampling points uniformly selected on the square boundary C. Plots of ΔE_{bc} and ΔH_{bc} for different values of N_v are presented in Fig. 2.6. If we take (ΔE_{bc} and ΔH_{bc}) $< 2\%$ as a criteria to determine the necessary number of sources, $N_v = 16$ would be sufficient, which amounts to 64 sources per region and a total of 128 unknowns for the square cylinder computation. The determined number of sources under the (ΔE_{bc} and ΔH_{bc}) $< 2\%$ criterion is valid for the cases with $k_0a \leqslant 2.5$, the (ΔE_{bc} and the criterion should be retested when $k_0a > 2.5$. It can be seen in Fig. 2.6 that the largest errors occur near the corners or the cylinders, i.e. in the C_e interval where the MFCM applies no point matching. The normalized bistatic scattering width versus the scattering angle under the TM polarization computed with the MFCM is presented in Fig. 2.7. The general trends of the three curves are similar but large differences occur near the maximums, especially with the results of [41]. The expected symmetry of the results with respect to $\phi = 90^\circ$ is clearly observed in the MFCM solution, but the solution of [41] has obviously asymmetry, as for example between results at $\phi = 60^\circ$ and $\phi = 120^\circ$. It is reasonable to have small differences between our results and

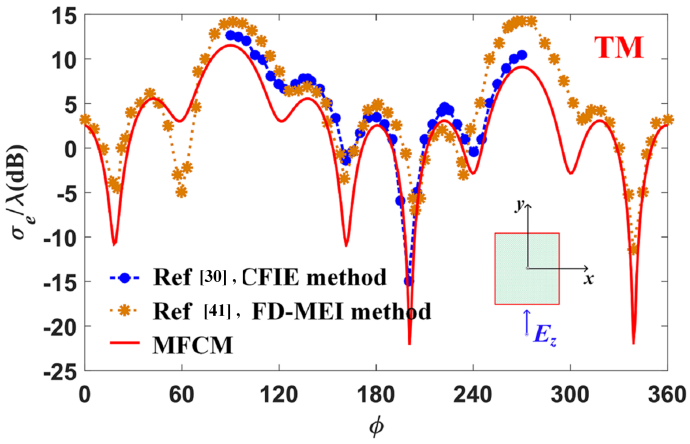

Figure 2.7 Bistatic normalized scattering width response of an anisotropic square cylinder under the TM polarization. ($k_0a = 2.5$, $\mu_{xx} = 2$, $\mu_{yy} = 4$, $\mu_{xy} = \mu_{yx} = 0$, $\epsilon_{zz} = 2$, $\phi_{inc} = 270°$).

published ones because the treatments on the problem differ. It is hard to say with absolute certainty which one of these methods gives the best result.

The next example is a gyrotropic-type square cylinder with three different k_0a values, characterized by $\mu_{xx} = \mu_{yy} = 4$, $\mu_{xy} = -\mu_{yx} = 2$, and $\epsilon_{zz} = 2$. The incident wave is TM polarized with $\phi_{inc} = 180°$. The boundary condition error is also tested and the criterion $\Delta E_{bc}(\Delta H_{bc}) < 2\%$ is taken to determine the necessary number of sources as well as parameters c_1 and c_2. Using $c_1 = 0.995$ and $c_2 = 0.85$, this convergence criterion is obtained with $N_v = 17$ for the three simulated k_0a values. The bistatic normalized scattering width responses of the gyrotropic-type square cylinder are presented in Fig. 2.8. It indicates the scattering responses at different frequencies differ, and an asymmetric response with respect to $\phi = 180°$ is obtained due to the gyrotropic anisotropy.

The next example is the monostatic normalized scattering width responses of an anisotropic rectangular cylinder with $k_0b = 5$ and various k_0a values under the TM situation. The medium parameters are $\mu_{xx} = 4$, $\mu_{xy} = -\mu_{yx} = 2 - j$, $\mu_{yy} = 2$ and $\epsilon_{zz} = 2$. We assume that N_v is the number of sources associated with upper or lower side boundaries, whereas N_h is the number of sources associated with left or right side boundaries. N_v was equal to N_h for the computation of a square cylinder, whereas in the case of a rectangular cylinder, the N_v and N_h are distinct. Once again, a convergence criterion (ΔE_{bc} and ΔH_{bc}) $< 2\%$ is considered. The calculated scattering widths are shown in Fig. 2.9. To obtain the three curves, N_v was found to be 19 whereas N_h was 44 for $k_0a = 2$, 39 for $k_0a = 3$ and 31 for $k_0a = 4$, along with c_1=0.995 and $c_2 = 0.85$. The different width ratios of the rectangular geometry will lead to similar scattering responses yet with dissimilar details, as Fig. 2.9 indicates.

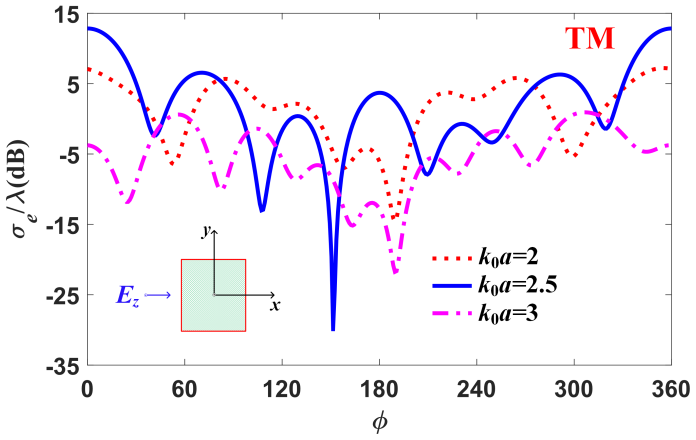

Figure 2.8 Bistatic scattering width response of a gyrotropic-type square cylinder under the TM polarization. ($\mu_{11} = \mu_{22} = 4$, $\mu_{12} = -\mu_{21} = 2$, $\epsilon_{33} = 2$, $\phi_{inc} = 180^\circ$).

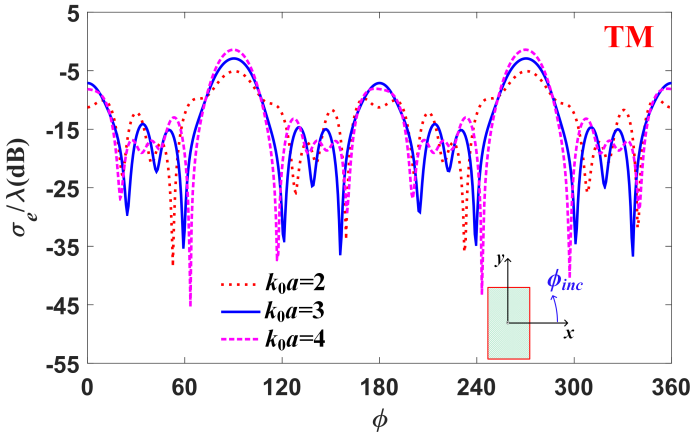

Figure 2.9 Monostatic scattering width response of an anisotropic rectangular cylinder under the TM polarization. ($k_0b = 5$, $\mu_{xx} = 4$, $\mu_{xy} = -\mu_{yx} = 2 - j$, $\mu_{yy} = 2$, $\epsilon_{zz} = 2$).

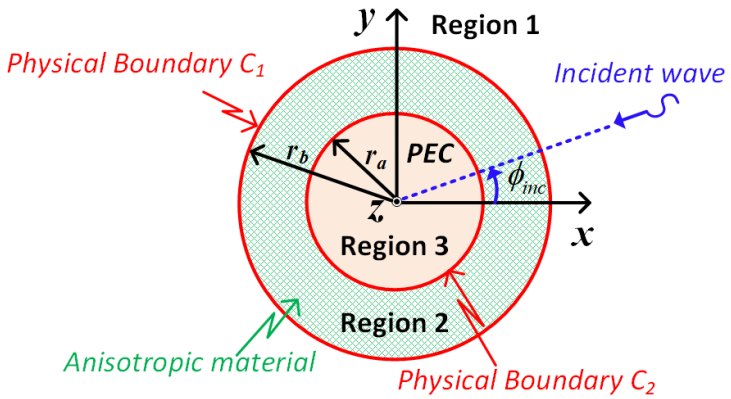

(a)

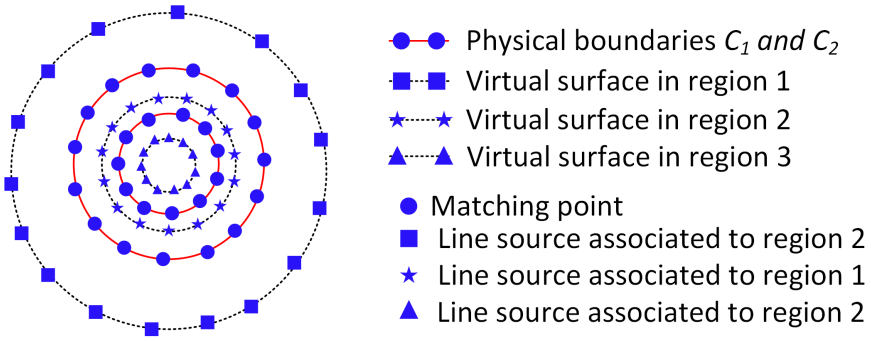

(b)

Figure 2.10 The PEC cylinder coated with an anisotropic material scenario. (a)Geometry and (b) locations of matching points and sources

The scattering from a PEC cylinder coated with an anisotropic shell, as depicted in Fig. 2.10(a), also can be handled straightforwardly without more modifications in the formulation. Compared to the previous examples, three regions instead of two are presented in this scenario. The outermost region 1 is free space, the region 2 is a shell with two physical boundaries C_1 and C_2 occupied with the anisotropic material, and the innermost region 3 is a PEC rod with a radius r_a. The locations of matching points and sources are shown in Fig. 2.10(b). The formulation is similar to that of circular anisotropic cylinders. The only difference is that two sets of filamentary sources, associated to the two physical boundaries of the region 2, are required to simulate the fields inside of the anisotropic shell. The *ad hoc* $R/2 - 2R$ rule is also adopted for the source location. The anisotropic shell and PEC rod have dimensions of $k_0 r_a = 1$ and $k_0 r_b = 2$, and the medium parameters of the anisotropic material are $\mu_{xx} = 1.5$, $\mu_{yy} = 2.5$, $\mu_{xy} = -\mu_{yx} = 3$, and $\epsilon_{zz} = 1.5$. The normalized scattering width responses are presented in Fig. 2.11 under the TM polarization with different incident angles. Our calculated result for the scenario of $\phi_{inc} = 0^\circ$ has an excellent agreement with that of [38]. Scattering responses with another three different incident angles are also shown in Fig. 2.11, the scattering widths are the same between $\phi_{inc} = 0^\circ$ and $\phi_{inc} = 180^\circ$ cases, or $\phi_{inc} = 90^\circ$ and $\phi_{inc} = 270^\circ$ cases except for a π angle shift, whereas the scattering widths between $\phi_{inc} = 0^\circ$ and $\phi_{inc} = 90^\circ$ differ due to the gyrotropic anisotropy of the shell. Although only the circular shape is considered in this example, the proposed technique has no restrictions on the geometry of the cross section.

2.4 The behaviors of filament currents in terms of scattered fields singularities and matrix ill-conditioning

The singularities of the analytic continuation of the scattered field in the interior of scatterers with circular and noncircular shapes have been discussed in [2,106–110] under a plane wave or line source illumination. Yet only PEC and isotropic dielectric scatterers have been considered so far. To complete the analysis of the proposed MFCM on ansiotropic materials, we conduct the study of scattered fields singularties for an anisotropic elliptical cylinder with a TM incident plane wave. The configuration of the anisotropic elliptical cylinder is depicted in Fig. 2.12. The dimensions of the cylinder are $k_0 a = 2\pi$ and $k_0 b = 1.6\pi$ with $a = 1\lambda$ and $b = 0.8\lambda$, and the material in region 2 is characterized by $\mu_{yy} = 4\mu_{xx} = 4$, $\mu_{xy} = \mu_{yx} = 0$, and $\epsilon_{zz} = 2$. The incident TM wave is assumed to propagate normally in the negative x-direction ($\phi_{inc} = 0^\circ$). The eccentricity of the elliptical contour is $e = 0.6$. The locations of matching points and sources are displayed in Fig. 2.12(b). Two virtual curves where sources are placed, C_1 and C_2, are similar ellipses inside and outside C with the same eccentricity e but different

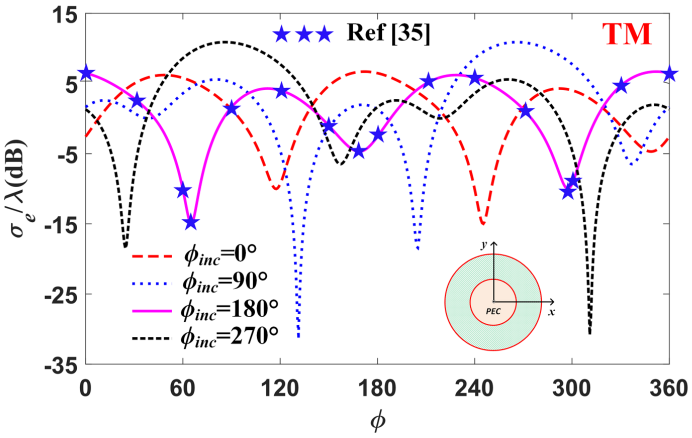

Figure 2.11 Bistatic scattering width response of an anisotropic shell coated PEC cylinder with various incident angles under the TM polarization. ($k_0 r_a = 1$, $k_0 r_b = 2$, $\mu_{xx} = 1.5$, $\mu_{yy} = 2.5$, $\mu_{xy} = -\mu_{yx} = 3$, $\epsilon_{zz} = 1.5$).

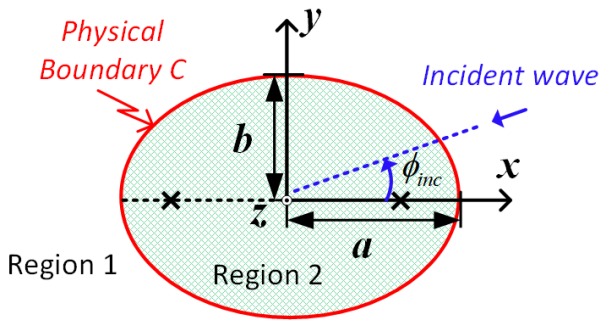

(a)

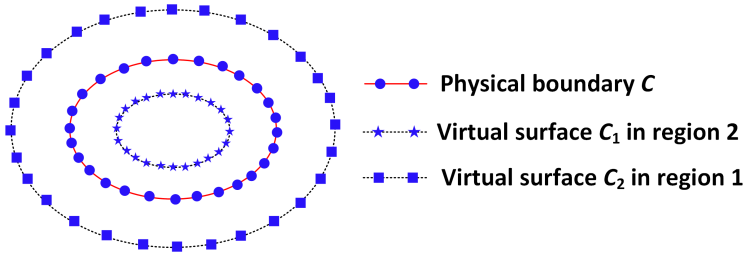

(b)

Figure 2.12 (a) Configuration of an anisotropic elliptical cylinder, and (b) locations of matching points and sources. (The two crosses represent the position of singular points).

semiaxes lengths. We define the semiaxes lengths of C_1 as $a_{in} = \xi_{in}a$ and $b_{in} = \xi_{in}b$, while $a_{out} = \xi_{out}a$ and $b_{out} = \xi_{out}b$ are the semiaxes lengths for C_2. The singularities of the analytic continuation of the scattered field inside the elliptical boundary C, as described in Fig. 2.12(a) with two crosses, lie at two focal points [2], i.e. $(x, y) = (\pm c, 0)$ where $c = 0.6$ in this scenario. Two numerical examples are conducted herein. Sixty matching points and sixty sources per region are enough to satisfy the imposed boundary condition criteria and are used to do the simulation in each example. The strategy for the placements of matching points and sources refers to [2], and a bit more sources and matching points are placed around $\phi = 0^\circ$ and $\phi = 180^\circ$ areas.

The first example contains two scenarios: 1) $\xi_{in} = 0.75$ and $\xi_{out} = 1.25$, and 2) $\xi_{in} = 0.75$ and $\xi_{out} = 1.55$. Therefore the two internal singularities are enclosed by C_1 in both case of the first example. The investigation for behaviors of filament currents lying in the interior of the scatterer is conducted by considering different placements of outside filament currents, i.e., $\xi_{out} = 1.25$ and $\xi_{out} = 1.55$. The second example also contains two scenarios: 1) $\xi_{in} = 0.45$ and $\xi_{out} = 1.25$, and 2) $\xi_{in} = 0.45$ and $\xi_{out} = 1.55$. Therefore the singularities inside C are not enclosed by C_1 in both cases this time. Also, the investigation is conducted with different placements of outside filament currents. The real and imaginary parts of normalized currents inside and outside the scatterer are computed. The computed results for the first and second examples are shown in Fig. 2.13 and Fig. 2.14, respectively. From Fig. 2.13(a) and 2.13(b), we can see that the normalized currents placed on C_1 are relatively smooth and have relatively small values when inside singularities are enclosed, and the behaviors of inside filament currents are not affected by the placement of outside currents. It is noteworthy that the variation of currents in Fig. Fig. 2.13(a) and 2.13(b) is not very smooth. This phenomenon slightly violates with the observation from [2] where a PEC elliptical cylinder is considered. The reason is due to the anisotropy of the material since a smooth oscillation was observed if we change the value of μ_{xx} from 1 to 4 in our code. In this case the material is isotropic with $\epsilon_r = 2$ and $\mu_r = 4$. The calculations of scattered fields on the physical boundary using the two sets of currents are almost the same, which coincides with that observed in [2, 108, 110], and they have a good agreement with that obtained from commercial software package CST, as Fig, 2.13(c) shows.

On the other hand, the normalized inside currents present rapid oscillations and reach large values, as Figs. 2.14(a) and 2.14(b) indicate, when the inside singularities are not enclosed, and this phenomenon is also not affected by the currents placed outside. However, an interesting thing is that the calculated scattered fields on the physical boundary using the two sets of currents, as shown in Fig. 2.14(c), are different in this example. The fields generated in case 2 are not as accurate as case 1, but the accuracy can be improved to as good as case

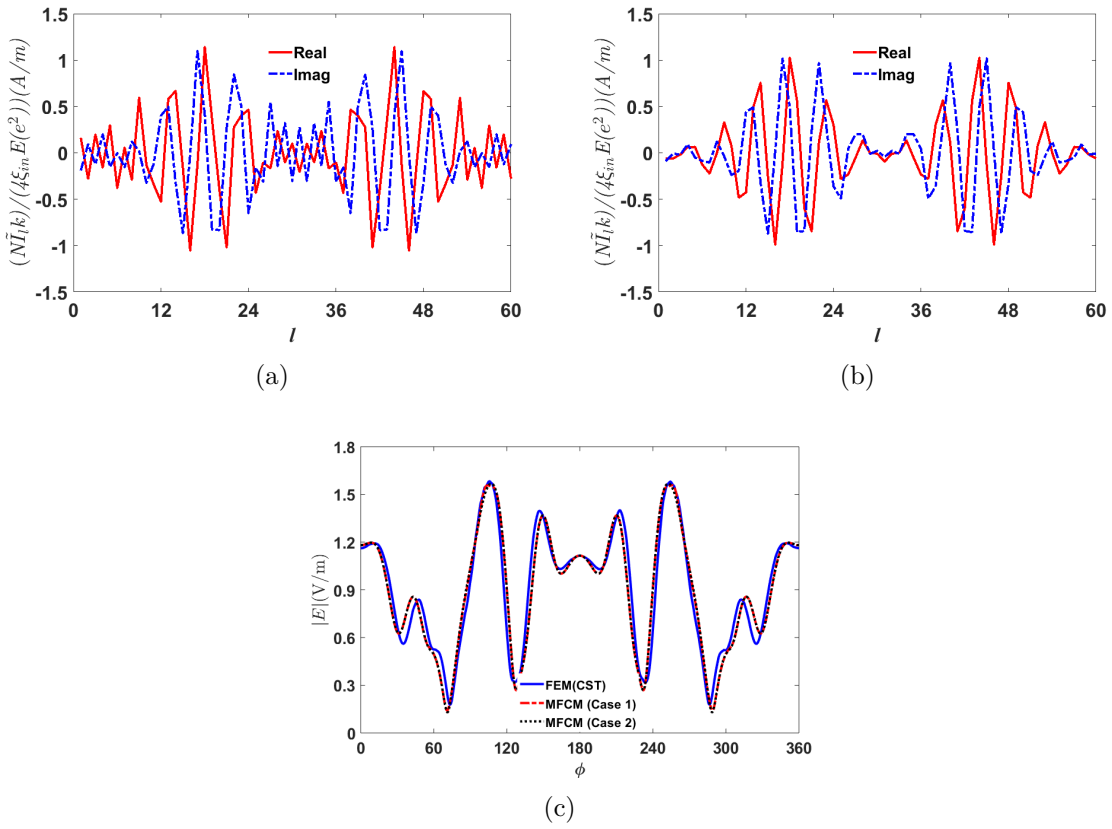

Figure 2.13 The computed real and imaginary parts of normalized inside currents on virtual internal surface C_1 using $\xi_{in} = 0.75$, (a) $\xi_{out} = 1.25$ and (b) $\xi_{out} = 1.55$ versus filament index l. (E is the complete elliptic integral of the second kind, and the normalization method of currents is referred to [2]). (c) The comparison between the calculated electric field on the boundary using FEM (CST) and proposed MFCM. In all cases, the first filament current is located at $\phi = 0^\circ$.

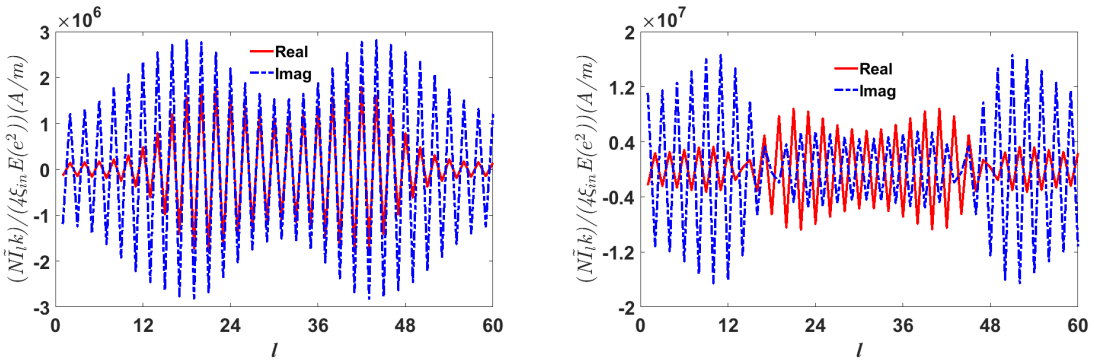

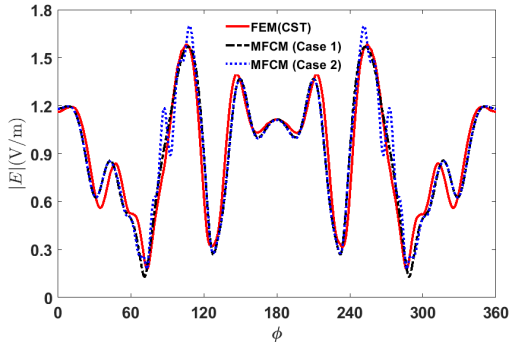

Figure 2.14 The computed real and imaginary parts of normalized filament currents on virtual surfaces C_1 (internal region) with $\xi_{in} = 0.45$, (a) $\xi_{out} = 1.55$ and (b) $\xi_{out} = 1.25$ versus filament current index l. (c) The comparison between the calculated electric field on the boundary using FEM (CST) and proposed MFCM.

1 by increasing the numbers of matching points and sources.

Based on the two examples, we can draw the following conclusions:

a. Only when the inside two singularities are enclosed by the virtual curve C_1, the currents placed within the scatterer are relatively smooth and have relatively small values, otherwise they will be divergent and have big values. This phenomenon is not affected by the placement of outside currents. In addition, the placement of the outside sources would not affect the calculated results if it is not placed too close to the physical surface.

b. The calculation of scattered fields on the physical boundary is taken as a reference standard. The accuracy and efficiency of the two cases in the first example are almost the same. The calculated results have a good agreement with that obtained from the FEM (CST), but the efficiency of the proposed MFCM has a clear advantage over FEM (CST). The CPU time and required memory are 611 s/7.50 GB for the FEM (CST) whereas only 1.58 s/0.00037 GB for the proposed MFCM. These phenomena coincide with that reported in [2] where PEC cylinders are considered. Yet in the second example, the accuracy of the scenario 2 is not as good as scenario 1 or the scenarios in the first example. The performance in scenario 2 can be improved by increasing the numbers of matching points and sources, which means the efficiency of scenario 2 is also affected when the placements of sources are wrongly selected.

The matrix ill-conditioning issue is another important aspect of the proposed MFCM. The condition number of a constructed linear system matrix will increase as the numbers of matching points and sources increase. It has been shown in [107, 109, 111] that there is a tradeoff between the attained boundary condition error and matrix condition number in terms of the numbers of matching points and sources in the case of isotropic materials, and the same phenomenon occurs in the anisotropic scenario. The condition number of the constructed matrix $[Q]$ and the average E-field boundary condition error $\Delta\tilde{E}_{bc}$ versus the parameter ξ_{in} under different number of matching points are shown in Fig. 2.15. The $\Delta\tilde{E}_{bc}$ is defined as:

$$\Delta\tilde{E}_{bc} = \frac{1}{N_t}\sum_{i=1}^{N_t}\Delta E_{bc}^{i} \tag{2.23}$$

where ΔE_{bc}^{i} is ΔE_{bc} response defined in (2.22a) at the ith testing point selected on the physical boundary. The strategy to place the test points is the same with that to place matching points, but more testing points ($N_t = 2N$) were selected in our programme to obtain Fig. 2.15. When ξ_{in} becomes very small, $[Q]$ becomes high and unstable in all cases. In addition, the $log(cond([Q]))$ decreases more rapidly with a smaller N value when increasing the ξ_{in}. On the other hand, placing the inside sources too close to or too far from the physical boundary leads to a bad $\Delta\tilde{E}_{bc}$ response as shown in Fig. 2.15 for $N = 60$ and $N = 80$. It

is interesting to see that the $\Delta\tilde{E}_{bc}$ increases sharply as the sources approach the physical boundary whereas is not accompanied with an increase of $log(cond([Q]))$. This increase of error is therefore due to the fast variations of the Hankel functions with small arguments, and is not related to numerical errors in matrix operations. The $N = 40$ scenario, which means 40 matching points and sources per region, is insufficient to obtain a solution with an acceptable accuracy though a smaller condition number of $[Q]$ is attained. The observations in Fig. 2.15 are consistent with results shown in [106, 107, 111]. The rapid oscillation of filament currents observed in Fig. 2.14(a) is not caused by round-off errors or matrix ill-conditioning since the choices of $\xi_{in} = 0.45$ and $\xi_{in} = 0.75$ with $N = 60$ and $\xi_{out} = 1.5$ lead to a solution with an acceptable $\Delta\tilde{E}_{bc}$ and a reasonable condition number as indicated in Fig. 2.15.

2.5 Possible applications and conclusion

The artificial material, such as uniaxial wire medium, carbon-fiber composite material, ferromagnetic nanowire metamaterials, behaves as anisotropic materials and has found growing applications in practice. The systematically proposed MFCM could be a good candidate to handle the EM simulation in a set of scenarios where anisotropic materials are involved. For example:

a. The contents presented in this chapter can be applied directly to analyze periodic anisotropic cylinders, as shown in Fig. 2.16. The formulation is similar to that discussed in [68] by plugging-in the 2D Green's function which derived in this paper. The slab embedded with periodic anisotropic cylinders inside is expected to have more freedom to control the scattered waves in comparison to that embedded with isotropic cylinders, and it also could be used to construct novel optical waveguides. Our proposed MFCM could be used to do the simulation of this kind of slabs.

b. As shown in [112], an array of dielectric cylinders could be used to build a flat lens. Therefore, it is possible for a flat lens to have extra performances if the inside isotropic cylinders are replaced by anisotropic ones. The proposed MFCM combined with the periodic boundary consideration [112] could be exploited to simulate the EM performance of a flat lens built with periodic anisotropic cylinders in an efficient manner.

c. The proposed MFCM could be used to simulate the EM performance of a wire medium. The description of a wire medium is shown in Fig. 2.17 [113]. As discussed in [113], the wire medium can be treated as a homogeneous uniaxial material. By using the proposed MFCM, it is possible to study the wave propagation of a uniaxial wire medium illuminated by line sources or plane waves in an efficient way.

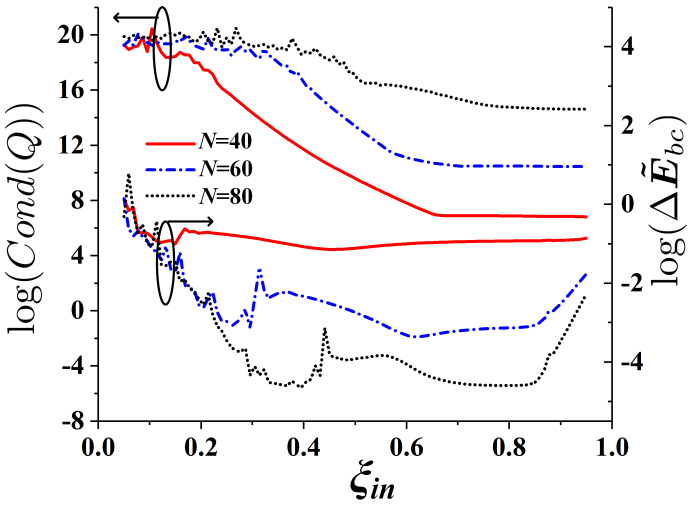

Figure 2.15 The responses of condition number of matrix $[Q]$ and average E-field boundary condition error $\Delta\tilde{E}_{bc}$ versus the parameter ξ_{in} with different N values. ($\xi_{out} = 1.5$.)

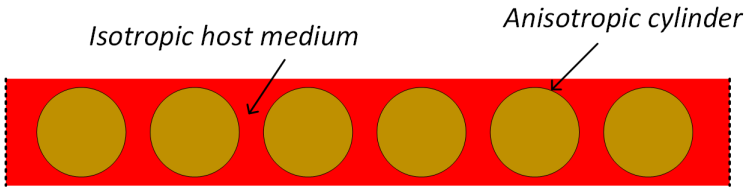

Figure 2.16 The description of a slab embedded with periodic anisotropic cylinders which could be made by stacking two distinct dielectric slabs periodically.

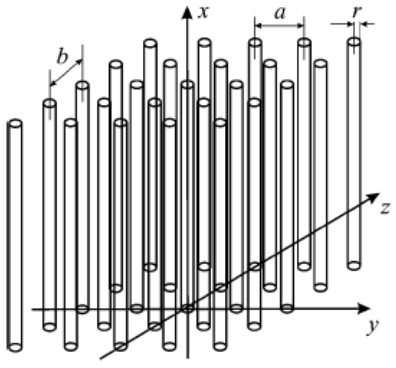

Figure 2.17 The geometry of the wire medium: a rectangular lattice of parallel ideally conducting thin wires.

A method to estimate 2D electromagnetic scattering from a homogeneous anisotropic cylinder has been proposed in this chapter. The radiation fields of a line source placed in an unbounded region occupied with the anisotropic material has been derived. The formulation of the MFCM which employs derived radiation fields is systematically presented to deal with anisotropic materials for the first time. Several numerical examples are provided. Monostatic and bistatic normalized scattering widths are computed with reference to different scenarios such as incident wave polarizations, material characteristics, and cross section shapes. A boundary condition error is proposed and tested in order to determine the necessary numbers of sources and matching points. The analyses of the oscillation of filament currents associated with the singularities of the scattered fields' analytic continuation and the matrix ill-conditioning are also presented and discussed in detail. Our computed responses are in good agreement with results already published, which prove that we have succeeded in extending the application of the MFCM to anisotropic materials. Moreover, our proposed method has its merits on simplicity and conciseness in the formulation. The CPU time and required memory are 611 s/7.50 GB for the FEM (CST) whereas only 1.58 s/0.00037 GB for the ESM when computing the field on the surface of an elliptical cylinder under the illumination of a TM plane wave. The necessity of integrating surface currents and the singularity issue (the filament current and the physical boundary coincide) are also avoided in the MFCM. Some potential applications are also briefly introduced.

CHAPTER 3 ELECTROMAGNETIC SIMULATIONS USING ANISOTROPIC BOUNDARY CONDITIONS

In this chapter, we will explore the application of the MFCM (therefore 2D scenario) on anisotropic shells by deploying correspond boundary conditions into the formulation. Specifically, we will focus on the carbon-fiber composites (CFC) material, which has been widely used in modern spacecraft and aircraft industries to realize lightweight aircraft fuselage, tail or wings, as seen for instance in the Boeing-787 and Airbus-220 jetliner. The CFC material is usually characterized by a tensor permittivity according the effective medium theory [93], and based on this tensor model, we will formulate a tensorial impedance boundary condition (TIBC) to represent multilayered CFC-based slabs, as will be introduced in Sec. 3.1. Subsequently, in Sec. 3.2, the scattering and shielding analyses of CFC-based cylindrical shells using the MFCM are introduced by deploying the formulated TIBC. The slot shell is discussed in Sec. 3.3 by using a hybrid boundary condition. In Sec. 3.4, we will study the scattering from a shell characterized by the generalized sheet transition condition (GSTC), which has been used to represent a metasurface. Finally, the induced currents on the surface of a CFC-based shell under the illumination of line sources are analyzed in Sec. 3.5 using the proposed MFCM.

3.1 Formulation of the TIBC of the multilayered CFC material

3.1.1 Generalized impedance boundary condition (GIBC)

Before considering the CFC material, we firstly discuss an isotropic lossy material filled slab, as shown in Fig. 3.1. The GIBC is commonly used to relate the tangential $\boldsymbol{E}$ and $\boldsymbol{H}$ field components on the two sides of a dielectric slab. The proposed GIBC in [22, 114] is able to consider an isotropic dielectric slab with arbitrary thickness and arbitrary losses, and it reads:

$$\begin{bmatrix} E_{1x} \\ E_{2x} \\ E_{1y} \\ E_{2y} \end{bmatrix} = \begin{bmatrix} z_s & -z_t & 0 & 0 \\ z_t & -z_s & 0 & 0 \\ 0 & 0 & -z_s & z_t \\ 0 & 0 & -z_t & z_s \end{bmatrix} \begin{bmatrix} H_{1y} \\ H_{2y} \\ H_{1x} \\ H_{(2x} \end{bmatrix} \tag{3.1}$$

with

$$z_s = -jc\cot(k_z d); \quad z_t = -jc\csc(k_z d)$$
$$c = \omega\mu_0/k_z; \quad k_z = \sqrt{\omega^2\mu_0\epsilon - k_t^2}$$

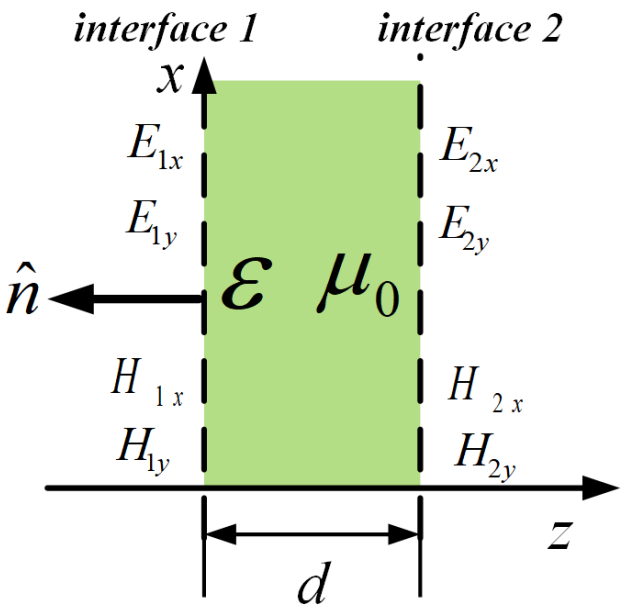

Figure 3.1 The description of a dielectric slab with notation of fields.

where k_t is the tangential component of the wave number. Variable d is the thickness of dielectric slab panel and k_0 is the wave number in the incident air region.

3.1.2 Propagation modes in unbounded CFC-filled region

Fig. 3.2 shows the layout of a single planar CFC-based slab. It consists of a binding matrix reinforced by carbon fiber inclusions. The effective medium theory (EMT) provides an accurate and concise solution to represent the CFC material as a homogeneous uniaxial nonmagnetic ($\mu = \mu_0$) material. D is the diameter of inside carbon fiber rod, and P is the distance between two adjacent fiber rods. Two coordinates are shown in Fig. 3.2, one is global coordinates (represented with xyz), the other is local coordinates (represented with $x'y'z'$). z and z' are overlapped in the two coordinate systems. The local coordinates are used to characterize the directions along the fiber orientation (x') and perpendicular to the fiber orientation (y'). The relationship between these two coordinates depends on the fiber orientation ξ and will be discussed later.

According to the EMT method, if we use ϵ_a and ϵ_b to represent the complex permittivity of directions along and perpendicular to the fiber orientation, the complex permittivity tensor [93] in local cylindrical coordinates is defined as

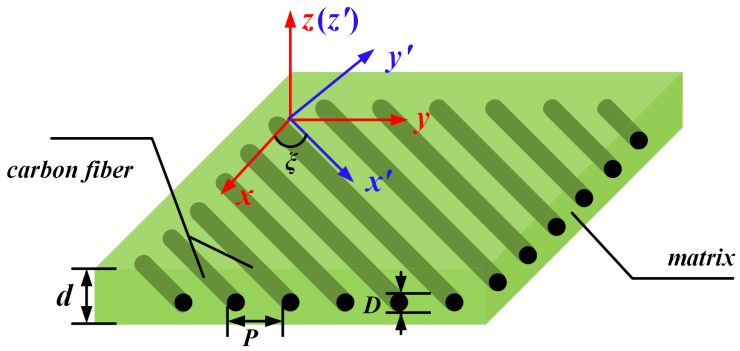

Figure 3.2 Layout of the single CFC-based planar layer.

$$\bar{\epsilon} = \begin{bmatrix} \epsilon_a & 0 & 0 \\ 0 & \epsilon_b & 0 \\ 0 & 0 & \epsilon_a \end{bmatrix}_{x'y'z'} \tag{3.2}$$

This bulk tensor permittivity is accurate enough to represent the electromagnetic characteristics of a single CFC-based layer as long as the condition $P/\lambda << 1$ is satisfied according to the EMT, where P is the distance between two fiber rods as shown in Fig. 3.2. This condition is generally met in practical composites used aerospace applications. The range of validity of the EMT as well as its limitation are beyond the scope of this thesis. We will assume the condition $P/\lambda << 1$ is always satisfied and the bulk tensor permittivity will be used to represent the CFC material in all the following discussions and numerical examples.

The complex permittivity in the z' direction, in this case, is chosen to be the same as that in the x' direction as referred from [93]. While the complex permittivity also can be chosen to equal to that in the y' direction as used in [115], [116]. Both choices have no influence on the numerical results due to the prorogation modes of unbounded CFC material are only related to the complex permittivities in x' and y' directions. The two propagation modes are discussed in Appendix A in detail, and read:

$$k_{za}'^2 = \omega^2 \mu_0 \epsilon_a - k_x'^2 - k_y'^2 \tag{3.3a}$$

for the TM$'$ case, and

$$k_{zb}'^2 = \omega^2 \mu_0 \epsilon_b - k_x'^2 - \frac{\epsilon_b}{\epsilon_a} k_y'^2 \tag{3.3b}$$

for the TE$'$ case. Where k_x' and k_y' are the tangential components of the wave number in the unbounded CFC material. Notice that the z and z' are overlapped in two coordinate systems.

In practice, the CFC materials are lossy. The conductivities of commonly used CFC materials in the aircraft industry are around 10^4 S/m and 10^1 S/m in the directions parallel and perpendicular to the fiber orientation, respectively. In our scattering and shielding effectiveness (SE) analyses, the conductivity involved in the imaginary part of ϵ_a is around 40000 S/m, as suggested in [117], [115] and [116]. The conductivity contributing to the imaginary part ϵ_b is around 50 S/m [115], and in this case, the propagation modes derived in (A.4) will degenerate as

$$k_{za}'^2 = \omega^2 \mu_0 \epsilon_a \tag{3.4a}$$

for the TM$'$ case, and

$$k_{zb}'^2 = \omega^2 \mu_0 \epsilon_b \tag{3.4b}$$

for the TE$'$ case in our investigated frequency range (10Hz∼10GHz). (3.4) indicates that the two prorogation modes can be independent to the tangential components k_x' and k_y', relating to the incident waves from exterior region due to the continuity of tangential fields at the interface of two mediums, under certain conditions of CFC materials containing high conductivities. Since the TIBC is constructed on the base of the prorogation modes in (3.4) as will be shown later, the incident angle independent propagation modes will finally result in an incident angle independent TIBC. This type of impedance boundary condition would be much more useful in 3D electromagnetic field solvers since in practical problems, the incident field is not a plane wave with a well-defined polarization and angle of incidence, but it could be a non-uniform spherical wave coming from a nearby source such as an antenna. In Appendix B, we provide a condition when the incident angel could be omitted in terms of the conductivities of the CFC material, and this condition is satisfied in all CFC material related numerical examples presented in this chapter.

Observe that there exists distinct propagation constants for the TE$'$ and TM$'$ cases in the unbounded CFC material filled region. The field components in global system are easily obtained through coordinate rotation matrix (R) which defined with respect to fiber orientation ξ and will be introduced later.

3.1.3 TIBC of a multilayered CFC-based shell

The CFC-based cylindrical shell model is obtained by rolling the planar slab so as to form a one-layer cylinder of radius r_a parallel to the z-axis. It is convenient to assume that this cylinder is centered on the z-axis. By doing so, the carbon fibers inside of the rolled slab will form helices, as shown in Fig. 3.3(a). The distance P between two fibers in Fig. 3.2 is the pitch length in Fig. 3.3(a), and the fiber orientation ξ in Fig. 3.2 is the pitch angle

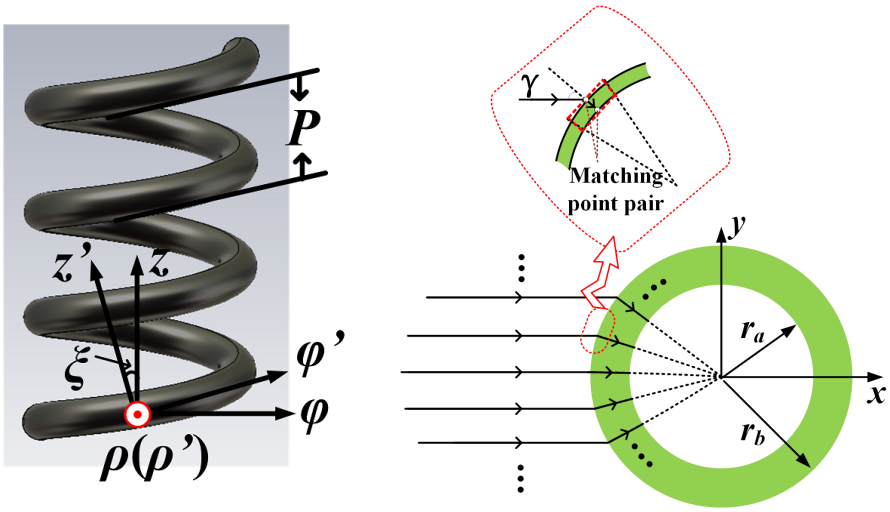

(a) (b)

Figure 3.3 (a)Carbon fiber path of the single CFC-based cylindrical layer. (b) Homogenized cylinder discretization approach.

indicated in Fig. 3.3(a). The EMT approach used in the case of the planar shape is also applicable to the cylindrical scenario. For the convenience, the cylindrical coordinate system is utilized as shown in Fig. 3.3(a). Two coordinate systems are shown in Fig. 3.3(a), one is the global coordinates (represented with $\rho\phi z$), the other is the local coordinates (represented with $\rho'\phi'z'$). ρ and ρ' are overlapped in the two coordinate systems. The fiber orientation in the cylindrical shell is parallel to ϕ' and perpendicular to z' directions. The relationship between these two coordinates also depends on the fiber orientation ξ. The tensor permittivity which defined in (3.2) should be modified in the cylindrical coordinate system as

$$\bar{\epsilon} = \begin{bmatrix} \epsilon_a & 0 & 0 \\ 0 & \epsilon_a & 0 \\ 0 & 0 & \epsilon_b \end{bmatrix}_{\rho'\phi'z'} \tag{3.5}$$

and the two propagation modes in the cylindrical coordinate system read

$$k_{\rho a}'^2 = \omega^2 \mu_0 \epsilon_a \tag{3.6a}$$

for the TM$'$ case, and

$$k_{\rho b}'^2 = \omega^2 \mu_0 \epsilon_b \tag{3.6b}$$

for the TE$'$ case. The plane wave in free space will be refracted into the ρ-direction when it enters the highly conductive shell as shown in Fig. 3.3(b) due to

$$\frac{k_0 \sin\gamma}{k_{\rho a}} << 1 \tag{3.7a}$$

$$\frac{k_0 \sin\gamma}{k_{\rho b}} << 1 \tag{3.7b}$$

are always well satisfied in our investigated frequency range (10 Hz∼10 GHz). Here γ is the incident angle shown in Fig. 3.3(b). The tangential part of the wave vector $k_0 \sin\gamma$ is small compared with the radial part k_ρ. Therefore it is reasonable to assume that waves propagate along the radial direction in the CFC-based shell.

As discussed in Sec. 3.1.1, for isotropic material which only contains one propagation mode, the tangential field components at the two interfaces of a slab can be related by the GIBC [114, 118]. However, as seen in the previous discussion, two different propagation constants k_ρ are present under the TE$'$ and TM$'$ cases. Therefore, the GIBC needs to be modified as a tensorial impedance boundary condition (TIBC) to represent the physics of the problem. With the help of GIBC, the TIBC for a planar CFC-based slab as shown in Fig. 3.2 is easily obtained by introducing two propagation modes in the impedance matrix. On the other hand, for a CFC-based shell, the circular boundary is discretized by a set of matching point pairs in our proposed numerical technique, as shown in Fig. 3.3(b). In our scattering and SE analyses, the thickness of a single layer CFC-based shell is d=0.127 mm, and it is much smaller than the radius of the shell (around 1 m). Based on these conditions, the curved boundary can be locally approximated by a set of planar boundaries. Moreover, it also has been shown in [119] that the differences between those thin shell examples with or without considering the curvature effect were not significant. Therefore the TIBC for a planar CFC-based slab can be directly exploited at each matching point pair without considering the curvature effect. The number of matching points is increased until a convergence of the solution is achieved. A useful rule to determine the numbers of matching points and sources for structure with a smooth boundary is using $SPW = 5$ which means placing 5 points in each λ, where SPW means samples per wavelength. The relationship of tangential field components in local coordinates for the ith CFC-based layer at each matching point pair reads

$$\begin{bmatrix} E'_{i\phi} \\ E'_{(i+1)\phi} \\ E'_{iz} \\ E'_{(i+1)z} \end{bmatrix} = \begin{bmatrix} z_{sE} & -z_{tE} & 0 & 0 \\ z_{tE} & -z_{sE} & 0 & 0 \\ 0 & 0 & -z_{sM} & z_{tM} \\ 0 & 0 & -z_{tM} & z_{sM} \end{bmatrix} \begin{bmatrix} H'_{iz} \\ H'_{(i+1)z} \\ H'_{i\phi} \\ H'_{(i+1)\phi} \end{bmatrix} \tag{3.8}$$

with

$$\begin{aligned} z_{sE} &= -jc_1 \cot(k_{i\rho a} d); \quad z_{sM} = -jc_2 \cot(k_{i\rho b} d) \\ z_{tE} &= -jc_1 \csc(k_{i\rho a} d); \quad z_{tM} = -jc_2 \csc(k_{i\rho b} d) \end{aligned} \tag{3.9}$$

where $c_1 = \omega\mu_0/k_{i\rho a}$, $c_2 = \omega\mu_0/k_{i\rho b}$, and d is the layer thickness, which will be assumed constant for all layers for the simplicity. For an arbitrary cross section as depicted in Fig. 3.4, a local orthogonal coordinate system represented by $\zeta\tau\vartheta$ with respect to the planar boundary obtained after discretizing should be constructed, and a relationship between local orthogonal and main coordinate systems must be carefully established. For the multilayered situation, as shown in Fig. 3.5, the chain matrix (ABCD-matrix) relationship of tangential fields should be exploited. It is easy to obtain the chain matrix via (3.8), and it can be written as

$$\begin{bmatrix} E'_{i\phi} \\ H'_{iz} \\ E'_{iz} \\ H'_{i\phi} \end{bmatrix} = [A_i] \begin{bmatrix} E'_{(i+1)\phi} \\ H'_{(i+1)z} \\ E'_{(i+1)z} \\ H'_{(i+1)\phi} \end{bmatrix} \tag{3.10}$$

where $[A_i]$ is the ABCD-matrix for the arbitrary ith layer in local coordinates. In global coordinates, the coordinate rotation matrix (R) in terms of the fiber orientation (ξ) in the ith layer needs to be introduced:

$$[R] = \begin{bmatrix} \cos\xi & 0 & \sin\xi & 0 \\ 0 & \cos\xi & 0 & -\sin\xi \\ -\sin\xi & 0 & \cos\xi & 0 \\ 0 & \sin\xi & 0 & \cos\xi \end{bmatrix} \tag{3.11}$$

With this rotation matrix, the chain matrix relationship for a single CFC-based layer in global coordinates is then constructed as $R^{-1} \cdot A \cdot R$. For multilayered CFC-based shell, say M layers, the chain matrix is straightforwardly perceived by continually multiplying the coefficient of each layer:

$$\begin{bmatrix} E_{1\phi} \\ H_{1z} \\ E_{1z} \\ H_{1\phi} \end{bmatrix} = \prod_{i=1}^{M} \left([R_i]^{-1} [A_i] [R_i] \right) \begin{bmatrix} E_{2\phi} \\ H_{2z} \\ E_{2z} \\ H_{2\phi} \end{bmatrix} = [A] \begin{bmatrix} E_{2\phi} \\ H_{2z} \\ E_{2z} \\ H_{2\phi} \end{bmatrix} \tag{3.12}$$

The interfaces 1 and 2 shown in Fig. 3.5 are defined as cylindrical surfaces with radiuses $r_a + Md$ and r_a, respectively. The TIBC for a multilayered CFC-based cylindrical shell is

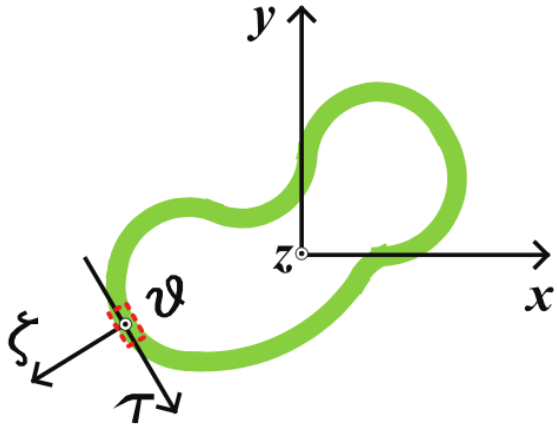

Figure 3.4 An arbitrary cross section with local orthogonal coordinates.

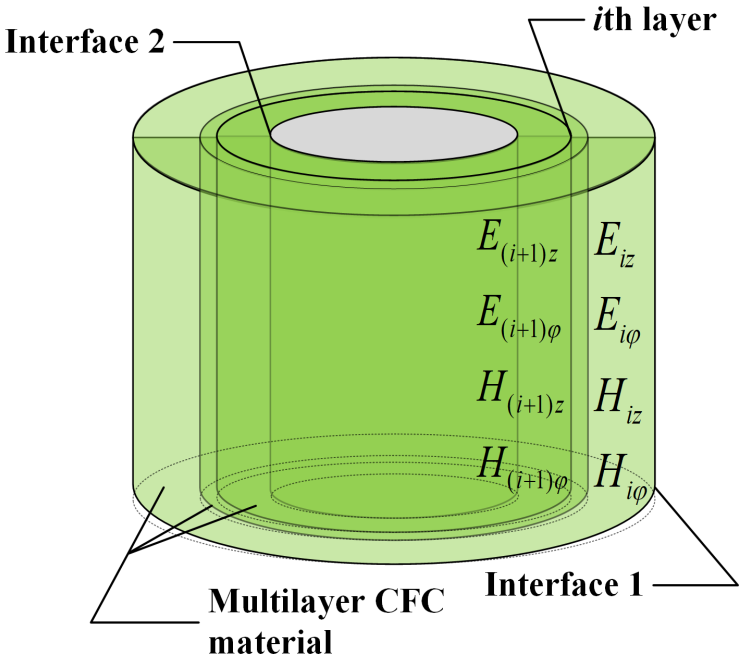

Figure 3.5 The multilayered CFC-based cylindrical shell.

then derived from (3.12) through a mathematical transformation:

$$\begin{bmatrix} E_{1\phi} \\ E_{2\phi} \\ E_{1z} \\ E_{2z} \end{bmatrix} = [Z] \begin{bmatrix} H_{1z} \\ H_{2z} \\ H_{1\phi} \\ H_{2\phi} \end{bmatrix} \tag{3.13}$$

Equation (3.13) is the TIBC for a multilayered CFC-based shell at each matching point pair. The mathematical transformation from $[A]$ to $[Z]$ is given below as:

$$\begin{bmatrix} Z_{11} & Z_{13} \\ Z_{31} & Z_{33} \end{bmatrix} = ([P]^{-1} - [Q])^{-1} \begin{bmatrix} B_{12} & B_{14} \\ B_{32} & B_{34} \end{bmatrix}$$

$$\begin{bmatrix} Z_{21} & Z_{23} \\ Z_{41} & Z_{43} \end{bmatrix} = ([E] - [Q]\,[P])^{-1} \begin{bmatrix} B_{12} & B_{14} \\ B_{32} & B_{34} \end{bmatrix}$$

$$\begin{bmatrix} Z_{24} & Z_{22} \\ Z_{44} & Z_{42} \end{bmatrix} = ([Q]^{-1} - [P])^{-1} \begin{bmatrix} A_{14} & A_{12} \\ A_{34} & A_{32} \end{bmatrix}$$

$$\begin{bmatrix} Z_{14} & Z_{12} \\ Z_{34} & Z_{32} \end{bmatrix} = ([E] - [P]\,[Q])^{-1} \begin{bmatrix} A_{14} & A_{12} \\ A_{34} & A_{32} \end{bmatrix}$$

$$[P] = \begin{bmatrix} A_{11} & A_{13} \\ A_{31} & A_{32} \end{bmatrix}; [Q] = \begin{bmatrix} B_{11} & B_{13} \\ B_{31} & B_{32} \end{bmatrix}; [B] = [A]^{-1}$$

where $[A]$ is defined in (3.12).

The derived TIBC is powerful in the numerical calculations of scattering and shielding performances. The multilayered CFC-based shell will be accurately represented by a 4×4 matrix which can significantly reduce the complexity of problem formulation as well as the simulation time.

3.2 EM evaluations of multilayered CFC-based shells

3.2.1 Problem formulation

The TIBC of a multilayered CFC-based shell has been introduced in the previous section. The MFCM based on this TIBC to solve scattering and shielding problems will be developed in this section. The problem is depicted in Fig. 3.6. There are three regions in our situation, the outer region 1, the inner region 2, both considered as vacuum or filled with isotropic materials,

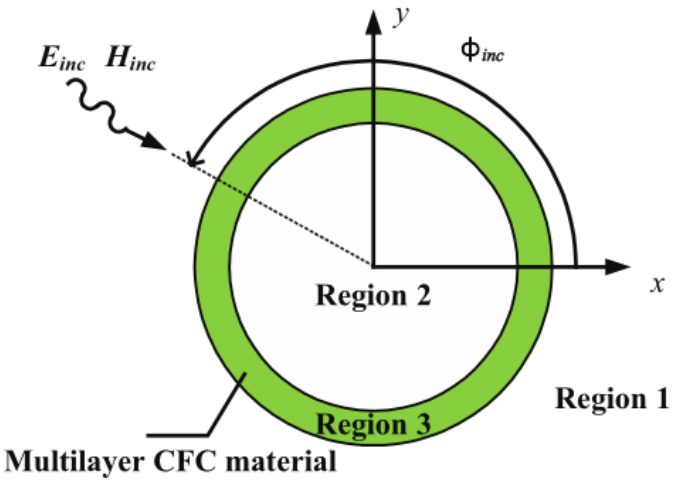

Figure 3.6 Problem description for the MFCM.

and region 3 filled with the multilayered CFC material. Regions 1 and 2 are separated by the smooth boundaries of the region 3, and the tangential fields on those two boundaries are connected through the TIBC. The concept of the MFCM is illustrated in Fig. 3.7. It is worthwhile to mention that only one type of filament current is placed in inner and outer regions for TM or TE cases in the MFCM formulation for an anisotropic cylinders discussed in Chap. 2. However the TE and TM cases are coupled in the presence of a shell constituted by multilayered CFC materials since the four tangential field components are required in the formulated TIBC. In order to consider co- and cross-polarized fields under TE and/or TM incidences simultaneously, we uniformly place doublet current units in regions 1 and 2, each doublet current unit contains two z-directed filament currents, one is an electric current and the other is a magnetic current. Within a doublet, the two types of currents overlap. The formulation of the MFCM is conducted through two equivalences. Firstly, the scattered fields in the region 1 are generated by the equivalent doublet sources placed in region 2, and secondly, the scattered fields in the region 2 are generated by all doublet sources placed in region 1.

Region 1 contains the incident and scattered fields. Only the plane wave incidence is considered in this chapter, however, the proposed method has no restriction of the external field excitation as long as it is homogeneous along the z-axis.

The scattered fields in region 1 are produced by all z-directed doublet current in the region 2, and vice versa. They can be directly written in terms of the Green's function in unbounded

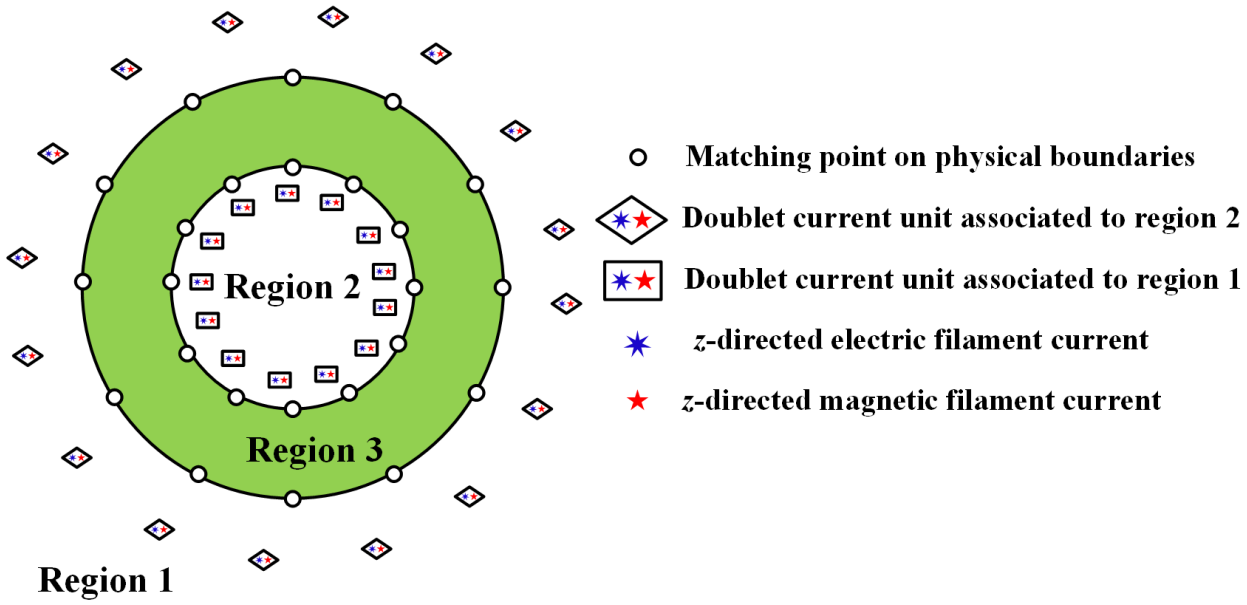

Figure 3.7 Formulation of the MFCM.

free space as:

$$E^s_{1(2)\phi} = \frac{k_0}{4j}\sum_{i=1}^{N_1(N_2)} K_{1(2)i}\frac{r_{1(2)is}\cos(\phi-\phi_{1(2)is})-r}{R_{1(2)i}}H_1^2(k_0R_{1(2)i}) \tag{3.14}$$

$$E^s_{1(2)z} = -\frac{k_0\eta_0}{4}\sum_{i=1}^{N_1(N_2)} I_{1(2)i}H_0^2(k_0R_{1(2)i}) \tag{3.15}$$

$$H^s_{1(2)\phi} = \frac{k_0}{4j}\sum_{i=1}^{N_1(N_2)} I_{1(2)i}\frac{r-r_{1(2)is}\cos(\phi-\phi_{1(2)is})}{R_{1(2)i}}H_1^2(k_0R_{1(2)i}) \tag{3.16}$$

$$H^s_{1(2)z} = -\frac{k_0}{4\eta_0}\sum_{i=1}^{N_1(N_2)} K_{1(2)i}H_0^2(k_0R_{1(2)i}) \tag{3.17}$$

with

$$R_{1(2)i} = \sqrt{r^2+r^2_{1(2)is}-2rr_{1(2)is}\cos(\phi-\phi_{1(2)is})} \tag{3.18}$$

where 1 and 2 stand for regions 1 and 2. The cylindrical coordinates are used in all our

derivations for convenience in circular cylinder examples. The $I_{1(2)i}$ and $K_{1(2)i}$ are the unknown complex magnitudes of electric and magnetic current sources yet to be determined in regions 2 and 1, respectively. N_1 and N_2 are the numbers of doublet current units in regions 2 and 1, respectively. The (r_{1is}, ϕ_{1is}) is the ith filament source position in the region 2, whereas (r_{2is}, ϕ_{2is}) gives the source position in the region 1 and the (r, ϕ) is the observation point. The $R_{1(2)i}$ is the distance between the ith doublet current unit and the observation point. Since the TIBC defines the relationship between tangential fields, only tangential field components are expressed herein.

The total tangential fields in region 1 are

$$\boldsymbol{E}_{1tan} = \boldsymbol{E}_{inc} + E^s_{1z}\hat{z} + E^s_{1\phi}\hat{\phi} \tag{3.19}$$

$$\boldsymbol{H}_{1tan} = \boldsymbol{H}_{inc} + H^s_{1z}\hat{z} + H^s_{1\phi}\hat{\phi} \tag{3.20}$$

and the total tangential fields in the region 2 are

$$\boldsymbol{E}_{2tan} = E^s_{2z}\hat{z} + E^s_{2\phi}\hat{\phi} \tag{3.21}$$

$$\boldsymbol{H}_{2tan} = H^s_{2z}\hat{z} + H^s_{2\phi}\hat{\phi} \tag{3.22}$$

The differences between TE and TM cases appear in the incident field components presented in (3.19) and (3.20).

The bridge to connect the tangential fields in regions 1 and 2 is the TIBC which we have formulated and expressed in (3.13). By imposing the TIBC at a number of matching points on the region 3, a linear system is then created and used to determine the unknown coefficients of currents. As indicated in Fig. 3.7, the two boundaries limit the cylindrical surfaces of the region 3. Each boundary is imposed an equal number of matching points (N_m), and the total number of matching points ($2N_m$) must satisfy the inequality

$$2N_m \geqslant N_1 + N_2 \tag{3.23}$$

in order to have a solution for the total current coefficients ($2N_1$ in region 2 and $2N_2$ in region 1).

Upon the application of a point-matching procedure, we will finally obtain a matrix expression of the type

$$[Q]\,\boldsymbol{X} = \boldsymbol{B} \tag{3.24}$$

where $\boldsymbol{X}$ is a column vector contains the unknown current coefficients (K_1, K_2, I_1 and I_2),

and $\boldsymbol{B}$ is another column vector containing samples of the incident tangential fields at the matching points on the physical boundaries. $[Q]$ is a matrix whose entries are obtained from the tangential fields of filaments at matching points, and it could be rectangular or square depending on whether oversampling is used or not. If it is in a square form, a unique solution can be found, otherwise the smallest least-square error solution should be pursued.

As for the source location, we will adopt the *ad hoc* $R/2-2R$ rule which was used in [119–121]. This rule consists in uniformly placing the doublet current units in regions 1 and 2 with radii $2r_a$ and $r_b/2$, respectively, where r_a and r_b are the radii of the inner and outer boundaries of the region 3. The matching point location is also uniformly placed on the outer and inner boundaries of region 3, and each boundary has the same number of matching points. Moreover, each matching point on the outer boundary has a corresponding matching point on the inner boundary as Fig. 3.7 suggests, which means the two points have the same ϕ angle. It is convenient to neglect the thickness of a thin shell in the numerical computation, like the thin CFC-based shell used in this chapter. This is a reasonable assumption because $Md \ll \lambda$ in the case of practical interests. By merging the inner and outer surfaces of the region 3, the computed results are found to be almost the same. So far, all information for the linear system has been provided, and once it is solved, the fields and related parameters of interests (e.g. scattering and shielding) can be evaluated in a straightforward manner.

A convergence criterion ΔC, based on the continuity of the tangential fields halfway between the matching points along the boundaries of the region 3, is defined as follows:

$$\Delta C = \frac{|\,[\boldsymbol{E}] - [\boldsymbol{Z}]\,[\boldsymbol{H}]\,|}{max\{|\boldsymbol{E}|, |\,[\boldsymbol{Z}]\,[\boldsymbol{H}]\,|\}} \tag{3.25}$$

where the division should be done in a term-by-term manner, and $[\boldsymbol{E}]$, $[\boldsymbol{Z}]$ and $[\boldsymbol{H}]$ are three matrices defined in (3.13) tested on the physical boundary. The numbers of sources and matching points ($N_1 = N_2 = N_m$) are augmented iteratively until a good convergence is achieved. In the following examples, $\Delta C < 1\%$ is used to determine $N_1 = N_2 = N_m$.

3.2.2 Scattering analysis

The proposed MFCM combined with the TIBC is now used to estimate the scattering performance of a multilayered CFC-based cylindrical shell. In this study, the echo widths are defined as

$${}_M W_e = \lim_{r\to\infty}(2\pi r \frac{|E_z^s|^2}{|E_z^i|^2}) \tag{3.26}$$

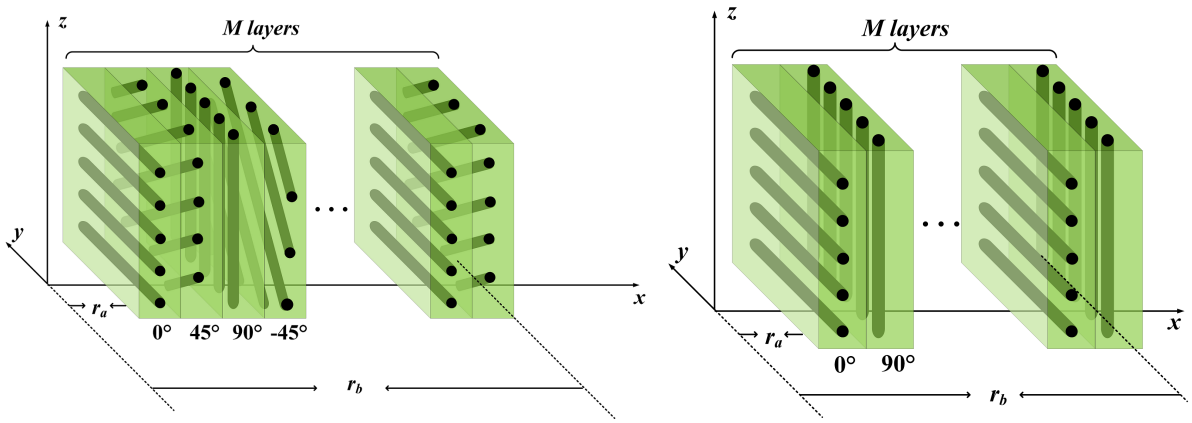

Figure 3.8 Two different fiber patterns, (a) [0/45/90/-45] and (b) [0/90].

$$ {}_{M}W_m = \lim_{r\to\infty}(2\pi r\frac{|\eta_0 H_z^s|^2}{|E_z^i|^2}) \tag{3.27} $$

for the TM case, and

$$ {}_{E}W_e = \lim_{r\to\infty}(2\pi r\frac{|E_z^s|^2}{|\eta_0 H_z^i|^2}) \tag{3.28} $$

$$ {}_{E}W_m = \lim_{r\to\infty}(2\pi r\frac{|H_z^s|^2}{|H_z^i|^2}) \tag{3.29} $$

for the TE case. The subscripts "e "and "m "are associated with the electric and magnetic fields, respectively. The E_z^s and H_z^s fields with respect to a specific ϕ in (3.26)-(3.29) are generated by the doublet sources which placed in the interior region of the cylindrical shell.

Considering a composite shell with M layers and the interior radius r_a=2 m, each layer has the same $\epsilon_a = 5.0\epsilon_0 - j40000/\omega$ and $\epsilon_b = 5.0\epsilon_0 - j50/\omega$ as well as the thickness $d = 0.127mm$, as in [117], [115]. The configurations of the composites used in current and next examples are similar to those found in the aerospace applications. For all the computations in this section, an incident plane wave propagating along the x-direction ($\phi_{inc} = 180^\circ$, $\theta = 90^\circ$) is assumed. The two fiber orientation patterns with M layers shown in Fig. 3.8 are investigated in our examples. One is a periodic repetition of four layers with fiber orientations [0/45/90/-45], and the other is a periodic repetition of two layers with fiber orientations [0/90]. The angles in these patterns correspond to the fiber orientation ξ defined in Fig. 3.3(a). In both cases, the arrangement of M layers in total is obtained by concatenating these 4-layer or 2-layer basic patterns several times in the radial direction.

Fig. 3.9 shows the monostatic scattering response versus $k_0 r_a$ of a CFC-based shell. Different fiber orientation patterns, layer numbers as well as polarizations are investigated. It is

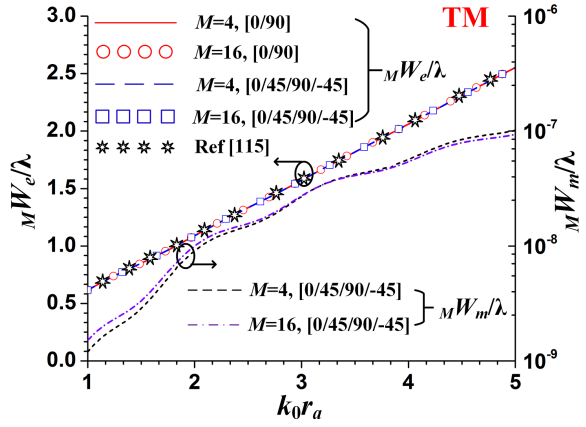

(a)

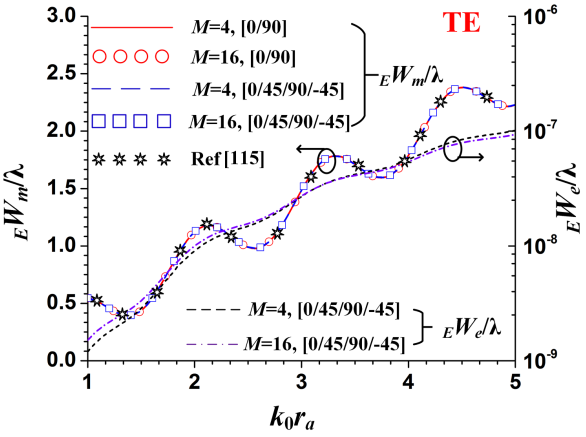

(b)

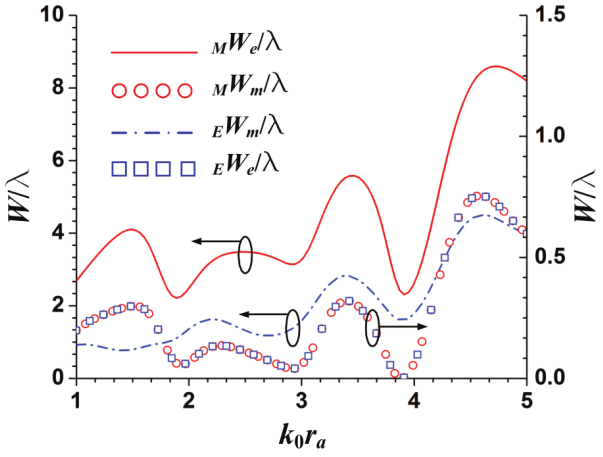

(c)

Figure 3.9 Monostatic co- and cross-polarization echo widths of a cylindrical shell in various situations, $\phi_{inc} = 180^\circ$. The multilayered CFC-based shell situations under (a) TM and (b) TE cases, and (c) the single layered CFC-based shell with fiber orientation as 30°. ($\epsilon_a = 5.0\epsilon_0 - j40000/\omega$, $\epsilon_b = 5.0\epsilon_0 - j50/\omega$ and d=0.127 mm for each single CFC-based layer, r_a=2 m).

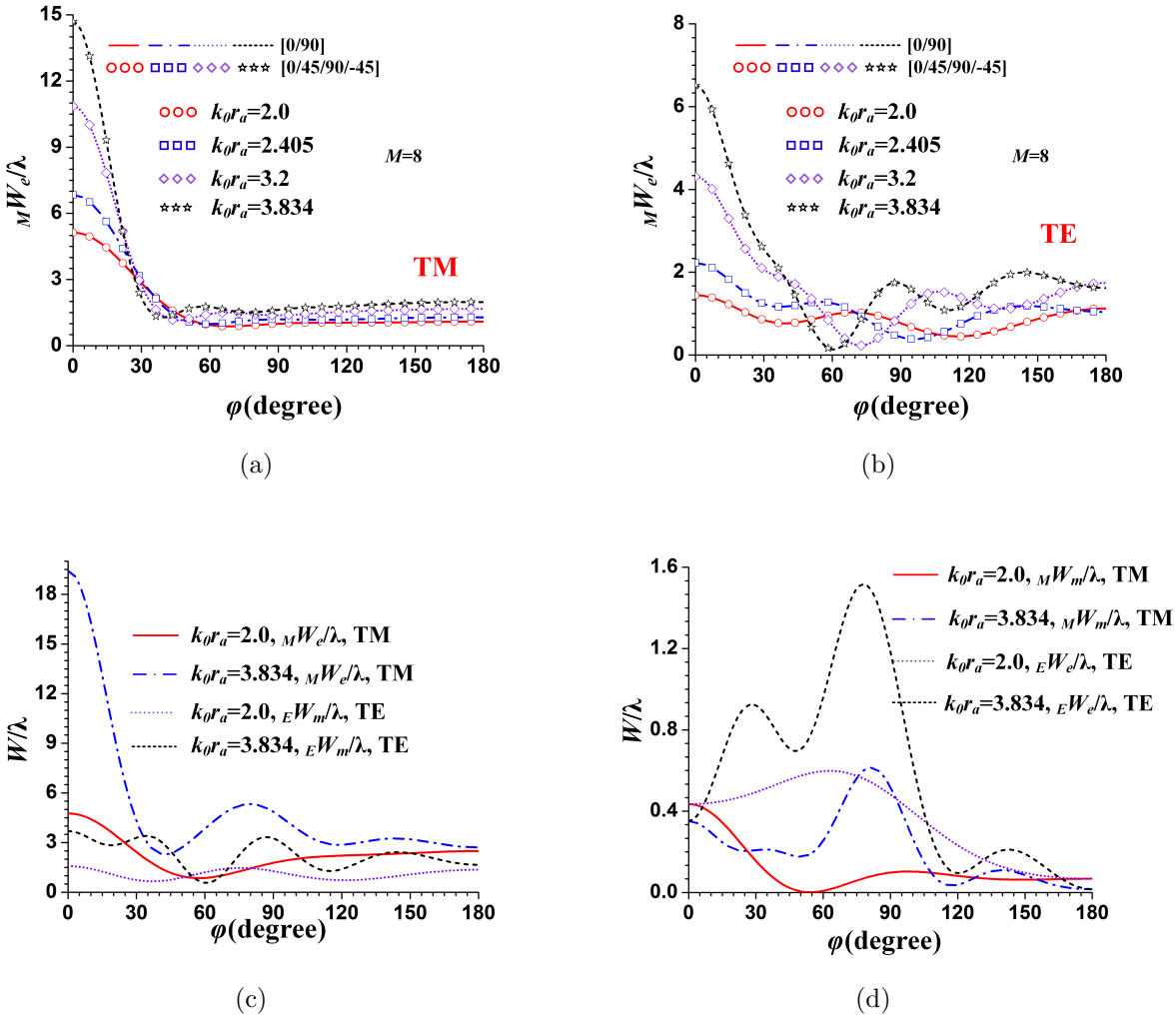

(a) (b)

(c) (d)

Figure 3.10 Bistatic echo widths of a cylindrical multilayered CFC-based shell under (a) TM and (b) TE polarizations. (c) Co- and (d) cross-polarization bistatic echo widths of a single CFC-based shell with fiber orientation as 30°, $\phi_{inc} = 180°$. ($\epsilon_a = 5.0\epsilon_0 - j40000/\omega$, $\epsilon_b = 5.0\epsilon_0 - j50/\omega$ and d=0.127 mm for each single CFC-based layer, r_a=2 m).

interesting to note that the monostatic echo widths ${}_MW_e$ and ${}_EW_m$ versus $k_0 r_a$ are almost not sensitive to the number of layers or the fiber orientation patterns under TE or TM cases. This suggests that the reflection of the incident wave occurs in the first outer layers of the multilayered CFC-based shell. Moreover, the magnitudes of cross-polarized scattering terms ${}_MW_m$ and ${}_EW_e$ presented for the [0/45/90/-45] fiber pattern are quite small whereas they are null (not shown) for the pattern [0/90]. Although the TIBC for the multilayered CFC material is a 4×4 full matrix, if we symmetrically divide it into four 2×2 submatrices, the off-diagonal submatrices have quite small values for the [0/45/90/-45] pattern and are zero for the [0/90] pattern. This explains why a small cross-polarization scattering is observed in Fig. 3.9(a) and 3.9(b). To show an evidence of the anisotropic property of the CFC material, a single layer case is examined with the fiber orientation $\xi = 30^\circ$. Fig. 3.9(c) shows the co- and cross-polarized scattering results for this single layer scenario. A strong cross-polarized scattering appears, which reveals a strong anisotropic property of the CFC material. Comparing our presented results with those presented in [117] at each integer $k_0 r_a$, an excellent agreement is achieved. The multilayered CFC-based shell is represented by a 4×4 TIBC matrix in the MFCM without modeling the internal geometrical details of the structure. This differs from the finite-difference algorithm used in [117] which needs to consider every interface in the multilayered structure for determining the total reflection and transmission coefficients.

The bistatic scattering results are shown in Fig. 3.10. The configuration of composites is the same as the previous example. Again, the co-polarized scattering terms ${}_MW_e$ and ${}_EW_m$ versus ϕ, as Fig. 3.10(a) and 3.10(b) indicate, are not sensitive to the number of layers under TE or TM cases with different fiber patterns. Various $k_0 r_a$ scenarios are considered, including $k_0 r_a$ of values 2.405 and 3.834 which are the resonances of a circular waveguide. A single layer example with the fiber orientation as 30° is also investigated to reveal its strong anisotropic characteristic. The cross-polarization scattering is smaller but comparable to the co-polarization scattering, as Figs. 3.10(c) and 3.10(d) suggest. To obtain the results of Figs. 3.9 and 3.10, the numbers of matching points per boundary and the sources in each region are the same ($N_1 = N_2 = N_m$). A unique solution for the coefficients of all current sources can be found since a square matrix $[Q]$ defined in (3.44) is formulated. Only 30 doublet currents per region ($N_1 = N_2 = 30$), for the TM case, and 45 doublet current units ($N_1 = N_2 = 45$) per region for the TE case are chosen to reach a good result of convergence.

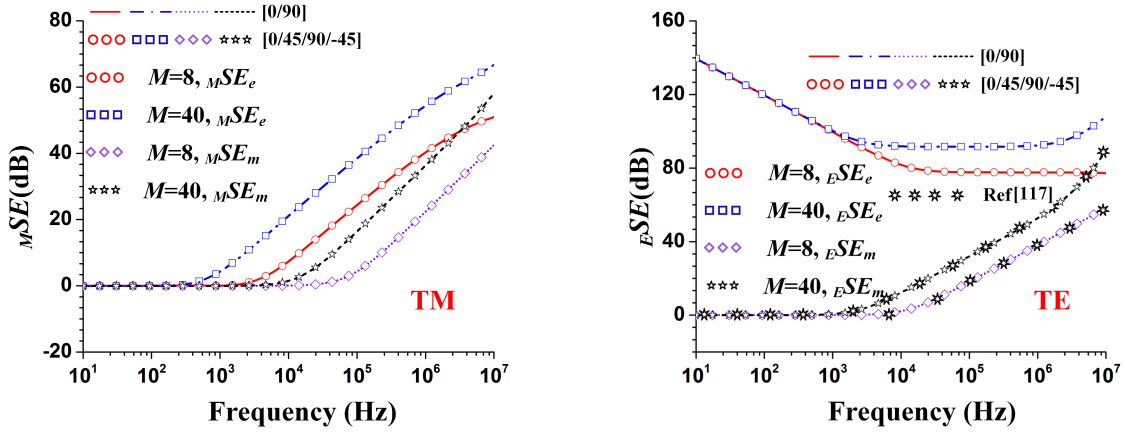

Figure 3.11 SE performances under various situations in the low frequency range. (a) TM and (b) TE cases. ($\epsilon_a = 3.4\epsilon_0 - j40000/\omega$, $\epsilon_b = 5.0\epsilon_0 - j50/\omega$ and d=0.127 mm for each single CFC material layer, r_a=1 m).

3.2.3 Shielding effectiveness (SE) analysis

In this section, we will investigate the SE properties of a cylindrical shell constituted of the multilayered CFC material. In this study, the SE is defined by

$$_{M}SE_e = -20\log_{10}(\frac{|E^s_{max}|)}{|E^z_{inc}|} \tag{3.30}$$

$$_{M}SE_m = -20\log_{10}(\frac{|\eta_0 H^s_{max}|)}{|E^z_{inc}|} \tag{3.31}$$

for the TM case, and

$$_{E}SE_e = -20\log_{10}(\frac{|E^s_{max}|)}{|\eta_0 H^z_{inc}|} \tag{3.32}$$

$$_{E}SE_m = -20\log_{10}(\frac{|H^s_{max}|)}{|H^z_{inc}|} \tag{3.33}$$

for the TE case. The subscriptes "e"and "m"are associated with the electric and magnetic fields shielding, respectively. The E^s_{max} and H^s_{max} in (3.30)-(3.33) are the maximum fields within the shell and are generated by the doublet current sources placed outside of the shell. The SE definition in [116] only takes the field magnitude at the center of a cylindrical shell into consideration. The position of the field sampling for SE calculation is not so important when the frequency is low since no resonance occurs in the cylindrical shell. However, it becomes important at high frequencies where resonances lead to a highly non-uniform distribution of fields within the shell.

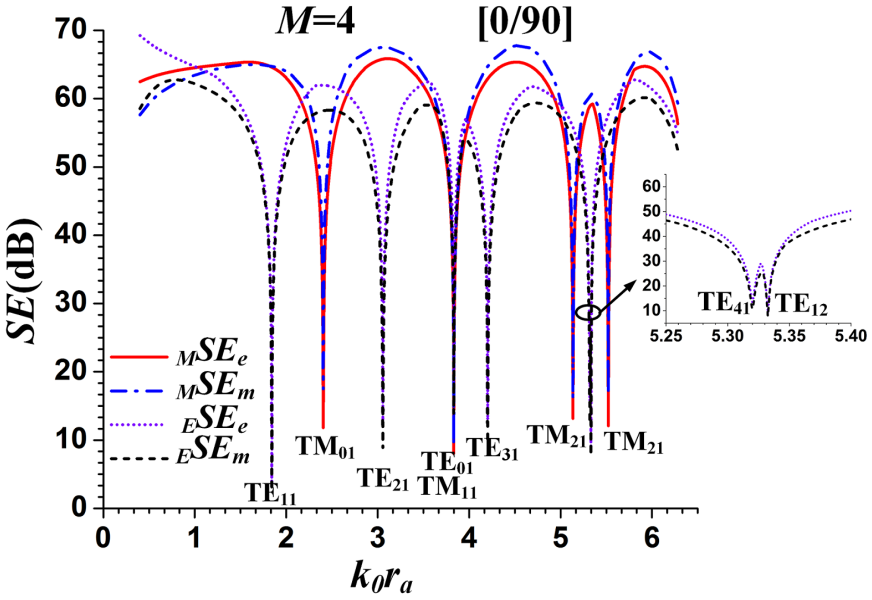

(a)

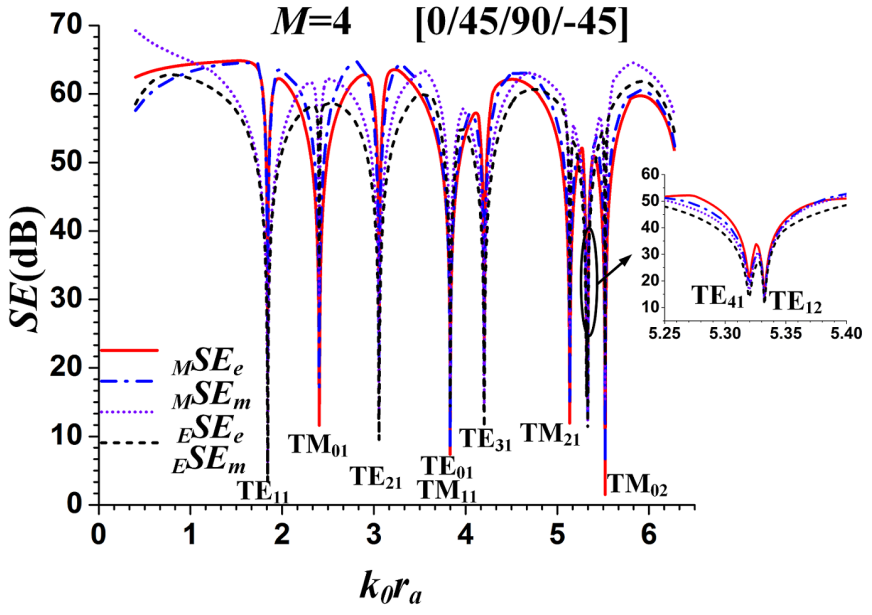

(b)

Figure 3.12 SE performance under various situations in the high frequency range with fiber orientation patterns (a) [0/90] and (b) [0/45/90/-45]. ($\epsilon_a = 3.4\epsilon_0 - j40000/\omega$, $\epsilon_b = 5.0\epsilon_0 - j50/\omega$ and d=0.127 mm for each single CFC-based layer, r_a=1 m).

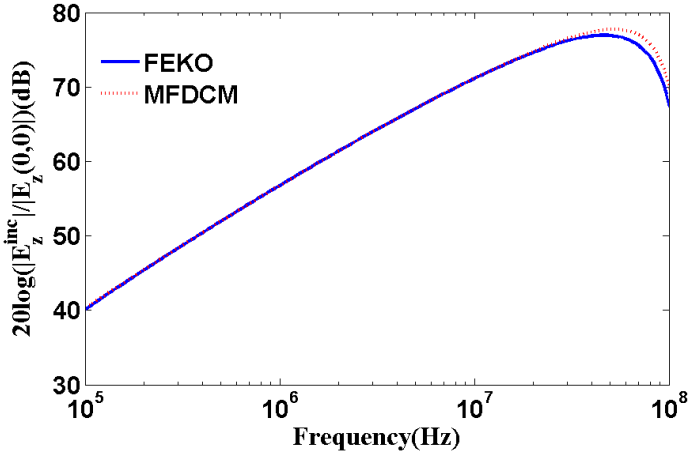

Figure 3.13 The normalized magnitude of E_z component at the center of shell versus frequency under the TM incidence. The shell is made by four layered CFC material and the fiber orientation is [90/90/90/90]. ($\epsilon_a = 3.4\epsilon_0 - j40000/\omega$, $\epsilon_b = 5.0\epsilon_0 - j50/\omega$ and d=0.127 mm for each single CFC-based layer, r_a=1 m).

Considering a composite shell with M layers and the interior radius r_a=1 m, each layer has the same $\epsilon_a = 3.4\epsilon_0 - j40000/\omega$ and $\epsilon_b = 3.4\epsilon_0 - j50/\omega$ as well as the thickness d=0.127 mm, as referred from [115], [116]. Fig. 3.11 shows the SE performance in a low frequency range. It is interesting to observe that the SE performance is essentially the same of two different fiber orientation patterns, both under TM or TE cases. As can be seen, more layers lead to a greater shielding, as expected. Both electric and magnetic fields shielding responses are presented in Fig. 3.11. By comparing our results with [116], an excellent agreement is also achieved. Once again, our method represents the multilayered CFC-based shell with a 4×4 matrix whereas the method used in [116] needs to apply a finite-difference to each interface of the multilayered structure.

Resonances occur in the shell at higher frequencies, which dramatically reduces the SE performance, as observed in Fig. 3.12. This effect was not pronounced in [116] where the SE calculation is based on the field at the center of the cylinder. It is interesting to see in Fig. 3.12(b) that the TE and TM modes are both excited by TE or TM incident waves for the fiber orientation pattern [0/45/90/-45]. Whereas the TE modes are excited only under the TE incidence, so does the TM case, for the fiber pattern[0/90]. The field distributions of modes shown in Fig. 3.12(b) are presented in Appendix C.

In order to validate our numerical implementation of the MFCM method, a comparison of the normalized magnitude of E_z field at the center of the shell versus frequency, obtained with the proposed method and with commercial software FEKO (from Altair) was conducted. It is

fair to compare with FEKO (MoM-based solver) because the proposed MFCM is a variant of MoM. Since curved anisotropic multilayered material cannot be modelled in FEKO, a four-layer CFC-based shell with fiber orientation [90/90/90/90] under TM incidence was used. Under these conditions, the shell can be considered as an isotropic material which makes the comparison with FEKO possible. The results for both methods are compared in Fig. 3.13, which shows that an excellent agreement is achieved. In FEKO, the 2D cylindrical structure is built with a finite height $h = r_a$. Then, one-dimensional periodic boundaries are applied in the z-direction to mimic an infinitely long cylindrical shell. A logarithmic sweep of 200 frequencies was done for both methods in the frequency range 0.1 MHz∼100MHz. The MFCM code which is implemented in a Matalb script took 34 seconds to obtain the results whereas it took 1.5 hour for FEKO, both codes running on the same hardware platform.

In the SE calculations presented in this section, the numbers of matching points and filamentary sources are equal, and the values are the same as that used in the Section 3.2.2.

A method to estimate the scattering and SE performances of multilayered CFC-based cylindrical shells has been proposed. A TIBC of a multilayer CFC-based shell is formulated to represent the shell with a 4×4 matrix at each matching point. In light of the TIBC and MFCM, the scattering and shielding performances of multilayered CFC-based shells are studied and discussed through several numerical examples. Our results are in excellent agreement with the published ones. The proposed technique shows its advantages in formulating and solving the problem with a simple and concise way. An interesting observation is that the anisotropic characteristic of the multilayered CFC material is negligible in scattering analyses since the cross-polarized fields are quite small compared with the main polarized counterpart. Anisotropy has a significant impact on the SE performance at high frequencies since both TE and TM modes are excited within the cylindrical shell under arbitrary incident plane waves. Although all the numerical examples discussed in this chapter are circular cylindrical shells, our proposed MFCM is also able to solve problems of shells with arbitrary smooth cross sections as long as the impedance boundary condition of the shell could be established. Also, since the TIBC is applied independently at each matching point, non-homogeneous shells where the property of the material varies with ϕ can be handled without additional considerations in the formulation.

3.3 Slot shells

In a metallic fuselage aircraft, shielding against incoming interference is essentially dependent on the penetration through apertures such as windows. When the fuselage is made of CFC, incident waves could also propagate through the material at certain frequencies. A simple

and fast simulation tool, proposed in this section, to assess the relative contribution of these two interference paths through the aperture and the CFC-based fuselage would be useful to better predict how CFC properties could affect the level of interference coming from external high-intensity radiated fields (HIRF) emitters. Since the lowest level of SE occurs when the cabin is illuminated at normal incidence, a simple 2D multilayered CFC-based slotted shell can be used as an acceptable simplified model to represent the CFC-based fuselage with a row of windows. By comparing with the closed multilayered CFC-based shell which has been discussed in [122], the slotted shell model is closer to the practical situation of interest. Moreover, the strategy used for the placements of matching points and sources is totally different for a slotted shell in comparison to that for a closed shell. Although windows are located at the two sides of a fuselage, which means that a CFC-based shell with two slots is closer to the practical composite fuselage case, the proposed numerical technique can be straightforwardly extended to the case where multiple slots present.

The scattering and SE analyses of a slotted cylindrical shell have generated a great interest among researchers for many years. An extensive literature review on this issue was reported in [123]. By incorporating a modal expansion of aperture fields, the scattered and penetrated fields have been investigated efficiently in [124]. The dual-series approach is a powerful technique to handle a series of mixed boundary-value problems of slotted cylindrical shells as reported in [125–127]. Three methods have been proposed to study the penetration fields of a slotted conducting cylinder under TM excitation in [128]. The multifilament current method (MFCM) was used in [129] to analyze the scattering from a slotted PEC shell, yet the MFCM is not capable to handle the situation where an anisotropic material is considered. A series of field integral equations were built in [130] and a mode-matching technique was used in [131] to calculate the EM evaluations from slotted shells.

The tensorial boundary condition (TBC), incorporated in the MFCM, is used for representing the multilayered CFC-based slot shell with a chain matrix. A specified strategy on the placements of matching points and sources is given by considering singular field behaviors near the slotted edge in this section. A convergence study is conducted in order to test the accuracy of the proposed technique. Several numerical examples are presented to analyze the SE performance in various situations.

3.3.1 Formulation

The problem is depicted in Fig. 3.14. The solution domain contains three regions, namely outer region 1, inner region 2, and region 3. Regions 1 and 2 are considered as air. Region 3 is constituted of multilayered CFC materials. The slot area is represented by a virtual boundary

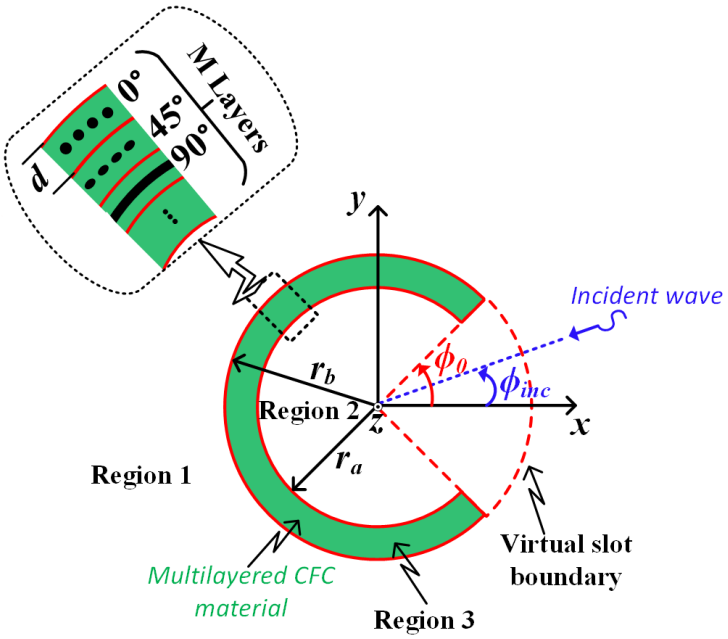

Figure 3.14 Layout of the single CFC-based planar layer.

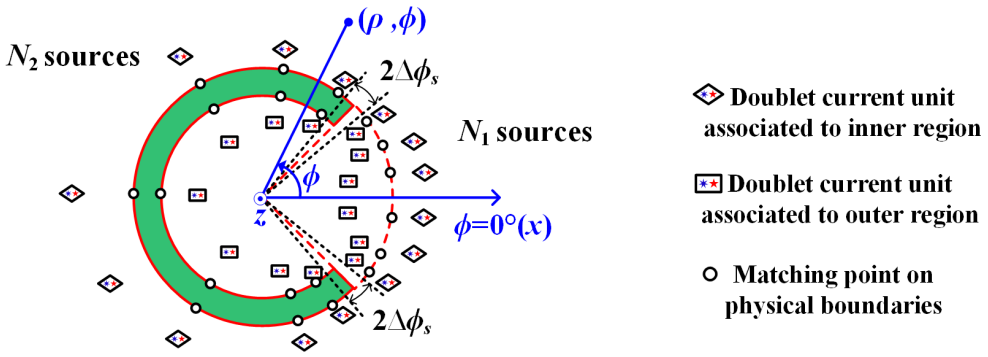

Figure 3.15 Formulation of MFCM for a multilayered CFC-based slotted shell

with slot angle $2\phi_0$ as indicated in Fig. 3.14. Regions 1 and 2 are separated by the region 3 and the virtual slot boundary. The modeling of CFC is discussed in Sec. 3.1.2 in detail. The carbon fibers inside of a single layer CFC-based shell will form helices, as shown in Fig. 3.3(a). According to the EMT [91], a single layer CFC material could be characterized by a tensor permittivity, which reads

$$\overline{\epsilon} = \begin{bmatrix} \epsilon_a & 0 & 0 \\ 0 & \epsilon_a & 0 \\ 0 & 0 & \epsilon_b \end{bmatrix}_{\rho'\phi'z'} \tag{3.34}$$

where $\epsilon_a = \epsilon_0\epsilon_{ra} - j\sigma_a/\omega$ and $\epsilon_b = \epsilon_0\epsilon_{rb} - j\sigma_b/\omega$ represent the complex permittivity of directions along and perpendicular to the fiber orientation.

The physical boundary, depicted in Fig. 3.14, contains two parts. The material part is made up of M-layer CFC-based curved slabs, and each layer has a different fiber orientation. The slot part is a virtual arc boundary defined with respect to the slot angle. For the material part, the TBC is easy to obtain and reads

$$\begin{bmatrix} E_{1\phi} \\ H_{1z} \\ E_{1z} \\ H_{1\phi} \end{bmatrix} = [A] \begin{bmatrix} E_{2\phi} \\ H_{2z} \\ E_{2z} \\ H_{2\phi} \end{bmatrix} \tag{3.35}$$

where $[A]$ is the chain matrix of the M-layer CFC-based shell. The details are discussed in Sec. 3.1.3. For the slot part, $[A]$ is a 4×4 identity matrix. The subscripts 1 and 2 for the material boundary are defined as circular arcs of the region 3 with radiuses $r_a + Md$ and r_a, respectively, and d is the thickness of each layer. While for the slot part, the subscripts 1 and 2 are defined as the outer and inner faces of the virtual arc with radius $r_a + Md$, as shown in Fig. 3.14.

The formulation of the MFCM combined with the TBC for a slotted CFC-based cylindrical shell is similar to that was introduced in Sec. 3.2.1 where a closed shell is considered. As Fig. 3.15 shows, a set of doublet current units are placed in regions 1 and 2. Each doublet current unit contains two z-directed co-located filament currents, one is the electric current and the other is the magnetic current, with complex magnitudes yet to be determined. Two equivalences are conducted in the MFCM. Firstly, the scattered fields in region 1 are generated by the equivalent doublet sources placed in region 2, and secondly, the scattered fields in region 2 are generated by all doublet sources placed in region 1. The expressions of scattered fields were given in Sec. 3.2.1. The main difference in the MFCM for the slotted and closed

cylindrical shells appears in the locations of matching points and doublet current units. The uniform placement strategy which was deployed in Sec. 3.2.1 by placing filament currents on virtual circular boundaries for a closed shell fails for the slotted scenario due to a poor approximation on the field behaviors near the slot edges. By considering the physical phenomenon of a slotted shell, we locate sources closer to the edges and then gradually place the others a distance away in order to better approximate the singular field behavior near the slotted edges as Fig. 3.15 indicates. The location of matching points on the physical boundary also obeys the same rule. Specifically, we place a total of N_1 sources per region in front of the virtual arc boundary and N_1 matching points on the virtual arc boundary. The virtual arc boundary is defined with respect to the slot angle, and a total of N_2 sources per region in front of on the remaining boundary and N_2 matching point pairs on the remaining boundary. The remaining boundary is associated to the material part. Each matching point pair contains one matching point on the outer and one on the inner boundaries, and the two points have the same ϕ angle as shown in Fig. 3.15. A useful empirical formula [129] for the matching points and sources is given below. For the ith source position (ρ_s, ϕ_s) (the cylindrical coordinate system is exploited herein for the convenience) placed in front of the material boundary in region 1 is given by

$$\rho_s(i) = \rho_{max} - (\rho_{max} - \rho_{min}) \sin(\frac{\pi(i-1)}{N_2 - 1}), \qquad 1 \leqslant i \leqslant N_2 \tag{3.36a}$$

$$\phi_{s(m)}(i) = \pi - (\pi - \phi_0 - \Delta\phi_s) \cos(\frac{\pi(i-1)}{N_2 - 1}), \qquad 1 \leqslant i \leqslant N_2 \tag{3.36b}$$

where $\rho_{max} = 1.4r_b$, $\rho_{min} = 1.001r_b$ are obtained empirically and used in our numerical examples. Equation (3.36b) also can be used to position the matching point pairs on the boundary associated to the multilayered CFC material. The inner and outer source locations associated to the material part are symmetrical with respect to the material boundary. For the ith source position placed in front of the virtual arc boundary in region 1 is given by

$$\rho_s(i) = \rho_{max} - (\rho_{max} - \rho_{min}) \sin(\frac{\pi(i-1)}{N_1 - 1}), \qquad 1 \leqslant i \leqslant N_1 \tag{3.37a}$$

$$\phi_{s(m)}(i) = \begin{cases} (\phi_0 - \Delta\phi_s) \cos(\frac{\pi(i-1)}{N_1-1}), 1 \leqslant i \leqslant \frac{N_1-1}{2} \\ 2\pi - (\phi_0 - \Delta\phi_s) \cos(\frac{\pi(i-1)}{N_1-1}), \frac{N_1-1}{2} \leqslant i \leqslant N_1 \end{cases} \tag{3.37b}$$

Similarly, equation (3.37b) also can be used to position the matching points on the virtual arc boundary. The inner and outer source locations associated to the slot part are symmetrical with respect to the virtual arc boundary. The distributions of sources in both regions and the matching point pairs on the boundary according to the introduced strategy of placements

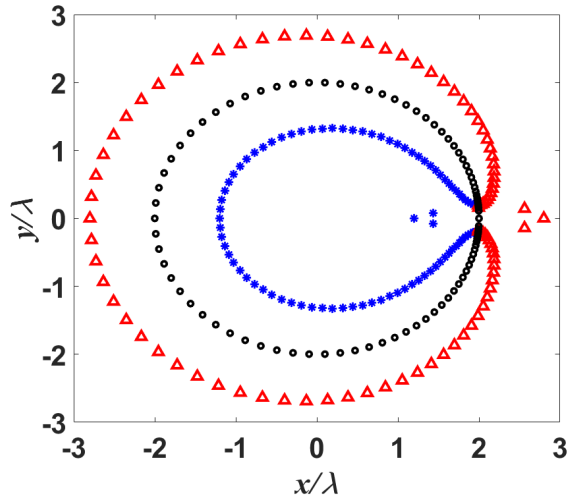

Figure 3.16 The distributions of sources inside and outside as well as matching points for a slot CFC-based shell with radius r_a=2 m and $\phi_0 = 5^\circ$. The locations of inside sources are marked with star, and outside sources are marked with triangle. The matching points are marked with dots.($N_1 = 5$ and $N_2 = 85$).

are presented in Fig. 3.16. $\Delta\phi_s$ denotes a suitably chosen angular section in the azimuthal direction relative to each edge position as shown in Fig. 3.15. Two small sections of the physical boundary defined in terms of $2\Delta\phi_s$ at each edge as indicated in Fig. 3.15, are not considered in the MFCM formulation. There are no matching points placed on it. $\Delta\phi_s$ is chosen as 0.5°, which works well in the range $r_a/\lambda \leqslant 5$, and it makes the length of the untouched boundary very small compared with the incident wavelength and therefore the scattered far field and penetrated field are not greatly affected in our numerical examples.

Based on the formulation of the MFCM and the constructed TBC, a linear system is easy to establish for solving the unknown current magnitudes. The monostatic echo width normalized to the incident wavelength and SE at the origin of the slotted shell under a TM excitation in terms of electric field are the parameters of interest to be evaluated once these current magnitudes are determined. They are defined as:

$$\frac{W}{\lambda} = \lim_{r\to\infty}(2\pi r\frac{|E_z^s|^2}{\lambda\,|E_z^{inc}|^2}) \tag{3.38a}$$

$$SE = -20\log_{10}(\frac{|E_2(0,0)|)}{|E_z^{inc}|} \tag{3.38b}$$

where λ is the incident wavelength and E_z^{inc} is the electric field of the incident plane wave.

3.3.2 Numerical examples

The commercial software tools at hand (FEKO [132], HFSS [133] and CST [101]) are unable to do the simulation of a multilayered CFC-based shell with a continuous space-varying permittivity tensor. Consequently, the validation of our solutions will be based on a convergence study of the boundary condition error. A boundary condition error calculated at a set of testing points along the boundaries, is defined as follows:

$$\Delta C = max\{\frac{|\,[F_1] - [A]\,[F_2]\,|}{max\{|F_1|, |F_2|\}}\} \tag{3.39}$$

where the division should be done in a term-by-term manner. $[F_1]$ and $[F_2]$ contain four field components, as defined in equation (3.12), which are tangential fields in regions 1 and 2 respectively. $[A]$ is the formulated TBC defined in equation (3.12). ΔC is the maximum value out of four calculated field components at each testing point. The number of testing points is three times of the number of matching point used in the MFCM solution. To illustrate this, we consider a 4-layered CFC-based slotted shell. Each layer has the same configurations as: $\epsilon_a = 5\epsilon_0 - j40000/\omega$, $\epsilon_b = 5\epsilon_0 - j200/\omega$ and d=0.127 mm. The fiber orientation ξ in each layer is $[0^\circ/45^\circ/90^\circ/-45^\circ]$, and $\xi = 90^\circ$ means the fiber orientation is parallel to the xoy plane. The interior radius is r_a=2 m, and the incident angle is $\phi_{inc} = 0^\circ$. $\phi_0 = 5^\circ$ is selected as an example to study the convergence response. The frequency is set as $k_0 r_a = 5$ (f = 119 MHz). ΔC responses with respect to three different choices of N_1 and N_2 are shown in Fig. 3.17. If we take $\Delta C \leqslant 1\%$ as the criterion, using $N_1 = 5$ and $N_2 = 85$ can generate results with the desired accuracy. The convergence of all the numerical examples shown later satisfy the prescribed criterion $\Delta C \leqslant 1\%$.

In addition, we consider a scenario where an isotropic lossy slotted shell is considered in order to validate the accuracy of the proposed technique with a commercial simulation tool. The shell, with a finite thickness d=0.5 mm, is constituted of a lossy material with σ=10000 S/m. In FEKO, the 2D cylindrical shell is built with a finite height $h = 0.5r_a$. Then, one-dimensional periodic boundaries are applied in the z-direction to mimic an infinitely long cylindrical shell. The calculated magnitudes of the electric field along the x-axis within the slotted shell using the proposed MFCM and FEKO with different slot angles are presented in Fig. 3.18. An excellent agreement is obtained even if the slot edges are not modelled accurately in the $\Delta\phi_s$ intervals as Fig. 3.18 shows, which confirms the accuracy of the proposed technique for the isotropic case.

We then consider a 4-layer CFC-based slotted shell. Each layer has the same configurations as: $\epsilon_a = 5\epsilon_0 - j40000/\omega$, $\epsilon_b = 5\epsilon_0 - j200/\omega$ and d=0.127 mm. The fiber orientation ξ in each

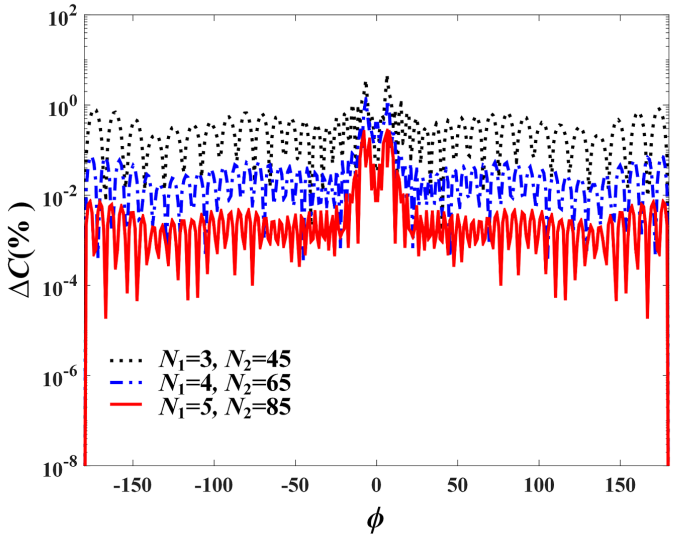

Figure 3.17 A convergence study regarding to the boundary condition error of a 4-layered CFC-based slotted shell with $\phi_0 = 5^\circ$ and $k_0 r_a = 5$

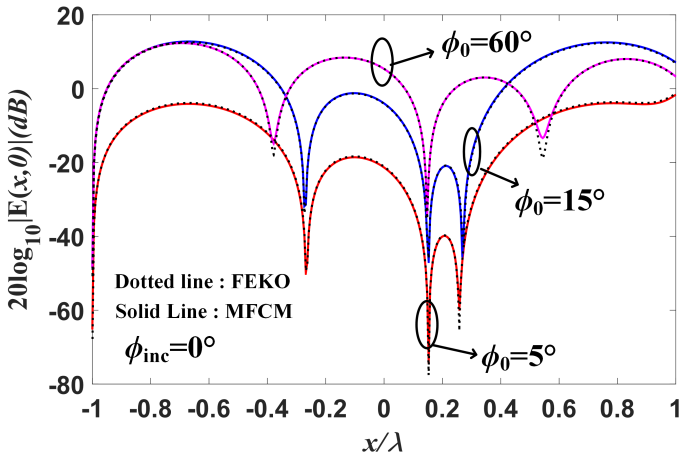

Figure 3.18 Comparisons of the E-field along x-axis within the slotted lossy shell between the proposed method and FEKO, for different slot angles.(σ=10000 S/m, d=0.5 mm, $r_a = \lambda = 1$ m. $N_1 = 5, 12, 22$ and $N_2 = 35, 28, 22$ are used for the MFCM to do the simulations of $\phi_0 = 5^\circ, 15^\circ, 60^\circ$, respectively.)

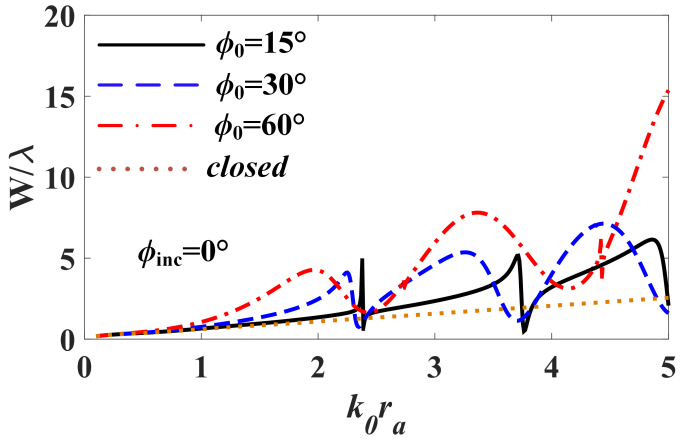

Figure 3.19 The monostatic scattering responses of the 4 layered CFC-based slotted shell for different slot angles.($\epsilon_a = 5.0\epsilon_0 - j40000/\omega$, $\epsilon_b = 5.0\epsilon_0 - j200/\omega$ and d=0.127 mm for each single CFC-based layer, r_a=2 m, $N_1 = 12, 16, 22$ and $N_2 = 78, 68, 63$ are used for the MFCM to do the simulations of $\phi_0 = 15°, 30°, 60°$, respectively.)

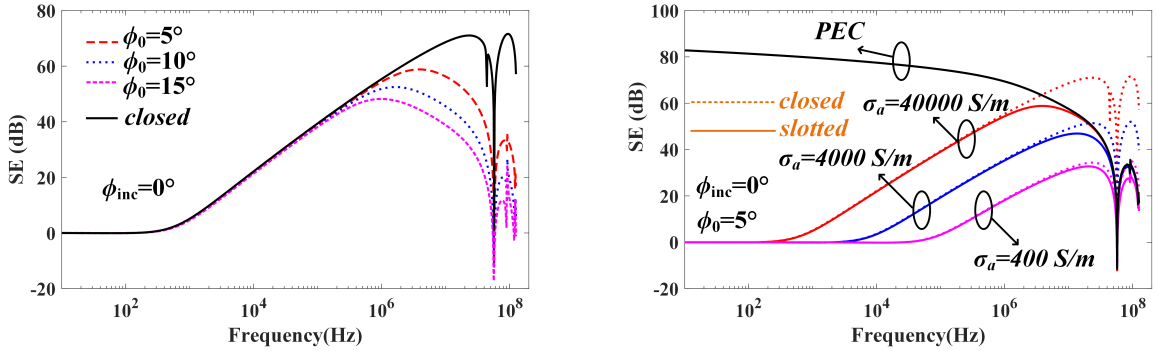

(a) (b)

Figure 3.20 The SE responses of the 4 layered CFC-based slotted shell under (a) different slot angles, and $\epsilon_a = 5.0\epsilon_0 - j40000/\omega$, $\epsilon_b = 5.0\epsilon_0 - j200/\omega$ for each single CFC-based layer, $N_1 = 5, 9, 12$ and $N_2 = 85, 83, 78$ are used for the MFCM to do the simulations of $\phi_0 = 5°, 10°, 15°$, respectively, and (b) different σ_a, and $\epsilon_a = 5.0\epsilon_0 - j\sigma/\omega$, $\epsilon_b = 5.0\epsilon_0 - j200/\omega$, $N_1 = 5$ and $N_2 = 85$ are used for the CFC-based shell and $N_1 = 5$ and $N_2 = 35$ are used for the PEC shell in the MFCM.) (d=0.127 mm for each single CFC-based layer, r_a=2 m.)

layer is $[0^\circ/45^\circ/90^\circ/-45^\circ]$. The interior radius is r_a=2 m, and the incident angle is $\phi_{inc} = 0^\circ$. Fig. 3.19 shows the normalized monostatic echo width responses of a slotted CFC-based shell with different slot angles. The slot will lead to more scattering compared with the closed shell when frequency goes higher, and the normalized echo width also increases as the slot angle increases in the higher frequency range. Several sharp changes in the scattering responses as observed in Fig. 3.19 are due to the internal resonances of the slotted shell [124].

The SE analysis of a slotted shell with a small slot angle is more of practical interests in the electromagnetic compatibility. The configuration of the CFC material is the same as in the previous example. Generally, there are two paths for the external fields to couple into the slotted shell, one is coupled through the multilayered CFC material and the other is via the aperture. Fig. 3.20(a) shows the SE performances of a slotted 4-layer CFC-based shell versus different slot angles. Obviously, the three considered slots do not affect the SE responses when frequency is low, which indicates that the penetration is mainly through CFC-based layers. However, SE decreases drastically when frequency increases to a certain point where the incident wavelength is comparable to the arc length of the slot, and the slot then plays an important role in coupling external fields into the inner region, as Fig. 3.20(a) suggests. As expected, the larger slot angle will decrease the SE response earlier and result in a lower SE compared with the slot with a smaller value in the higher frequency range.

Fig. 3.20(b) describes the SE responses versus σ_a, the conductivity of the direction parallel to the fiber orientation in a single CFC-based layer. The slot angle is fixed at 5° in this scenario. As expected, the higher conductivity will provide more shielding, as can be seen from Fig. 3.20(b). Moreover, the SE responses of closed and slotted CFC-based shells overlap in the low frequency range. The SE of a slotted PEC shell, which represents the infinite conductivity situation, is also presented in Fig. 3.20(b). The slotted PEC shell exhibits a high SE level in the lower frequency range, because the inner and outer fields can only be coupled via the aperture. The SE responses of the slotted PEC shell and the slotted CFC-based shells with $\sigma_a = 4000$ S/m and $\sigma_a = 40000$ S/m overlap in the high frequency range as Fig. 3.20(b) indicates, which means the coupling of fields between the outer and inner regions are dominated by the slots. However, for the case of $\sigma_a = 400$ S/m, the SE response is a bit lower in the high frequency range, which suggests that coupling through the multilayered CFC-based shell is comparable to that via a slot.

3.4 Simulation of cylindrical metasurfaces using GSTC-MFCM

The generalized sheet transition conditions (GSTC) is proposed to investigate the guided waves on a metafilm (metasurface), a surface distribution of electrically small scatterers

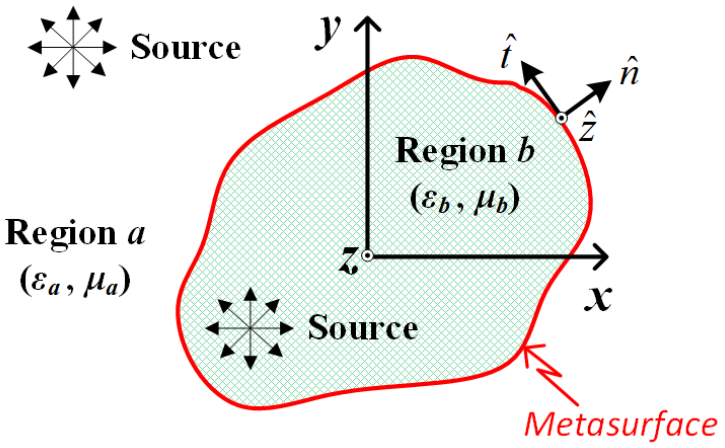

Figure 3.21 Problem description.

characterized by electric and magnetic surface susceptibilities, and it expresses the relationship between tangential electric and magnetic fields on both sides of a metasurface [134–136]. Usually, the thickness of a metesurface is much smaller than the operating wavelength and is considered as 0. The FDTD [137] and FEM [138] formulations, incorporating the GSTC, have been fully developed as efficient analysis tools to study the electromagnetic evaluation of planar metasurfaces, yet there are few efficient computational tools have been developed so far for curved metasurfaces. The MoM introduced in [139, 140] combined with the GSTC were developed to simulate a cylindrical metasurface with arbitrary cross sections in 2D scenario. But a singularity issue is encountered when the distance between source and observation points vanishes, and therefore a special treatment on Hankel function with augment approaching zero should be considered. Several wave-controlled designs using cylindrical and spherical metasurfaces could be found in [141–144]. By considering the potential applications of curved metasurfaces, the development of an efficient and accurate simulation tool should be considered. In this section, we will explore the application of the MFCM on EM evaluations of cylindrical metasurfaces by deploying the GSTC into the formulation.

3.4.1 Impedance-type GSTC and Metasurface Synthesis Procedure

The problem of interest is depicted in Fig. 3.21. The outer region a and inner region b are considered to be occupied by isotropic materials characterized by the permittivity and permeability couple (ϵ_a, μ_a) and (ϵ_b, μ_b), respectively. Regions a and b are separated by a cylindrical metasurface with an arbitrary cross section. We assume that the cylindrical metasurface is infinite in z-direction and a 2-D condition, $\partial/\partial z \equiv 0$, is applied. The cross section of the

metasurface could be closed or slotted with an arbitrary shape. Two orthogonal coordinate systems are provided in Fig. 3.21. One is the global (Cartesian) coordinate system (x, y, z) and the other is the local coordinate system (n, t, z). The z components in two coordinate systems overlap. In our proposed numerical method, the contour of the considered cylindrical metasurface is discretized via matching points, and the tangential electromagnetic fields are forced to obey GSTC at each matching point. The vector form or scalar form of GSTC was introduced in [134–136, 145–147], and it usually casts in the form relating the difference and average of transverse electric and magnetic fields on the two sides of a metasurface. Yet the impedance-type boundary condition is more common in moment method solutions for the convenience of problem formulation. In this section, the impedance-type GSTC at each matching point in the local coordinate system on the contour of a cylindrical metasurface is developed and reads

$$[L]\begin{bmatrix} E_{1t} \\ E_{2t} \\ E_{1z} \\ E_{2z} \end{bmatrix} = [R]\begin{bmatrix} H_{1z} \\ H_{2z} \\ H_{1t} \\ H_{2t} \end{bmatrix} \tag{3.40}$$

with

$$[L] = \begin{bmatrix} A_{11} & A_{11} & A_{12} & A_{12} \\ A_{21} & A_{21} & A_{22} & A_{22} \\ D_{11} & D_{11} & D_{12}+1 & D_{12}-1 \\ D_{21}-1 & D_{21}+1 & D_{22} & D_{22} \end{bmatrix}$$

$$[R] = -\begin{bmatrix} B_{12}-1 & B_{12}+1 & B_{11} & B_{11} \\ B_{22} & B_{22} & B_{21}+1 & B_{21}-1 \\ C_{12} & C_{12} & C_{11} & C_{11} \\ C_{22} & C_{22} & C_{21} & C_{21} \end{bmatrix}$$

$$\begin{bmatrix} A_{11} & A_{12} \\ A_{21} & A_{22} \end{bmatrix} = \frac{1}{2}j\omega\epsilon_0\begin{bmatrix} \chi_{ee}^{tt} & \chi_{ee}^{tz} \\ \chi_{ee}^{zt} & \chi_{ee}^{zz} \end{bmatrix}; \begin{bmatrix} B_{11} & B_{12} \\ B_{21} & B_{22} \end{bmatrix} = \frac{1}{2}jk_0\begin{bmatrix} \chi_{em}^{tt} & \chi_{em}^{tz} \\ \chi_{em}^{zt} & \chi_{em}^{zz} \end{bmatrix}$$

$$\begin{bmatrix} C_{11} & C_{12} \\ C_{21} & C_{22} \end{bmatrix} = \frac{1}{2}j\omega\mu_0\begin{bmatrix} \chi_{mm}^{tt} & \chi_{mm}^{tz} \\ \chi_{mm}^{zt} & \chi_{mm}^{zz} \end{bmatrix}; \begin{bmatrix} D_{11} & D_{12} \\ D_{21} & D_{22} \end{bmatrix} = \frac{1}{2}jk_0\begin{bmatrix} \chi_{me}^{tt} & \chi_{me}^{tz} \\ \chi_{me}^{zt} & \chi_{me}^{zz} \end{bmatrix}$$

where χ_{ee}, χ_{mm}, χ_{em} and χ_{me} are the electric/magnetic (first e/m subscripts) surface susceptibilities reacting to electric/magnetic (second e/m subscripts) excitations, $k_0 = \omega\sqrt{\epsilon_0\mu_0}$ is the wave number in free space. The subscripts 1 and 2 in (3.40) refer to region 1, where the incident and reflected fields are involved, and region 2, where only the transmitted fields are involved, respectively. Either the region a or b in Fig. 3.21 could be the region 1 or 2 depend-

ing on the locations of excitations. The normal polarization densities are assumed to be 0 by considering the subwavelength thickness of a metasurface, the four surface susceptibility, $[A]$, $[B]$, $[C]$ and $[D]$, appear with a 2×2 dyadic form. The derivation of impedance-type GSTC can be found in Appendix D.

Theoretical synthesis procedure to obtain surface susceptibilities was conducted in [145]. To solve for 16 unknown susceptibilities, up to 4 independent wave triplet bases are required for the systhesis input. Each wave triplet ($\boldsymbol{\psi}$) includes incident ($\boldsymbol{\psi}^{inc}$), reflected ($\boldsymbol{\psi}^{ref}$) and transmited ($\boldsymbol{\psi}^{tra}$) waves, $\boldsymbol{\psi} = \{\boldsymbol{E}, \boldsymbol{H}\}$. Although given more independent wave triplets may provide a possibility to synthesize a metasurface which could control electromagnetic waves in a peculiar way, the synthesized surface susceptibilities must be realizable in practice. One or two wave triplets, in most cases, are input into the synthesis procedure in order to obtain up to 8 surface susceptibilities. Providing one specified wave triplet, up to 4 surface susceptibilities can be synthesized to make the metasurface behaves monoanisotropic ($[B] = [D] = 0$) and uniaxial ($\chi_{ee}^{tz} = \chi_{ee}^{zt} = \chi_{mm}^{tz} = \chi_{mm}^{zt} = 0$) medium characteristics. Given two independent wave triplets, up to 8 susceptibilities could be synthesized. The choices of selecting 8 from total 16 susceptibilities could be random. There are two meaningful alternatives, one is for a metasurface with monoanisotropic properties ($[B] = [D] = 0$) but not uniaxial ($[A]$ and $[C]$ are nonzero matrices), and the other case of interest is for a metasurface with bianisotropic ($[A]$, $[B]$, $[C]$ and $[D]$ are all nonzero matrices) medium characteristic. Once the impedance-type GSTC of a metasurface is established, it will be subsequently deployed in the MFCM to analyze the electromagnetic performances of an investigated metasurface.

3.4.2 GSTC-MFCM Formulation

The concept of MFCM is illustrated in Fig. 3.22. We place a set of doublet current units in inner and outer regions. Each doublet current unit contains two co-located z-directed filament currents, one is electric current and the other is magnetic current. The formulation of MFCM is simple and conducted through two equivalences. Firstly, the scattered fields in the outer region a are generated by the equivalent sources placed in the inner region b, and those filament sources are treated as source currents radiating in an unbounded region constituted of the isotropic material with permittivity ϵ_a and permeability μ_a. Secondly, the scattered fields in the inner region b are generated by all equivalent sources placed in the outer region a, and those filament sources are treated as source currents radiating in an unbounded region constituted of the isotropic material with permittivity ϵ_b and permeability μ_b. The scattered fields generate by doublet current units could be either reflected or transmitted fields.

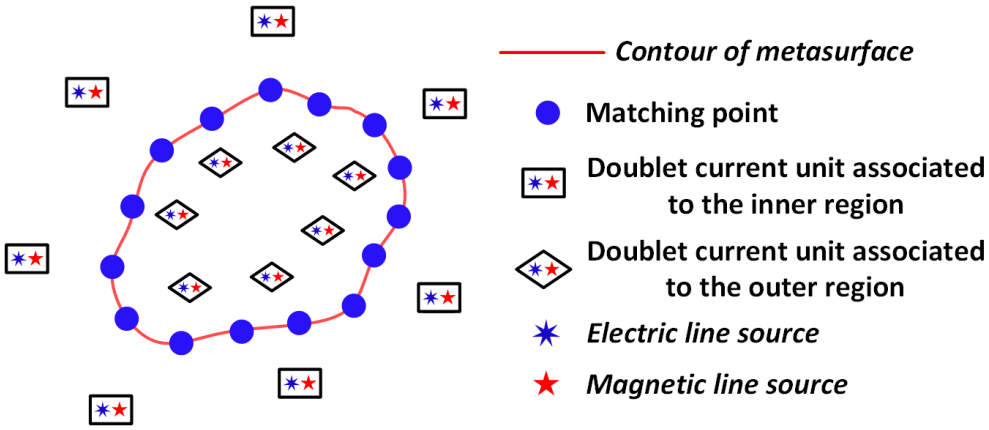

Figure 3.22 Formulation of MFDCM

Fields Expressions in Regions 1 And 2

The region 1 contains the incident and scattered fields. The scattered fields in region 1 are produced by all z-directed filament currents in region 2, and vice versa. Either the region a or b in Fig. 3.21 could be the region 1 or 2 depending on the locations of incident excitations. Assuming that the outer and inner regions of a metasurface are occupied by isotropic materials, the scattered fields in each region can be directly written in terms of the 2-D dyadic isotropic Green's function, and the total fields in each region read:

$$\begin{aligned}\boldsymbol{E_q} =& \frac{k_q}{4j}\sum_{i=1}^{N_q} K_{qi}\frac{(y-y_{qis})\hat{\boldsymbol{x}}+(x_{qis}-x)\hat{\boldsymbol{y}}}{R_{qi}}H_1^{(2)}(k_qR_{qi}) \\ &-\frac{k_q^2}{4\omega\epsilon_q}\sum_{i=1}^{N_q} I_{qi}H_0^{(2)}(k_qR_{qi})\hat{\boldsymbol{z}}+\delta(q-1)\boldsymbol{E^{inc}}\end{aligned} \tag{3.41}$$

$$\begin{aligned}\boldsymbol{H_q} =& \frac{k_q}{4j}\sum_{i=1}^{N_q} I_{qi}\frac{(y_{qis}-y)\hat{\boldsymbol{x}}+(x-x_{qis})\hat{\boldsymbol{y}}}{R_{qi}}H_1^{(2)}(k_qR_{qi}) \\ &-\frac{k_q^2}{4\omega\mu_q}\sum_{i=1}^{N_q} K_{qi}H_0^{(2)}(k_qR_{qi})\hat{\boldsymbol{z}}+\delta(q-1)\boldsymbol{H^{inc}}\end{aligned} \tag{3.42}$$

with

$$R_{qi}=\sqrt{(x-x_{qis})^2+(y-y_{qis})^2}$$

$$k_q=\omega\sqrt{\epsilon_q\mu_q}$$

where $q = \{1, 2\}$ indicates the region 1 or 2. δ is the Kronecker delta function, and equal to 1 when the region 1 is considered. The I_{qi} and K_{qi} are the unknown electric and magnetic current coefficients we need to determine in two regions. N_1 and N_2 are the number of the doublet current units in regions 2 and 1, respectively, and for the convenience, an equal number of doublet current units, $N_1 = N_2$, are used in our numerical examples. (x_{qis}, y_{qis}) is the ith doublet current unit position in the region 1 or region 2 and (x, y) is the observation point. The R_{qi} is the distance between ith filament source and observation point. The k_q is the wavenumber in the correspond region.

Boundary Conditions

The connection between the fields in regions 1 and 2 is dictated by the impedance-type GSTC which has been expressed in (3.40) at the contour of the meatsurface indicated in Fig. 3.21. A linear system is then created by imposing the GSTC at a number of matching points on the physical boundary in order to determine the unknown current coefficients. An equal number of matching points is placed on the inner and outer surfaces of the cylindrical metasurface, and the outer and inner matching points merge by considering the zero thickness of the metasurface. The number of matching points (N_m) must satisfy the inequality

$$2N_m \geqslant N_1 + N_2 \tag{3.43}$$

to determine the total current coefficients ($2N_1$ in region 2 and $2N_2$ in region 1). Notice that each matching point is tested twice for the fields in the outer and inner regions by considering zero thickness metasurface.

Upon the application of a point-matching procedure, we will finally obtain a matrix expressions of the type

$$[Q]\,\boldsymbol{X} = \boldsymbol{B} \tag{3.44}$$

where $\boldsymbol{X}$ is a column vector containing the unknown current coefficients (K_1, I_1, K_2, and I_2) in two regions, and $\boldsymbol{B}$ is another column vector containing samples of incident tangential fields at the matching points. $[Q]$ is a matrix whose entries are obtained from the filament's tangential fields at matching points, and it could be rectangular or square depending whether oversampling is used or not. If it is in square form, a unique solution can be found, otherwise the smallest least-square error solution is pursued [58]. In our case, we will always adopt the square matrix $[Q]$ by letting $N_1 = N_2 = N_m$.

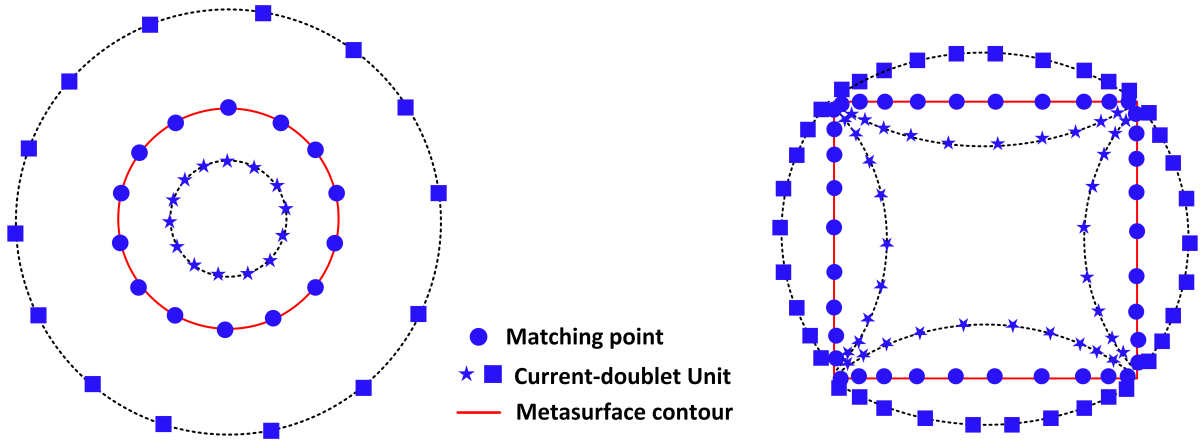

(a) (b)

Figure 3.23 Source location strategies for (a) circular and (b) rectangular contours.

Source Location

The source location is dependent on the shape of the contour. For the contour with a smooth boundary, the sources are placed on two virtual contours which have the same shape as the physical boundary but are located inside and outside of the metasurface. For example, the *ad hoc* $R/2-2R$ rule which used in [119–121] is effective for a circular boundary as shown in Fig. 3.23(a). The doublet current units in outer region are uniformly placed on a virtual circle with a radius $2r$, and the units in inner region are uniformly placed on a virtual circle with a radius $r/2$, where r is the radius of a circular cylindrical metasurface. For an unsmooth boundary as suggested in Fig. 3.23(b) which contains sharp edges, the *ad hoc* $R/2-2R$ rule does not apply. Experiments have shown that better convergence is achieved by locating the sources closer to the edges and then gradually place the others a distance away. This approach better approximates the singular field behavior near the edges [27, 105]. The inner and outer locations of doublet current units are symmetrical with respect to the boundary, as shown in Fig. 3.23(b). The location of matching points on the physical contour also obey the same rule. A useful empirical formula of the source and matching point locations for a contour with edges can be found in [105, 148], and also provided in (3.36) and (3.37). It is noteworthy that the singularity problem appears in [139, 140] when the distance between source and observation points vanishes, therefore a special treatment on Hankel function with argument approaching zero should be considered. However, this singularity is avoided completely in the MFCM by placing sources at a prescribed distance away from the matching points.

So far, all information have been presented for the linear system. Once these current magnitudes are determined, the fields and related parameters of interest can be evaluated in a

straightforward manner.

3.4.3 Illustrating examples

Two examples will be discussed in this section in order to prove the ability of proposed method in the simulation of a cylindrical metasurface incorporating GSTC. The first example concerns a rectangular cylindrical metasurface camouflaging origin-located actual source by an fictitious source placed within the metasurface. The second example is about a bianisotropic metasurface with a circular contour cloaking incident plane waves with given incident angles.

Camouflage Metasurface

Region 1 which contains the incident and reflected waves is defined as the inner region of the metasurface shell in this example, and the incident fields are generated by an electric line source with a unit magnitude placed at the origin. The reflected fields within the shell are assumed as null. The transmitted fields in the region 2 assumed to be generated by an electric line source placed at $(x_a,\, y_a)$ within the metasurface. In this case, the original electric line source is camouflaged by the cylindrical metasurface. The contour of the shell is rectangular as indicated in Fig. 3.24.

Only incident fields are presented in the region 1 in this case, and read

$$\boldsymbol{E^{inc}} = -\frac{k_0^2}{4\omega\epsilon_0} H_0^{(2)}(k_0 R)\hat{\boldsymbol{z}} \tag{3.45a}$$

$$\boldsymbol{H^{inc}} = \frac{k_0}{4j}\frac{x\hat{\boldsymbol{y}} - y\hat{\boldsymbol{x}}}{R} H_1^{(2)}(k_0 R) \tag{3.45b}$$

with

$$R = \sqrt{x^2 + y^2}$$

where $(x,\, y)$ is the observation point.

The transmitted fields which generated by a fictitious source placed at $(x_a,\, y_a)$ are present in the region 2, and read

$$\boldsymbol{E^{tra}} = -\frac{k_0^2}{4\omega\epsilon_0} H_0^{(2)}(k_0 R_a)\hat{\boldsymbol{z}} \tag{3.46a}$$

$$\boldsymbol{H^{tra}} = \frac{k_0}{4j}\frac{(x - x_a)\hat{\boldsymbol{y}} + (y_a - y)\hat{\boldsymbol{x}}}{R} H_1^{(2)}(k_0 R_a) \tag{3.46b}$$

with

$$R_a = \sqrt{(x - x_a)^2 + (y - y_a)^2}$$

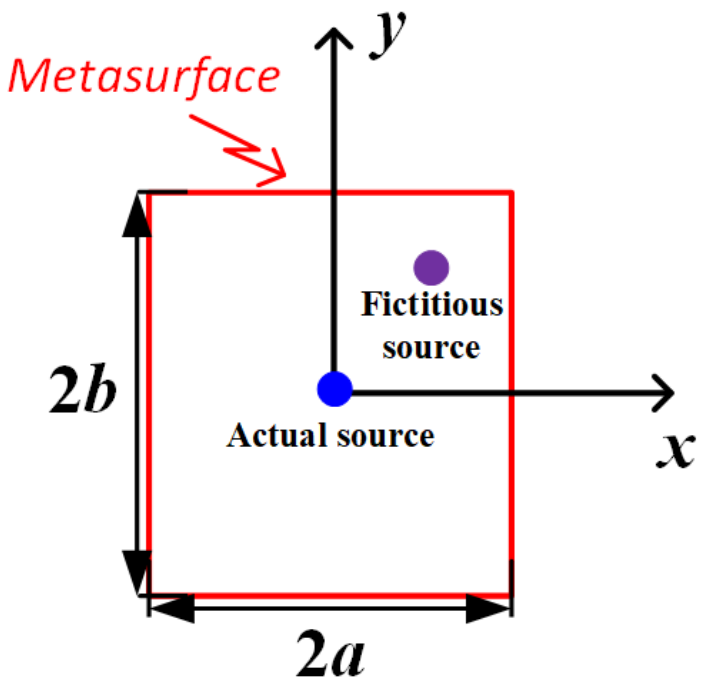

Figure 3.24 Problem description of a camouflaged rectangular metasurface.

Inserting these specified fields into (3.40) yields

$$A_{22} = \frac{1}{2} j\omega\epsilon_0 \chi_{ee}^{zz} = \frac{H_t^{tra} - H_t^{inc}}{E_z^{inc} + E_z^{tra}} \tag{3.47a}$$

$$C_{11} = \frac{1}{2} j\omega\mu_0 \chi_{mm}^{tt} = \frac{E_z^{tra} - E_z^{inc}}{H_t^{tra} + H_t^{inc}} \tag{3.47b}$$

We consider the square metasurface with $a = b = 1$ m, and the displaced source is placed at ($x_a = 0.5$, $y_a = 0.5$). The operation wavelength is 1 m. The simulation results are presented in Fig. 3.25. The magnitude difference of reflected and transmitted electric fields between the calculated ones using GSTC-MFCM and the preset ones is presented in Fig. 3.25(a). The value of the difference varies in the range of 10^{-6}, which indicates the simulated reflected and transmitted field have a good agreement with the prescribed ones. The magnitude of the total electric field in the two regions is presented in Fig. 3.25(b). It is clearly to see that the actual source has been successfully replaced by the illusion source after coating the rectangular metasurface.

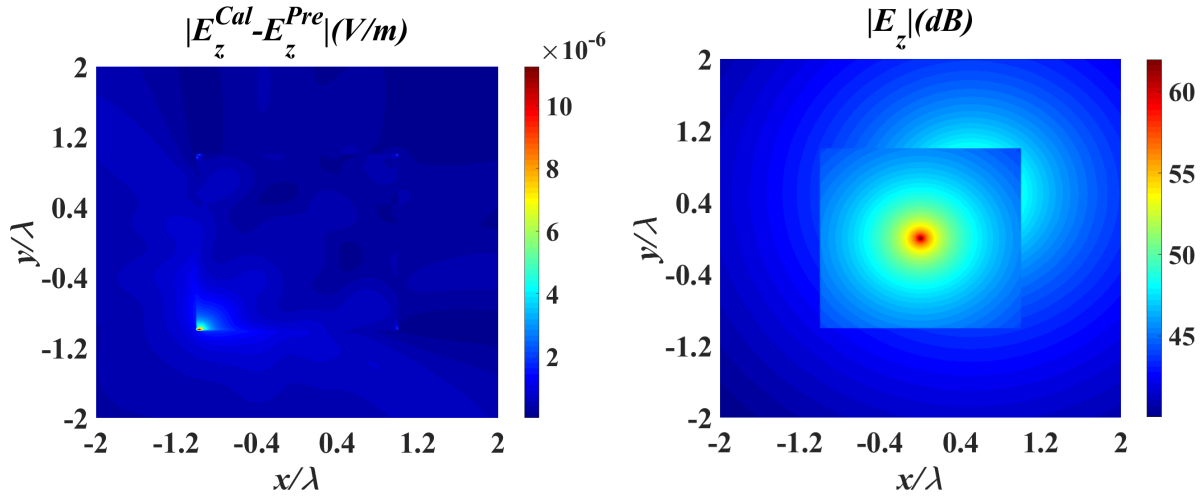

(a) (b)

Figure 3.25 (a) The magnitude difference between the calculated and preset E_z in the two regions. (b) The E_z component of the total electric fields in the two regions.

Bianisotropic Metasurface

The second example is a metasurface with a circular contour cloaking TE_z incident waves with two prescribed directions of propagation. In this case, the reflected fields are considered as null in the outer region 1 which is occupied by vacuum. The inner region 2 is occupied by a dielectric with $\epsilon_b = 4\epsilon_0$ and $\mu_b = \mu_0$. Two independent wave triplets, both including TE_z incident waves but with different incidence angles, are presented in this example in order to synthesize a bianisotropic metasurface. Since the reflected fields are null, only the expressions of preset incident and transmitted waves in two wave triplets, distinguished by a and b, respectively, are given and read in the cylindrical coordinates for convenience:

$$H_{za}^1 = H_{za}^{inc} = e^{jk_0 r p_a}; E_{\phi a}^1 = E_{\phi a}^{inc} = -\eta_0 p_a e^{jk_0 r p_a} \tag{3.48a}$$

$$H_{za}^2 = H_{za}^{tra} = T e^{jk_2 r p_a}; E_{\phi a}^2 = E_{\phi a}^{tra} = -T\eta_2 p_a e^{jk_2 r p_a} \tag{3.48b}$$

$$H_{zb}^1 = H_{zb}^{inc} = e^{jk_0 r p_b}; E_{\phi b}^1 = E_{\phi b}^{inc} = -\eta_0 p_b e^{jk_0 r p_b} \tag{3.48c}$$

$$H_{zb}^2 = H_{zb}^{tra} = T e^{jk_2 r p_b}; E_{\phi b}^2 = E_{\phi b}^{tra} = -T\eta_2 p_b e^{jk_2 r p_b} \tag{3.48d}$$

with

$$p_a = \cos(\phi - \phi_{inc}^a); \quad p_b = \cos(\phi - \phi_{inc}^b)$$

$$k_2 = k_0\sqrt{\epsilon_b \mu_b}; \quad \eta_2 = \sqrt{\mu_b/\epsilon_b}$$

Here, only tangential fields which are used for synthesis are considered. The transmission coefficient is imposed as $T = \sqrt{\eta_b/\eta_0}$. (r, ϕ) is the position of the observation point, and ϕ^a_{inc} and ϕ^b_{inc} are the incident angles of two independent TE_z polarized plane waves, respectively. η_0 and k_0 are the impedance and wave number of free space, respectively.

By substituting (3.48) into (3.40) and assuming nonzero A_{11}, B_{12}, C_{22} and D_{21}, we will have

$$B_{12} = \frac{(H^{tra}_{za} - H^{inc}_{za})(E^{inc}_{\phi b} + E^{tra}_{\phi b}) - (H^{tra}_{zb} - H^{inc}_{zb})(E^{inc}_{\phi a} + E^{tra}_{\phi a})}{(H^{tra}_{zb} + H^{inc}_{zb})(E^{inc}_{\phi a} + E^{tra}_{\phi a}) - (H^{inc}_{za} + H^{tra}_{za})(E^{inc}_{\phi b} + E^{tra}_{\phi b})} \tag{3.49a}$$

$$A_{11} = \frac{(1 - B_{12})H^{inc}_{za} - (1 + B_{12})H^{tra}_{za}}{E^{inc}_{\phi a} + E^{tra}_{\phi a}} \tag{3.49b}$$

$$D_{21} = \frac{(E^{tra}_{\phi a} - E^{inc}_{\phi a})(H^{inc}_{zb} + H^{tra}_{zb}) - (E^{tra}_{\phi b} - E^{inc}_{\phi b})(H^{inc}_{za} + H^{tra}_{za})}{(H^{tra}_{zb} + H^{inc}_{zb})(E^{inc}_{\phi b} + E^{tra}_{\phi b}) - (H^{inc}_{zb} + H^{tra}_{zb})(E^{inc}_{\phi a} + E^{tra}_{\phi a})} \tag{3.49c}$$

$$C_{22} = \frac{(1 - D_{21})E^{inc}_{\phi a} - (1 + D_{21})E^{tra}_{\phi a}}{H^{inc}_{za} + H^{tra}_{za}} \tag{3.49d}$$

We consider a circular cylindrical metasurface with a radius $r_m = 1$ m. The metasurface is excited simultaneously by two TE_z polarized plane waves propagating in -x direction ($\phi^a_{inc} = 180^\circ$) and propagating in x direction ($\phi^b_{inc} = 0^\circ$). The calculated reflected and transmitted fields are compared with the preset ones, and the differences between them are below 10^{-10} as shown in Fig. 3.26(a) and 3.26(b), which indicate a high simulation accuracy is achieved by using the proposed MFCM. The phase distribution of H_z component of total magnetic field in two regions for the scenario that the metasurface is solely illuminated by a TE_z polarized plane wave propagating in -x direction is shown in Fig. 3.26(c). Obviously, the metasurface can successfully cloak the incident plane wave as prescribed.

Simulation performances

To obtain simulation results in Fig. 3.25, 200 doublet current units per region and 200 matching points are used in the MFCM for the calculation. The CPU time and required memory for solving 800 unknowns are 1.4063 s and 0.0478 GB, respectively. We use 70 doublet current units per region and 70 matching points in the second example to obtain results in Fig. 3.26. The CPU time and required memory for solving 280 unknowns are 0.5781 s and 0.0059 GB, respectively. All simulations were run on the desk computer with an intel(R) Core(TM) i7-7700@3.6 GHz. Simulation performances are not provided in [139,140] therefore a comparison is not possible. But according to [3, 149], the MFCM has been proven to have relative significant advantages with respect to efficiency, complexity, accuracy, and ease of implementation over the MoM, and these advantages are definitely inherited in this work for

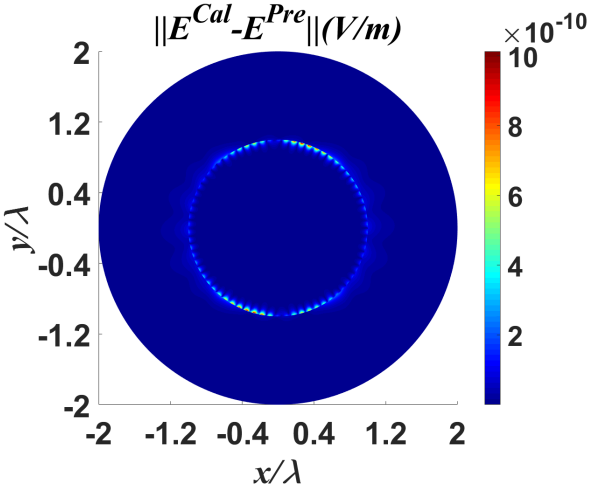

(a)

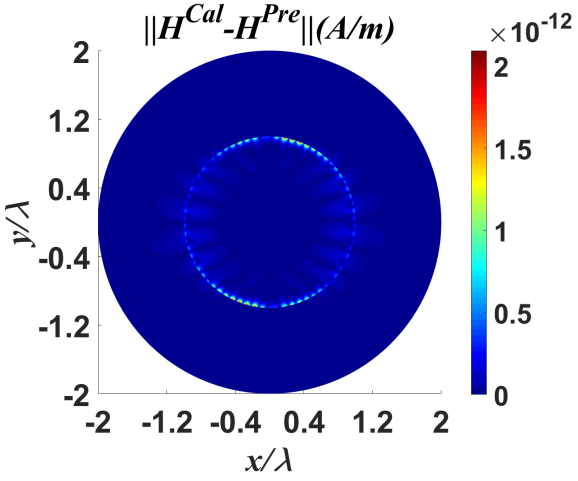

(b)

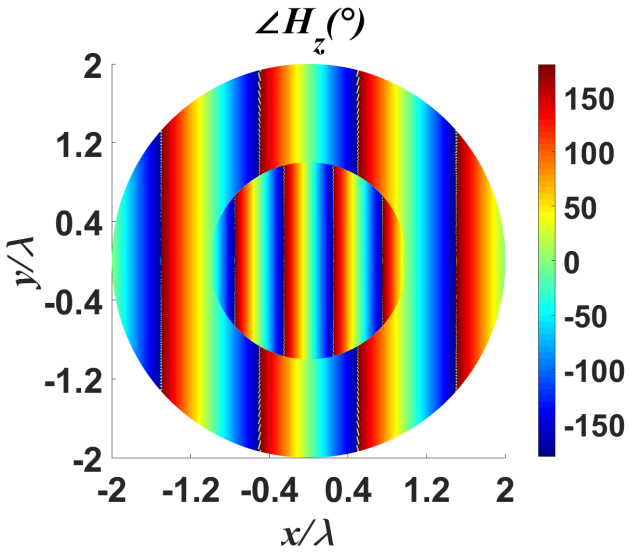

(c)

Figure 3.26 The magnitude differences between the calculated and preset (a) electric and (b) magnetic fields in two regions. (c) Phase distribution of H_z component of total magnetic field in two regions for the case that the metasurface is solely illuminated by a TE_z polarized plane wave propagating in -x direction.

the simulation of GSTC-characterized metasurfaces.

3.5 Analyses of induced current on a CFC-based shell excited by line sources

The problem of routing conducting wires and cables is an attractive topic in electromagnetic interference (EMI) and electromagnetic compatibility (EMC). Ensuring EMC of electrical wiring system in an aircraft, which may contain many kilometers of wires, is a real engineering challenge. Usually cables are installed in close proximity of the conductive aircraft skin, which provides a good return path when unexpected unbalanced (common mode) current develop on the cables. This is true for aluminum aircraft, but the situation may be different when the aircraft skin is made of anisotropic CFC material. The conducting wires, usually contains driving and returning wires therefore differential wire pairs, would generate magnetic induction on the surface of the fuselage. To study induced currents on the surface of a CFC-based shell is meaningful for the installation of electric systems mounted on the CFC-based fuselage. In this section, we will study the problem of a CFC-based shell enclosing two differential wires. For the simplicity, we use line sources to represent the conducting wires. The problem is depicted in Fig. 3.27. A set of z-directed line sources carrying different phase terms ($e^{-jk_z z}$) are placed within the shell, and each line source could be either electric or magnetic currents. The incident fields are generated by these line sources. For the simplicity, the inner and outer regions of the shell are considered as vacuum in this section, and therefore $k_0 = k_1 = k_2$, where k_0 is the wavenumber of free space. In addition, since the shell is infinitely long in the z-direction.

The problem formulation is the same as that discussed in Sec. 3.2.1, but the filament currents within the doublet current unit carry the $e^{-jk_z z}$ phase term in this case. Therefore the expressions of four tangential scattered fields generated by filament currents are different with that introduced in (3.14)∼(3.17) and should be slightly modified by considering the phase term of filament currents:

$$\begin{aligned} E^s_{q\phi} = & \frac{k_\rho}{4j}\sum_{i=1}^{N_q} K_{qi}\frac{r_{qis}\cos(\phi-\phi_{qis})-r}{R_{qi}}H_1^2(k_\rho R_{qi})e^{-jk_z z} \\ & + \frac{k_\rho k_z}{4j\omega\epsilon}\sum_{i=1}^{N_q} I_{qi}\frac{r_{qis}\sin(\phi-\phi_{qis})}{Rqi}H_1^2(k_\rho R_{qi})e^{-jk_z z} \end{aligned} \tag{3.50a}$$

$$E^s_{qz} = -\frac{k_\rho^2}{4\omega\epsilon}\sum_{i=1}^{N_q} I_{qi}H_0^2(k_\rho R_{qi})e^{-jk_z z} \tag{3.50b}$$

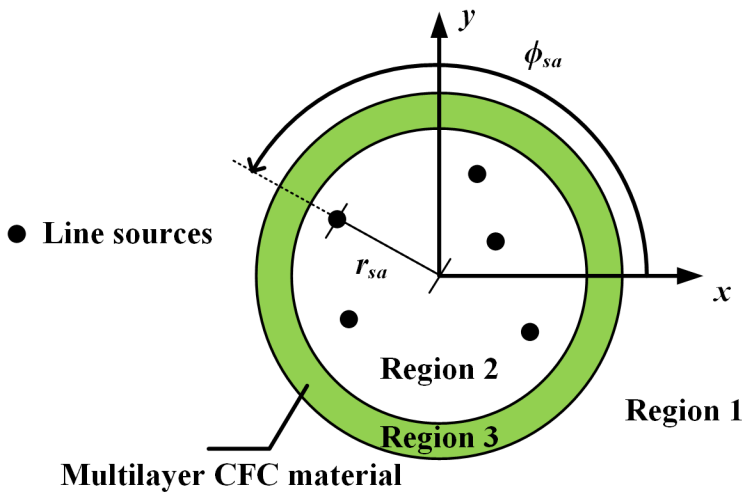

Figure 3.27 The problem description of a CFC-based shell excited by a set of line sources

$$H^s_{q\phi} = \frac{k_\rho k_z}{4j\omega\mu}\sum_{i=1}^{N_q} K_{qi}\frac{r_{qis}\sin(\phi-\phi_{qis})}{R_{qi}}H_1^2(k_\rho R_{qi})e^{-jk_z z} + \frac{k_\rho}{4j}\sum_{i=1}^{N_q} I_{qi}\frac{r-r_{qis}\cos(\phi-\phi_{qis})}{R_{qi}}H_1^2(k_\rho R_{qi})e^{-jk_z z} \tag{3.50c}$$

$$H^s_{qz} = -\frac{k_\rho^2}{4\omega\mu}\sum_{i=1}^{N_q} K_{qi}H_0^2(k_\rho R_{qi})e^{-jk_z z} \tag{3.50d}$$

with

$$R_{qi} = \sqrt{r^2 + r_{qis}^2 - 2rr_{qis}\cos(\phi-\phi_{qis})}$$

$$k_0^2 = k_\rho^2 + k_z^2$$

where $q = \{1, 2\}$ indicates the region 1 or 2. The I_{qi} and K_{qi} are the unknown electric and magnetic current coefficients that need to be determined in two regions. N_1 and N_2 are the numbers of doublet current unit in region 2 and region 1, respectively. (r_{qis}, ϕ_{qis}) is the ith filament source position in the region 1 or region 2 and (r, ϕ) is the observation point. The R_{qi} is the distance between ith filament source and the observation point.

We assume the incident fields are generated by a set of electric line sources placed within the shell. The $z = 0$ plane is selected in all numerical examples and the common term $e^{-jk_z z}$ can be assumed and omitted. For one electric line source expressed as $\boldsymbol{J_0} = I_0 e^{-jk_z z}\delta(r - r_{sa})\delta(\phi - \phi_{sa})\hat{\boldsymbol{z}}$ placed at (r_{sa}, ϕ_{sa}), the generated incident tangential fields read

$$E^{inc}_\phi = I_0\frac{k_z k_{\rho 1}}{4j\omega\epsilon_0}\frac{r_{sa}\sin(\phi-\phi_{sa})}{R_a}H_1^{(2)}(k_\rho R_a) \tag{3.51a}$$

$$E_z^{inc} = -I_0 \frac{k_{\rho 1}^2}{4\omega\epsilon_0} H_0^{(2)}(k_\rho R_a) \tag{3.51b}$$

$$H_\phi^{inc} = I_0 \frac{k_{\rho 1}}{4j} \frac{r - r_{sa}\cos(\phi - \phi_{sa})}{R_a} H_1^{(2)}(k_\rho R_a) \tag{3.51c}$$

with

$$k_0^2 = k_z^2 + k_\rho^2$$

$$R_a = \sqrt{r^2 + r_{sa}^2 - 2rr_{sa}\cos(\phi - \phi_{sa})}$$

The incident fields generated by a magnetic line source can be obtained from (3.51) through the duality theory. The total incident fields generated by a set of line sources can be easily obtained by superposition. It is worthwhile to mention that the Hankel function in (3.50) must be replaced by the modified Bessel function of the second kind when $k_z > k_0$ (the slow wave case) in order to represent the physics of the problem.

The shell considered in this section is made up of 4-layer CFC material. Each layer has the same configurations as $\epsilon_a = 5\epsilon_0 - j40000/\omega$, $\epsilon_b = 5\epsilon_0 - j50/\omega$ and d=0.127 mm (see equation (3.2)). The fiber orientation ξ in each layer is $[0^\circ/45^\circ/90^\circ/-45^\circ]$, and the outermost layer with a fiber orientation 0°. $\xi = 0^\circ$ means the fiber orientation is parallel to the z-axis. The interior radius is r_a=1 m. It is assumed that the line sources operate at 300 MHz, corresponding to a free-space wavelength of 1 meter. Two electric line sources with differential uniform magnitudes are placed within the shell, and the locations of two line sources are (r_{sa}, ϕ_{sa}) and (r_{sb}, ϕ_{sb}) respectively. Two scenarios are considered. In the first case, the k_z is set as $0.5k_0$ (fast wave) whereas k_z is set as $1.5k_0$ (slow wave) in the second case.

3.5.1 Convergence study

The convergence of the situations where the closed shell is illuminated by a plane wave is easy to achieve. When the line sources illuminate the shell, the convergence response is highly related to the positions of line sources and therefore needs to be studied in detail. The convergence definition has been given in (3.39), and for the convenience, we rewrite it here:

$$\Delta C = \frac{|\,[\boldsymbol{E}] - [\boldsymbol{Z}]\,[\boldsymbol{H}]\,|}{max\{|\boldsymbol{E}|, |\,[\boldsymbol{Z}]\,[\boldsymbol{H}]\,|\}} \tag{3.52}$$

where the division should be done in a term-by-term manner, and $[\boldsymbol{E}]$, $[\boldsymbol{Z}]$ and $[\boldsymbol{H}]$ are three matrices defined in (3.13).

For the first investigated scenario, the four components of ΔC with respect to each component of the tangential electric and magnetic fields are plotted in Fig. 3.28 for different locations of

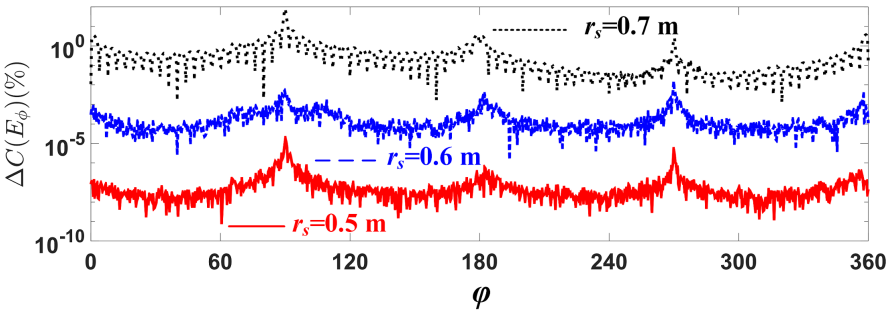

(a)

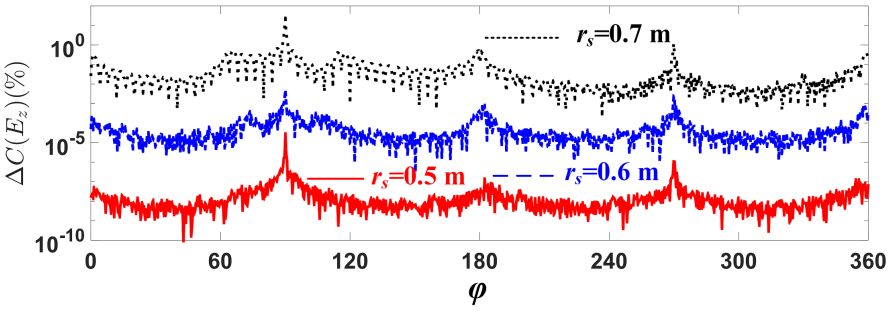

(b)

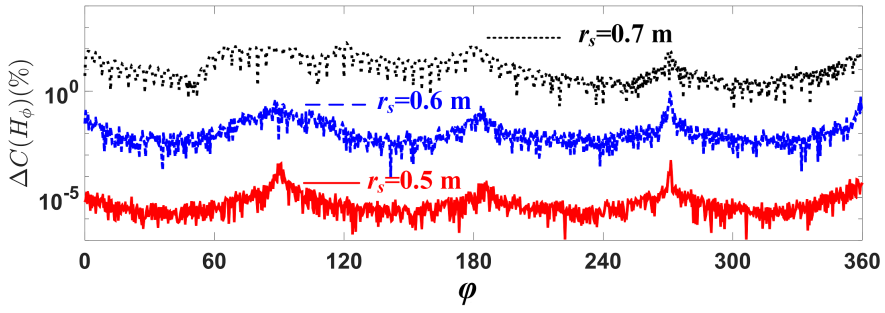

(c)

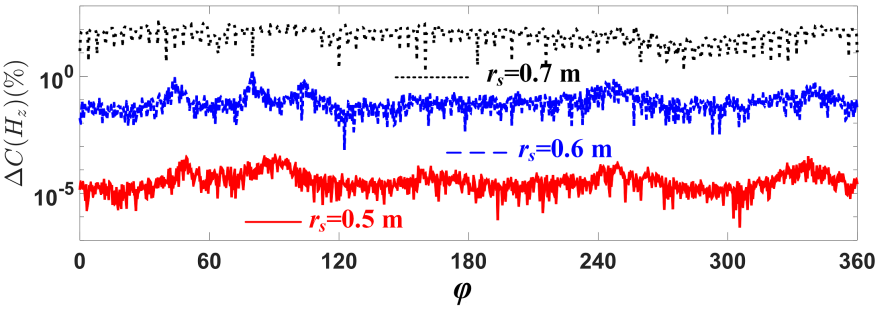

(d)

Figure 3.28 Convergence responses on the boundary with respect to the locations of the two differential line sources for the case $k_z = 0.5k_0$. (a) $\Delta C(E_\phi)$, (b)$\Delta C(E_z)$, (c) $\Delta C(H_\phi)$ and (d) $\Delta C(H_z)$. ($r_s = r_{sa} = r_{sb}$, $\phi_{sa} = 5^\circ$, and $\phi_{sb} = -5^\circ$).

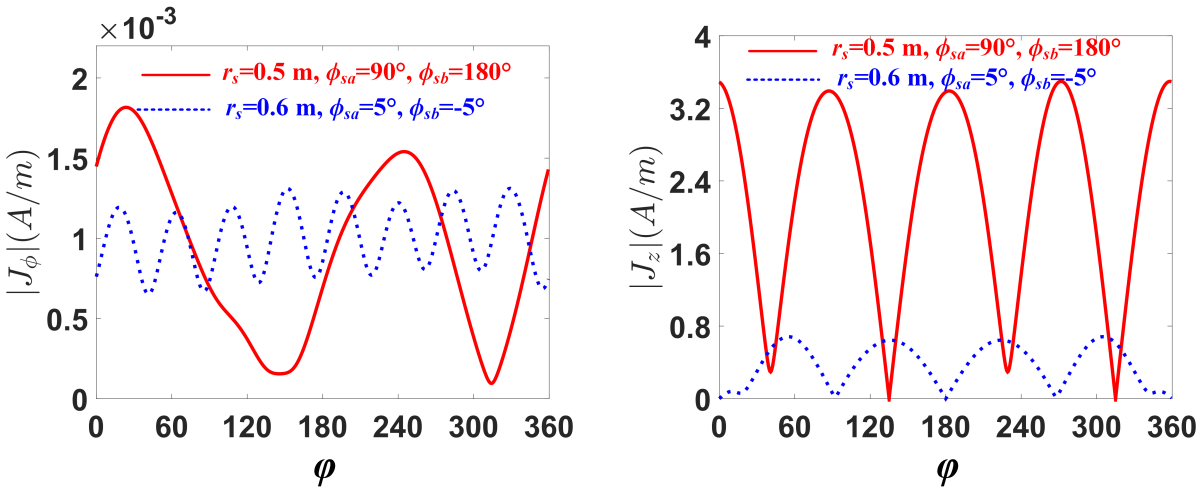

(a) (b)

Figure 3.29 The magnitudes of induced currents (a) J_ϕ and (b)J_z for the first scenario.

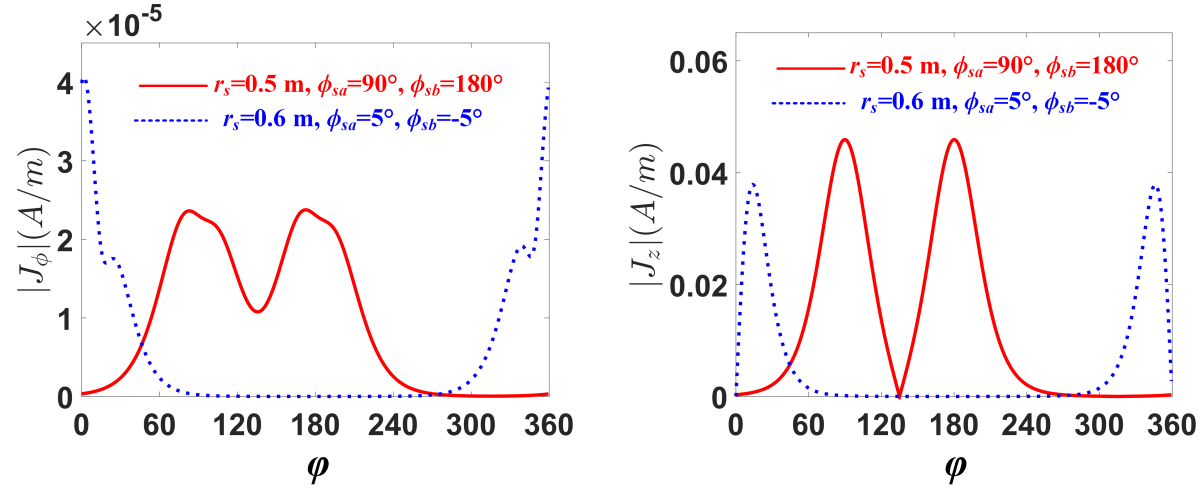

(a) (b)

Figure 3.30 The magnitudes of induced currents (a) J_ϕ and (b)J_z for the second scenario.

the two line sources with differential currents, and $r_{sa} = r_{sb} = r_s$, $\phi_{sa} = 5^\circ$ and $\phi_{sb} = -5^\circ$. We use 120 doublet current units and matching point pairs for the solution to obtain unknown current coefficients and 1000 test point pairs are selected on the the shell to do the convergence test. It is obvious that the response of the convergence deteriorates as the two sources come closer to the shell. The convergence response cannot be improved by increasing the number of doublet current units and matching point pairs. This is because the incident fields are highly non-uniformly distributed on the inner surface of the shell in this case. Since the fields vary rapidly in the area close to the line sources, the proposed MFCM cannot capture details of the fields behavior and therefore a bad convergence is obtained as shown in Fig. 3.28. If we use $\Delta C < 1\%$ as the criteria for the convergence response, a converged result can be achieved when the location parameter $r_s = r_{sa} = r_{sb}$ of the differential line sources is smaller than 0.6 m in this case. One possible solution to improve the convergence response when the line sources are placed closer to the shell is to use other type of weighting (for instance the RWG test technique [150]) instead of point matching technique. Those findings in the first scenario are also true in the second scenario where $k_z = 1.5k_0$ is considered.

3.5.2 Calculation of induced currents

The induced current on the inner surface of the shell can be calculated once the prescribed criteria for the convergence is achieved. The induced current is calculated with the tangential magnetic fields on the physical boundary:

$$\boldsymbol{J} = \hat{\boldsymbol{n}} \times (\boldsymbol{H}|_{\boldsymbol{r}=\boldsymbol{r_a}} - \boldsymbol{H}|_{\boldsymbol{r}=\boldsymbol{r_a}+\boldsymbol{4d}}) \tag{3.53}$$

where $\hat{\boldsymbol{n}}$ is a unit vector normal to the inner surface and point to the inner region of the shell, and r_a is the radius of inner surface of the shell.

In Fig. 3.29, the magnitudes of induced currents J_ϕ and J_z on the inner surface of a 4 layered CFC-based shell are presented for the first scenario, i.e., $k_z = 0.5k_0$. For the second scenario, i.e., $k_z = 1.5k_0$, the calculated magnitudes of induced currents are presented in Fig. 3.30. Two different locations of the differential line sources with uniform magnitudes are investigated in both scenarios, one is the case where two line sources are placed closely, and the location parameters are $r_{sa} = r_{sb} = r_s = 0.6$ m, $\phi_{sa} = 5^\circ$ and $\phi_{sb} = -5^\circ$. The other is the case where the location parameters are $r_{sa} = r_{sb} = r_s = 0.5$ m, $\phi_{sa} = 90^\circ$ and $\phi_{sb} = 180^\circ$. In both scenarios, the magnitude of J_ϕ is much smaller than that of J_z as indicated in Fig. 3.29 and 3.30, and this is because the electric line sources used as excitations carrying current in the z direction, which generates only a ϕ component of incident magnetic field. In a PEC shell,

there would be no scattered H_z. When the shell is made composite, the H_z field is induced by the fibers not aligned with the z axis. In addition, the magnitudes of induced current in the second case are also much smaller than that in the first case, and this is because the fields generated by the line source in the second case decay rapidly. Since the magnitudes of two sources are differential, there will be a null point once they are placed closely as shown in Fig. 3.29(b) and 3.30(b) with dotted lines.

3.6 Conclusion

In this chapter, we have exploited applications of the MFCM on anisotropic shells by deploying boundary conditions in the formulation. The impedance boundary condition for a multilayered CFC-based shell and GSTC for a cylindrical metasurface have been discussed in detail. The closed and slotted shells also have been taken into consideration. The plane wave and line source excitations have been investigated in the MFCM. Many numerical examples have been presented and discussed, and they have proven the ability of the proposed MFCM in handling simulations under the presence of anisotropic impedance boundary conditions.

CHAPTER 4 THREE-DIMENSIONAL SCATTERING FROM OBJECTS MADE OF UNIAXIAL MATERIALS

The 3D scattering analyses from uniaxial objects using the equivalent source method (ESM) are discussed in this chapter. The multiple infinitesmall dipole method (MIDM) is a commonly used name to designate the ESM in the 3D scenario. Therefore the term, MIDM, is used throughout this chapter. We start with a derivation, as introduced in Sec. 4.1, of dyadic Green's functions of uniaxial materials. The fields within the investigated uniaxial objects are expressed in terms of the derived dyadic Green's functions, and subsequently deployed in the formulation of the proposed MIDM. The formulation for an object with a smooth boundary is introduced in Sec. 4.2. While for an object with sharp edges, the formulation should include additional treatment to consider the edge effect and is presented in Sec. 4.3. The boundary conditions, singularities in using the dyadic Green's functions as well as convergence study are presented in Sec. 4.4. Two sets of examples regarding the smoothness of the boundary of an object are computed in Sec. 4.5. Apart from good agreements of calculated results between our proposed MIDM and commercial software packages, our proposed computational technique has advantages on CPU time and/or required memory in comparison to commercial software.

4.1 Closed-form dyadic Green's functions of uniaxial material

The uniaxial characteristic seems to be the most widely used type of anisotropic materials. This is because the uniaxial material can be either easily found in many natural crystals [82, 85], or artificially made by a stacked dielectric sheet structure consisting of alternative layers of two isotropic materials [78,79,86], or obtained by homogenizing a mixture of several different materials via effective medium theory [87,88]. If the uniaxial material is considered, the tensor permittivity and tensor permeability are characterized as

$$\overline{\boldsymbol{\epsilon}} = \begin{pmatrix} \epsilon_1 & 0 & 0 \\ 0 & \epsilon_1 & 0 \\ 0 & 0 & \epsilon_2 \end{pmatrix}_{\hat{\boldsymbol{u}}\hat{\boldsymbol{v}}\hat{\boldsymbol{c}}} \tag{4.1a}$$

$$\overline{\boldsymbol{\mu}} = \begin{pmatrix} \mu_1 & 0 & 0 \\ 0 & \mu_1 & 0 \\ 0 & 0 & \mu_2 \end{pmatrix}_{\hat{\boldsymbol{u}}\hat{\boldsymbol{v}}\hat{\boldsymbol{c}}} \tag{4.1b}$$

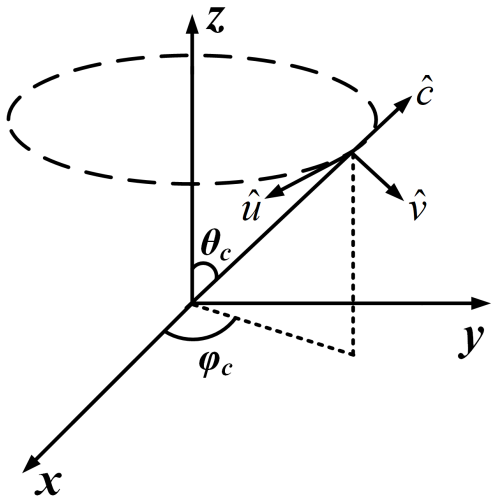

Figure 4.1 The configurations of local and global coordinates.

where the local orthogonal coordinates, represented by unit vectors $\hat{\boldsymbol{u}}$, $\hat{\boldsymbol{v}}$ and $\hat{\boldsymbol{c}}$ as shown in Fig. 4.1, are used to express the uniaxial medium in local coordinate system. Vector $\hat{\boldsymbol{c}}$ is the unit vector parallel to the distinguished axis of the medium. Parameters ϵ_1, μ_1 and ϵ_2, μ_2 are the permittivity and permeability associated with the directions perpendicular and parallel to the distinguished axis ($\hat{\boldsymbol{c}}$), respectively. The relationship between the unit vectors in the local and global coordinates is written as

$$\begin{bmatrix} \hat{\boldsymbol{u}} \\ \hat{\boldsymbol{v}} \\ \hat{\boldsymbol{c}} \end{bmatrix} = \begin{bmatrix} \sin\varphi_c & -\cos\varphi_c & 0 \\ \cos\theta_c\cos\varphi_c & \cos\theta_c\sin\varphi_c & -\sin\theta_c \\ \sin\theta_c\cos\varphi_c & \sin\theta_c\sin\varphi_c & \cos\theta_c \end{bmatrix} \begin{bmatrix} \hat{\boldsymbol{x}} \\ \hat{\boldsymbol{y}} \\ \hat{\boldsymbol{z}} \end{bmatrix} \tag{4.2}$$

where θ_c and φ_c are defined in Fig. 4.1.

The closed-form dyadic Green's functions represent the electric and magnetic fields radiated into an unbounded region filled with uniaxial materials by electric and magnetic point sources (infinitesimal dipoles). A brief introduction of the derivation is given herein, more details can be found in [54]. The time dependence of $e^{j\omega t}$ is assumed and suppressed throughout this section. The investigations are carried out in the time-harmonic regime, and the Maxwell's equations can be written as

$$-j\omega\boldsymbol{D} + \nabla\times\boldsymbol{H} = \boldsymbol{J} \tag{4.3a}$$

$$\nabla\times\boldsymbol{E} + j\omega\boldsymbol{B} = -\boldsymbol{M} \tag{4.3b}$$

where the vector fields $\boldsymbol{E}$, $\boldsymbol{D}$, $\boldsymbol{H}$ and $\boldsymbol{B}$ stand for electric field, dielectric displacement, mag-

netic field, and magnetic induction. $\boldsymbol{J}$ and $\boldsymbol{M}$ represent impressed electric and magnetic current density distribution. By considering the constitutive relations of a homogeneous medium, we have

$$\boldsymbol{D} = \overline{\boldsymbol{\epsilon}} \cdot \boldsymbol{E} \tag{4.4a}$$

$$\boldsymbol{B} = \overline{\boldsymbol{\mu}} \cdot \boldsymbol{H} \tag{4.4b}$$

where $\overline{\boldsymbol{\epsilon}}$ and $\overline{\boldsymbol{\mu}}$ are the tensor permittivity and permeability of the investigated uniaxial material, defined in (4.1).

Equations 4.3 and 4.4 can be written in the compact form

$$(j\omega \begin{pmatrix} \overline{\epsilon} & 0 \\ 0 & \overline{\mu} \end{pmatrix} + \begin{pmatrix} 0 & -\nabla \times \overline{\boldsymbol{I}} \\ \nabla \times \overline{\boldsymbol{I}} & 0 \end{pmatrix}) \cdot \begin{pmatrix} \boldsymbol{E} \\ \boldsymbol{H} \end{pmatrix} = - \begin{pmatrix} \boldsymbol{J} \\ \boldsymbol{M} \end{pmatrix} \tag{4.5}$$

where $\overline{\boldsymbol{I}}$ is the unit dyadic in three dimensional orthogonal coordinates. If we set $\boldsymbol{J} = \delta(\boldsymbol{r}-\boldsymbol{r}')$ and $\boldsymbol{M} = \delta(\boldsymbol{r}-\boldsymbol{r}')$, which are the electric and magnetic infinitesimal dipoles, respectively, the solution for the $\boldsymbol{F}(\boldsymbol{r})$ of equation 4.5 corresponds to the closed-form dyadic Green's function exactly. Vector $\boldsymbol{r}'$ is the position of the infinitesimal dipole, and $\delta(\boldsymbol{r}-\boldsymbol{r}')$ is the Dirac delta function. In this case, the equation 4.5 reduces to

$$(j\omega \begin{pmatrix} \overline{\epsilon} & 0 \\ 0 & \overline{\mu} \end{pmatrix} + \begin{pmatrix} 0 & -\nabla \times \overline{\boldsymbol{I}} \\ \nabla \times \overline{\boldsymbol{I}} & 0 \end{pmatrix}) \cdot \overline{\boldsymbol{G_s}}(\boldsymbol{r}, \boldsymbol{r}') = -\delta(\boldsymbol{r}-\boldsymbol{r}')\overline{\boldsymbol{I}}_{\boldsymbol{s}} \tag{4.6}$$

where $\overline{\boldsymbol{I}}_{\boldsymbol{s}}$ is the 6×6 unit dyadic. It is convenient to revert the above compact notation to standard 3×3 dyadic for actual calculations [54], then

$$\overline{\boldsymbol{G}}_{\boldsymbol{s}}(\boldsymbol{r}, \boldsymbol{r}') = \begin{pmatrix} \overline{\boldsymbol{G}}_{\boldsymbol{ee}}(\boldsymbol{r}, \boldsymbol{r}') & \overline{\boldsymbol{G}}_{\boldsymbol{em}}(\boldsymbol{r}, \boldsymbol{r}') \\ \overline{\boldsymbol{G}}_{\boldsymbol{me}}(\boldsymbol{r}, \boldsymbol{r}') & \overline{\boldsymbol{G}}_{\boldsymbol{mm}}(\boldsymbol{r}, \boldsymbol{r}') \end{pmatrix} \tag{4.7a}$$

$$\overline{\boldsymbol{I}}_{\boldsymbol{s}} = \begin{pmatrix} \overline{\boldsymbol{I}} & 0 \\ 0 & \overline{\boldsymbol{I}} \end{pmatrix} \tag{4.7b}$$

where $\overline{\boldsymbol{G}}_{\boldsymbol{ee}}(\boldsymbol{r}, \boldsymbol{r}')$, $\overline{\boldsymbol{G}}_{\boldsymbol{mm}}(\boldsymbol{r}, \boldsymbol{r}')$, $\overline{\boldsymbol{G}}_{\boldsymbol{em}}(\boldsymbol{r}, \boldsymbol{r}')$ and $\overline{\boldsymbol{G}}_{\boldsymbol{me}}(\boldsymbol{r}, \boldsymbol{r}')$ are the dyadic Green's functions of the electric type, the magnetic type and the hybrid type. By substituting equation 4.7 into 4.6, we can further develop equation 4.6 as

$$\overline{\boldsymbol{L}}_{\boldsymbol{e}} \cdot \overline{\boldsymbol{G}}_{\boldsymbol{ee}}(\boldsymbol{r}, \boldsymbol{r}') = -j\omega\overline{\boldsymbol{I}}\delta(\boldsymbol{r}-\boldsymbol{r}') \tag{4.8a}$$

$$\overline{\boldsymbol{L}}_{\boldsymbol{m}} \cdot \overline{\boldsymbol{G}}_{\boldsymbol{me}}(\boldsymbol{r}, \boldsymbol{r}') = (\nabla \times \overline{\boldsymbol{I}}) \cdot \overline{\boldsymbol{\epsilon}}^{-\mathbf{1}}\delta(\boldsymbol{r}-\boldsymbol{r}') \tag{4.8b}$$

$$\overline{\boldsymbol{L}}_{\boldsymbol{e}} \cdot \overline{\boldsymbol{G}}_{\boldsymbol{em}}(\boldsymbol{r}, \boldsymbol{r}') = -(\nabla \times \overline{\boldsymbol{I}}) \cdot \overline{\boldsymbol{\mu}}^{-\mathbf{1}} \delta(\boldsymbol{r} - \boldsymbol{r}') \tag{4.8c}$$

$$\overline{\boldsymbol{L}}_{\boldsymbol{m}} \cdot \overline{\boldsymbol{G}}_{\boldsymbol{mm}}(\boldsymbol{r}, \boldsymbol{r}') = -j\omega\overline{\boldsymbol{I}} \delta(\boldsymbol{r} - \boldsymbol{r}') \tag{4.8d}$$

with the differential operators $\overline{\boldsymbol{L}}_{\boldsymbol{e}}$ and $\overline{\boldsymbol{L}}_{\boldsymbol{m}}$, which are

$$\overline{\boldsymbol{L}}_{\boldsymbol{e}} = (\nabla \times \overline{\boldsymbol{I}}) \cdot \overline{\boldsymbol{\mu}}^{-\mathbf{1}} \cdot (\nabla \times \overline{\boldsymbol{I}}) - \omega^2 \overline{\boldsymbol{\epsilon}}$$

$$\overline{\boldsymbol{L}}_{\boldsymbol{m}} = (\nabla \times \overline{\boldsymbol{I}}) \cdot \overline{\boldsymbol{\epsilon}}^{-\mathbf{1}} \cdot (\nabla \times \overline{\boldsymbol{I}}) - \omega^2 \overline{\boldsymbol{\mu}}$$

To solve equation 4.8 is difficult and complicated, and pursing the solution for it is beyond the scope of this thesis. Several techniques have been introduced in [53, 54, 151–156] for the solution of equation 4.8. The solution for the dyadic uniaxial Green's functions in the global coordinates reads [53]:

$$\overline{\boldsymbol{G}}_{\boldsymbol{ee}} = -j\omega\mu_1(\epsilon_2\overline{\boldsymbol{\epsilon}}^{-1} + \frac{\nabla\nabla}{k_u^2})g_e + j\omega\mu_1\overline{\boldsymbol{T}} \tag{4.9a}$$

$$\begin{aligned}\overline{\boldsymbol{G}}_{\boldsymbol{me}} = (g_e - g_m)(\boldsymbol{R} \cdot \hat{\boldsymbol{c}})\frac{[\hat{\boldsymbol{c}} \times \boldsymbol{R}_{\boldsymbol{c}}]\boldsymbol{R}_{\boldsymbol{c}} + \boldsymbol{R}_{\boldsymbol{c}}[\hat{\boldsymbol{c}} \times \boldsymbol{R}_{\boldsymbol{c}}]}{|\boldsymbol{R}_{\boldsymbol{c}}|^4} \\ + \frac{(1 + jk_uR_e)\epsilon_2 g_e}{\epsilon_1 R_e^2}\frac{\boldsymbol{R}_{\boldsymbol{c}}[\boldsymbol{R} \times \boldsymbol{R}_{\boldsymbol{c}}]}{|\boldsymbol{R}_{\boldsymbol{c}}|^2} \\ - \frac{(1 + jk_uR_m)\mu_2 g_m}{\mu_1 R_m^2}\frac{[\boldsymbol{R} \times \boldsymbol{R}_{\boldsymbol{c}}]\boldsymbol{R}_{\boldsymbol{c}}}{|\boldsymbol{R}_{\boldsymbol{c}}|^2}\end{aligned} \tag{4.9b}$$

$$\overline{\boldsymbol{G}}_{\boldsymbol{mm}} = -j\omega\epsilon_1(\mu_2\overline{\boldsymbol{\mu}}^{-1} + \frac{\nabla\nabla}{k_u^2})g_m - j\omega\epsilon_1\overline{\boldsymbol{T}} \tag{4.9c}$$

$$\overline{\boldsymbol{G}}_{\boldsymbol{em}} = \overline{\boldsymbol{G}}_{\boldsymbol{me}}^T \tag{4.9d}$$

with

$$k_u = \omega\sqrt{\epsilon_1\mu_1}, \quad \boldsymbol{R}_{\boldsymbol{c}} = \boldsymbol{R} \times \hat{\boldsymbol{c}}, \quad g_e = \frac{e^{-jk_uR_e}}{4\pi R_e}, \quad g_m = \frac{e^{-jk_uR_m}}{4\pi R_m}$$

$$R_e = \sqrt{\epsilon_2\boldsymbol{R} \cdot \overline{\boldsymbol{\epsilon}}^{-1} \cdot \boldsymbol{R}}, \quad R_m = \sqrt{\mu_2\boldsymbol{R} \cdot \overline{\boldsymbol{\mu}}^{-1} \cdot \boldsymbol{R}}$$

$$\overline{\boldsymbol{T}} = (\frac{\epsilon_2}{\epsilon_1}g_e - \frac{\mu_2}{\mu_1}g_m)\frac{\boldsymbol{R}_{\boldsymbol{c}}\boldsymbol{R}_{\boldsymbol{c}}}{|\boldsymbol{R}_{\boldsymbol{c}}|^2} + (\hat{\boldsymbol{u}}\hat{\boldsymbol{u}} + \hat{\boldsymbol{v}}\hat{\boldsymbol{v}} - \frac{2\boldsymbol{R}_{\boldsymbol{c}}\boldsymbol{R}_{\boldsymbol{c}}}{|\boldsymbol{R}_{\boldsymbol{c}}|^2})\frac{j(R_eg_e - R_mg_m)}{k_u|\boldsymbol{R}_{\boldsymbol{c}}|^2}$$

If we substitute $\overline{\boldsymbol{\epsilon}}$=$\epsilon\overline{\boldsymbol{I}}$ and $\overline{\boldsymbol{\mu}}$=$\mu\overline{\boldsymbol{I}}$ into equation 4.9, the dyadic Green's functions for the isotropic material (characterized by the permittivity ϵ and permeability μ) read

$$\overline{\boldsymbol{G}}_{\boldsymbol{ee}} = -j\omega\mu(\overline{\boldsymbol{I}} + \frac{\nabla\nabla}{k^2})\frac{e^{-jkR}}{4\pi R} \tag{4.10a}$$

$$\overline{\boldsymbol{G}}_{\boldsymbol{me}} = -(1+jkR)\frac{e^{-jkR}}{4\pi R^3}(\boldsymbol{R}\times\overline{\boldsymbol{I}}) \tag{4.10b}$$

$$\overline{\boldsymbol{G}}_{\boldsymbol{mm}} = (\epsilon/\mu)\overline{\boldsymbol{G}}_{\boldsymbol{ee}} \tag{4.10c}$$

$$\overline{\boldsymbol{G}}_{\boldsymbol{em}} = -\overline{\boldsymbol{G}}_{\boldsymbol{me}} \tag{4.10d}$$

with

$$\boldsymbol{R} = \boldsymbol{r} - \boldsymbol{r}', \quad R = |\boldsymbol{R}|$$

where $\boldsymbol{r}'$ and $\boldsymbol{r}$ are the locations of the source and observation points, respectively. The term $\overline{\boldsymbol{I}}$ is the identity dyad defined in global coordinates. With the help of the dyadic Green's functions of the uniaxial materials, the formulation of scattering evaluations from a uniaxial object using the proposed MIDM is ready to be introduced. Though we only focus on the uniaxial material, the proposed MIDM can also be applied to other kinds of anisotropic materials as long as the corresponding dyadic Green's functions are available.

4.2 Problem formulation for an object with a smooth boundary

The geometry of a smooth boundary problem is illustrated in Fig. 4.2. Two regions are presented, the outer region 1 is free space and the inner region 2 is occupied by an homogeneous uniaxial material characterized by (4.1). The concept of the MIDM is illustrated in Fig. 4.3. We place a set of infinitesimal dipole doublets (IDDs) in regions 1 and 2. Each IDD contains two co-located orthogonal polarized infinitesimal dipoles, namely point sources. The formulation of the proposed MIDM is conducted through two equivalences. Firstly, the scattered fields in the region 1 are generated by equivalent IDDs placed in the region 2, and those point sources are treated as source currents radiating in unbounded vacuum. Secondly, the scattered fields in region 2 are generated by equivalent IDDs placed in the region 1, and those point sources are radiating in unbounded space filled with an homogeneous uniaxial material identical to that constituting the scatterer.

4.2.1 Fields Expressions in Regions 1 And 2

Region 1, considered as free space, contains the incident ($\boldsymbol{E_{inc}}$, $\boldsymbol{H_{inc}}$) and the scattered fields ($\boldsymbol{E_1^s}$, $\boldsymbol{H_1^s}$). If the incident fields are those of a plane wave, they can be written as:

$$\boldsymbol{E_{inc}} = \hat{\boldsymbol{p}}e^{-jk(x\sin\theta_{inc}\cos\varphi_{inc}+y\sin\theta_{inc}\sin\varphi_{inc}+z\cos\theta_{inc})} \tag{4.11a}$$

$$\boldsymbol{H_{inc}} = \frac{1}{\eta_0}\hat{\boldsymbol{k}}\times\boldsymbol{E_{inc}} \tag{4.11b}$$

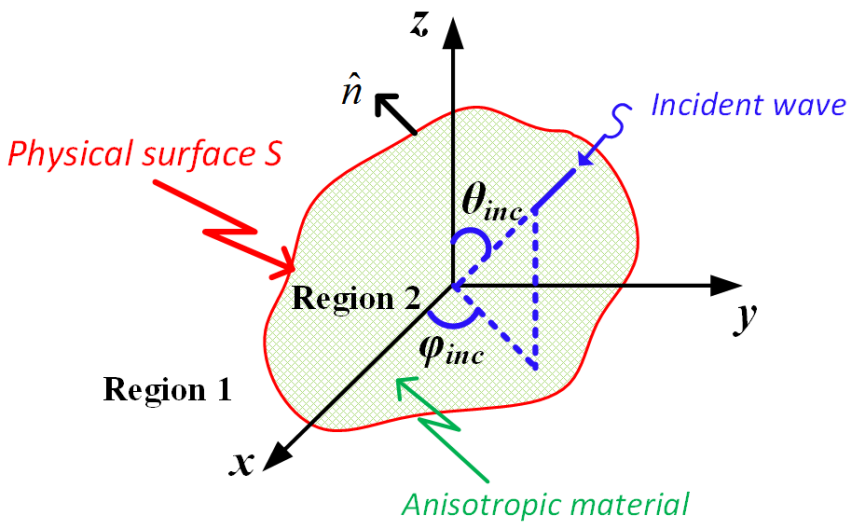

Figure 4.2 Geometry of the problem.

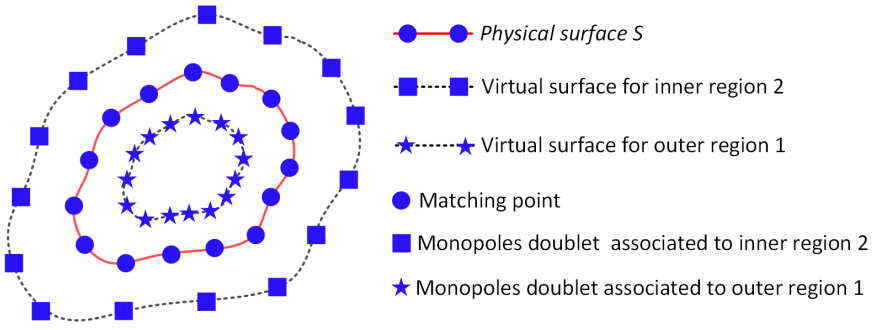

Figure 4.3 The concept of the MIDM.

where $\hat{\boldsymbol{p}}$ is the polarization direction of the incident electric field, and $\hat{\boldsymbol{k}}$ is the normalized wave vector. The scattered fields could be evaluated in a simple manner and expressed in terms of the dyadic Green's functions. So the total fields ($\boldsymbol{E_1}$, $\boldsymbol{H_1}$) could be expressed as:

$$\boldsymbol{E_1} = \boldsymbol{E_{inc}} + \sum_{i=1}^{N_1} \overline{\boldsymbol{G}}_{\boldsymbol{ee}}^{\boldsymbol{1}} \cdot (\boldsymbol{J}_{\boldsymbol{i1}}^{\boldsymbol{1}}(\boldsymbol{r}') + \boldsymbol{J}_{\boldsymbol{i2}}^{\boldsymbol{1}}(\boldsymbol{r}')) \tag{4.12a}$$

$$\boldsymbol{H_1} = \boldsymbol{H_{inc}} + \sum_{i=1}^{N_1} \overline{\boldsymbol{G}}_{\boldsymbol{me}}^{\boldsymbol{1}} \cdot (\boldsymbol{J}_{\boldsymbol{i1}}^{\boldsymbol{1}}(\boldsymbol{r}') + \boldsymbol{J}_{\boldsymbol{i2}}^{\boldsymbol{1}}(\boldsymbol{r}')) \tag{4.12b}$$

where $\boldsymbol{J}_{\boldsymbol{i1}}^{\boldsymbol{1}}$ and $\boldsymbol{J}_{\boldsymbol{i2}}^{\boldsymbol{1}}$ are the two orthogonal electric point sources in the ith IDD associated to the region 1. It has been proven in [157] that using two orthogonal electric point sources, i.e. IDD, is efficient to handle the scatterer with a smooth boundary, yet using three orthogonal electric point sources, i.e. infinitesimal dipole triplets (IDT), could be more general to deal with a scatterer with/without a smooth boundary. The IDD is used in this section whereas the IDT will be deployed in Sec. 4.3 and Chap. 5. Noticing that one electric and one magnetic or two magnetic point sources can also be deployed in each IDD, and dyadic Green's functions ($\overline{\boldsymbol{G}}_{\boldsymbol{em}}$ and $\overline{\boldsymbol{G}}_{\boldsymbol{mm}}$) are then required with respect to the magnetic point source. In (4.12), N_1 is the number of IDDs placed in the region 2. The two Green's functions, $\overline{\boldsymbol{G}}_{\boldsymbol{ee}}^{\boldsymbol{1}}$ and $\overline{\boldsymbol{G}}_{\boldsymbol{me}}^{\boldsymbol{1}}$, in (4.12) are the dyadic Green's functions of isotropic materials, corresponding to the electric and magnetic fields radiated into the region 1 by an electric point source, which are presented in (4.10).

The region 2 only contains the scattered fields generated by the IDDs placed outside of it, and the expressions of fields read

$$\boldsymbol{E}_{\boldsymbol{2}}^{\boldsymbol{s}} = \sum_{i=1}^{N_2} \overline{\boldsymbol{G}}_{\boldsymbol{ee}}^{\boldsymbol{2}} \cdot (\boldsymbol{J}_{\boldsymbol{i1}}^{\boldsymbol{2}}(\boldsymbol{r}') + \boldsymbol{J}_{\boldsymbol{i2}}^{\boldsymbol{2}}(\boldsymbol{r}')) \tag{4.13a}$$

$$\boldsymbol{H}_{\boldsymbol{2}}^{\boldsymbol{s}} = \sum_{i=1}^{N_2} \overline{\boldsymbol{G}}_{\boldsymbol{me}}^{\boldsymbol{2}} \cdot (\boldsymbol{J}_{\boldsymbol{i1}}^{\boldsymbol{2}}(\boldsymbol{r}') + \boldsymbol{J}_{\boldsymbol{i2}}^{\boldsymbol{2}}(\boldsymbol{r}')) \tag{4.13b}$$

where $\boldsymbol{J}_{\boldsymbol{i1}}^{\boldsymbol{2}}$ and $\boldsymbol{J}_{\boldsymbol{i2}}^{\boldsymbol{2}}$ are the two orthogonal electric point sources in the ith IDD associated to the region 2. N_2 is the number of IDDs placed in the region 1. Since region 2 is occupied by the uniaxial material, the two Green's functions, $\overline{\boldsymbol{G}}_{\boldsymbol{ee}}^{\boldsymbol{2}}$ and $\overline{\boldsymbol{G}}_{\boldsymbol{me}}^{\boldsymbol{2}}$, in (4.13) are the uniaxial dyadic Green's functions, corresponding to the electric and magnetic fields radiated into the region 2 by an electric point source, which are presented in (4.9).

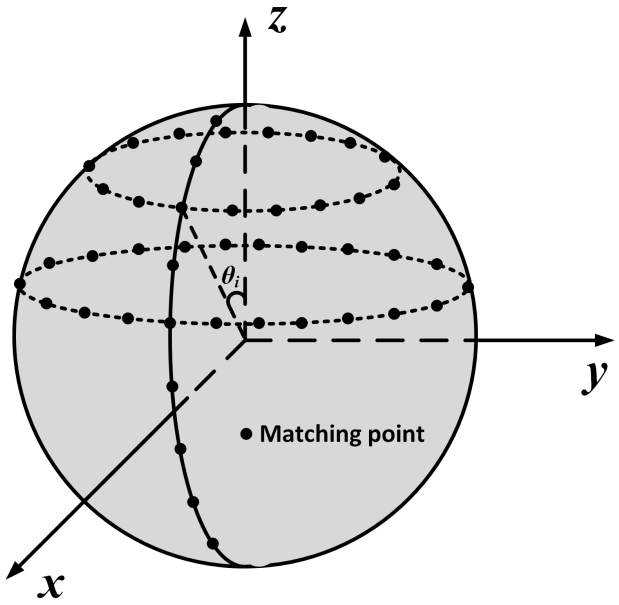

Figure 4.4 The strategy of matching points placement for a spherical object.

4.2.2 Placements of matching points and sources

For an object with a smooth boundary, the matching points could be distributed as uniformly as possible on the surface of a scatterer. However, non-uniform placement also works well for structures with a smooth boundary. Taking a spherical shape depicted in Fig. 4.4 as an example, we can evenly distribute N_{m1} points along the θ direction firstly, and then a latitudinal closed circle of radius $r_a \sin\theta_I$ is constructed with respect to the ith point on the θ direction. The matching points are then uniformly placed on each closed circle in terms of the samples per wavelength (SPW). Specifically, the total number of matching points (N_m) is given as

$$N_m = \sum_{i=1}^{N_{m1}} \lceil \frac{2\pi r_a \sin\theta_i SPW}{\lambda} \rceil \tag{4.14}$$

with

$$\theta_i = \frac{(i-1)\pi}{N_{m1}-1}$$

where r_a is the radius of the sphere, and λ is the wavelength of the incident wave. The $\lceil\ \rceil$ symbol represents the ceiling function used to obtain an integer value.

For the placement of the sources, the IDDs are placed on closed virtual smooth surfaces which are some distance away from the smooth physical surface. The placement should be

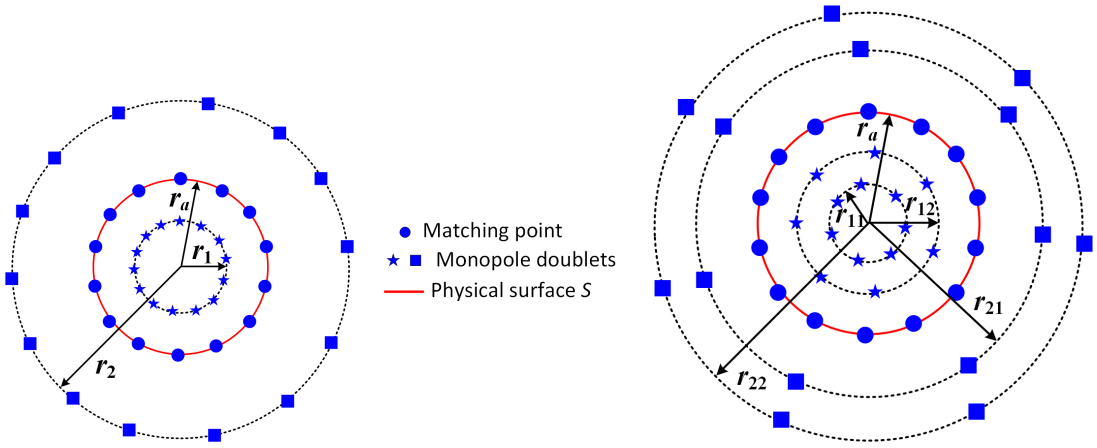

(a) (b)

Figure 4.5 The strategies of sources placement for a spherical object. (a) Single-layered and (b) double-layered.

as uniform as possible. The orientations of the two point sources inside the IDD are set to be parallel to the virtual surface in order to have a fast convergence. Two strategies are used for the placements of IDDs. One is the traditional single-layered distribution used in [157], and the other is the proposed double-layered distribution. Taking the spherical shape as an example, the single-layered scheme is performed by placing a set of IDDs on a closed spherical surface with radius r_1 in the region 2 whereas with radius r_2 in the region 1, as shown in Fig. 4.5(a). We can set $r_1 = 0.2r_a$ and $r_2 = 2.0r_a$ as referred from [157] where only isotropic materials were considered. The distribution of the IDDs on the surface should be as uniform as possible. A convenient way to achieve the "uniform" criteria for a spherical object is to project the location parameters (azimuthal angle and polar angle) of each matching point to the surfaces where the IDDs are placed. Therefore the total number of IDDs (N_s) per region is expressed as

$$N_s = \sum_{i=1}^{N_{m1}} \lceil \frac{2\pi r_a \sin\theta_i SPW}{\lambda} \rceil \tag{4.15}$$

The numbers of matching points and IDDs per region are equal in this scenario.

The proposed double-layered scheme is performed by placing the IDDs on two closed spherical surfaces with radii r_{11} and r_{12} in the region 2 whereas with radii r_{21} and r_{22} in the region 1, as shown in Fig. 4.5(b). The determinations of the four radii are given as

$$r_{11} = \frac{r_a^2}{\lambda + r_a} \tag{4.16a}$$

$$r_{12} = 0.5 * r_{11} \tag{4.16b}$$

$$r_{21} = 2r_a - r_{11} \tag{4.16c}$$

$$r_{22} = 2r_a - r_{12} \tag{4.16d}$$

The surfaces with radii r_{11} and r_{21} are closer to the physical surface than those with radii r_{12} and r_{22}. In order to avoid positioning the IDDs too close to (r_{11} and r_{21} approach r_a) or too far away from (r_{12} is much smaller than r_a) the physical surface when a relatively large or small object is encountered, we set upper and lower limits as $r_{11}^{max} = 0.95r_a$, $r_{12}^{min} = 0.15r_a$, $r_{21}^{min} = 1.2$ and $r_{22}^{min} = 1.6$. The strategy in (4.16) is proposed for the case of a spherical scatterer. In the case of other smoothly curved structures, r_a should be replaced with the local radius of curvature. The proposed *adhoc* rule is suitable for an object with the size ranging from $0.2\lambda \times 0.2\lambda$ to $4\lambda \times 4\lambda$. The distribution of IDDs on each closed surface also should be as uniform as possible, and a strategy for the uniform placement is given as

$$N_s = 2\sum_{i=1}^{N_{s1}} \lceil N_{max} - (N_{max} - N_{min})|1.3\cos\theta_{is}| \rceil \tag{4.17}$$

with

$$\theta_{is} = \frac{(i-1)\pi}{N_{s1} - 1}$$

where N_{s1} and θ_{is} have the same relationships with N_{m1} and θ_i in (4.14), respectively. The number 1.3 in (4.17) is obtained after trying several cases and found to be an optimised value for the placement of sources. N_s is the total number of IDDs per region. For the convenience, the number of IDDs per region can be set equal, i.e. $N_1 = N_2 = N_s$. N_{max} and N_{min} are the coefficients used to adjust the distribution density of IDDs. $N_{max} = 3.0N_{s1}$ and $N_{min} = 1.0N_{s1}$ are utilized in our numerical examples. It is convenient but not mandatory to use the same angular positions (azimuthal angle and polar angle) of the IDDs on each layer.

4.3 Problem formulation for an object with sharp edges

We can consider a cylinder of finite length as an example to illustrate the formulation of an object with sharp edges. The proposed strategy for a cylinder also can be straightforwardly applied to other geometries where sharp edges are involved. The geometry of a problem is illustrated in Fig. 4.6, as before, two regions are presented. The outer region 1 is free space and the inner region 2 is occupied by an homogeneous uniaxial material characterized by (4.1). Instead of placing a set of IDDs in regions 1 and 2 as was done in Sec. 4.2, a set of infinitesimal dipole triplets (IDTs) are utilized this time. Each IDT contains three co-located orthogonal polarized infinitesimal dipoles, namely point sources. Definitely, the IDTs can also

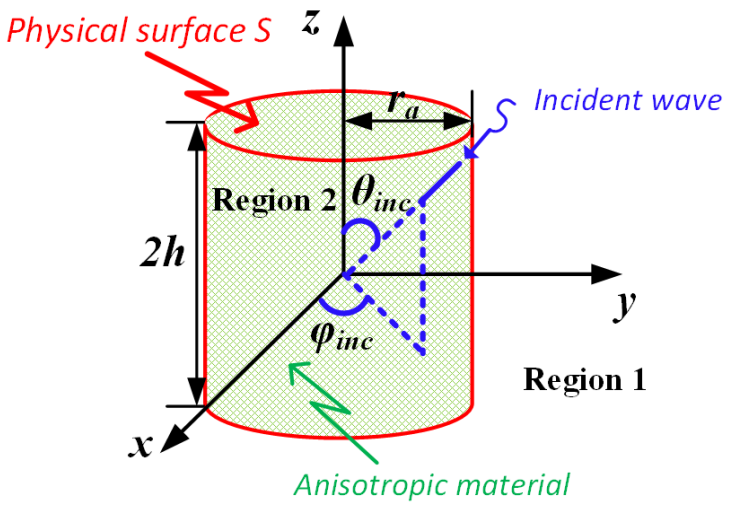

Figure 4.6 Problem description for an anisotropic cylinder.

be used for case where a smooth boundary is considered, and it is found that performances of simulation using the IDTs and IDDs are almost the same. The scattered fields from equivalent sources expressed in (4.12) and (4.13) require a modification when IDTs are deployed, and read

$$\boldsymbol{E}^{\boldsymbol{s}} = \sum_{i=1}^{N} \overline{\boldsymbol{G}}_{\boldsymbol{ee}} \cdot (\boldsymbol{J}_{\boldsymbol{i1}}(\boldsymbol{r}') + \boldsymbol{J}_{\boldsymbol{i2}}(\boldsymbol{r}') + \boldsymbol{J}_{\boldsymbol{i3}}(\boldsymbol{r}')) \tag{4.18a}$$

$$\boldsymbol{H}^{\boldsymbol{s}} = \sum_{i=1}^{N} \overline{\boldsymbol{G}}_{\boldsymbol{me}} \cdot (\boldsymbol{J}_{\boldsymbol{i1}}(\boldsymbol{r}') + \boldsymbol{J}_{\boldsymbol{i2}}(\boldsymbol{r}') + \boldsymbol{J}_{\boldsymbol{i3}}(\boldsymbol{r}')) \tag{4.18b}$$

where $\boldsymbol{E}(\boldsymbol{H})^{\boldsymbol{s}}$ are the scattered fields generated by N IDTs. $\boldsymbol{J}_{\boldsymbol{i1}}$, $\boldsymbol{J}_{\boldsymbol{i2}}$ and $\boldsymbol{J}_{\boldsymbol{i3}}$ are the three co-located orthogonal polarized infinitesimal dipoles. $\overline{\boldsymbol{G}}_{\boldsymbol{ee}}$ and $\overline{\boldsymbol{G}}_{\boldsymbol{me}}$ are the dyadic Green's functions with respect to the investigated region.

4.3.1 Placement of matching points

According to the experience of a 2D scenario where sharp edges are encountered as discussed in Sec. 2.2.3, more matching points are required near the edges in order to capture the fast variation behavior of the fields. A simple way to place the matching point is to make use of the RWG mesh [150] information which could be exported directly from the commercial software. Fig. 4.7(a) shows a cylinder which is adaptively meshed with the RWG basis functions in the commercial software FEKO [132]. The mesh size in FEKO is defined with respect to the triangle edge length (TEL). Two different mesh sizes can be applied on one object in FEKO in order to have an adaptive mesh on the physical surface of an investigated scatterer.

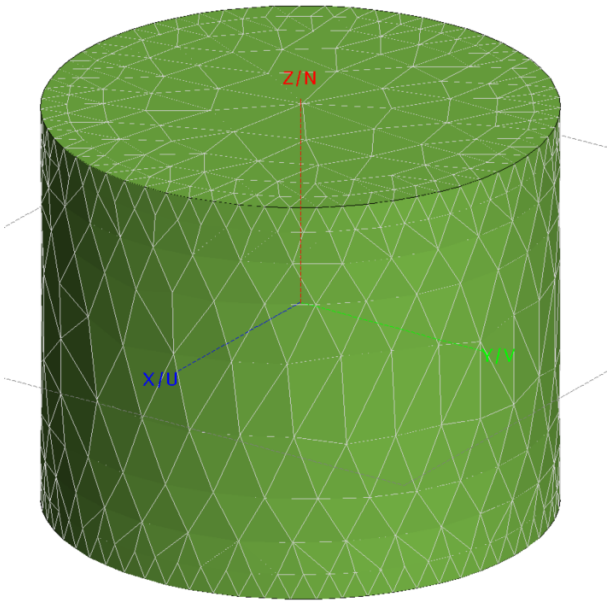

(a)

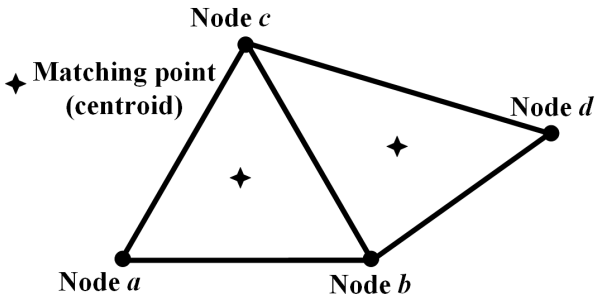

(b)

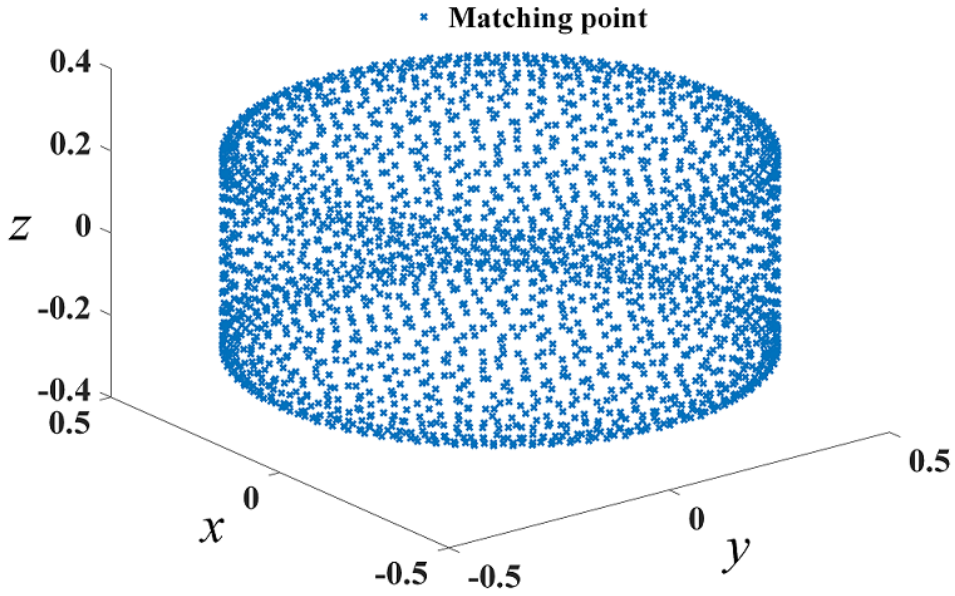

(c)

Figure 4.7 (a) RWG adaptive mesh for a cylinder in the commercial software FEKO. (b) The triangle patches generated by the RWG mesh. (c) Placement of matching points for a cylinder with $r_a = 0.5\lambda$ and $h = 0.25\lambda$. (λ=1 m, TELe=0.035 and TELg=0.07 are set in FEKO to generate adaptive RWG mesh).

One is called local mesh size (TELe), which is used to apply on the area where a finer mesh is required, such as the edge of a cylinder, and the other one is called is global mesh size (TELg), which is used to apply on the remaining part of the physical surface, such as the top, bottom and side curved surfaces of a cylinder. In our numerical examples, we set the local mesh size to be half of the global one and therefore a finer mesh is conducted near edges. The exported mesh file from FEKO contains the geometric information of triangle patches and nodes. The matching points are subsequently placed at the centroid of each triangle patch as shown in Fig. 4.7(b), and their locations can be determined easily from the nodes information exported from FEKO. In Fig. 4.7(c), the placement of matching points according to the introduced strategy is displayed for a cylinder with a radius $r_a = 0.5\lambda$ and height $2h = 0.5\lambda$ (λ=1 m). The TELe and TELg are set as 0.035 and 0.07, respectively, in FEKO to generate the adaptive RWG mesh. It is clearly seen that a finer mesh is constructed around the edge according to the proposed scheme.

An important practical strategy regarding the point matching technique for nonuniform sampling of testing points is to weigh the fields evaluated in (4.18) by an area. This is considered as using an approximated pulse by the middle-point testing function instead of pure testing points. Therefore, a more practical solution is prefered to use $\boldsymbol{E}(\boldsymbol{H})(r_i) \cdot A_i$ rather than just $\boldsymbol{E}(\boldsymbol{H})(r_i)$ in (4.18), where r_i is the distance between the source and the centroid of the ith patch and A_i is the area of the ith triangle patch, which can be easily calculated from the information of the RWG mesh.

4.3.2 Placement of sources

The placement of sources is conducted through two steps. Firstly, we uniformly place the sources on the surfaces which are obtained by scaling the physical surface to the inner and outer regions of a scatterer with respect to the samples per wavelength (SPW). Double-layered and single-layered distribution strategies for equivalent sources are considered in this scenario. Secondly, we place additional sources near the edge in order to better approximate the singular fields behaviors around edge areas.

For the uniform placement in the first step, we initially determine points on the physical surface with respect to $SPWs$ and $SPWd$, where $SPWs$ corresponds to single-layered whereas $SPWd$ corresponds to double-layered distributions of sources, respectively. Then, the locations of these points are moved to the inner and outer surfaces by defining scaling parameters. One IDT is placed at each point. For the top and bottom faces of the cylinder, we define a

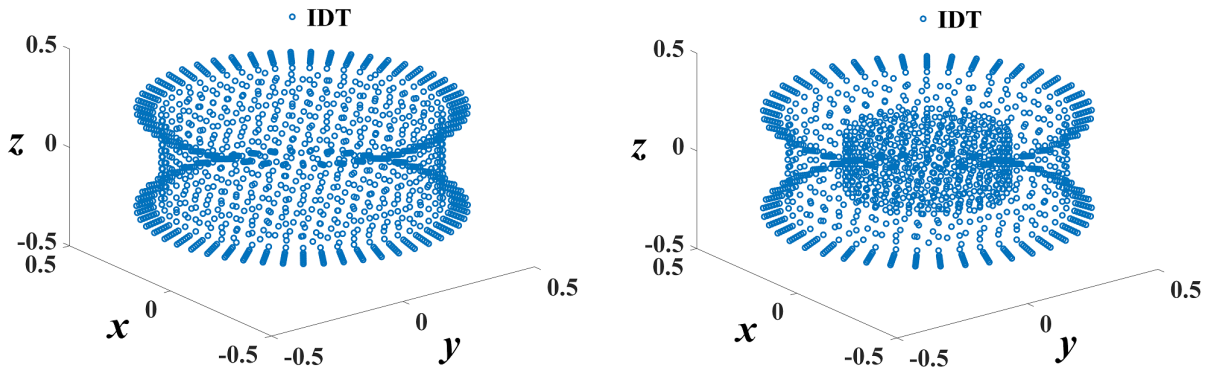

(a) (b)

Figure 4.8 Inside sources placements of (a) single-layered and (b) double-layered schemes for a cylinder with $r_a = 0.5\lambda$ and $h = 0.25\lambda$. (λ=1 m, $SPWs$=16 and $SPWd$=13 are set to generate the placement. $S_1 = 0.85$ for single-layered strategy and $S_{11} = 0.5$ and $S_{12} = 0.85$ for double-layered one).

parameter N_a regarding the SPW as

$$N_a = \lceil \frac{2r_a SPWs(d)}{\lambda} \rceil \tag{4.19}$$

where r_a is the radius of the cylinder and λ is the incident wavelength. $\lceil\rceil$ symbol represents the ceiling function used to obtain an integer value. There are several ways to uniformly place points on the top and bottom surfaces, and one strategy used herein consists of considering a square area in the $z = h$ plane (top face) or $z = -h$ plane (bottom face) defined by $x \in [-r_a, r_a]$ and $y \in [-r_a, r_a]$ and grided with N_a points in each dimension. Each grid node is then tested and stored once it is located within a circular area defined by $r = r_a - r_a/(N_a - 1)$ in the $z = h$ or $z = -h$ planes. Finally, a number of points, recorded as N_{s1}, are uniformly located on the top and bottom faces of the cylinder. For the side of the cylinder, we define a parameter N_b as

$$N_b = \lceil \frac{2hSPW_{s(d)}}{\lambda} \rceil \tag{4.20}$$

where $2h$ is the height of the cylinder. The height of the cylinder is then grided with N_b points evenly, and at each height, $\lceil 2\pi r_a SPWs(d)/\lambda \rceil$ points are placed on the side face of the cylinder. Finally, a number of points, recorded as N_{s2}, are uniformly located on the side face of the cylinder. The total number, $N_{uni} = N_{s1} + N_{s2}$, of points are finally generated uniformly on the surface of the cylinder.

The scaling parameters are subsequently defined in order to move these points determined

on the physical surface to the inner and outer regions of the scatterer. For single-layered distribution of sources, two parameters S_1 ($S_1 < 1$) and S_2 ($S_2 > 1$) are defined to move the determined points to the inner and outer regions of a scatterer, respectively. It is found that the selections of S_1 in the range (0.75∼0.85) and S_2 in the range (2.0∼4.0) can generate a stable solution with fast convergence. In our numerical examples, $S_1 = 0.85$ and $S_2 = 2$ are selected for the scattering simulation of an anisotropic cylinder. As for the double-layered distribution of sources, four parameters S_{11}, S_{12}, S_{21} and S_{22} are defined. S_{11} and S_{12}, both smaller than 1, are used to move the points to the inner region of a scatterer whereas S_{21} and S_{22}, both larger than 1, are used to move the points to the outer region. Also, the selections of S_{11}, S_{12} in the range (0.75∼0.85) and S_{21}, S_{22} in the range (2.0∼4.0) can generate a stable solution with fast convergence. In our numerical examples, $S_{11} = 0.75$, $S_{12} = 0.85$, $S_{21} = 2.0$ and $S_{22} = 3.0$ are selected for scattering simulations.

Additional sources are required to be placed near edges in order to capture the fast variation of fields around the edge. Two edges are presented in the cylinder geometry. A number of points are generated on the edge with respect to the $SPWs(d)$ firstly and are subsequently scaled to the inner and outer regions of the scatterer. To better approximate the physical phenomenon, these points are scaled to multiple layers with different scale parameters. Placing additional 5 to 10 layered sources around the edge gave a better simulated performance, and 7 layers are selected in our numerical examples. The scale parameters of the 7 layers are linearly selected in the range (0.9∼0.999) for the inner region and range (1.001∼1.10) for the outer region. In this case, a set of additional sources, recorded as N_{add}, are placed around the sharp edge. Fig. 4.8 shows the placement of inside sources according to the introduced strategy for a cylinder with a radius $r_a = 0.5\lambda$ and height $2h = 0.5\lambda$ (λ=1 m). The single-layered and double-layered schemes are displayed in Fig. 4.8(a) and 4.8(b), respectively. In order to make the double-layered placement clear to see, we have set $S_{11} = 0.5$ to generate the figure. The two-step placement of IDTs are clearly conducted as shown in Fig. 4.8.

In conclusion, the placement of matching point is determined by making use of the RWG mesh in commercial software package for an object with sharp edges. Two parameters, local mesh size (TELe) and global mesh size(TELg), are used to control the density and nonconformity of the placement. The numbers of IDTs uniformly and non-uniformly placed are designed to relate only one parameter, the $SPWs(d)$, in the formulation process. The proposed strategies for the placements of matching points and sources are tested and found suitable for the size of a cylinder in the range $0.5 \leqslant r_a/h \leqslant 2$, where r_a could vary from 0.2λ to 1λ. For an object with edges but a different geometry, the proposed strategy also can be utilized straightforwardly.

4.4 Boundary conditions, singularities in using dyadic Green's functions and convergence study

4.4.1 Boundary conditions

The connection between the fields in regions 1 and 2 is dictated by the boundary conditions of surface S shown in Fig. 4.2 and 4.6. Specifically, the tangential components of electric and magnetic fields must be continuous along the physical boundary S, which leads to

$$\begin{aligned} \hat{\boldsymbol{n}} \times (\boldsymbol{E}_{inc} + \boldsymbol{E}_1^s) &= \hat{\boldsymbol{n}} \times \boldsymbol{E}_2^s \\ \hat{\boldsymbol{n}} \times (\boldsymbol{H}_{inc} + \boldsymbol{H}_1^s) &= \hat{\boldsymbol{n}} \times \boldsymbol{H}_2^s \end{aligned} \tag{4.21}$$

where $\hat{\boldsymbol{n}}$ is a unit vector normal to the physical surface S. A linear system is then created by imposing the boundary condition at a number of generated matching points on S. For the smooth boundary involved scenario where IDDs are deployed, the number of matching points (N_m) must satisfy the inequality

$$N_m \geqslant N_s \tag{4.22}$$

in order to determine the total unknown current coefficients, $2N_s$ per region, where N_s is the total number of IDDs in each region.

While for the sharp edges involved scenario where IDTs are deployed, the number of matching points (N_m) must satisfy the inequality

$$2N_m \geqslant 3N_s \tag{4.23}$$

in order to determine the total unknown current coefficients, $3N_s$ per region, where N_s is the total number of IDTs in each region.

Upon the application of a point-matching procedure, we will finally obtain a matrix expression of the type

$$[Q]\,\boldsymbol{X} = \boldsymbol{B} \tag{4.24}$$

where $\boldsymbol{X}$ is a column vector containing the unknown current coefficients, and $\boldsymbol{B}$ is another column vector containing samples of incident tangential fields at the matching points. $[Q]$ is a matrix whose entries are obtained from the tangential fields of sources at matching points, and it could be rectangular or square depending on whether oversampling is used or not. If it is in a square form, a unique solution can be found, otherwise the smallest least-square error

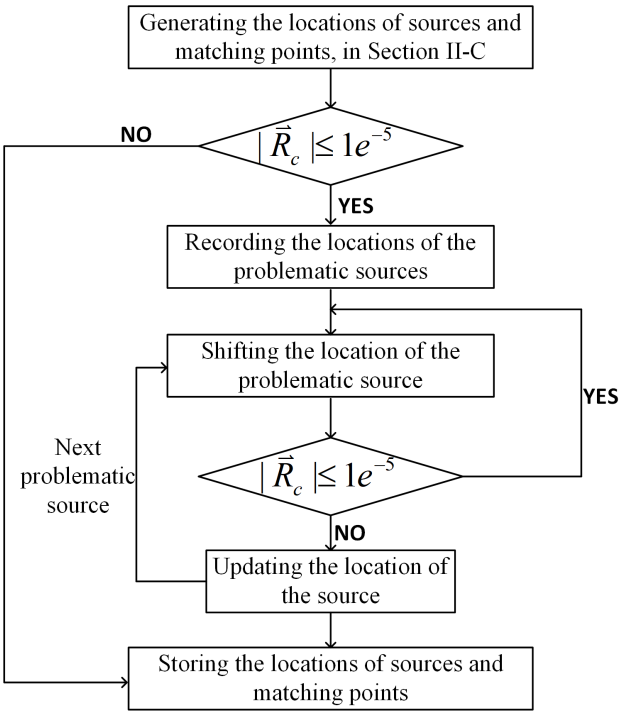

Figure 4.9 The proposed filtering strategy used to eliminate the singularity of the type $|\boldsymbol{R_c}| = 0$.

solution is pursued and known to be

$$\boldsymbol{X} = \left(\left[\tilde{Q}\right]^* [Q]\right)^{-1} \left[\tilde{Q}\right]^* \boldsymbol{B} \tag{4.25}$$

where $\left[\tilde{Q}\right]$ is the transpose of $[Q]$ and the asterisk denotes complex conjugate.

4.4.2 Singularities in using dyadic Green's functions

Two types of singularity issues usually appear when using the dyadic Green's functions. The first singularity issue is involved in both free space and uniaxial dyadic Green's functions when $|\boldsymbol{R}|$, the distance between source and matching points, is approaching zero. A special treatment on this issue should be considered in the VIE or SIE-based solution while this type of singularity is completely avoided in our case because the sources are placed at a certain distance away from the matching points. The other singularity appears in the usage of the uniaxial dyadic Green's functions when the term $|\boldsymbol{R_c}|$ vanishes, which occurs when $\boldsymbol{R}$ is parallel to the distinguished axis $\hat{\boldsymbol{c}}$. In this case, $\boldsymbol{R_c}/|\boldsymbol{R_c}|$ becomes undefined as can be seen from (4.9). A special treatment on this issue has been proposed in [48] for the SIE-based methodology. In our proposed method, once the locations of matching points and sources are generated as specified in Sec. 4.2 and 4.3, we implement a filtering strategy to firstly find

those locations of sources letting $\boldsymbol{R}$ to be parallel to $\hat{\boldsymbol{c}}$. Then we slightly shift the location of each problematic source. For the smooth boundary case, the location of each problematic source is shifted by adding $\theta_{is}/4$ to the azimuthal angle, where θ_{is} is defined in (4.17). For the sharp edges involved situation, each problematic source is moved $\lambda/(4SPWs(d))$ along x or y direction if the problematic source is on the top or bottom face of the cylinder, or along z direction if the problematic source is on the curved face of the cylinder. The flow chart of this singularity elimination strategy is shown in Fig. 4.9. This procedure handles the second type of singularity issue efficiently.

4.4.3 Convergence study

In order to study the convergence of results, we make use of the error on the imposed tangential boundary conditions as a metric, whose definitions read

$$\Delta E_{bc} = \frac{|\hat{n} \times (\boldsymbol{E}_1^s + \boldsymbol{E}_{inc} - \boldsymbol{E}_2^s)|}{|\boldsymbol{E}_{inc}|} \tag{4.26a}$$

$$\Delta H_{bc} = \frac{|\hat{n} \times (\boldsymbol{H}_1^s + \boldsymbol{H}_{inc} - \boldsymbol{E}_2^s)|}{|\boldsymbol{H}_{inc}|} \tag{4.26b}$$

where ΔE_{bc} and ΔH_{bc} are evaluated on the physical surface S, half away between the matching points used to solve (4.24). The necessary numbers of sources and matching points in the MIDM are increased until ΔE_{bc} and ΔH_{bc} reach the desired level of accuracy.

So far, all information has been presented for the linear system. Once the magnitudes of those infinitesimal dipoles are determined, the fields and related parameters of interest can be evaluated in a straightforward manner.

4.5 Computations of scattering analyses

Based on the numerical scheme described in the previous sections, a computer program has been implemented. The program computes the normalized bistatic radar cross section (RCS) (σ/λ^2) in xoz and yoz planes, defined as

$$\frac{\sigma}{\lambda^2} = \lim_{r\to\infty}(4\pi r^2 \frac{|E^s|^2}{\lambda^2 |E^i|^2}) \tag{4.27}$$

where $\boldsymbol{E^s}$ is the total scattered electric field in the region 1.

We take the sphere as a representation of the scenario where a smooth boundary is involved. N_{m1} which is defined in (4.14) and SPW are used to control the density of the matching

points. Increasing either of them leads to a finer mesh on the physical surface and a good boundary condition error response. In our numerical examples, 5 samples per wavelength (SPW=5) is fixed and an acceptable boundary condition error response is easily achieved by increasing the N_{m1}.

The finite length cylinder is considered as an application of the proposed method on a geometry with sharp edges. Parameters TELe and TELg are used to control the mesh density and result in nonuniform sampling points, and $SPWs(d)$ is used to control the number of IDTs, where $SPWs$ corresponds to the single-layered and $SPWd$ corresponds to the double-layered distributions of IDTs. In the simulation, the RWG mesh is firstly generated with respect to TELe and TELg, and the centroid of each triangle patch in the RWG mesh is selected as the location of a matching point. Subsequently, the number of sources, controlled by the $SPWs(d)$, is increased to a maximum value under the condition in (4.23). The increase step of $SPWs$ is set as 1 whereas the step of $SPWd$ is set as 0.5. Two sets of examples regarding the smoothness of the boundary are presented in the following sections.

4.5.1 Scattering from uniaxial spheres

The first example is a both electrically and magnetically uniaxial sphere with radius $r_a = 0.5\lambda$ illuminated by a plane wave with an unit magnitude of $\hat{\boldsymbol{x}}$ polarized electric field and propagating along the z axis. The uniaxial medium parameters are $\epsilon_1 = 2\epsilon_0$, $\epsilon_2 = 4\epsilon_0$, $\mu_1 = 3\mu_0$, $\mu_2 = 5\mu_0$. The distinguished axis $\hat{\boldsymbol{c}}$ is parallel to the z axis ($\theta_c = 0^\circ$) and $\varphi_c = 0^\circ$. The normalized bistatic RCS responses in xoz and yoz planes are shown in Fig. 4.10. The computed results of single-layered and double-layered distribution schemes are compared with the simulation results from commercial software HFSS [133] where the finite-elements method (FEM) is applied and FEKO [132] where the FDTD is applied. Excellent agreement can be observed. The details of the necessary numbers of matching points and IDDs are displayed in Table 4.1. N_{s1} is defined in (4.15) for the single-layered scheme whereas N_{s1} is

Table 4.1 The numbers of matching points and infinitesimal dipole doublets in single-layer and double-layer sources placement strategies.

	Single-layered	Double-layered
Fig. 4.10	$N_m = N_s = 626(N_{m1} = N_{s1} = 60)$	$N_m = 626, N_s = 602(N_{m1} = 60, N_{s1} = 15)$
Fig. 4.11(a) and 4.11(b)	$N_m = N_s = 708(N_{m1} = N_{s1} = 35)$	$N_m = 604, N_s = 602(N_{m1} = 30, N_{s1} = 15)$
Fig. 4.11(c)	$N_m = N_s = 604(N_{m1} = N_{s1} = 30)$	$N_m = 604, N_s = 602(N_{m1} = 30, N_{s1} = 15)$
Fig. 4.12(a) and 4.12(b)	$N_m = N_s = 2174(N_{m1} = N_{s1} = 54)$	$N_m = 2174, N_s = 1950(N_{m1} = 54, N_{s1} = 27)$
Fig. 4.12(c)	$N_m = N_s = 2582(N_{m1} = N_{s1} = 64)$	/
Fig. 4.15($r_b = 0.5\lambda$)	/	$N_m = 2516, N_s = 2272(N_{m1}^{S_1} = 2N_{s1}^{S_1} = 54, N_{m1}^{S_2} = 3N_{s1}^{S_2} = 33)$
Fig. 4.15($r_b = 1.0\lambda$)	/	$N_m = 2782, N_s = 2552(N_{m1}^{S_1} = 2N_{s1}^{S_1} = 54, N_{m1}^{S_2} = 2N_{s1}^{S_2} = 30)$
Fig. 4.15($r_b = 1.5\lambda$)	/	$N_m = 3188, N_s = 2720(N_{m1}^{S_1} = 2N_{s1}^{S_1} = 50, N_{m1}^{S_2} = 2N_{s1}^{S_2} = 32)$

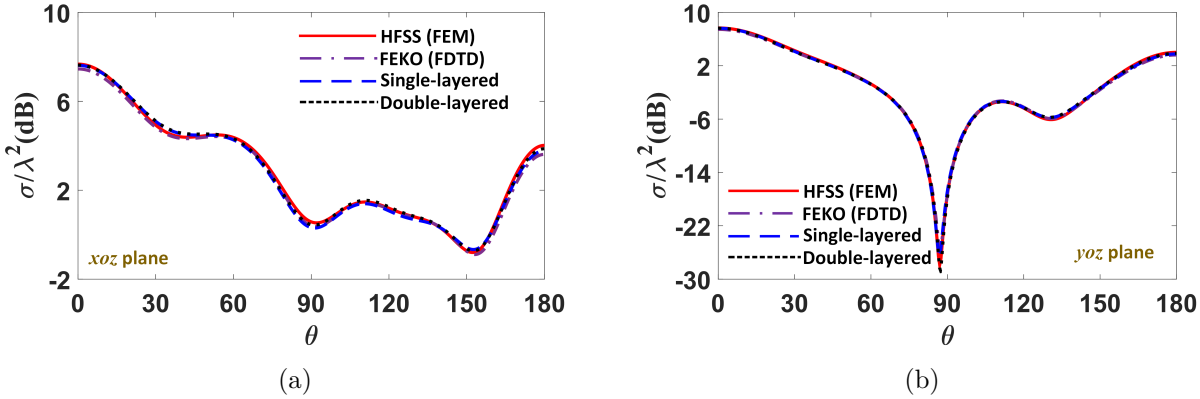

(a) (b)

Figure 4.10 Normalized bistatic RCS responses of a uniaxial sphere illuminated by a plane wave with $\hat{\boldsymbol{x}}$ polarized electric field propagating along the z axis in (a) xoz plane and (b) yoz plane. ($r_a = 0.5\lambda$, $\epsilon_1 = 2\epsilon_0, \epsilon_2 = 4\epsilon_0, \mu_1 = 3\mu_0, \mu_2 = 5\mu_0, \theta_c = 0^\circ, \varphi_c = 0^\circ$).

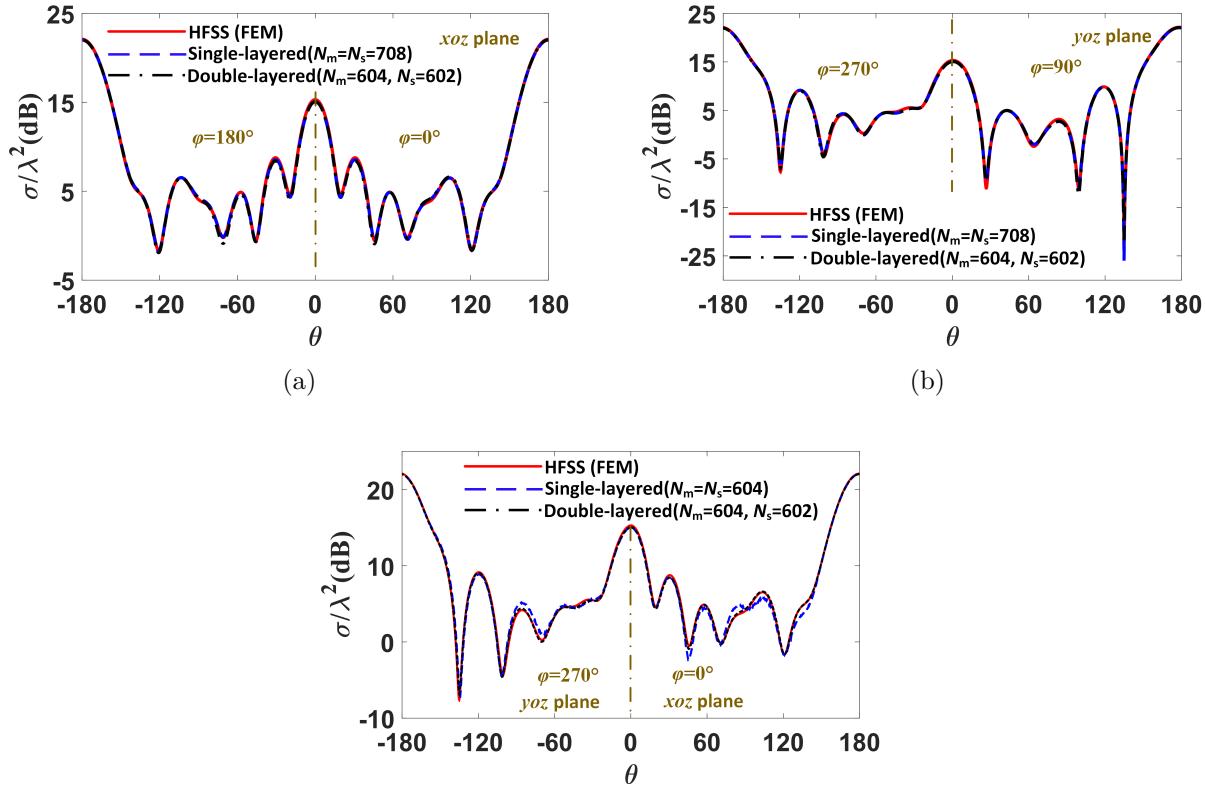

(a) (b)

(c)

Figure 4.11 Normalized bistatic RCS responses of a uniaxial sphere illuminated by a plane wave with $\hat{\boldsymbol{x}}$ polarized electric field propagating along the $-z$ axis in (a) xoz plane, (b) yoz plane and (c) both xoz and yoz planes whereas less numbers of matching points and IDDs of the single-layered scheme are used. ($r_a = 1\lambda$, $\epsilon_1 = 5\epsilon_0, \epsilon_2 = 9\epsilon_0, \mu_1 = \mu_2 = \mu_0, \theta_c = 45^\circ, \varphi_c = 90^\circ$).

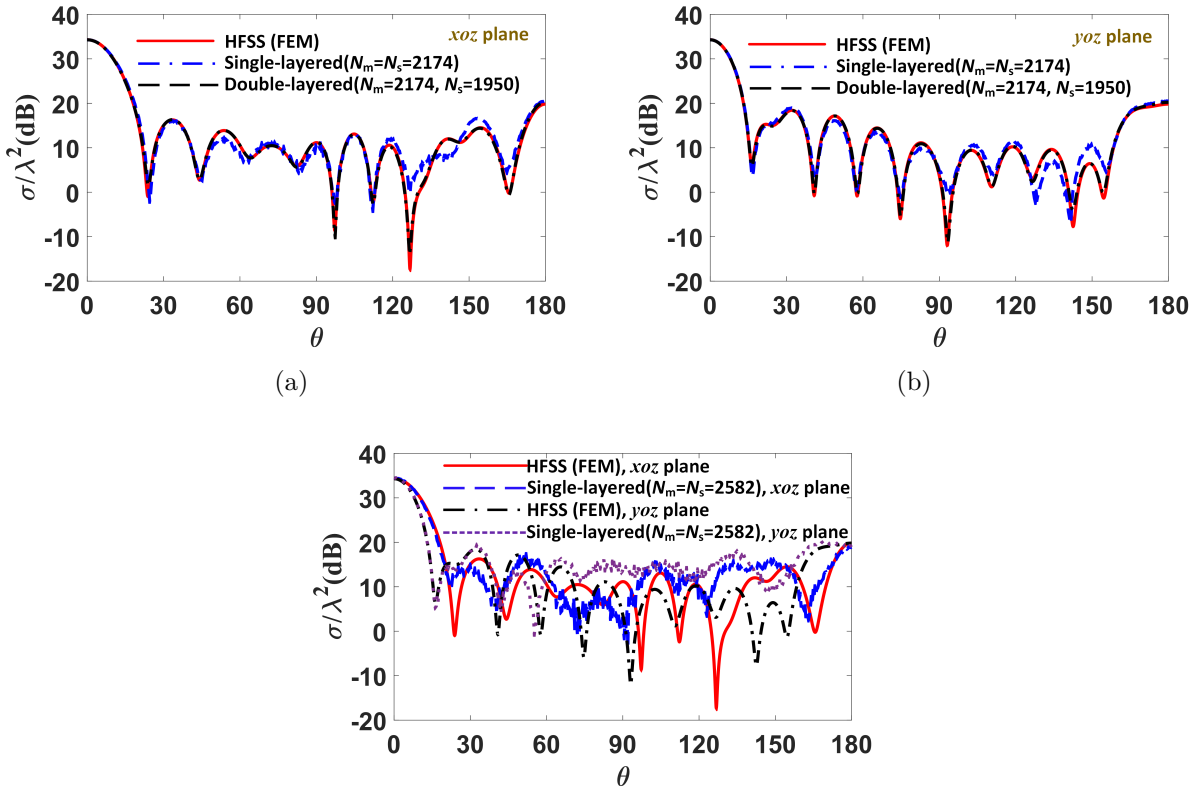

Figure 4.12 Normalized bistatic RCS responses of a uniaxial T_iO_2 sphere illuminated by a plane wave with $\hat{\boldsymbol{x}}$ polarized electric field propagating along the z axis in (a) xoz plane, (b) yoz plane and (c) both xoz and yoz planes whereas more numbers of matching points and IDDs of the single-layered scheme are used. ($r_a = 2\lambda$, $\epsilon_1 = 5.913\epsilon_0, \epsilon_2 = 7.197\epsilon_0, \mu_1 = \mu_2 = \mu_0, \theta_c = 0^\circ, \varphi_c = 180^\circ$).

defined in (4.17) for the double-layered scheme. Although the calculated results from two IDDs distribution schemes are very close, the double-layered scheme has advantages on using less CPU time and memory compared with the single-layered strategy, as indicated in Table 4.2.

The second example is related to an electrically uniaxial sphere with radius $r_a = \lambda$ illuminated by a plane wave with an unit magnitude of $\hat{\boldsymbol{x}}$ polarized electric field and propagating along the $-z$ axis. The uniaxial medium parameters are $\epsilon_1 = 5\epsilon_0$, $\epsilon_2 = 9\epsilon_0$, $\mu_1 = \mu_2 = \mu_0$ and the orientation of $\hat{\boldsymbol{c}}$ is defined as $\theta_c = 45^\circ$ and $\varphi_c = 90^\circ$. The computed normalized RCS results in xoz and yoz planes of two IDDs distribution strategies agree well with the results from HFSS, as Fig. 4.11 suggests. Since the axis $\hat{\boldsymbol{c}}$ is oriented in the yoz-plane, the scattered field pattern in the yoz plane (including $\varphi = 90^\circ$ and $\varphi = 270^\circ$) will be asymmetric as observed in Fig. 4.11(b). In order to match the simulated results from HFSS, the single-layered strategy requires more matching points and IDDs than the double-layered counterpart as indicated in Fig. 4.11(a) and 4.11(b), leading to more CPU time and required memory as suggested in Table 4.2. On the other hand, if the similar numbers of matching points and IDDs used in the double-layered scheme are deployed in the single-layered scheme, as shown in Fig. 4.11(c), the computed results will have a clear disagreement with that from HFSS or the double-layered scheme in both xoz and yoz planes, which proves the merit of the double-layered strategy in terms of convergence in comparison to the single-layered scheme.

If the radius of the uniaxial sphere further increases, limitations of the single-layered scheme become more evident. To illustrate this, we consider a T_iO_2 sphere with radius $r_a = 2.0\lambda$ illuminated by a plane wave with an unit magnitude of $\hat{\boldsymbol{x}}$ polarized electric field and propagating along z axis. The medium parameters of T_iO_2 are $\epsilon_1 = 5.913\epsilon_0$, $\epsilon_2 = 7.197\epsilon_0$, $\mu_1 = \mu_2 = \mu_0$ as referred from [158]. The axis $\hat{\boldsymbol{c}}$ is parallel to the z axis. The normalized RCS results are computed in both xoz and yoz planes, and are presented in Fig 4.12. The same number of matching points is exploited in the two IDDs distribution schemes whereas a lower number of sources is used in the double-layered strategy as indicated in Table 4.1. Yet only the results generated by the double-layered scheme have an excellent agreement with the simulated results from HFSS as suggested in Fig. 4.12(a) and 4.12(b). The computed results using the single-layered scheme are unstable and do not match well with those from HFSS. The computed results are expected to improve if more matching points and sources are used, yet much worse results are obtained as shown in Fig. 4.12(c) for the single-layered strategy. The results are more unstable and have poorer agreements with those from HFSS.

To further study this phenomenon, we calculate the tangential electric field boundary condition error in the xoz plane for the two distribution schemes of sources. Fig. 4.13(a) shows

the ΔE_{bc} responses of the single-layered scheme with different numbers of matching points and IDDs. It can be seen that more matching points and sources degrade the ΔE_{bc} response. The instability of the single-layered scheme results in inaccurate RCS results, as shown in Fig. 4.12(c). On the other hand, the proposed double-layered scheme does not suffer from such instability problem. The more matching points and IDDs, the better performance of ΔE_{bc} is achieved as shown in Fig. 4.13(b). In addition, in the case where the same number of matching points is used in both schemes, the double-layered scheme with a less number of IDDs has a much better ΔE_{bc} response (around 0.01%) than that (around 1%) of the single-layered scheme but with greater number of IDDs as shown in Fig. 4.13. This indicates that the proposed double-layered scheme can accelerate the rate of convergence compared to the single-layered scheme.

The scattering from a PEC sphere coated with a uniaxial layer, as depicted in Fig. 4.14, can also be handled straightforwardly without more modifications in the formulation. Comparing with the previous examples, three regions instead of two are presented in this scenario. The outermost region 1 is free space, the region 2 is a layer with two physical boundaries S_1 and S_2 occupied with an anisotropic T_iO_2 material, and the innermost region 3 is a PEC sphere with a radius r_b. The incident plane wave has an unit magnitude of $\hat{\boldsymbol{x}}$ polarized electric field and is propagating along z axis. The formulation is similar to previous examples. The only difference is that additional sources located within the region 3 are required to simulate the fields inside of the anisotropic layer. The double-layered scheme is deployed in this example. The radii of the closed surfaces where IDDs are placed are determined via (4.16) for the physical boundary S_1, and the radii for the closed surfaces where IDDs are placed within the region 3 for the physical boundary S_2 are defined with respect to an average radius (r_{av}) as

$$r_{11} = \frac{0.5 r_{av} r_b}{\lambda + r_{av}} \tag{4.28a}$$

$$r_{12} = \frac{r_{av} r_b}{\lambda + r_{av}} \tag{4.28b}$$

Table 4.2 The comparisons of CPU time (s) and memory (GB) between the proposed method and commercial software (HFSS and FEKO)(All simulations were run on the same server with an Intel(R) Xeon(R) E5-2680@2.70 GHz)

	HFSS(FEM)		Single-layered		Double-layered		FEKO(FDTD)	
	CPU time	Memory	CPU time	Memory	CPU time	Memory	CPU time	Memory
Fig. 4.10($r_a = 0.5\lambda$)	547	5.017	374.14	0.28	287.26	0.27	37569.60	0.642
Fig. 4.11(a) and 4.11(b)($r_a = 1.0\lambda$)	2989	14.82	261.97	0.36	216.47	0.26	/	/
Fig. 4.12(a) and 4.12(b)($r_a = 2.0\lambda$)	82980	170.20	6695.63	2.88	4421.52	2.40	/	/
Fig. 4.15($r_a = 2.0\lambda, r_b = 1.0\lambda$)	12068	61.93	/	/	10563.33	3.99	/	/

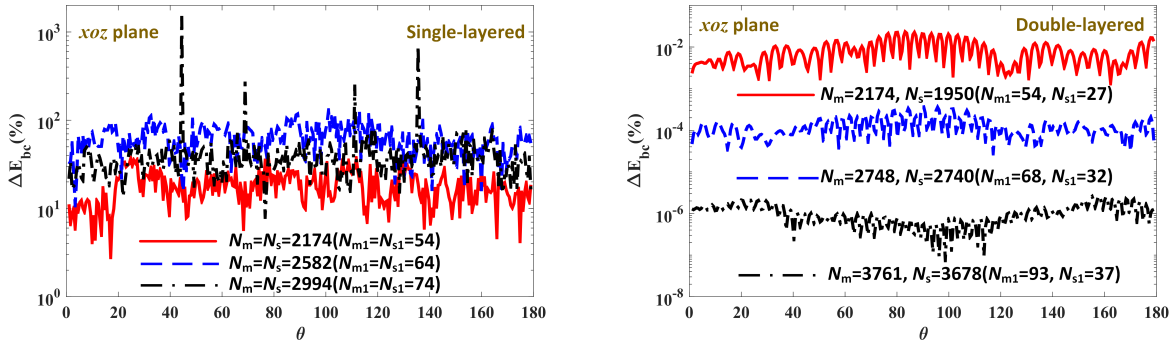

(a) (b)

Figure 4.13 The boundary condition error of electric field under different numbers of matching points and IDDs (a) the single-layered scheme and (b) the double-layered scheme. ($r_a = 2\lambda$, $\epsilon_1 = 5.913\epsilon_0, \epsilon_2 = 7.197\epsilon_0, \mu_1 = \mu_2 = \mu_0, \theta_c = 0°, \varphi_c = 180°$).

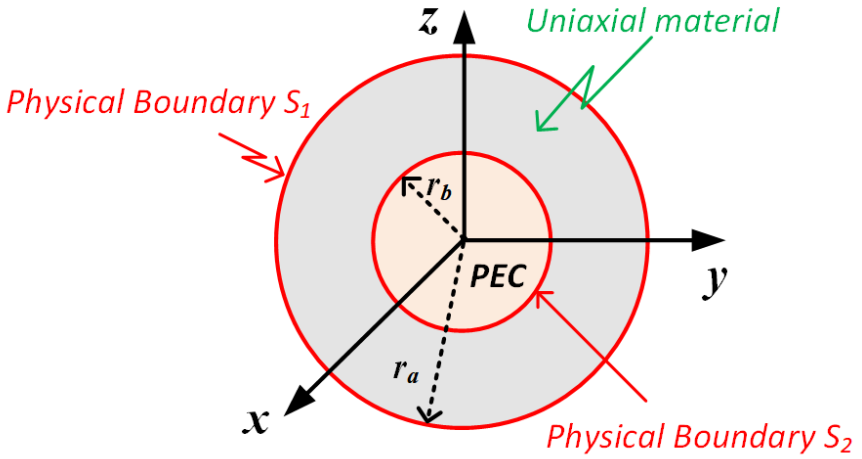

Figure 4.14 Geometry of the PEC sphere coated with an T_iO_2 layer.

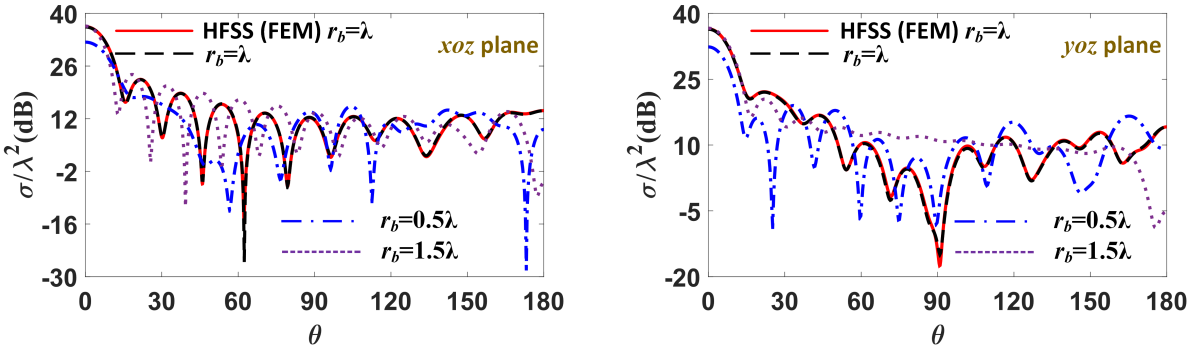

(a) (b)

Figure 4.15 Normalized bistatic RCS responses of a T_iO_2 layer coated PEC sphere with different values of r_b illuminated by a plane wave with $\hat{\boldsymbol{x}}$ polarized electric field propagating along the z axis in (a) xoz plane and (b) yoz plane. ($r_a = 2\lambda$, $\epsilon_1 = 5.913\epsilon_0, \epsilon_2 = 7.197\epsilon_0, \mu_1 = \mu_2 = \mu_0, \theta_c = 0^\circ, \varphi_c = 180^\circ$).

where $r_{av} = 0.5(r_a + r_b)$. The normalized RCS responses in both xoz and yoz planes are computed with different radii of the inside PEC sphere and presented in Fig. 4.15. The configurations of the numbers of matching points and IDDs are also given in Table 4.1. The computed results with $r_b = \lambda$ are compared with the simulated results from HFSS, and an excellent agreement is achieved as shown in Fig. 4.15.

So far, four numerical examples have been presented and computed. The first three examples suggest that the proposed double-layered scheme has obvious advantages on the convergence and the stability in handling larger objects in comparison to the traditional single-layered scheme. Moreover, the computed results using the proposed double-layered scheme have an excellent agreement with the simulated results generated from commercial software for each example. However, the proposed MIDM has great advantages on the simulation performance including the CPU time and the required memory over commercial software as displayed in Table 4.2. The CPU time has been significantly reduced with proposed technique in the first three examples, but the CPU time of the fourth example under $r_b = \lambda$, the multiple-region problem, is comparable to that of HFSS. This is because additional sources and matching points are required in multiple-region scenarios. The required memory in all the cases are drastically reduced (by 71 times in the third example) compared with the commercial software. The FEM (deployed in HFSS and CST [101] frequency domain solver), FDTD (deployed in FEKO) and Finite integration technique (FIT, deployed in CST time domain solver) are existing computational algorithms which support the simulation with anisotropic materials in commercial software packages. Since FDTD and FIT are time domain solutions, they will take a much longer time and relatively larger memory to do the simulation at a single fre-

quency point. Therefore, a comparison at only one frequency point, as indicated in Table 4.2, is unfair. The FEM has been applied in both HFSS and CST, we only take the results from HFSS to conduct comparisons. Obviously, a very high computational requirement is needed in FEM as suggested in Table 4.2. This is due to the discretization of the entire body of a scatterer. This drawback will also happen in the VIE-based methods. The only comparable technique is the SIE-based MoM proposed in [48]. Although a different CPU configuration is employed in [48], the required memory for the scattering computation of a uniaxial sphere with $r_a = \lambda$ has been reduced from 0.59 GB in [48] to 0.26 GB by using the proposed MIDM. It is noteworthy that our programs are written in MATLAB [159], and the computing time of the MIDM can be improved if a compiled programming language is utilized.

4.5.2 Scattering from uniaxial cylinders and limitations

The first example is related to an electrically uniaxial cylinder with a radius $r_a = 0.5\lambda$ and a height $h = 0.25\lambda$, therefore $r_a/h = 2$, illuminated by a plane wave with an unit magnitude of $\hat{\boldsymbol{x}}$ polarized electric field and propagating along $-z$ axis. The uniaxial medium parameters are $\epsilon_1 = 5\epsilon_0$, $\epsilon_2 = 9\epsilon_0$, $\mu_1 = \mu_2 = \mu_0$ and the axis $\hat{\boldsymbol{c}}$ is parallel to the z axis. The computed normalized RCS results in xoz and yoz planes of two IDTs distribution strategies are compared with that obtained from HFSS, in Fig. 4.16. The TELe and TELg are defined as 0.035 and 0.07 respectively in FEKO in order to generate an adaptive mesh for the cylinder resulting in $N_m = 2312$ matching points in the MIDM. The $SPWs = 16$, resulting in $N_s = 1434$ IDTs, is used for the single-layered distribution of sources and $SPWd = 13$, resulting in $N_s = 1536$ IDTs, is used for the double-layered case. Obviously, the calculated results using the single-layered strategy do not agree well whereas using double-layered have a good agreement with that obtained from HFSS.

The second example is about a uniaxial cylinder with a radius $r_a = 0.25\lambda$ and a height $h = 0.5\lambda$, therefore $r_a/h = 0.5$. The excitation is the same as in the previous example. The uniaxial medium parameters are $\epsilon_1 = 5.913\epsilon_0$, $\epsilon_2 = 7.197\epsilon_0$, $\mu_1 = \mu_2 = \mu_0$ and axis $\hat{\boldsymbol{c}}$ is parallel to the z axis. The computed normalized RCS results in xoz and yoz planes of

Table 4.3 The comparisons of CPU time (s) and memory (GB) between the proposed method and commercial software HFSS (All simulations were run on the same server with an Intel(R) Core(TM) i7-7700@3.6 GHz)

	HFSS(FEM)		Single-layered		Double-layered	
	CPU time	Memory	CPU time	Memory	CPU time	Memory
Fig. 4.16($r_a = 0.5\lambda$, $h = 0.25\lambda$)	185	3.14	1096.21	1.19	1248.61	1.27
Fig. 4.17($r_a = 0.25\lambda$, $h = 0.5\lambda$)	201	7.728	1468.63	1.39	1440.30	1.34

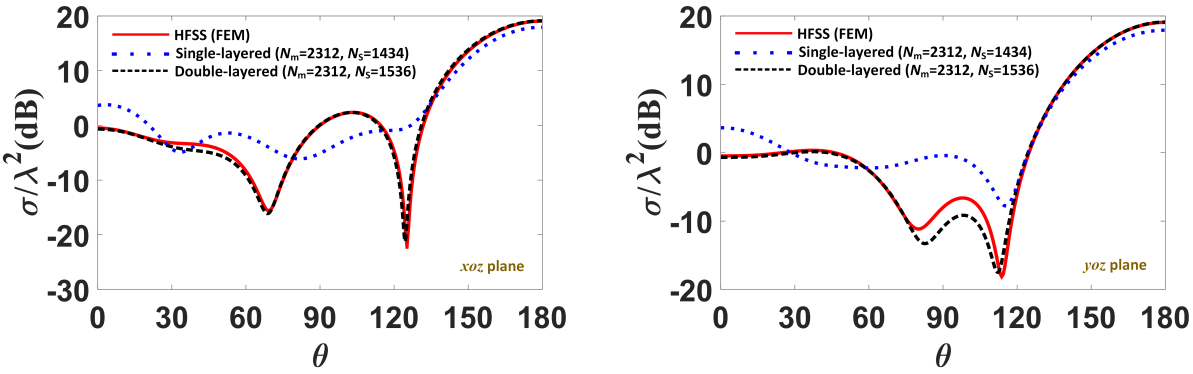

(a) (b)

Figure 4.16 Normalized bistatic RCS responses of a uniaxial cylinder illuminated by a plane wave with $\hat{\boldsymbol{x}}$ polarized electric field propagating along the $-z$ axis in (a) xoz plane and (b) yoz plane. ($r_a = 0.5\lambda$, $h = 0.25\lambda$, $\epsilon_1 = 5\epsilon_0, \epsilon_2 = 9\epsilon_0, \mu_1 = \mu_2 = \mu_0, \theta_c = 0^\circ$).

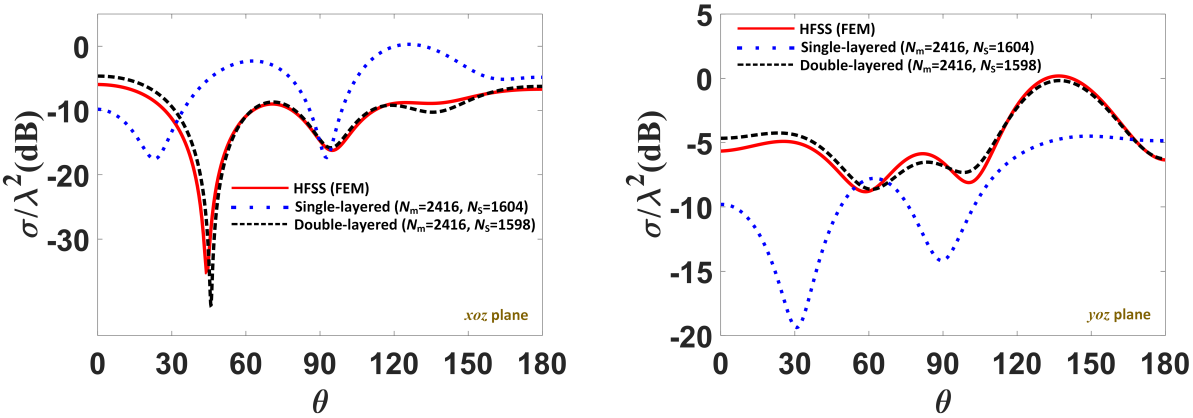

(a) (b)

Figure 4.17 Normalized bistatic RCS responses of a T_iO_2 cylinder illuminated by a plane wave with $\hat{\boldsymbol{x}}$ polarized electric field propagating along the $-z$ axis in (a) xoz plane and (b) yoz plane. ($r_a = 0.25\lambda$, $h = 0.5\lambda$, $\epsilon_1 = 5.913\epsilon_0, \epsilon_2 = 7.197\epsilon_0, \mu_1 = \mu_2 = \mu_0, \theta_c = 0^\circ, \varphi_c = 0^\circ$).

two IDTs distribution strategies are compared with that obtained from HFSS, as Fig. 4.17 suggests. The TELe and TELg are defined as 0.025 and 0.05 respectively in FEKO resulting in $N_m = 2416$ matching points in the MIDM. The $SPWs = 24$, resulting in $N_s = 1604$ IDTs, is used for the single-layered distribution of sources and $SPWd = 18$, resulting in $N_s = 1598$ IDTs, is used for the double-layered case. Again, the single-layered strategy fails to have accurate results whereas the double-layered one can generate results agreeing well with that from HFSS.

Unlike the case where an object with a smooth boundary is encountered, the CPU time and required memory in the simulation for an object with sharp edges increase a lot. This is because larger numbers of matching points and sources are required in the formulation in order to capture the fast variation behavior of fields near edges. The simulation performance is displayed in Table 4.3. Although the required memory of the proposed MIDM is less than that used in HFSS, the CPU time of the MIDM is larger than the commercial software. It is noteworthy that our programs are written in MATLAB. The performance of the MIDM can be improved if a compiled programming language is utilized and the codes are optimized.

This method is acceptable to handle a cylinder with a relatively small size ($(r_a \& h) \leqslant 1\lambda$) and a moderate ratio between r_a and h, i.e., $0.5 \leqslant r_a/h \leqslant 2$. However, the proposed strategy becomes unstable when the electrical size or the ratio is not covered in the ranges introduced before. We will study the limitation of this method by conducting another example.

A cylinder with $r_a = 0.9\lambda$ and $h = 0.3\lambda$, therefore $r_a/h = 3$, illuminated by a plane wave with an unit magnitude of $\hat{\boldsymbol{z}}$ polarized electric field and propagating along $-x$ axis is considered herein. Since the difference between the isotropic and anisotropic material in the ESM formulation only appears in the utilization of the dyadic Green's function, only the isotropic dielectric material with $\epsilon_r = 4$ is considered in this section for the case of investigating the limitation of the ESM on sharp objects. The double-layered distribution of IDTs are used in the numerical examples.

The computed normalized RCS results in xoz and yoz planes using three different sets of mesh parameters, TELe and TELg, in the MIDM are compared with results obtained from FEKO as shown in Fig. 4.18. None of the three choices of mesh parameters in the MIDM can generate accurate results. This means the solved complex coefficients of currents in the MIDM cannot satisfy the equivalence theory accurately, and the reason may appear in two aspects. The first one is the testing method enforced on the physical boundary, and the other is the placements of IDTs in each region. In 2D scenario, placing more matching points and sources near the edge can easily capture behaviors of singular fields near the edge, whereas the behaviors of singular fields near edges in a 3D scenario may be hard to be captured by

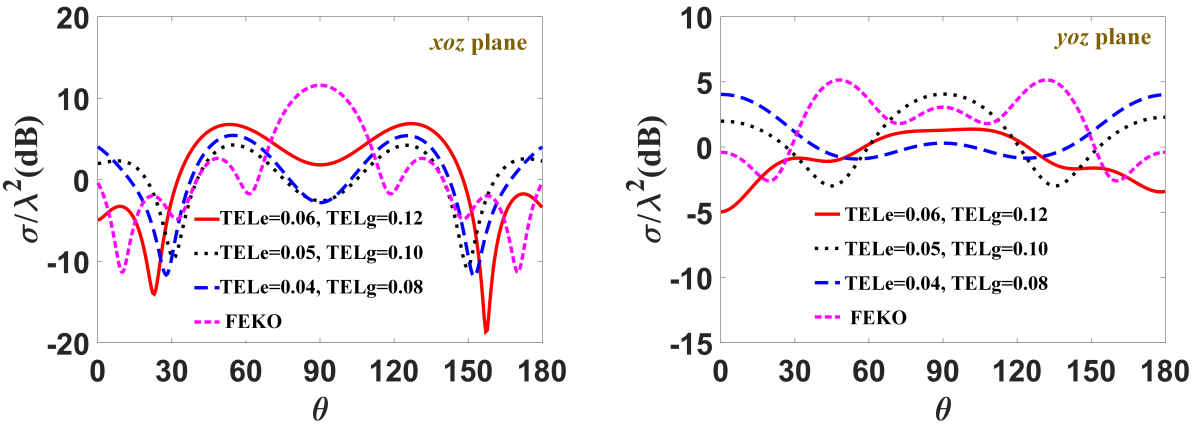

Figure 4.18 Normalized bistatic RCS simulations of a dielectric cylinder with different mesh parameters illuminated by a plane wave with $\hat{\boldsymbol{z}}$ polarized electric field propagating along the -x axis in (a) xoz plane and (b) yoz plane.

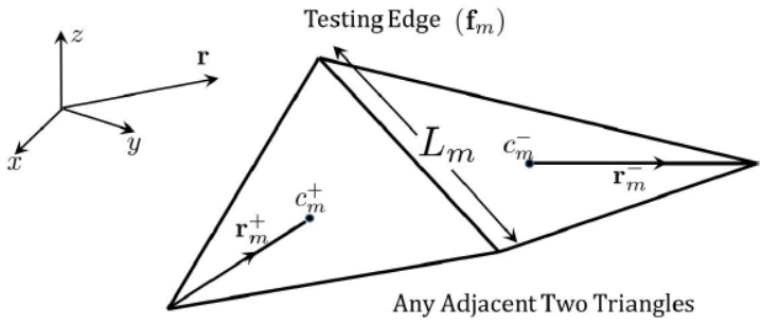

Figure 4.19 The triangle patches generated by the RWG mesh.

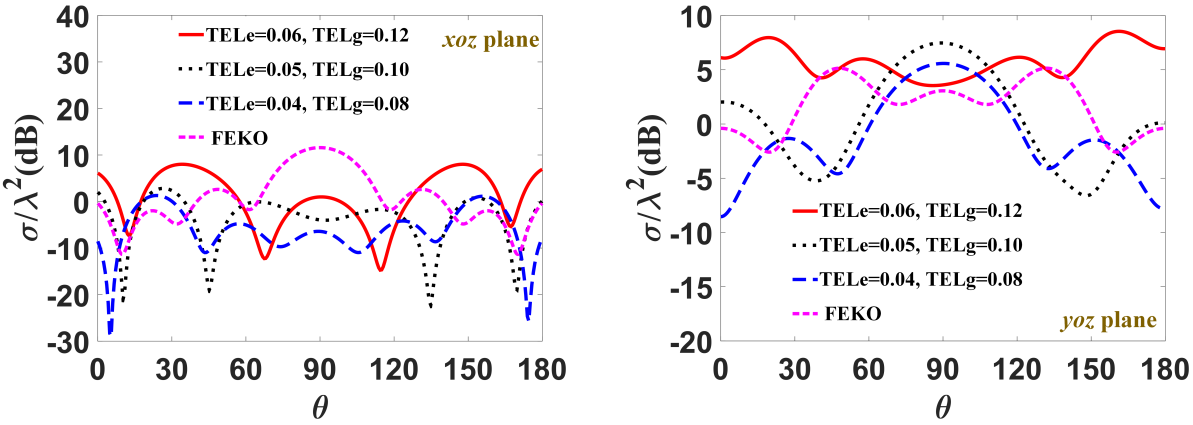

(a) (b)

Figure 4.20 Normalized bistatic RCS simulations of a dielectric cylinder using the RWG testing method of different mesh parameters illuminated by a plane wave with $\hat{\boldsymbol{z}}$ polarized electric field propagating along the -x axis in (a) xoz plane and (b) yoz plane.

the point-matching technique since the fields vary faster near the edge in 3D scenario. In this case, we deploy the RWG testing procedure in the MIDM in order to provide a more accurate way to apply the boundary condition on the physical boundary. Fig. 4.19 provides an illustration of the RWG edge testing function ($\boldsymbol{f_m}$), where $c_m^{+(-)}$ are the centroid of the two triangles forming the testing edge m. The testing procedure can be approximated as

$$\langle \{ \begin{matrix} \boldsymbol{E}^{i(s)}(\boldsymbol{r}) \\ \boldsymbol{H}^{i(s)}(\boldsymbol{r}) \end{matrix} \} \cdot \boldsymbol{f_m} \rangle \cong \frac{L_m}{2} \times \left(\{ \begin{matrix} \boldsymbol{E}^{i(s)}(\boldsymbol{r}^{c_m^+}) \\ \boldsymbol{H}^{i(s)}(\boldsymbol{r}^{c_m^+}) \end{matrix} \} \cdot \boldsymbol{r_m^+} + \{ \begin{matrix} \boldsymbol{E}^{i(s)}(\boldsymbol{r}^{c_m^-}) \\ \boldsymbol{H}^{i(s)}(\boldsymbol{r}^{c_m^-}) \end{matrix} \} \cdot \boldsymbol{r_m^-} \right) \tag{4.29}$$

where $\boldsymbol{E}(\boldsymbol{H})^{i(s)}$ indicates the incident (scattered) electric (magnetic) field and $\boldsymbol{r}^{c_m^+}$ is a radius vector between the source and the centroid c_m^+ and c_m^-, pointing at the centroid c_m^+ and c_m^-, respectively.

The computed results are shown in Fig. 4.20. Unfortunately, the MIDM using the RWG testing method still suffers the inaccuracy of dealing with the investigated cylinder. However, the RWG testing method has been proven in [4] to be better than the point-matching technique in handling an object with sharp edges in the RAS method, a MIDM-like method, and many complex geometries can be solved using the RWG testing procedure as reported in [4]. Therefore the reason for obtaining inaccurate calculated results using the RWG testing method in our proposed MIDM may be due to the placements of the sources. Actually, the scattered fields in each region are highly related to the placements of sources. Two steps are conducted in our proposed MIDM for the placement of sources. Firstly, we place the sources uniformly

by scaling the physical surface to the inner and outer regions of the scatterer with respect to the samples per wavelength. Secondly, we place additional sources near the edge in order to better approximate the singular fields behaviors around edge areas. It is reasonable to place more sources near the edges by considering the singular behavior of fields near the edges, yet placing the sources on two virtual surfaces inside and outside of an investigated object may be not appropriate for a relatively larger object or an object with a complex geometry, such as the cylinder considered herein with $r_a/h = 3$. The random placement of sources, as introduced in [3, 4, 160], is a good strategy to approximate the scattered fields in the MIDM for isotropic objects and should also work well for the anisotropic scatterers with complex geometries. Currently, we are working on this issue.

4.6 Conclusion

In this chapter, we have explored the application of the ESM on uniaxial objects in 3D scenario. The dyadic uniaxial Green's functions have been introduced firstly and subsequently deployed in the formulation of the proposed method. It is worthwhile to mention that it is the first time for the GMT-like method, namely the proposed MIDM, to deploy the dyadic Green's functions of anisotropic materials in the formulation. The key parameters, the placements of matching points and sources, have been discussed in detail in the formulation of an object with or without a smooth boundary. The boundary condition and convergence study also have been introduced and discussed. A simple strategy to deal with the singularities in using the dyadic Green's functions has been introduced, and it handles the singularity issue efficiently and therefore simplifies the problem formulation drastically in comparison to the traditional MoM. Several numerical examples have been presented, and a good agreement has been achieved in comparison to the simulated results obtained from commercial software packages. The simulation performance of the proposed technique in terms of CPU time and required memory has clear advantages over the commercial software packages used for comparisons if an object with a smooth boundary is considered. While for an object with sharp edges, our simulation tool only has advantages on required memory compared with HFSS. Yet the CPU time performance can be improved when a compiled programming language is utilized and the codes are written in a professional way. Only uniaxial materials have been considered in this work, yet the MIDM also can handle other types of anisotropic materials as long as the corresponding Green's functions are available, such as the biisotropic, chiral materials or uniaxial bianisotropic materials.

CHAPTER 5 APPLICATIONS TO LARGE SCATTERERS

Based on the discussions introduced in previous chapters, it is obvious that the ESM is powerful in comparison to commercial software packages for the EM evaluations of an object with a smooth boundary in both 2D and 3D scenarios. Once an object with sharp edges is encountered, the problem still can be solved efficiently in 2D situation, but in the 3D scenario, the ESM suffers from costly simulation performance in comparison to the commercial software packages. By considering this limitation, in this chapter, the ESM is extended to scattering evaluations of a relatively large object with a smooth boundary in 3D scenario. In addition, the investigated object is assumed to be symmetrical with respect to the coordinate system, which is often satisfied in many situations, such as spheroids and lens antennas. In addition, the characteristic of a considered material inside an object is also assumed to be symmetrical. Therefore only isotropic materials or PEC bodies are considered throughout this chapter.

The problem formulation is discussed in Sec. 5.1. The construction of the impedance matrix is introduced in Sec. 5.2. Several numerical examples with respect to scattering evaluations of PEC and dielectric objects as well as near fields calculation are presented in Sec. 5.3.

5.1 Problem formulation

We take the sphere as an example to illustrate the formulation of our proposed MIDM. In Sec. 4.2, we have introduced two parameters, N_{m1} (the number of points placed along the longitude direction) and SPW (samples per wavelength), to control the density of distribution of matching points, and an empirical formula (4.17) was proposed to control the number of sources. The strategy proposed there worked well for a scatterer with a spherical geometry, yet it seems not concise since two parameters are involved in controlling the placement of matching points , and the proposed empirical formula (4.17) may be not efficient for the placement of sources of a relatively large scatterer. In this section, we will propose a more concise way for the placements of matching points and sources. In addition, the IDT (infinitesimal dipole triplet) introduced in Sec. 4.3 is exploited.

Taking the spherical shape shown in Fig. 5.1 as an example. The sphere is divided into eight parts according to the three symmetric planes. Each octant contains one part of the sphere. Only the part in the first octant of the sphere ($(x\&y\&z>=0)$) is required to be considered in the placements of matching points and sources. Once the placements in the first octant are done, the placements in other octants could be obtained directly through the symmetry.

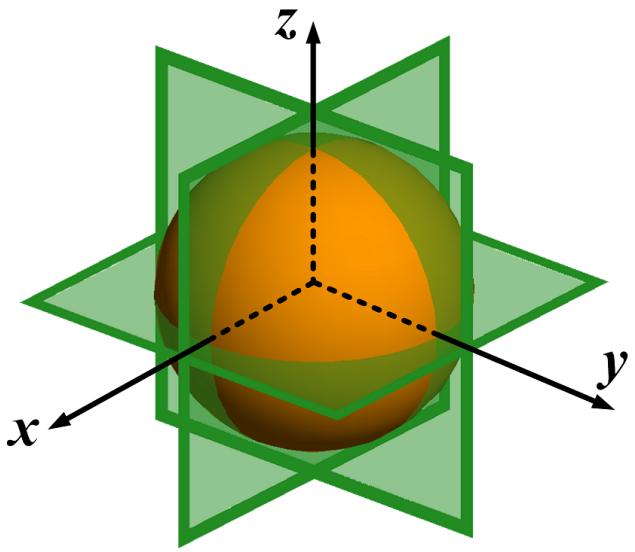

Figure 5.1 The symmetric sphere with respect to three coordinate planes

As for the placement of matching points, the $SPWm$, samples per wavelength for matching points, is firstly defined. Then the number of points selected along the longitude (θ) direction determined in terms of the $SPWm$. A latitudinal closed circle is constructed with respect to the ith point on the θ direction. The matching points are then uniformly placed on each closed circle in terms of the $SPWm$. Specially, the total number of matching points in the first octant (N_m^b) is given as

$$N_m^b = \sum_{i=1}^{N_a} \lceil \frac{\pi r_a \sin\theta_i SPWm}{2\lambda} \rceil \tag{5.1}$$

with

$$N_a = \lceil \frac{\pi r_a SPWm}{2\lambda} \rceil$$

$$\theta_i = Gap + (i-1)\frac{0.5\pi - 2Gap}{N_a - 1}$$

where r_a is the radius of a sphere, and λ is the incident wavelength. Gap is used to avoid overlapped matching points generated on the physical surface, and $Gap = 0.25\pi/(N_a - 1)$ is used in our numerical method. The $\lceil\ \rceil$ symbol represents the ceiling function and is used to obtain an integer value. So the total number of matching points are $N_m = 8N_m^b$.

As for the placement of sources, we firstly place the points on the physical surface with respect to the $SPWs$, samples per wavelength for sources, using the previously introduced

strategy. Then the locations of these points are moved to the inner and outer surfaces by defining scaling parameters. One IDT is placed at each point. The total number of IDTs is recorded as $N_s = 8N_s^b$, where N_s^b is the total number of IDTs in each part. Only double-layered distribution strategy of sources is used in this chapter, the single-layered strategy has been proven in Sec. 4.5.1 to be not capable in handling relatively large scatterers. The scaling parameters for a sphere can be found in (4.16) in Sec. 4.2, and we place it below for the convenience

$$r_{11} = \frac{r_a^2}{\lambda + r_a} \tag{5.2a}$$

$$r_{12} = 0.5 r_{11} \tag{5.2b}$$

$$r_{21} = 2r_a - r_{11} \tag{5.2c}$$

$$r_{22} = 2r_a - r_{12} \tag{5.2d}$$

where r_a is the radius of a sphere. In order to avoid positioning the IDTs too close to (r_{11} and r_{21} approach r_a) or too far away from (r_{12} is much smaller than r_a) the physical surface when a relatively large or small object is encountered, we set upper and lower limits as $r_{11}^{max} = 0.95 r_a$, $r_{12}^{min} = 0.15 r_a$, $r_{21}^{min} = 1.2$ and $r_{22}^{min} = 1.6$. If a non-spherical geometry is encountered, the r_a should be replaced by r_{max}, which is the maximum one of distances among the matching points and the origin point.

The number of matching points relates to only one parameter, $SPWm$, rather than being determined by two parameters, N_{m1} and SPW, as discussed in Sec. 4.2.2. The number of sources relates to $SPWs$ rather than being controlled by an empirical formula. The strategy proposed herein is more concise and general than that introduced in previous chapter.

In the simulation, the $SPWm$ is firstly given and the initial value, for a large scatterer with a radius bigger than 3λ, is recommended to set as 2.0 and the initial value for the $SPWs$ is recommended as 1.0. The increasing steps for the $SPWm$ and $SPWs$ are 0.25 and 0.125, respectively. In addition, only the matching points and sources in the first octant need to be specified. The locations of matching points and sources in other octants can be directly obtained through the symmetry of the investigated object.

5.2 Construction of the impedance matrix

By imposing the standard boundary condition expressed in (4.21) on matching points generated on the physical surface of a scatterer, a linear system is created. As discussed in the previous section, the geometry of an investigated object could be divided into 8 parts if it is symmetrical to three coordinate planes as indicated in Fig. 5.1. In this case, 8×8 blocks are

Figure 5.2 Constructed impedance matrix.

generated in the impedance matrix but only the tangential fields generated by the sources in the first octant need to be calculated. Fig. 5.2 shows the description of a constructed impedance matrix. The first column of the block matrix is required to be calculated, which represents the tangential fields generated by the sources in the first octant at matching points in each octant. The remain 7×8 blocks can be filled directly according to the fields relationships among the eight octants as shown in the Fig. 5.2. For examples, once the tangential fields at matching points in the first octant generated by the sources in the first octant are calculated, indicated as 1 in the first column of Fig. 5.2, the blocks in the diagonal of the matrix can be obtained directly by considering the fields relationships.

By making use of the symmetry of the investigated object, the construction time of the impedance matrix is reduced to around 1/8 of the time used for calculating all blocks of the impedance matrix. However, the tangential fields generated by each source at each matching point are recorded and therefore the required memory is not saved.

5.3 Numerical examples and discussions

The first example is a PEC sphere illuminated by a plane wave with an unit magnitude of $\hat{\boldsymbol{x}}$ polarized electric field and propagating in the $-z$ direction. The normalized bistatic RCS responses in xoz and yoz planes are shown in Fig. 5.3(a) and 5.3(b) for a sphere with a radius $r_a = 5\lambda$, and in Fig. 5.3(c) and 5.3(d) for a sphere with a radius $r_a = 10\lambda$. The computed results are compared with the simulation results obtained from commercial software FEKO

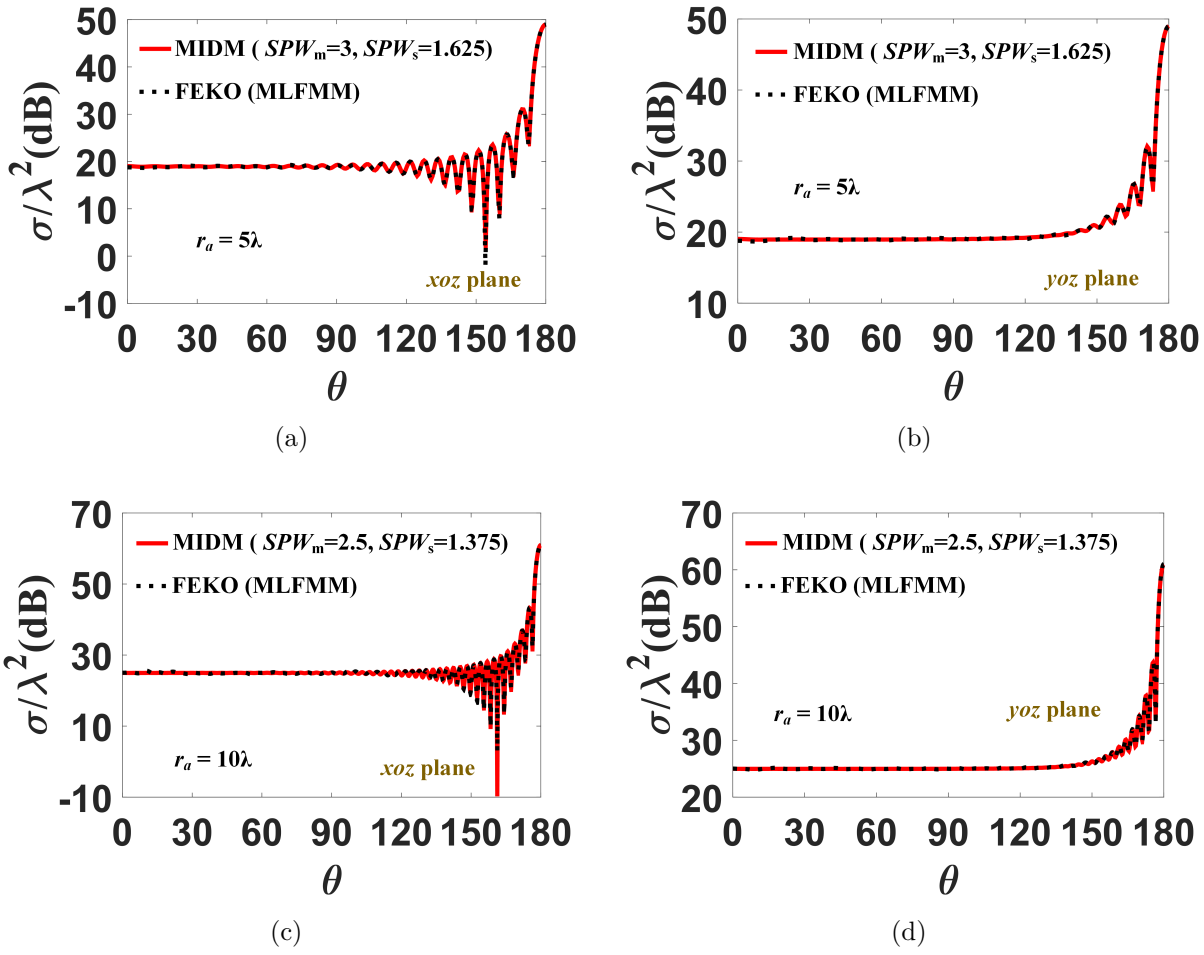

Figure 5.3 Normalized bistatic RCS responses of a PEC sphere illuminated by a plane wave with $\hat{\boldsymbol{x}}$ polarized electric field propagating along the -z axis in (a) xoz plane and (b) yoz plane for $r_a = 5\lambda$, and (c) xoz plane and (b) yoz plane for $r_a = 10\lambda$.

Table 5.1 The matrix sizes and unknowns as well as the CPU time (s) of the matrix construction and matrix solution (All simulations were run on the same server with an Intel(R) Xeon(R) E5-2680@2.70 GHz)

	Matrix Size	Unknowns	Matrix Construction(symmetric)	Matrix Construction(traditional)	Matrix Solution
Fig. 5.3($r_a = 5\lambda$)	5968×5376	5376	84.23	412.41	686.7188
Fig. 5.3 and 5.4($r_a = 10\lambda$)	16320×14976	14976	1371.22	6200.20	12648.14
Fig. 5.5($r_a = 5\lambda$)	20960×20256	20256	514.83	2458.61	28177.18

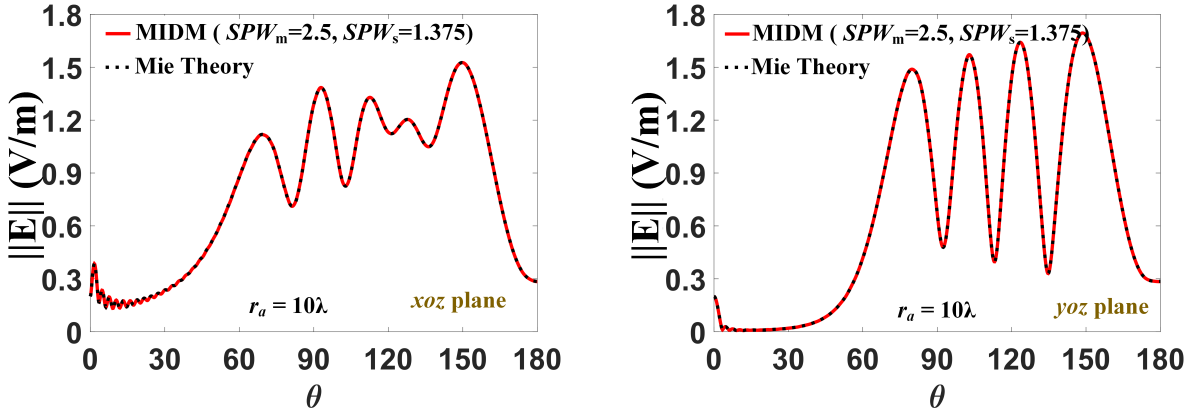

(a) (b)

Figure 5.4 The magnitudes of scattered electric field of a PEC sphere illuminated by a plane wave with $\hat{\boldsymbol{x}}$ polarized electric field propagating in the z direction in (a) xoz plane and (b) yoz plane at $r = 1.2r_a$, $r_a = 10\lambda$.

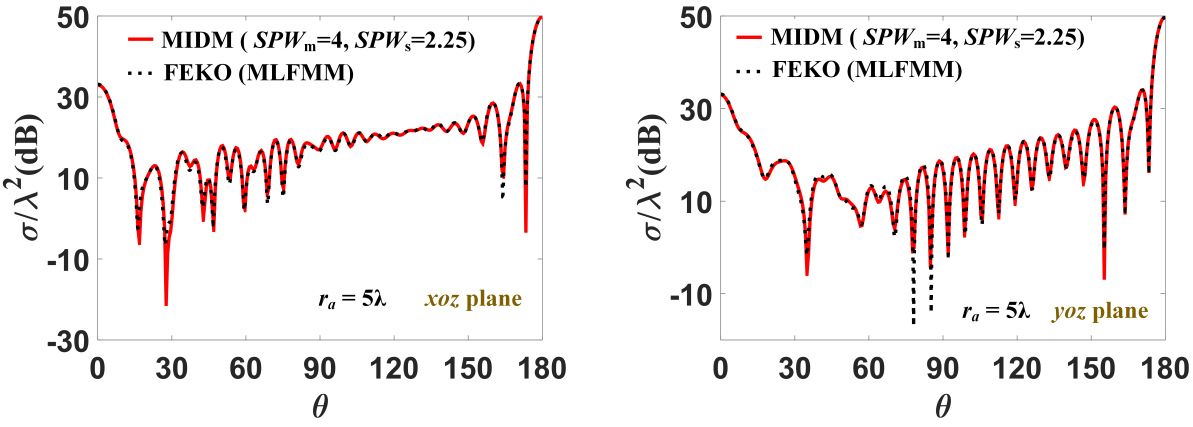

(a) (b)

Figure 5.5 Normalized bistatic RCS responses of a dielectric sphere with $\epsilon_r = 4$ illuminated by a plane wave with $\hat{\boldsymbol{x}}$ polarized electric field propagating in the -z direction in (a) xoz plane and (b) yoz plane for $r_a = 5\lambda$.

Table 5.2 The comparisons of CPU time (s) and memory (GB) between the proposed method and commercial software FEKO (All simulations were run on the same server with an Intel(R) Xeon(R) E5-2680@2.70 GHz)

	FEKO(MoM)		FEKO(MLFMM)		MIDM	
	CPU time	Memory	CPU time	Memory	CPU time	Memory
Fig. 5.3($r_a = 5\lambda$)	64708.16	40.813	8329.05	3.726	796.78	0.48
Fig. 5.3($r_a = 10\lambda$)	/	/	33362.51	11.17	14740.55	3.64
Fig. 5.4($r_a = 10\lambda$)	/	/	/	/	16217.45	3.64
Fig. 5.5($r_a = 5\lambda$)	/	/	7621.63	19.69	28728.46	12.65

where MLFMM [161] solver is applied. Excellent agreement can be observed. The $SPWm = 3$ and $SPWs = 1.625$ are selected in the simulation for the PEC sphere with $r_a = 5\lambda$ whereas $SPWm = 2.5$ and $SPWs = 1.375$ are selected for the PEC sphere with $r_a = 10\lambda$. The resulted matrix sizes and unknowns are shown in Table 5.1. The CPU time of the impedance matrix construction and matrix solution are also provided in Table 5.1. It is obvious to see that the CPU time for the matrix construction by making use of the symmetry has been reduced a lot compared with the time used for the impedance construction through the traditional approach. However, in both cases, the CPU time for matrix solution is much larger than that for matrix construction.

In the second example, the MIDM is used to calculate the near fields of a PEC sphere with a radius $r_a = 10\lambda$ illuminated by a plane wave with an unit magnitude of $\hat{\boldsymbol{x}}$ polarized electric field and propagating in the z direction. The monitor sphere for the near fields calculation is selected with a radius $r = 1.2r_a$. The magnitudes of scattered electric field in xoz plane and yoz plane are calculated and compared with Mie theory, as shown in Fig. 5.4. Excellent agreements are achieved. $SPWm = 3$ and $SPWs = 1.625$ are selected in the simulation in this case. The resulting matrix sizes and unknowns as well as the CPU time of the matrix construction and solution are presented in Table 5.1.

The last example is about a dielectric sphere with $\epsilon_r = 4$ and a radius $r_a = 5\lambda$ illuminated by a plane wave with an unit magnitude of $\hat{\boldsymbol{x}}$ polarized electric field and propagating along the $-z$ axis. The normalized bistatic RCS responses in xoz and yoz planes are shown in Fig. 5.5(a) and 5.5(b), respectively. The computed results are compared with the simulation results obtained from commercial software FEKO where MLFMM is applied. Excellent agreement can be observed. The $SPWm = 4$ and $SPWs = 2.25$ are selected in the simulation. The relevant information about the impedance matrix is provided in Table 5.1.

The simulation performances regarding to the CPU time and required memory of above three examples using the proposed MIDM and commercial software FEKO are displayed in

Table 5.2. Two solvers are used in FEKO for the simulation, one is based on the MoM and the other is based on MLFMM. The computational cost of the MoM based general solver in FEKO is quite higher than the MLFMM based solver as indicated in Table 5.2 for the first example. In this case, the MoM solver is not used for the simulation where a larger or a dielectric scatterer is encountered. The required memory for the scattering evaluations of a PEC or dielectric sphere using the MIDM is less than that using the MLFMM solver in FEKO, yet the proposed MIDM only has the advantage on the CPU time where PEC spheres are considered.

Based on the three numerical examples, it is obvious that the proposed MIDM is an efficient and powerful simulation tool for the EM evaluations of a relatively large scatterer with a smooth boundary. While for a relatively large dielectric scatterer or an electrical large PEC scatterer (for example a PEC sphere with a radius bigger than 10λ), the advantages on simulation performances of the MIDM become not obvious or even poorer than the commercial software FEKO (MLFMM based solver). Actually this is the common drawback, which appears in the costly construction, storage, and solution of a dense linear system, of MoM-like methods. This drawback has led to the development of other fast algorithms such as AIM [162], MLFMM [161], MLMDA [163–165] and SVD-MDA [166]. But several desirable features of the MoM-like methods, including: few problem-dependent parameters; fixed time solution avoiding convergence problems; and high efficiency for multiple excitation problems [e.g., monostatic radar cross section (RCS)], are emphasized in comparison to the fast algorithms introduced previously for a moderate electric large problems (up to several tens of thousands of unknowns) as discussed in [161–166].

5.4 Conclusion

In this chapter, we have investigated the MIDM on the application of relatively larger scatterers. The time of constructing impedance matrix is accelerated by making use of the symmetry of investigated scatterers. However, the computation cost spent on the matrix solution is quite high as indicated in the Table 5.1 and 5.2. The smallest least-square error solution or the LU decomposition solution becomes time-consuming when the matrix is dense. One possible solution to solve this issue is to use the block decomposition algorithm (BDA) proposed in [167, 168] to calculate the unknowns. But a new problem rises in deploying the BDA in the MIDM is that the BDA cannot handle an ill-conditioned matrix which is usually generated in the MIDM. In this case, a pre-processing method should be firstly applied on the constructed impedance matrix in order to have a well-conditioned matrix. Then the BDA can be applied to solve the linear system fast and accurately. More details will be discussed in Appendix E.

CHAPTER 6 CONCLUSIONS AND FUTURE WORK

6.1 Summary of the contributions

In this thesis, the ESM has been exploited in the EM evaluations of scatterers with anisotropic characteristics in both 2D (a specific name, MFCM, is used to represent ESM) and 3D (a specific name, MIDM, is used to represent ESM) scenarios. An efficient, concise, and accurate simulation tool has been proposed, formulated and further utilized for EM evaluations of anisotropic scatterers. Several research works have been conducted, as listed below:

In Chapter 2, we have succeed in analyzing the scattering of an anisotropic cylinder using the MFCM. The radiation fields of a line source placed in an unbounded region occupied with anisotropic materials have been derived. The formulation of the MFCM which employs derived radiation fields is discussed systematically. Several numerical examples are provided. Monostatic and bistatic normalized scattering widths are computed in different scenarios such as incident wave polarizations, material characteristics, and cross section shapes. A boundary condition error is proposed and tested in order to determine the necessary numbers of sources and matching points for an object with sharp edges. The analyses of the oscillation of filament currents associated with the singularities of the scattered fields' analytic continuation and the matrix ill-conditioning are also presented and discussed. Our computed results are in good agreement with results already published, which prove that we have succeeded in extending the application of the MFCM to anisotropic materials. Moreover, our proposed method has its merits on simplicity and conciseness in the formulation. The CPU time and required memory are 611 s/7.50 GB for the FEM (CST) whereas only 1.58 s/0.00037 GB for the ESM when computing the field on the surface of an elliptical cylinder in 2D case under the illumination of a TM plane wave. The necessity of integrating surface currents and the singularity issue (the filament current and the physical boundary coincide) are also avoided in the MFCM.

In Chapter 3, we have studied the MFCM with respect to anisotropic boundary conditions. Specifically, two types of anisotropic boundary conditions have been considered. One is the tensorial impedance boundary condition (TIBC) which is used to represent multilayered CFC material, and the other is the generalized sheet transition condition (GSTC) which is used to represent a metasurface. The formulations of the TIBC and GSTC have been introduced in detail and subsequently deployed in the MFCM to study EM estimations of interest.

Several numerical examples have been presented with respect to the scattering and shielding analyses of multilayered CFC-based cylindrical shells. Our results are in excellent agreement

with the published ones. The proposed technique shows its advantages in formulating and solving the problem with a simple and concise way. An interesting observation is that the anisotropy of the multilayered CFC material is negligible in scattering analyses since the cross-polarized fields are quite small compared with the main polarized counterpart. While the anisotropic property has a significant impact on SE performances at high frequencies as seen from that both TE and TM modes are excited within the cylindrical shell under arbitrary incident plane waves.

Several illustrated numerical examples also have been provided by employing the GSTC. The simulated fields are in a good agreement with the preset fields, which prove the proposed method is capable to handle a spatial-varying impedance boundary condition. In addition, the slotted multilayered CFC-based shells also have been considered by using the MFCM. A hybrid tensorial boundary condition is constructed in order to represent the slotted shell. A specific strategy to place the sources and matching points with respect to the slot is proposed in order to consider the singularities of fields near the slot. Finally, the induced currents distribution on the surface of a multilayered CFC-based shell under the illumination of line sources has been investigated by using the MFCM. Several numerical examples also have been presented and discussed.

In Chapter 4, we bring applications of the ESM from 2D to 3D. The dyadic Green's functions of anisotropic materials have been deployed in the GMT-like method, namely the proposed MIDM, for the first time. A brief introduction for the derivation of dyadic Green's functions has been presented. The dyadic Green's function regarding to the uniaxial materials is then considered in the MIDM to study the scattering performance from uniaxial scatterers. A strategy to avoid the singularity issue when using the dyadic Green's functions has been proposed. The placements of matching points as well as sources, which play a key role in the MIDM, have been discussed and specified in detail, for objects with a smooth boundary or with sharp edges. Both infinitesimal dipole doublet (IDD) and infinitesimal dipole triplet (IDT) are used to simulate the scattered fields in the MIDM. In addition, the proposed double-layered distribution scheme of sources can handle the scattering evaluation from electrically large objects in a stable and efficient way in comparison to the traditional single-layered counterpart. Several numerical examples are investigated under different scenarios, and the computed results for each example have an excellent agreement with simulated results obtained from commercial software packages. The simulation performance of the MIDM in terms of CPU time and required memory has clear advantages over the commercial software packages for an object with a smooth boundary, for example, the CPU time and required memory are 82980 s/170.2 GB for the FEM (HFSS) whereas only 4421.52 s/2.40 GB for the ESM when computing scattering from an uniaxial sphere with a 2λ radius, while the CPU

time for an object with sharp edges is larger by using the MIDM. It is noteworthy that our programs are written in MATLAB, by a non-professional programmer. The performance of the MIDM can be improved if a compiled programming language is utilized and the codes are written in a professional way. The limitation of the proposed MIDM on simulating a structure with sharp edges was also studied there.

In Chapter 5, we have extended the application of MIDM to relatively large isotropic scatterers. The construction time for the impedance matrix is reduced by making use of the symmetry of an object. Several numerical examples have been provided and discussed in detail. The simulation performance in terms of CPU time and required memory of the MIDM has clear advantages over the commercial software packages where the MoM are used to do the simulation.

6.2 Future Research

(1). The main direction of our future work is try to provide a stable solution for the simulation of an anisotropic object with sharp edges in 3D scenario. As discussed in Sec. **??**, the proposed MIDM is not capable to handle an arbitrary object with sharp edges, and the reason is highly due to the placement of sources. In this case, placing the infinitesimal sources inside and outside an investigated object randomly , as introduced in [3, 4, 160], could be an alternative solution to address this issue. The RWG [150] testing method was also utilized for a complex geometry in [4]. The physical boundary is adaptively meshed with respect to the edges, which is similar to the strategy proposed in our method as introduced in Sec. 4.3.2. More random sources are placed near the edges in order to better approximate the singular behaviors of fields near edges as shown in Fig. 6.2. It has been proven this strategy can handle problems with complex shapes and sharp edges accurately. An iterative scheme also has been proposed to satisfy the boundary condition on the physical surface with a prescribed criterion as shown in Fig. 6.1. This is an efficient way to guarantee the solution is convergent. Although the ill-conditioned issue of the constructed impedance matrix was not considered there, an accurate calculation can still be obtained. Currently, we are working on using the RAS method to simulate scattering performances of uniaxial objects with arbitrary geometries.

(2). As discussed in Appendix E, the BDA can accelerate the computation of the constructed dense linear system. However, ill-conditioned impedance matrices cannot be used with the BDA approach. In this case, our second future work is to find a pre-processing method which can be applied on the constructed impedance matrix in order to have a well-conditioned impedance matrix. A possible pro-processing method could be singular value decomposition method. Then the BDA can be applied to solve the linear system rapidly and accurately.

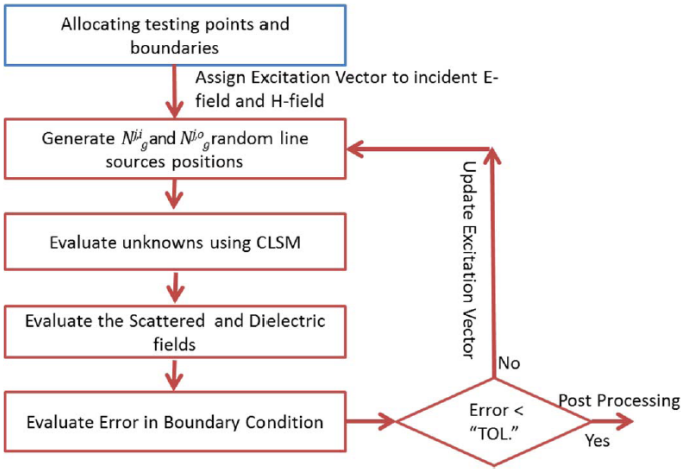

Figure 6.1 Iterative RAS procedure flowchat. [3]

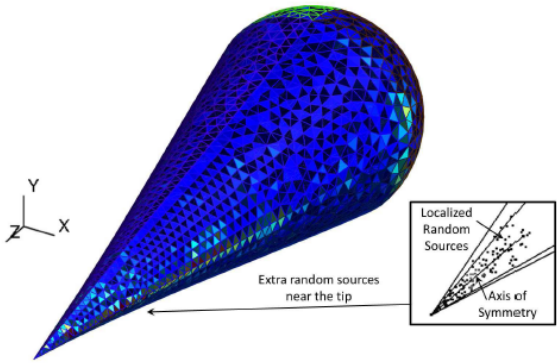

Figure 6.2 Adaptive mesh of a cone-sphere structure and the placement of random sources near the edges. [4]

The ESM could handle general-purpose EM problems if the above two problems could be tackled. Specifically for symmetrical objects, for example the dielectric resonator antenna, the lens antenna and so on, the ESM is a powerful simulation tool.

(3). The ESM also can be used to do modal analyses for a waveguide filled with uniaxial materials or uniaxial dielectric resonators. The natural frequencies of cavities and scatterers using the ESM were reported in [169]. Instead of solving the $\boldsymbol{Ax} = \boldsymbol{b}$ problem, for example the scattering problem with specific excitations $\boldsymbol{b}$, the solution of $\boldsymbol{Ax} = \boldsymbol{0}$ corresponds to the eigen modes of an investigated structure. Specifically, the eigen modes are found by searching the real or complex roots of the determinant of the impedance matrix in a considered frequency range [169]. For a metallic waveguide or metallic cavity with a smooth boundary filled with uniaxial material, the formulation discussed in Chapter 4 can be directly applied to analyze the resonant modes by setting the excitation as null. These modes can be easily found by searching the real roots of the determinant of the impedance matrix in a frequency range. Yet for an open dielectric resonator, the resonant modes are complex. The real part of the modes represents the resonant frequency and the imaginary part relates to the Q-factor of the resonator. To find these complex modes, the roots searching of the determinant of the impedance matrix should be conducted in two dimensions and usually it is very time-consuming. Recently, the study of resonant modes in rectangular DRA based on the RCS was introduced in [170]. The commercial software HFSS is utilized to simulate the monostatic RCS of a rectangular DRA in an investigated frequency range, and the peaks in the monostatic RCS response correspond to the resonant modes. The drawback in using the HFSS appears in the simulation time due to a very fine step in the frequency sweep should be set in order to accurately determine the resonant frequency of each mode, and this drawback will be more obvious when an uniaxial object is considered. The MIDM could be a potential candidate to calculate the monostatic RCS of a uniaxial dielectric resonator with a symmetrical geometry rapidly , and an adaptive sampling algorithm introduced in [171] could be used to fast determine the locations of modes.

REFERENCES

[1] N. V. Nayak, "Composite materials in aerospace applications," *International Journal of Scientific and Research Publications*, vol. 4, no. 9, pp. 1–10, 2014.

[2] N. L. Tsitsas *et al.*, "On methods employing auxiliary sources for two-dimensional electromagnetic scattering by non-circular shapes," *IEEE Trans. Antennas Propagat.*, vol. 66, no. 10, pp. 5443–5452, Oct. 2018.

[3] M. A. Moharram and A. A. Kishk, "Electromagnetic scattering from two-dimensional arbitrary objects using random auxiliary sources," *IEEE Antennas and Propag. Mag.*, vol. 57, no. 1, pp. 204–216, 2015.

[4] M. A. M. Hassan and A. A. Kishk, "Solutions for general-purpose electromagnetic problems using the random auxiliary sources method," *IEEE Trans. Antennas Propagat.*, vol. 66, no. 4, pp. 1947–1956, Apr. 2018.

[5] L. Rayleigh, "On the electromagnetic theory of light," *The London, Edinburgh, and Dublin Philosophical Magazine and Journal of Science*, vol. 12, no. 73, pp. 81–101, 1881.

[6] G. Mie, "Beiträge zur optik trüber medien, speziell kolloidaler metallösungen," *Annalen der physik*, vol. 330, no. 3, pp. 377–445, 1908.

[7] F. Frezza, F. Mangini, and N. Tedeschi, "Introduction to electromagnetic scattering: tutorial," *J. Opt. Soc. Am. A*, vol. 35, no. 1, pp. 163–173, Jan. 2018.

[8] J. Richmond, "Scattering by a dielectric cylinder of arbitrary cross section shape," *IEEE Transactions on Antennas and Propagation*, vol. 13, no. 3, pp. 334–341, May 1965.

[9] R. F. Harrington, *Time-harmonic electromagnetic fields*. McGraw-Hill, 1961.

[10] ——, *Field computation by moment methods*. Wiley-IEEE Press, 1993.

[11] L. Mendes, "Scattering by conducting, chiral, and dielectric cylinders of arbitrary cross-section: Surface and volume formulations." 1992.

[12] A. Taflove and S. C. Hagness, *Computational electrodynamics: the finite-difference time-domain method*. Artech house, 2005.

[13] J.-M. Jin, *The finite element method in electromagnetics*. John Wiley & Sons, 2015.

[14] L. Bouchet *et al.*, "Calculation of acoustic radiation using equivalent-sphere methods," *The Journal of the Acoustical Society of America*, vol. 107, no. 5, pp. 2387–2397, 2000.

[15] M. Johnson *et al.*, "An equivalent source technique for calculating the sound field inside an enclosure containing scattering objects," *The Journal of the Acoustical Society of America*, vol. 104, no. 3, pp. 1221–1231, 1998.

[16] P. A. Nelson and S.-H. Yoon, "Estimation of acoustic source strength by inverse methods: Part i, conditioning of the inverse problem," *Journal of sound and vibration*, vol. 233, no. 4, pp. 639–664, 2000.

[17] C. Hafner, *Generalized multipole technique for computational electromagnetics*. Artech House, 1990.

[18] T. Wriedt, *Generalized Multipole Techniques for Electromagnetic and Light Scattering*. Elsevier, 1999.

[19] ——, "A review of elastic light scattering theories," *Particle & Particle Systems Characterization: Measurement and Description of Particle Properties and Behavior in Powders and Other Disperse Systems*, vol. 15, no. 2, pp. 67–74, 1998.

[20] A. B. Evlyukhin, C. Reinhardt, and B. N. Chichkov, "Multipole light scattering by nonspherical nanoparticles in the discrete dipole approximation," *Physical Review B*, vol. 84, no. 23, p. 235429, 2011.

[21] S. V. Yuferev and N. Ida, *Surface impedance boundary conditions: a comprehensive approach*. CRC press, 2009.

[22] K. M. and H. SINGER, "Numerical computation of anisotropic shielding materials based on the method of moments," in *Proc. IEEE Int. Symp. EMC*, 1996, pp. 87–91.

[23] J. H. Beggs *et al.*, "Finite-difference time-domain implementation of surface impedance boundary conditions," *IEEE Transactions on Antennas and propagation*, vol. 40, no. 1, pp. 49–56, 1992.

[24] K. Yee, K. Shlager, and A. Chang, "An algorithm to implement a surface impedance boundary condition for fdtd (em scattering)," *IEEE transactions on antennas and propagation*, vol. 40, no. 7, pp. 833–837, 1992.

[25] A. W. Glisson, "Electromagnetic scattering by arbitrarily shaped surfaces with impedance boundary conditions," *Radio science*, vol. 27, no. 06, pp. 935–943, 1992.

[26] D. J. Hoppe, *Impedance boundary conditions in electromagnetics*. CRC Press, 1995.

[27] H. T. Anastassiu *et al.*, "Electromagnetic scattering analysis of coated conductors with edges using the method of auxiliary sources (mas) in conjunction with the standard impedance boundary condition (sibc)," *IEEE Trans. Antennas Propagat.*, vol. 50, no. 1, pp. 59–66, Jan. 2002.

[28] R. D. Gragli, "Integral equations for anisotropic scatterer," in *Ph.D. dissertation*, Univ. Illinois, Chicago, 1983.

[29] P. L. E. Uslenghi and R. D. Gragli, "Electromagnetic scattering from anisotropic materials, part I: General theor," *IEEE Trans. Antennas Propagat.*, vol. 32, no. 8, pp. 867–869, Aug. 1984.

[30] B. Beker and K. R. Umashankar, "Analysis of electromagnetic scattering by arbitrarily shaped two-dimensional anisotropic objects: Combined field surface integral equation formulation," *Electromagnetics*, vol. 9, pp. 215–229, Apr. 1989.

[31] B. Beker, K. R. Umashankar, and A. Taflove, "Numerical analysis and validation of the combined field surface integral equations for electromagnetic scattering by arbitrarily shaped two-dimensional anisotropic objects," *IEEE Trans. Antennas Propagat.*, vol. 37, no. 12, pp. 1573–1581, Dec. 1989.

[32] ——, "Electromagnetic scattering by arbitrarily shaped two-dimensional perfectly conducting objects coated with homogeneous anisotropic material," *Electromagnetics*, vol. 10, pp. 387–406, Apr. 1990.

[33] J. C. Monzon, "On a surface integral representation for homogeneous anisotropic regions: Two-dimensional case," *IEEE Trans. Antennas Propagat.*, vol. 36, no. 10, pp. 1401–1406, Oct. 1988.

[34] ——, "Two-dimensional scattering by a homogeneous anisotropic rod„" *IEEE Trans. on Electromagn. Compat.*, vol. 34, no. 10, pp. 1243–1249, Oct. 1986.

[35] J. Monzon, "Three-dimensional scattering by an infinite homogeneous anisotropic circular cylinder: A spectral approach," *IEEE Trans. Antennas Propagat.*, vol. 35, no. 6, pp. 670–682, Jun 1987.

[36] S.-C. Mao and Z.-S. Wu, "Scattering by an infinite homogenous anisotropic elliptic cylinder in terms of mathieu functions and fourier series," *J. Opt. Soc. Am. A*, vol. 25, no. 12, pp. 2925–2931, Dec 2008.

[37] A. K. Hamid and F. R. Cooray, "Scattering of a plane wave by a homogeneous anisotropic elliptic cylinder," *IEEE Trans. Antennas Propagat.*, vol. 63, no. 8, pp. 3579–3587, Aug 2015.

[38] Z.-S. Wu, S.-C. Mao, and L. Yang, "Two-dimensional scattering by a conducting elliptic cylinder coated with a homogeneous anisotropic shell," *IEEE Trans. Antennas Propagat.*, vol. 57, no. 11, pp. 3638–3645, Sep. 2009.

[39] R.-B. Wu and C. H. Chen, "Variational reaction formulation of scattering problem for anisotropic dielectric cylinders," *IEEE Trans. Antennas Propagat.*, vol. 34, no. 5, pp. 640–645, May 1986.

[40] J. Wu and K. A. Michalski, "Hybrid FEM-MFCM for 2-D scattering by inhomogeneous anisotropic material cylinders," *IEEE Trans. on Magnetics*, vol. 31, no. 3, pp. 1558–1561, May 1995.

[41] Z. N. Chen, W. Hong, and W. X. Zhang, "Application of FD-MEI to electromagnetic scattering from transversally anisotropic inhomogeneous cylinders," *IEEE Trans. on Electromagn. Compat.*, vol. 40, no. 2, pp. 103–110, May 1998.

[42] R. D. Graglia, P. L. Uslenghi, and R. S. Zich, "Moment method with isoparametric elements for three-dimensional anisotropic scatterers," *Proceedings of the IEEE*, vol. 77, no. 5, pp. 750–760, May 1989.

[43] G. Kobidze and B. Shanker, "Integral equation based analysis of scattering from 3-d inhomogeneous anisotropic bodies," *IEEE Trans. Antennas Propagat.*, vol. 52, no. 10, pp. 2650–2658, Oct. 2004.

[44] C. Forestiere *et al.*, "A frequency stable volume integral equation method for anisotropic scatterers," *IEEE Trans. Antennas Propagat.*, vol. 65, no. 3, pp. 1224–1235, Mar. 2017.

[45] M. S. Tong *et al.*, "Fast solutions of volume integral equations for electromagnetic scattering by large highly anisotropic objects," *IEEE Trans. Microw. Theory Tech.*, vol. 62, no. 7, pp. 1429–1436, Jul. 2014.

[46] G. P. Zouros and G. C. Kokkorakis, "Electromagnetic scattering by a general rotationally symmetric inhomogeneous anisotropic sphere," *IEEE Trans. Antennas Propagat.*, vol. 63, no. 10, pp. 3054–3065, Oct. 2015.

[47] G. D. Kolezas and G. P. Zouros, "Cfvie formulation for em scattering on inhomogeneous anisotropic—metallic objects," *IEEE Trans. Antennas Propagat.*, vol. 65, no. 7, pp. 3788–3793, Jul. 2017.

[48] G. Mumcu, K. Sertel, and J. L. Volakis, "Surface integral equation solutions for modeling 3d uniaxial media using closed-form dyadic green's functions," *IEEE Trans. Antennas Propagat.*, vol. 56, no. 8, pp. 2381–2388, Aug. 2008.

[49] Y. Shi and C.-H. Liang, "Analysis of uniaxial media using calderón-preconditioned single-source combined field integral equation," *IEEE Antennas Wireless Propag. Lett.*, vol. 13, pp. 491–494, 2014.

[50] J. Schneider and S. Hudson, "A finite-difference time-domain method applied to anisotropic material," *IEEE Trans. Antennas Propagat.*, vol. 41, no. 7, pp. 994–999, Jul. 1993.

[51] X.-Q. Sheng and Z. Peng, "Analysis of scattering by large objects with off-diagonally anisotropic material using finite element-boundary integral-multilevel fast multipole algorithm," *IET Microw. Antennas Propag.*, vol. 4, no. 4, pp. 492–500, 2010.

[52] Y.-L. Geng *et al.*, "Mie scattering by a uniaxial anisotropic sphere," *Phys. Rev. E*, vol. 70, no. 5, Nov. 2004.

[53] W. S. Weiglhofer, "Dyadic green's functions for general uniaxial media," *IEE Proceedings H*, vol. 137, no. 1, pp. 5–10, Feb. 1990.

[54] ——, "Analytic methods and free-space dyadic green's functions," *Radio Science*, vol. 28, no. 5, pp. 847–857, 1993.

[55] C. Hafner and N. Kuster, "Computations of electromagnetic fields by the multiple multipole method (generalized multipole technique)," *Radio Science*, vol. 26, no. 1, pp. 291–297, 1991.

[56] Y. A. Eremin and A. Sveshnikov, "The discrete source method for investigating three-dimensional electromagnetic scattering problems," *Electromagnetics*, vol. 13, no. 1, pp. 1–22, 1993.

[57] D. I. Kaklamani and H. T. Anastassiu, "Aspects of the method of auxiliary sources (mas) in computational electromagnetics," *IEEE Antennas Propag. Mag.*, vol. 44, no. 3, pp. 48–64, Jun. 2002.

[58] Y. Leviatan and A. Boag, "Analysis of electromagnetic scattering from dielectric cylinders using a multifilament current model," *IEEE Trans. Antennas Propagat.*, vol. 35, no. 10, pp. 1119–1127, Oct. 1987.

[59] F. Zolla, R. Petit, and M. Cadilhac, "Electromagnetic theory of diffraction by a system of parallel rods: The method of fictitious sources," *J. Opt. Soc. Amer. A, Opt. Image Sci.*, vol. 11, no. 3, pp. 1087–1096, Mar. 1994.

[60] R. Mathon and R. L. Johnston, "The approximate solution of elliptic boundary-value problems by fundamental solutions," *SIAM J. Numer. Anal.*, vol. 14, no. 4, pp. 638–650, 1977.

[61] S. M. Mikki and A. A. Kishk, "Theory and applications of infinitesimal dipole models for computational electromagnetics," *IEEE transactions on antennas and propagation*, vol. 55, no. 5, pp. 1325–1337, 2007.

[62] Y. Shifman, M. Friedmann, and Y. Leviatan, "Analysis of electromagnetic scattering from cylinders with edges using a hybrid moment method," *IEE Proceedings Part H.*, vol. 144, no. 4, pp. 235–240, Aug. 1997.

[63] A. Boag, Y. Leviatan, and A. Boag, "Analysis of two-dimensional electromagnetic scattering from nonplanar periodic surfaces using a strip current model," *IEEE Trans. Antennas Propagat.*, vol. 37, no. 11, pp. 1437–1446, Nov. 1989.

[64] A. Hochman and Y. Leviatan, "Analysis of strictly bound modes in photonic crystal fibers by use of a source-model technique," *J. Opt. Soc. Am. A*, vol. 21, no. 6, pp. 1073–1081, Jun. 2004.

[65] N. V. Larsen and O. Breinbjerg, "Analysis of circularly polarized hemispheroidal dielectric resonator antenna phased arrays using the method of auxiliary sources," *IEEE Trans. Antennas Propagat.*, vol. 55, no. 8, pp. 2163–2173, Aug. 2008.

[66] A. Ludwig and Y. Leviatan, "A source-model technique for the analysis of transient electromagnetic scattering by a periodic array of cylinders," *IEEE Trans. Antennas Propagat.*, vol. 55, no. 9, pp. 2579–2590, Sep. 2007.

[67] J. Liu *et al.*, "Method of auxiliary sources for analyzing half-mode substrate integrated waveguide," *IEEE Antennas Wireless Propag. Lett*, vol. 13, pp. 1043–1046, 2014.

[68] D. Szafranek and Y. Leviatan, "A source-model technique for analysis of scattering by a periodic array of penetrable cylinders partially buried in a penetrable substrate," *IEEE Trans. Antennas Propagat.*, vol. 64, no. 12, pp. 5393–5403, Dec. 2016.

[69] T. Wriedt and E. Yuri, *The Generalized Multipole Technique for Light Scattering: Recent Developments*. Elsevier, 2018.

[70] F. Bogdanov, D. Karkashadze, and R. Zaridze, "New materials design: scattering problems and the method of auxiliary sources," in *Proceedings of III International Seminar/Workshop on Direct and Inverse Problems of Electromagnetic and Acoustic Wave Theory.(IEEE Cat. No. 98EX163)*. IEEE, 1998, pp. 18–21.

[71] S. Hidouri and T. Aguili, "Study of scattering by large dielectric cylinder," in *2012 6th International Conference on Sciences of Electronics, Technologies of Information and Telecommunications (SETIT)*. IEEE, 2012, pp. 217–219.

[72] M. Zhang and W. X. Zhang, "Scattering of electromagnetic waves from a chiral cylinder of arbitrary cross section—gmt approach," *Microwave and Optical Technology Letters*, vol. 10, no. 1, pp. 22–25, 1995.

[73] N. B. Piller and O. J. Martin, "Extension of the generalized multipole technique to three-dimensional anisotropic scatterers," *Optics letters*, vol. 23, no. 8, pp. 579–581, Apr. 1998.

[74] V. V. Varadan, A. Lakhtakia, and V. K. Varadan, "Scattering by three-dimensional anisotropic scatterers," *IEEE Trans. Antennas Propagat.*, vol. 37, no. 6, pp. 800–802, Jun. 1989.

[75] D. Pozar, "Radiation and scattering from a microstrip patch on a uniaxial substrate," *IEEE Trans. Antennas Propagat.*, vol. 35, no. 6, pp. 613–621, Jun. 1987.

[76] T. W. Kim, J. S. Park, and S. O. Park, "A theoretical model for resonance frequency and radiation pattern on rectangular microstrip patch antenna on liquid crystal substrate," *early access, IEEE Trans. Antennas Propagat.*, pp. 1–1, 2018.

[77] P. Kopyt *et al.*, "Modeling of silicon-based substrates of patch antennas operating in the sub-thz range," *IEEE Trans. Antennas Propagat.*, vol. 7, no. 4, pp. 424–432, Jul. 2017.

[78] S. Fakhte, H. Oraizi, and L. Matekovits, "High gain rectangular dielectric resonator antenna using uniaxial material at fundamental mode," *IEEE Trans. Antennas Propagat.*, vol. 65, no. 1, pp. 342–347, Jan. 2017.

[79] S. Fakhte *et al.*, "Cylindrical anisotropic dielectric resonator antenna with improved gain," *IEEE Trans. Antennas Propagat.*, vol. 65, no. 3, pp. 1404–1409, Mar. 2017.

[80] A. Bostani and H. Oraizi, "Analysis and design of tapered uniaxial-anisotropic dielectric rod antennas," *IEEE Trans. Antennas Propagat.*, vol. 65, no. 11, pp. 5787–5795, Sep. 2017.

[81] A. Mehdipour *et al.*, "Reconfigurable tx/rx antenna systems loaded by anisotropic conductive carbon-fiber composite materials," *IEEE Trans. Antennas Propagat.*, vol. 62, no. 2, pp. 1002–1006, Feb. 2014.

[82] N. Alexopoulos, "Integrated-circuit structures on anisotropic substrates," *IEEE Trans. Microwave Theory Tech.*, vol. 33, no. 10, pp. 847–881, Oct. 1985.

[83] B. Ivsic, Z. Sipus, and S. Hrabar, "Analysis of uniaxial multilayer cylinders used for invisible cloak realization," *IEEE Trans. Antennas Propagat.*, vol. 57, no. 5, pp. 1521–1527, May 2009.

[84] C. Xiong, W. H. Pernice, and H. X. Tang, "Low-loss, silicon integrated, aluminum nitride photonic circuits and their use for electro-optic signal processing," *Nano Lett.*, vol. 12, no. 7, pp. 3562–3568, 2012.

[85] J. Krupka *et al.*, "Dielectric properties of single crystals of al2o3, laalo3, ndgao3, srtio3, and mgo at cryogenic temperatures," *IEEE Trans. Microwave Theory Tech.*, vol. 42, no. 10, pp. 1886–1890, Oct. 1994.

[86] R. E. Collin, "A simple artificial anisotropic dielectric medium," *IEEE Trans. Microwave Theory Tech.*, vol. 6, no. 2, pp. 206–209, Apr. 1958.

[87] C. L. Holloway, M. S. Sarto, and M. Johansson, "Analyzing carbonfiber composite materials with equivalent-layer models," *IEEE Trans. on Electromagn. Compat.*, vol. 47, no. 4, pp. 833–844, Nov. 2005.

[88] T. C. Choy, *Effective medium theory: principles and applications.* Oxford University Press, 2015, vol. 165.

[89] P. W. Beaumont and C. Soutis, *The Structural Integrity of Carbon Fiber Composites: Fifty Years of Progress and Achievement of the Science, Development, and Applications.* Springer, 2016.

[90] V. Préault *et al.*, "Shielding effectiveness of composite materials: effect of inclusion shape," *IEEE Trans. on Magnetics*, vol. 49, no. 5, pp. 1941–1944, May 2013.

[91] ——, "Effective permittivity of shielding composite materials for microwave frequencies," *IEEE Trans. on Electromagn. Compat.*, vol. 55, no. 6, pp. 1178–1186, Dec. 2013.

[92] Y. Liao *et al.*, "Equivalent modeling of the microwave dielectric properties for fiber reinforced shielding composites," in *Proc. IEEE Asia-Pacific Int. Symp.on Electromagn. Compat.(APEMC)*, Shenzhen, China, May 2016, pp. 101–104.

[93] C. L. Holloway, M. S. Sarto, and M. Johansson, "Analyzing carbon-fiber composite materials with equivalent-layer models," *IEEE Trans. on Electromagn. Compat.*, vol. 47, no. 4, pp. 833–844, Nov. 2005.

[94] K. F. Casey, "Emp penetration through advanced composite skin panels," *Interaction Notes 315*, Dec. 1976.

[95] M. S. Sarto, "A matrix surface impedance formulation for the analysis of eminteractions to finite laminated composite slabs," in *Proc. IEEE Int. Symp. EMC*, CA, USA, Aug. 1996, pp. 168–173.

[96] M. S. Sarto and C. L. Holloway, "Effective boundary conditions for the time-domain analysis of the emc performances of fiber composites," in *Proc. IEEE Int. Symp. EMC*, Seattle, USA, Aug. 1999, pp. 462–467.

[97] M. S. Sarto, "Fdtd analysis of field penetration inside thin composite shells," in *Proc. URSI Electromagnetic Theory Symp.*, Thessaloniki, Greece, May 1998, pp. 674–676.

[98] ——, "A new model for the fdtd analysis of the shielding performances of thin composite structures," *IEEE Trans. on Electromagn. Compat.*, vol. 41, no. 4, p. 298–306, Nov. 1999.

[99] K. Wang, J. J. Laurin, and K. Wu, "Shielding effectiveness analysis of carbon fiber composite material using tensor impedance boundary condition (tibc)," in *Proc. IEEE Int. Symp. EMC*, Washington,DC, USA, Aug. 2017, pp. 293–298.

[100] R. Paknys, *Applied frequency-domain electromagnetics.* John Wiley & Sons, 2016.

[101] Computer Simulation Technology, 2018. [Online]. Available: https://www.cst.com/

[102] C. A. Valagiannopoulos, "How nonreciprocal is an effective permittivity matrix?" *Microwave and Optical Technology Letters*, vol. 56, no. 9, pp. 2018–2021, 2014.

[103] C. A. Valagiannopoulos *et al.*, "Pockels cover for switchable control of the reflection from a grounded, isotropic, lossy dielectric slab," *Journal of Applied Physics*, vol. 117, no. 8, p. 083105, 2015.

[104] Y. Leviatan and A. Boag, "Analysis of te scattering from dielectric cylinders using a multifilament magnetic current model," *IEEE Trans. Antennas Propagat.*, vol. 36, no. 7, pp. 1026–1031, Jul. 1988.

[105] Y. Leviatan and M. Haller, "Analysis of electromagnetic scattering from a slot-perforated conducting cylindrical shell using a multifilament current model," *Journal of Electromagnetic Waves and Applications*, vol. 5, no. 1, pp. 59–74, 1991.

[106] Y. Leviatan, "Analytic continuation considerations when using generalized formulations for scattering problems," *IEEE Trans. Antennas Propagat.*, vol. 38, no. 8, pp. 1259–1263, Aug. 1990.

[107] H. T. Anastassiu and D. I. Kaklamani, "Error estimation and optimization of the method of auxiliary sources (mas) for scattering from a dielectric circular cylinder," *Radio Science*, vol. 39, no. 5, p. RS5015, 2004.

[108] G. Fikioris, "On two types of convergence in the method of auxiliary sources," *IEEE Trans. Antennas Propagat.*, vol. 54, no. 7, pp. 2022–2033, Jul. 2006.

[109] N. L. Tsitsas *et al.*, "Optimization of the method of auxiliary sources (mas) for oblique incidence scattering by an infinite dielectric cylinder," *Elect. Eng.*, vol. 89, pp. 353–361, May 2007.

[110] C. A. Valagiannopoulos, N. L. Tsitsas, and G. Fikioris, "Convergence analysis and oscillations in the method of ctitious sources applied to dielectric scattering problems," *J. Opt. Soc. Amer. A*, vol. 29, no. 1, pp. 1–10, Jan. 2012.

[111] H. T. Anastassiu, D. G. Lymperopoulos, and D. I. Kaklamani, "Accuracy analysis and optimization of the method of auxiliary sources (mas) for scattering by a circular cylinder," *IEEE Trans. Antennas Propagat.*, vol. 52, no. 6, pp. 1541–1547, Jun. 2004.

[112] E. Falek and S. Reuven, "A new concept for a flat lens design using dielectric cylinders," *IEEE Trans. Antennas Propagat.*, vol. 65, no. 11, pp. 5720–5731, Nov. 2017.

[113] Y. Zhao, P. A. Belov, and Y. Hao, "Modelling of wave propagation in wire media using spatially dispersive finite-difference time-domain method: Numerical aspects," *IEEE Trans. Antennas Propagat.*, vol. 55, no. 6, pp. 1506–1513, Jun. 2007.

[114] K. Mitzner, "Effective boundary conditions for reflection and transmission by an absorbing shell of arbitrary shape," *IEEE Trans. Antennas Propagat.*, vol. 16, no. 6, pp. 706–712, Nov. 1968.

[115] M.-S. Lin and C. H. Chen, "Plane-wave shielding characteristics of anisotropic laminated composites," *IEEE Trans. on Electromagn. Compat.*, vol. 35, no. 1, pp. 21–27, Feb. 1993.

[116] C. N. Chiu and C. H. Chen, "Plane-wave shielding properties of anisotropic laminated composite cylindrical shells," *IEEE Trans. on Electromagn. Compat.*, vol. 37, no. 1, pp. 109–113, Feb. 1995.

[117] C.-N. Chiu and C. H. Chen, "Scattering from an advanced composite cylindrical shell," *IEEE Trans. on Electromagn. Compat.*, vol. 38, no. 1, pp. 62–67, Feb. 1996.

[118] A. Karlsson, "Approximate boundary conditions for thin structures," *IEEE Trans. Antennas Propagat.*, vol. 57, no. 1, pp. 144–148, Jan 2009.

[119] P.-R. Renaud and J. J. Laurin, "Shielding and scattering analysis of lossy cylindrical shells using an extended multifilament current approach," *IEEE Trans. on Electromagn. Compat.*, vol. 41, no. 4, pp. 320–334, Nov. 1999.

[120] Y. Leviatan and A. Boag, "Analysis of electromagnetic scattering from dielectric cylinders using a multifilament current model," *IEEE Trans. Antennas Propagat.*, vol. 35, no. 10, pp. 1119–1127, Oct. 1987.

[121] ——, "Analysis of te scattering from dielectric cylinders using a multifilament magnetic current model," *IEEE Trans. Antennas Propagat.*, vol. 36, no. 7, pp. 1026–1031, Jul. 1988.

[122] K. Wang, J. Laurin, and K. Wu, "Scattering and shielding analyses of carbon fiber composites-based cylindrical shells using a multifilament doublet current method)," *IEEE Trans. on Electromagn. Compat.*, vol. pp, no. pp, pp. 1–10, Aug. 2018.

[123] C. M. Butler, Y. Rahmat-Samii, and R. Mittra, "Electromagnetic penetration through apertures in conducting surfaces," *IEEE Trans. on Electromagn. Compat.*, vol. 20, no. 1, pp. 82–93, Feb. 1978.

[124] J. R. Mautz and R. F. Harrington, "Electromagnetic penetration into a conducting circular cylinder through a narrow slot, tm case," *J. Electromagn. Waves Applicat.*, vol. 2, no. 3, pp. 269–293, 1988.

[125] R. W. Ziolkowski and J. Grant, "Scattering from cavity-backed apertures: The generalized dual series solution of the concentrically loaded -pol slit cylinder problem," *IEEE Trans. Antennas Propag.*, vol. 35, no. 5, pp. 504–528, May 1987.

[126] M. P. Ioannidou, "Em wave scattering by an axial slot on a circular pec cylinder with an eccentrically layered inner coating: A dual-series solution for te polarization," *IEEE Trans. Antennas Propagat.*, vol. 57, no. 11, pp. 3512–3519, Nov. 2009.

[127] M. P. Ioannidou, A. P. Moneda, and I. O. Vardiambasis, "Dual-series solution to em-wave scattering by a circular slit pec cylinder enclosing multiple dielectric cylindrical rods," *IEEE Trans. Antennas Propagat.*, vol. 60, no. 10, pp. 4822–4829, Oct. 2012.

[128] J. D. Shumpert and C. M. Butler, "Penetration through slots in conducting cylinders—part 2: Tm case," *IEEE Trans. Antennas Propagat.*, vol. 46, no. 11, pp. 1622–1628, Nov. 1998.

[129] A. Boag, Y. Leviatan, and A. Boag, "Analysis of electromagnetic scattering from a slot-perforated conducting cylindrical shell using a multifilament current model," *J. Electromagn. Waves Applicat.*, vol. 5, no. 1, pp. 59–74, 1991.

[130] J. A. Beren, "Diffraction of an h-polarized electromagnetic waveby a circular cylinder with an infinite axial slot," *IEEE Trans. Antennas Propagat.*, vol. 31, no. 3, pp. 419–425, May 1983.

[131] Y. C. Noh and S. D. Choi, "Tm scattering from a hollow slotted circular cylinder with thickness," *IEEE Trans. on Electromagn. Compat.*, vol. 45, no. 5, pp. 909–910, May 1997.

[132] Altair FEKO, 2018. [Online]. Available: https://altairhyperworks.com/product/FEKO

[133] ANSYS Electronics Desktop, version 19.0. [Online]. Available: https://www.ansys.com/

[134] E. F. Kuester *et al.*, "Averaged transition conditions for electromagnetic fields at a metafilm," *IEEE Trans. Antennas Propagat.*, vol. 51, no. 10, pp. 2641–2651, Oct. 2003.

[135] C. L. Holloway *et al.*, "Use of generalized sheet transition conditions to model guided waves on metasurfaces/metafilms," *IEEE Trans. Antennas Propagat.*, vol. 60, no. 11, pp. 5173–5186, Nov. 2012.

[136] ——, "An overview of the theory and applications of metasurfaces: The two-dimensional equivalents of metamaterials," *IEEE Antennas Propag. Mag.*, vol. 54, no. 2, pp. 10–35, 2012.

[137] Y. Vahabzadeh, K. Achouri, and C. Caloz, "Simulation of metasurfaces in finite difference techniques," *IEEE Transactions on Antennas and Propagation*, vol. 64, no. 11, pp. 4753–4759, 2016.

[138] S. Sandeep, J.-M. Jin, and C. Caloz, "Finite-element modeling of metasurfaces with generalized sheet transition conditions," *IEEE Transactions on Antennas and Propagation*, vol. 65, no. 5, pp. 2413–2420, 2017.

[139] S. Sandeep and S. Y. Huang, "Simulation of circular cylindrical metasurfaces using gstc-mom," *IEEE Journal on Multiscale and Multiphysics Computational Techniques*, vol. 3, pp. 185–192, 2018.

[140] M. Dehmollaian, N. Chamanara, and C. Caloz, "Wave scattering by a cylindrical metasurface cavity of arbitrary cross-section: Theory and applications," *IEEE Trans. Antennas Propagat.*, vol. 67, no. 6, pp. 4059–4072, Jun. 2019.

[141] A. Shahi and A. Abdolali, "Cylinder scattering pattern manipulation for dual-polarized radar cross-section reduction using inhomogeneous metasurface," in *Electrical Engineering (ICEE), 2017 Iranian Conference on.* IEEE, 2017, pp. 1691–1696.

[142] B. O. Raeker and S. M. Rudolph, "Verification of arbitrary radiation pattern control using a cylindrical impedance metasurface," *IEEE Antennas and Wireless Propagation Letters*, vol. 16, pp. 995–998, 2017.

[143] J. C. Soric *et al.*, "Controlling scattering and absorption with metamaterial covers," *IEEE Transactions on Antennas and Propagation*, vol. 62, no. 8, pp. 4220–4229, 2014.

[144] B. O. Raeker and S. M. Rudolph, "Arbitrary transformation of radiation patterns using a spherical impedance metasurface," *IEEE Transactions on Antennas and Propagation*, vol. 64, no. 12, pp. 5243–5250, 2016.

[145] K. Achouri, M. A. Salem, and C. Caloz, "General metasurface synthesis based on susceptibility tensors," *IEEE Trans. Antennas Propagat.*, vol. 63, no. 7, pp. 2977–2991, Jul. 2015.

[146] C. L. Holloway and E. F. Kuester, "A homogenization technique for obtaining generalized sheet-transition conditions for a metafilm embedded in a magnetodielectric interface," *IEEE Trans. Antennas Propagat.*, vol. 64, no. 11, pp. 4671–4686, Nov. 2016.

[147] ——, "Generalized sheet transition conditions for a metascreen—a fishnet metasurface," *IEEE Trans. Antennas Propagat.*, vol. 66, no. 5, pp. 2414–2427, May 2018.

[148] K. Wang, J. J. Laurin, and K. Wu, "Two-dimensional scattering from homogenous anisotropic cylinders using a multifilament current method (mfcm)," *Submitted to IEEE Trans. Antennas Propagat.*, vol. pp, no. pp, 2019.

[149] G. K. Avdikos and H. T. Anastassiu, "Computational cost estimations and comparisons for three methods of applied electromagnetics (mom, mas, mmas)," *IEEE Antennas and Propag. Mag.*, vol. 47, no. 1, pp. 121–129, 2005.

[150] S. Rao, D. Wilton, and A. Glisson, "Electromagnetic scattering by surfaces of arbitrary shape," *IEEE Transactions on antennas and propagation*, vol. 30, no. 3, pp. 409–418, May 1982.

[151] W. Weiglhofer, "Symbolic derivation of the electrodynamic green's tensor in an anisotropic medium," *American Journal of Physics*, vol. 56, no. 12, pp. 1095–1097, 1988.

[152] ——, "A simple and straightforward derivation of the dyadic green's function of an isotropic chiral medium," *AEU. Archiv für Elektronik und Übertragungstechnik*, vol. 43, no. 1, pp. 51–52, 1989.

[153] W. S. Weiglhofer, "A general inversion technique for a class of dyadic differential operators of electromagnetic theory," in *Proc. URSI Int. Symp. Electromag. Theory, Royal Institute of Technology, Stockholm, Sweden*, 1989, pp. 10–12.

[154] D. Kaklamani and N. Uzunoglu, "Radiation of a dipole in an infinite triaxial anisotropic medium," *Electromagnetics*, vol. 12, no. 3-4, pp. 231–245, 1992.

[155] A. Lakhtakia and W. Weiglhofer, "Scattering by an electrically small bianisotropic sphere in a gyroelectromagnetic uniaxial medium," *IEE Proc. H-Microwaves, Antennas and Propagation*, vol. 139, no. 3, pp. 217–220, 1992.

[156] J. Monzon, "Radiation and scattering in homogeneous general biisotropic regions," *IEEE Trans. Antennas Propagat.*, vol. 38, no. 2, pp. 227–235, Feb. 1990.

[157] Y. Leviatan and A. Boag, "Generalized formulations for electromagnetic scattering from perfectly conducting and homogeneous material bodies-theory and numerical solution," *IEEE Trans. Antennas Propagat.*, vol. 36, no. 12, pp. 1722–1734, Dec. 1988.

[158] Z.-S. Wu *et al.*, "Internal and external electromagnetic fields for on-axis gaussian beam scattering from a uniaxial anisotropic sphere," *J. Opt. Soc. Am. A*, vol. 26, no. 8, pp. 1778–1787, Aug. 2009.

[159] MathWorks, MATLAB R2017b. [Online]. Available: https://www.mathworks.com/

[160] M. A. Moharram and A. A. Kishk, "Efficient electromagnetic scattering computation using the random auxiliary sources method for multiple composite 3-d arbitrary objects," *IEEE Trans. Antennas Propagat.*, vol. 63, no. 8, pp. 3621–3633, Aug. 2015.

[161] J. Song, C. C. Lu, and W. C. Chew, "Multilevel fast multipole algorithm for electromagnetic scattering by large complex objects," *IEEE Trans. Antennas Propagat.*, vol. 45, no. 10, pp. 1488–1493, Oct. 1997.

[162] E. Bleszynski, M. Bleszynski, and T. Jaroszewicz, "Adaptive integral method for solving large-scale electromagnetic scattering and radiation problems," *Radio Sci.*, vol. 31, no. 5, pp. 1225–1251, Sep.-Oct. 1996.

[163] E. Michielsen and A. Boag, "A multilevel matrix decomposition algorithm for analyzing scattering from large structures," *IEEE Trans. Antennas Propagat.*, vol. 44, no. 8, p. 1086–1093, Aug. 1996.

[164] J. M. Rius *et al.*, "Multilevel matrix decomposition algorithm for analysis of electrically large electromagnetic problems in 3-d," *Microw. Opt. Technol. Lett.*, vol. 22, no. 3, pp. 177–182, Aug. 1999.

[165] J. Parrón, J. M. Rius, and J. R. Mosig, "Application of the multilevel decomposition algorithm to the frequency analysis of large microstrip antenna arrays," *IEEE Trans. Magn.*, vol. 38, no. 2, pp. 721–724, Mar. 2002.

[166] J. M. Rius *et al.*, "Fast iterative solution of integral equations with method of moments and matrix decomposition algorithm—singular value decomposition," *IEEE Trans. Antennas Propagat.*, vol. 56, no. 8, p. 2314–2324, Aug. 2008.

[167] A. Heldring *et al.*, "Fast direct solution of method of moments linear system," *IEEE Trans. Antennas Propagat.*, vol. 55, no. 11, pp. 3220–3228, Nov. 2007.

[168] ——, "Multiscale compressed block decomposition for fast direct solution of method of moments linear system," *IEEE Trans. Antennas Propagat.*, vol. 59, no. 2, pp. 526–536, Feb. 2011.

[169] E. Erez and L. Yehuda, "Analysis of natural frequencies of cavities and scatterers using an impulsive current model," *IEEE Trans. Antennas Propagat.*, vol. 38, no. 4, pp. 534–540, Apr. 1990.

[170] Y.-M. Pan, K.-W. Leung, and K. Lu, "Study of resonant modes in rectangular dielectric resonator antenna based on radar cross section," *early access on IEEE Trans. Antennas Propagat.*, 2019.

[171] A. Hochman and Y. Leviatan, "Efficient and spurious-free integral-equation-based optical waveguide mode solver," *Optics express*, vol. 15, no. 22, pp. 14 431–14 453, 2007.

[172] J. Shaeffer, "Direct solve of electrically large integral equations for problem sizes to 1 m unknowns," *IEEE Trans. Antennas Propagat.*, vol. 56, no. 8, pp. 2306–2313, Aug. 2008.

[173] A. Heldring *et al.*, "Accelerated direct solution of the method-of-moments linear system," *Proceedings of the IEEE*, vol. 101, no. 2, pp. 364–371, 2013.

[174] X. Fang *et al.*, "Multiscale compressed block decomposition method with characteristic basis function method and fast adaptive cross approximation," *IEEE Transactions on Electromagnetic Compatibility*, no. 61, pp. 191–199, 2019.

APPENDIX A PROPAGATION MODES OF UNBOUND REGION CONSTITUTE OF CARBON-FIBER COMPOSITE MATERIAL

With the tensor permittivity in (3.2), we will investigate the propagation modes inside of unbounded CFC material. The two vector wave equations are given below:

$$\nabla' \times \nabla' \times \boldsymbol{E}' - \omega^2 \mu_0 \bar{\epsilon} \boldsymbol{E}' = 0 \tag{A.1a}$$

$$\nabla' \times (\bar{\epsilon}^{-1} \cdot \nabla' \times \boldsymbol{H}') - \omega^2 \mu_0 \boldsymbol{H}' = 0 \tag{A.1b}$$

The $'$ is used to indicate the derivation is conducted in the local coordinates as shown in Fig. 3.2. Applying the condition $\nabla' \cdot \boldsymbol{H}' = 0$ to the y'-component (the distinguished axis of uniaxial CFC material) of (A.1b) yields a scalar equation for:

$$\frac{\partial^2 H'_y}{\partial x'^2} + \frac{\partial^2 H'_y}{\partial y'^2} + \frac{\partial^2 H'_y}{\partial z'^2} + \omega^2 \mu_0 \epsilon_a H'_y = 0 \tag{A.2}$$

The H'_y is used to find E'_x, E'_z, and then constituting the TM' case. Similarly, applying the condition $\nabla' \cdot (\bar{\epsilon} \cdot \boldsymbol{E}') = 0$ to the y'-component of (A.1a) yields a scalar equation for:

$$\frac{\partial^2 E'_y}{\partial x'^2} + \frac{\epsilon_b}{\epsilon_a} \frac{\partial^2 E'_y}{\partial y'^2} + \frac{\partial^2 E'_y}{\partial z'^2} + \omega^2 \mu_0 \epsilon_b E'_z = 0 \tag{A.3}$$

It is easy to obtain H'_x, H'_z from E'_y and then forming TE' case. By assuming oblique plane wave propagation of the form $E'(H')_z = \boldsymbol{M_0} e^{-j(k'_x x' + k'_y y' + k'_z z')}$, and substituting it into (A.2) and (A.3) will result in propagation modes:

$$k'^2_{za} = \omega^2 \mu_0 \epsilon_a - k'^2_x - k'^2_y \tag{A.4a}$$

for the TM$'$ case, and

$$k'^2_{zb} = \omega^2 \mu_0 \epsilon_b - k'^2_x - \frac{\epsilon_b}{\epsilon_a} k'^2_y \tag{A.4b}$$

for the TE$'$ case.

APPENDIX B INCIDENT ANGLE INDEPENDENT TIBC

Generally, the TIBC for an anisotropic material is highly related on incident angle (θ), however, the dependence on the incident angle can be neglected under certain conditions for CFC materials containing high conductivity carbon fibres. Moreover, in practical problems, the incident field is not a plane wave with a well-defined polarization and angle of incidence, but it could be a non-uniform spherical wave coming from a nearby source such as an antenna. Therefore, a TIBC which is not sensitive to incident angle would be much more useful in 3D electromagnetic field solvers. The incident angle is involved in the calculation of the propagation constants of the two orthogonal modes inside of the CFC material as shown in the expressions (A.4).

In the 3D case, as shown in Fig. B.1, $k_x = k_0 \sin\theta \cos\gamma$ and $k_y = k_0 \sin\theta \sin\gamma$,where γ is the azimuthal angle defining the plane of incidence. Let us consider the case where of a CFC material in which the fibre orientation is along x-axis. The conductivity in x direction will be quite high compared with that in perpendicular directions. Therefore the k_x and k_y items in (A.4a) are very small compared with the term $\omega^2\mu_0\epsilon_a$ and they can be neglected. We therefore have angle-independent propagation constants (B.1a). However, if the conductivity in the direction perpendicular to the fibre orientation is quite low, the k_x and k_y items in (A.4b) are comparable to $\omega^2\mu_0\epsilon_b$. In this case it may be inaccurate to ignore the two items randomly. However, the term containing k_y in (A.4b) can be neglected because the value of ϵ_b/ϵ_a is quite small.

$$k'^2_{za} \approx \omega^2\mu_0\epsilon_a \tag{B.1a}$$

$$k'^2_{zb} \approx \omega^2\mu_0\epsilon_b \tag{B.1b}$$

Under certain conditions, it is possible to neglect the k_x^2 and k_y^2 terms in (A.4b) and then make the resulting k_{zb} independent of the incidence angle as shown in (B.1b). Supposing the direction perpendicular to fibre orientation has a complex permittivity $\epsilon_u = \epsilon_r\epsilon_0 + j\sigma_u/\omega$, once the conditions expressed in (B.2) are satisfied, it is safe to omit the k_x^2 and k_y^2 terms in (A.4b), and form an incident angle independent TIBC.

$$\mid \sqrt{\frac{\epsilon_r}{\epsilon_r - 1}\frac{\cot(k_z d)}{\cot(kd)}} - 1 \mid \leqslant 5\% \tag{B.2a}$$

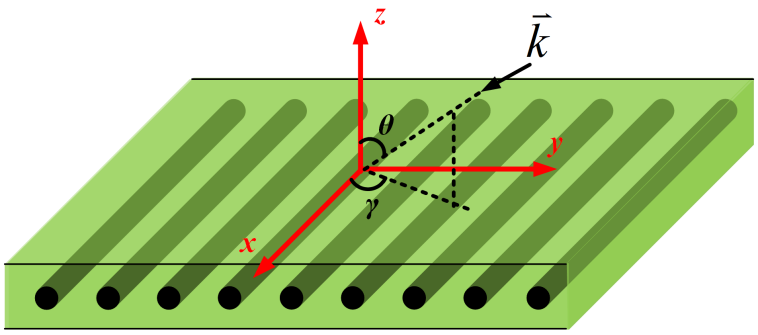

Figure B.1 Constructed impedance matrix in different levels.

$$|\sqrt{\frac{\epsilon_r}{\epsilon_r-1}\frac{\csc(k_z d)}{\csc(kd)}}-1|\leqslant 5\% \tag{B.2b}$$

where

$$k_z = k_0\sqrt{\epsilon_r - 1 - j\frac{\sigma_u}{\omega\epsilon_0}}; \quad k = k_0\sqrt{\epsilon_r - j\frac{\sigma_u}{\omega\epsilon_0}}$$

This condition is obtained by comparing the elements of TIBC matrix, defined in (3.8), under different propagation constants k_z and k as indicated in (B.2). Moreover, we have assumed $\theta = 90^\circ$ and $\gamma = 0^\circ$ to represent the worst case to obtain an incident angle-independent TIBC. When these conditions are satisfied, we can calculate the TIBC without considering the incident angles.

APPENDIX C MODES DISTRIBUTIONS OF A CFC-BASED CYLINDRICAL SHELL UNDER TM PLANE WAVE ILLUMINATION

In Fig. 3.12(b), the SE performance of a 4-layer CFC based shell with a fiber orientation pattern [0/45/90/-45] is presented under the illumination of TM and TE plane waves. The peaks of SE response correspond to the internal modes of the 4-layer CFC-based shell, and both TE and TM modes are excited under the TM or TE illumination. In this appendices, we plot the field distributions of the first ten modes under the TM plane wave illumination. The first four TM modes are plotted in Fig. C.1 and the first six TE modes are displayed in Fig. C.2. Since the 4-layer CFC-based shell can provide a good shielding of external fields, there is a big difference on the intensity of the fields inside and outside of the shell. In this case, the contrast of field distribution within the shell, for the modes TM_{01} and TM_{02}, would not be clear.

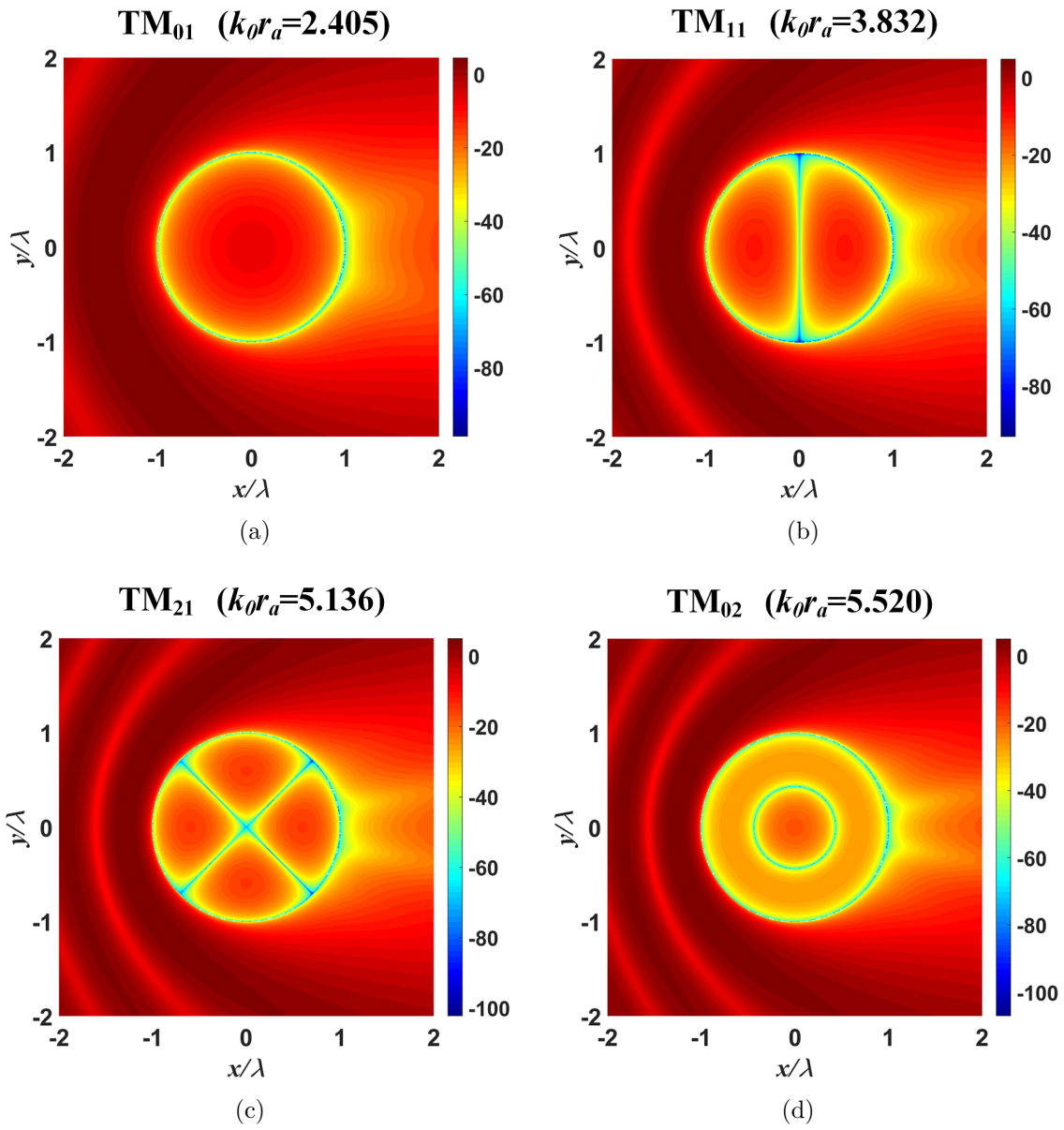

Figure C.1 $|E_z|$ (dB) component of the first four TM modes for a 4-layer CFC-based shell with with a fiber orientation pattern [0/45/90/-45] under the TM plane wave illumination.($\epsilon_a = 3.4\epsilon_0 - j40000/\omega$, $\epsilon_b = 5.0\epsilon_0 - j50/\omega$ and d=0.127 mm for each single CFC-based layer, r_a=1 m).

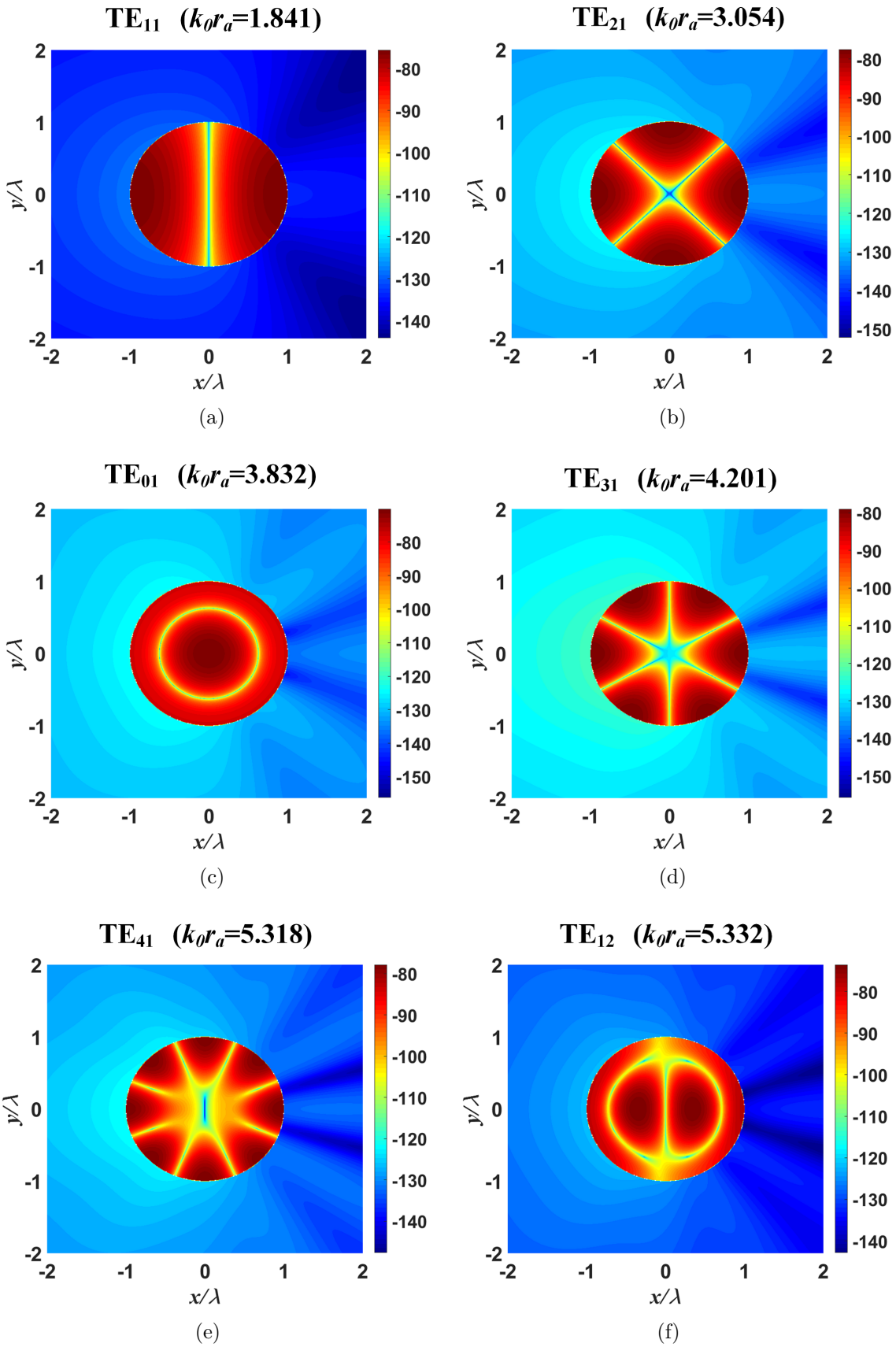

Figure C.2 $|H_z|$ (dB) component of the first six TE modes for a 4-layer CFC-based shell with with a fiber orientation pattern [0/45/90/-45] under the TM plane wave illumination.($\epsilon_a = 3.4\epsilon_0 - j40000/\omega$, $\epsilon_b = 5.0\epsilon_0 - j50/\omega$ and d=0.127 mm for each single CFC-based layer, r_a=1 m).

APPENDIX D DERIVATION OF IMPEDANCE-TYPE GSTC

The vector form or scalar form of GSTC was introduced in [134–136,145–147], and it usually casts in the form relating the difference and average of transverse electric and magnetic fields on the two sides of a metasurface. Considering a two-dimensional problem as shown in Fig. D.1, the GSTC in local coordinate system reads:

$$\begin{aligned}\begin{bmatrix} -\Delta H_z \\ \Delta H_t \end{bmatrix} =& j\omega\epsilon_0 \begin{bmatrix} \chi_{ee}^{tt} & \chi_{ee}^{tz} \\ \chi_{ee}^{zt} & \chi_{ee}^{zz} \end{bmatrix} \begin{bmatrix} E_{t,av} \\ E_{z,av} \end{bmatrix} \\ &+ jk_0 \begin{bmatrix} \chi_{em}^{tt} & \chi_{em}^{tz} \\ \chi_{em}^{zt} & \chi_{em}^{zz} \end{bmatrix} \begin{bmatrix} H_{t,av} \\ H_{z,av} \end{bmatrix}\end{aligned} \tag{D.1a}$$

$$\begin{aligned}\begin{bmatrix} \Delta E_z \\ -\Delta E_t \end{bmatrix} =& jk_0 \begin{bmatrix} \chi_{me}^{tt} & \chi_{me}^{tz} \\ \chi_{me}^{zt} & \chi_{me}^{zz} \end{bmatrix} \begin{bmatrix} E_{t,av} \\ E_{z,av} \end{bmatrix} \\ &+ j\omega\mu_0 \begin{bmatrix} \chi_{mm}^{tt} & \chi_{mm}^{tz} \\ \chi_{mm}^{zt} & \chi_{mm}^{zz} \end{bmatrix} \begin{bmatrix} H_{t,av} \\ H_{z,av} \end{bmatrix}\end{aligned} \tag{D.1b}$$

where χ_{ee}, χ_{mm}, χ_{em} and χ_{me} are the electric/magnetic (first e/m subscripts) surface susceptibilities reacting to electric/magnetic (second e/m subscripts) excitations. $k_0 = \omega\sqrt{\epsilon_0\mu_0}$ is the wave number in free space. The subscripts 1 and 2 are used for referring to region 1, where the incident and reflected fields are involved, and region 2, where only the transmitted fields are involved, respectively. Either the region a or b in Fig. D.1 could be the region 1 or 2 depending on the locations of excitations. $\Delta\psi = \psi_1 - \psi_2$ in (D.1) denotes the jump discontinuity of the tangential field component ψ, and $\psi_{av} = (\psi_1 + \psi_2)/2$, where $\psi = \{E, H\}$. We then expand (D.1) into four equations in terms of regions 1 and 2:

$$H_{2z} - H_{1z} = A_{11}(E_{1t} + E_{2t}) + A_{21}(E_{1z} + E_{2z}) + B_{11}(H_{1t} + H_{2t}) + B_{12}(H_{1z} + H_{2z}) \tag{D.2a}$$

$$H_{1t} - H_{2t} = A_{21}(E_{1t} + E_{2t}) + A_{22}(E_{1z} + E_{2z}) + B_{21}(H_{1t} + H_{2t}) + B_{22}(H_{1z} + H_{2z}) \tag{D.2b}$$

$$E_{1z} - E_{2z} = D_{11}(E_{1t} + E_{2t}) + D_{21}(E_{1z} + E_{2z}) + C_{11}(H_{1t} + H_{2t}) + C_{12}(H_{1z} + H_{2z}) \tag{D.2c}$$

$$E_{2t} - E_{1t} = D_{21}(E_{1t} + E_{2t}) + D_{22}(E_{1z} + E_{2z}) + C_{21}(H_{1t} + H_{2t}) + C_{22}(H_{1z} + H_{2z}) \tag{D.2d}$$

with

$$\begin{bmatrix} A_{11} & A_{12} \\ A_{21} & A_{22} \end{bmatrix} = \frac{1}{2} j\omega\epsilon_0 \begin{bmatrix} \chi_{ee}^{tt} & \chi_{ee}^{tz} \\ \chi_{ee}^{zt} & \chi_{ee}^{zz} \end{bmatrix}; \begin{bmatrix} B_{11} & B_{12} \\ B_{21} & B_{22} \end{bmatrix} = \frac{1}{2} jk_0 \begin{bmatrix} \chi_{em}^{tt} & \chi_{em}^{tz} \\ \chi_{em}^{zt} & \chi_{em}^{zz} \end{bmatrix}$$

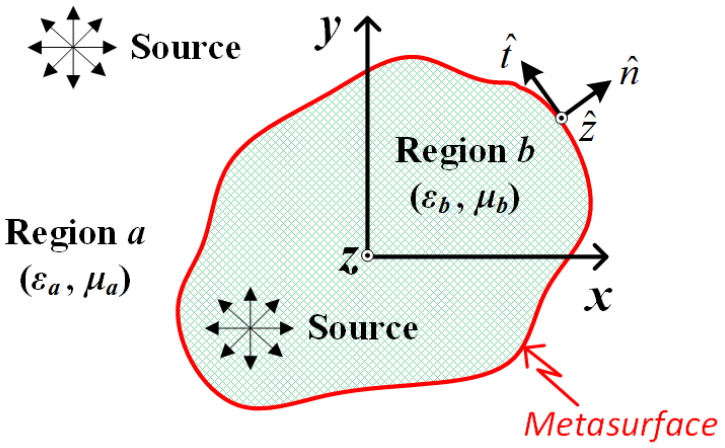

Figure D.1 Problem description.

$$\begin{bmatrix} C_{11} & C_{12} \\ C_{21} & C_{22} \end{bmatrix} = \frac{1}{2} j\omega\mu_0 \begin{bmatrix} \chi_{mm}^{tt} & \chi_{mm}^{tz} \\ \chi_{mm}^{zt} & \chi_{mm}^{zz} \end{bmatrix}; \begin{bmatrix} D_{11} & D_{12} \\ D_{21} & D_{22} \end{bmatrix} = \frac{1}{2} jk_0 \begin{bmatrix} \chi_{me}^{tt} & \chi_{me}^{tz} \\ \chi_{me}^{zt} & \chi_{me}^{zz} \end{bmatrix}$$

Now, classifying the tangential electric and magnetic fields to the left and right sides, respectively, and transforming (D.2) into matrix form, we will have

$$[L] \begin{bmatrix} E_{1t} \\ E_{2t} \\ E_{1z} \\ E_{2z} \end{bmatrix} = [R] \begin{bmatrix} H_{1z} \\ H_{2z} \\ H_{1t} \\ H_{2t} \end{bmatrix} \tag{D.3}$$

with

$$[L] = \begin{bmatrix} A_{11} & A_{11} & A_{12} & A_{12} \\ A_{21} & A_{21} & A_{22} & A_{22} \\ D_{11} & D_{11} & D_{12}+1 & D_{12}-1 \\ D_{21}-1 & D_{21}+1 & D_{22} & D_{22} \end{bmatrix}$$

$$[R] = -\begin{bmatrix} B_{12}-1 & B_{12}+1 & B_{11} & B_{11} \\ B_{22} & B_{22} & B_{21}+1 & B_{21}-1 \\ C_{12} & C_{12} & C_{11} & C_{11} \\ C_{22} & C_{22} & C_{21} & C_{21} \end{bmatrix}$$

Equation (D.3) is the derived impedance-type GSTC.

APPENDIX E LIMITATION ON USE OF BLOCK DECOMPOSITION ALGORITHM

A fast direct solution of MoM linear system has been proposed in [167, 168, 172–174]. This method approximates the impedance matrix with the concept of matrix decomposition algorithm (MDA) [163–165]. Once the impedance matrix is constructed, the block decomposition method (BDA) is applied to solve for the unknowns efficiently. It seems that the simulation performance of the ESM could be drastically improved if the BDA can be deployed for solving the established linear system, yet in fact there are problems in employing the BDA into the ESM.

In Chapter 5, we have explored the ESM on the simulation of a relatively large scatterer. Specifically, the construction time of an impedance matrix can be reduced significantly if the investigated object is symmetrical. Once the impedance matrix is constructed, the unknowns can be obtained by the multiplication between the inverse impedance matrix and excitation vectors. Usually, a non-square impedance matrix will be finally constructed according to the strategy introduced above. It is found the matrix in a rectangular form results a larger CPU time than the matrix in a square form, and this is due to the computation using smallest least-square error solution is more complex than using the LU decomposition for solving the unknown currents coefficients. Moreover, the non-square matrix can generate errors in using the block decomposition method. In this case, additional sources are added after the $SPWm$ and $SPWs$ are fixed for a specific object. These sources are uniformly placed on a quarter circle in the middle of a octant in order to satisfy the condition:

$$2N_m^b = 3N_s^b + 3N_{add}^b + N_{com} \tag{E.1}$$

with

$$N_{add}^b = \lfloor \frac{2N_m^b - 3N_s^b}{3} \rfloor$$

where $\lfloor\rfloor$ symbol represents the flooring function used to obtain an integer value. $N_{add}^b + \lceil N_{com}/3 \rceil$ points are then placed on a quarter circle. In the first octant, this quarter circle is specified with $\phi = 45^\circ$, θ ranges from 0 to $\pi/2$ and radius $r_{13} = (r_{12} + r_{21})/2$. In the first N_{add}^b points, each IDT is placed at each point. N_{com} could be 0, 1 or 2. If $N_{com} = 1$, the last point is placed with a $\hat{\boldsymbol{x}}$-polarized infinitesimal dipole with a uniform magnitude. Otherwise two infinitesimal dipoles with $\hat{\boldsymbol{x}}$ and $\hat{\boldsymbol{y}}$ polarizations are placed at the last point. Based on the above scheme, a square impedance matrix is finally generated.

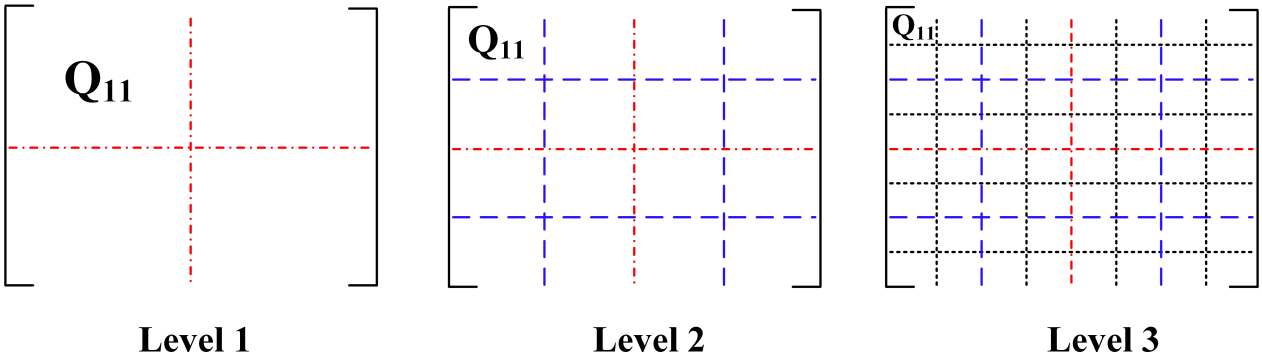

Figure E.1 Constructed impedance matrix in different levels.

The inverse operation of the impedance matrix is usually conducted with LU (or QR) decomposition for a square matrix, yet the inverse operation suffers a high computational cost when the matrix is dense, which happens when a large object is encountered. One possible solution to solve this issue is to utilized the block decomposition algorithm (BDA). The BDA is proposed in [167] for a impedance matrix with arbitrary number of blocks. A multiscale BDA is proposed in [168] for a matrix with $2^n \times 2^n$ blocks, where n is the number of levels. Since the impedance matrix constructed in our formulation has 8×8 blocks, the multiscale BDA with 3 levels is deployed herein. Fig. E.1 shows the constructed impedance matrix Q in different levels. In level 1, Q can be divided into 2×2 blocks, and Q_{11} in level 1 can be further divided into 2×2 sub-blocks in level 2. Subsequently, the Q_{11} in level 2 can be again divided into 2×2 sub-blocks in level 3. Finally, the Q_{11} in level 3 is a matrix with a small size, and it can be processed efficiently using LU decomposition method. The basic idea of multiscale BDA is that the computation of a dense matrix can be firstly conducted in the finest level, which is time-saving, and the computed results in the finest level are then substituted to the previous levels in order to obtain the final computed result of a dense matrix.

A simple description of the BDA is given herein, and more details can be found in [168]. Let us consider the linear system generated in the formulation

$$B = QX \tag{E.2}$$

where B is the excitation, Q is the constructed impedance matrix and X is the unknown

currents. It then can be partitioned with the form

$$\begin{bmatrix} B_1 \\ B_2 \end{bmatrix} = \begin{bmatrix} Q_{11} & Q_{12} \\ Q_{21} & Q_{22} \end{bmatrix} \begin{bmatrix} X_1 \\ X_2 \end{bmatrix} \tag{E.3}$$

The partitioned inverse matrix of Q is

$$Q^{-1} = \begin{bmatrix} \tilde{Q}_{11} & \tilde{Q}_{12} \\ \tilde{Q}_{21} & \tilde{Q}_{22} \end{bmatrix} \tag{E.4}$$

with

$$\tilde{Q}_{11} = Q_{11}^{-1} + Q_{11}^{-1} Q_{12} \tilde{Q}_{22} Q_{21} Q_{11}^{-1} \tag{E.5a}$$

$$\tilde{Q}_{12} = -Q_{11}^{-1} Q_{12} \tilde{Q}_{22} \tag{E.5b}$$

$$\tilde{Q}_{21} = -\tilde{Q}_{22} Q_{21} Q_{11}^{-1} \tag{E.5c}$$

$$\tilde{Q}_{22} = (Q_{22} - Q_{21} Q_{11}^{-1} Q_{12})^{-1} \tag{E.5d}$$

Let us define

$$D_{11} = Q_{11}^{-1} \tag{E.6a}$$

$$D_{12} = D_{11} Q_{12} \tag{E.6b}$$

$$D_{21} = Q_{21} D_{11} \tag{E.6c}$$

$$D_{22} = (Q_{22} - Q_{21} D_{12})^{-1} \tag{E.6d}$$

Equations (E.5) can be rewritten as

$$\tilde{Q}_{11} = D_{11} + D_{12} D_{22} D_{21} \tag{E.7a}$$

$$\tilde{Q}_{12} = -D_{12} D_{22} \tag{E.7b}$$

$$\tilde{Q}_{21} = -D_{22} D_{21} \tag{E.7c}$$

$$\tilde{Q}_{22} = D_{22} \tag{E.7d}$$

We wish to compute

$$X = Q^{-1} B \tag{E.8}$$

which in partitioned form (E.3),(E.4) is

$$X_1 = \tilde{Q}_{11}B_1 + \tilde{Q}_{12}B_2 \tag{E.9a}$$

$$X_2 = \tilde{Q}_{21}B_1 + \tilde{Q}_{22}B_2 \tag{E.9b}$$

Using equations in (E.7), we can compute X_1, X_2 in terms of D_{11}, D_{12}, D_{21} and D_{22} as

$$X_2 = D_{22}(B_2 - D_{21}B_1) \tag{E.10a}$$

$$X_1 = D_{11}B_1 - D_{12}X_2 \tag{E.10b}$$

The algorithm $D = BDA(Q)$, given below, returns the four D_{11}, D_{12}, D_{21} and D_{22} operators from (E.6) that together permit fast reconstruction of the partitioned inverse

---

Algorithm 1 FUNCTION D=BDA(Q)

if $Q \neq$ *partioned* **then**
  $D = LU\ of\ Z$
else
  $D_{11} = BDA(Q_{11})$
  $D_{12} = MULT(D_{11}, Q_{12})$
  $D_{21} = MULT(Q_{22}, D_{11})$
  $D_{22} = BDA(Q_{22} - Q_{21}D_{12})$
end if

When the Algorithm 1 is called, it calls itself recursively to compute the partitioned inverse operators for the two blocks, Q_{11} and $Q_{22} - Q_{21}D_{12}$. When the sub-blocks are not further partitioned, at the finest level (level 3 in our case), an LU decomposition is returned. The Algorithm 2 $X = MULT(D, B)$ is called in the second line of Algorithm 1, which returns the product of two matrices. The Algorithm 2 is given below based on (E.10)

Algorithm 2 FUNCTION X=MULT(D,B)

if $D \neq$ *partioned* **then**
  $X = U^{-1}L^{-1}B$
else
  $X_2 = D_{22}(B_2 - D_{21}B_1)$
  $X_1 = D_{11}B_1 - D_{12}X_2$
end if

Once the entire recursively partitioned impedance matrix Q has been converted into the recursively partitioned inverse operator D through the Algorithm 1, the solution of the linear system (E.2) is obtained by using Algorithm 2 according to (E.10). The entire inverse operator D, including D_{11}, D_{12}, D_{21} and D_{22}, is the first argument and the excitation B is the second argument of the Algorithm 2.

Usually, a non-square impedance matrix will be finally constructed according to the strategy introduced in Chapter 5.2. The non-square matrix can be solved by using the smallest least-square error solution as discussed in Sec. 4.4.1, yet it generates errors in using the block decomposition method. In this case, additional sources are added after the $SPWm$ and $SPWs$ are fixed for a specific object in order to form a square impedance matrix. These sources are uniformly placed on a quarter circle in the middle of a octant in order to satisfy the condition:

$$2N_m^b = 3N_s^b + 3N_{add}^b + N_{com} \tag{E.11}$$

with

$$N_{add}^b = \lfloor \frac{2N_m^b - 3N_s^b}{3} \rfloor$$

where $\lfloor\rfloor$ symbol represents the flooring function used to obtain an integer value. $N_{add}^b + N_{com}$ points are then placed on a quarter circle. In the first octant, this quarter circle is specified with $\phi = 45^\circ$, θ ranges from 0 to $\pi/2$ and radius $r_{13} = (r_{12} + r_{21})/2$. In the first N_{add}^b points, each IDT is placed at each point. N_{com} could be 0, 1 or 2. If $N_{com} = 1$, the last point is placed with a $\hat{\boldsymbol{x}}$-polarized infinitesimal dipole with a uniform magnitude. Otherwise two infinitesimal dipoles with $\hat{\boldsymbol{x}}$ and $\hat{\boldsymbol{y}}$ polarizations are placed at the last point. Based on the above scheme, a square impedance matrix is finally generated.

We take the example where a PEC sphere is illuminated by a plane wave with an unit magnitude of $\hat{\boldsymbol{x}}$ polarized electric field and propagating along the $-z$ axis. The the impedance matrix is constructed with $SPWm = 2.5$, $SPWs = 1.375$ and $N_{add}^b = 56$. The definitions of $SPWm$ and $SPWs$ can be found in Sec. 5.1. The size of the constructed matrix is 16320×16320. Two approaches are utilized for solving the unknown currents with complex magnitudes, one is the introduced BDA and the other is the LU. A relative error metric is defined as:

$$I^{error} = \frac{I^{BDA} - I^{LU}}{max\{I^{BDA}, I^{LU}\}} \tag{E.12}$$

The real and imaginary parts of I^{error} are calculated and shown in Fig. E.2. It is found that the LU decomposition can provide an accurate solution for the unknown complex coefficients of currents. In this case, the currents solved by BDA approach are not accurate since an extremely large difference is observed in Fig. E.2. The simulation is conducted on the server

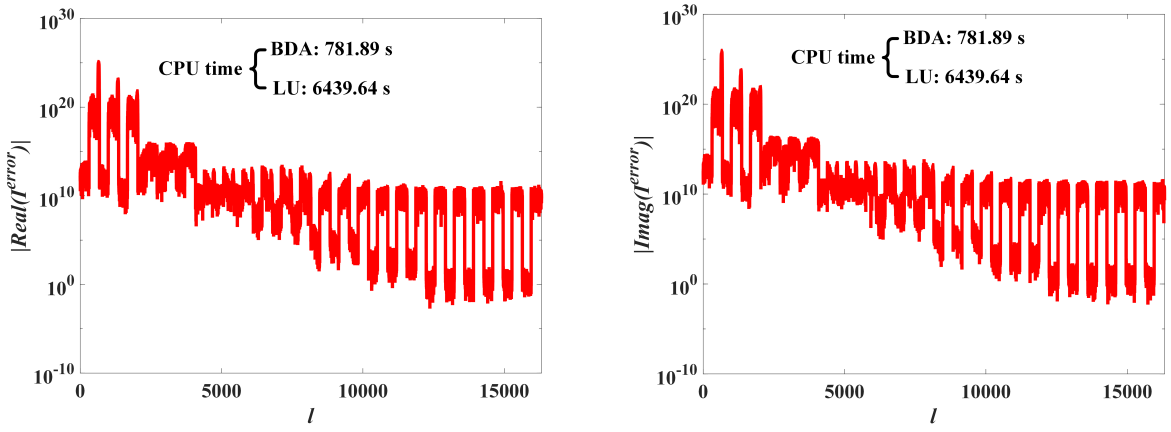

Figure E.2 (a)Real and (b) imaginary parts of I^{error} with respect to a matrix generated in the RCS calculation of a sphere illuminated by a plane wave.

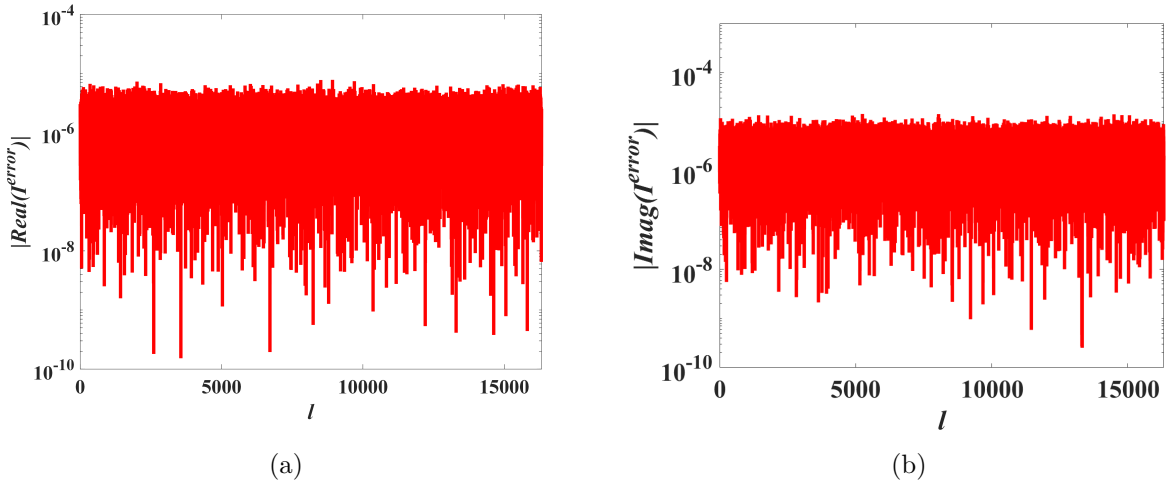

Figure E.3 (a)Real and (b) imaginary parts of I^{error} with respect to a matrix generated randomly.

with an Intel(R) Xeon(R) E5-2680@2.70 GHz. Although the CPU time for solving the currents coefficients has been reduced by using the BDA approach, the accuracy issue makes it unable to be used in the MIDM. The reason for the high value of I^{error} is due to the stability of the impedance matrix $[Q]$. $rcond([Q]) = 1.68 \times 10^{-18}$ is obtained for the constructed $[Q]$, where $rcond$ is a function defined in MATLAB used to test the stability of a matrix. If $[Q]$ is well conditioned, $rcond([Q])$ is near 1.0, and if $[Q]$ is badly conditioned, $rcond([Q])$ is near 0. To further study this issue, we replace the constructed matrix by a new matrix with the same size but generated through the function $rand$ in MATLAB. The $rcond([Q])$ of the new matrix is 1.503×10^{-7} this time. The excitation is kept the same with the previous example. The calculated I^{error} is shown in Fig. E.3, and this time, the error between the two approaches is quite small, which is around 10^{-5} level. The difference in obtaining Fig. E.2 and E.3 appears in the considered impedance matrix. Obviously, the BDA can be deployed in the MIDM to fast calculate a dense linear system as long as the ill-conditioned issue could be solved.